

# Capillary nanostamping with spongy mesoporous silica stamps

---

## **Doctoral Thesis**

By Mercedes Schmidt

Institute of Chemistry of New Materials and Center for Cellular Nanoanalytics  
(CellNanOs) – University Osnabrück

**2019**



Dissertation zur Erlangung des akademischen Grades Dr. rer. Nat.

Vorgelegt von Mercedes Schmidt, geb. 06.05.1986, Bad Urach

Im Institut für Chemie neuer Materialien, Physikalische Chemie, und dem Zentrum zellulärer Nanoanalytik (CellNanOs), Universität Osnabrück

Erstgutachter Prof. Dr. Martin Steinhart

Zweitgutachter Prof. Dr. Markus Haase

## Acknowledgments

First, I would like to thank **Prof. Dr. Martin Steinhart** for his great mind and ideas, for his achievement of the project of capillary nanostamping and for giving me the opportunity to join the project and contribute my part to it. I would like to thank him for being available almost all of the time, for great discussions and supporting me throughout the whole time.

I would like to thank **Prof. Dr. Markus Haase** for the opportunity to join the CellNanOs community and for sharing his laboratory with our group. I want to thank him for examining my doctoral thesis and for the nice discussions.

I would like to thank **Dr. Helmut Schäfer** for our great discussions and his ideas.

I would like to thank **Prof. Dr. Wolfgang Harneit** and **Dr. Carola Meyer** for their support and the collaboration in several projects within this work. Special thanks go to **René Wieczorek** for our collaboration, which evolved to a friendship. I am glad for your support and for the helpful discussions. René carried out ODMR,  $T_1$  relaxation and fluorescence microscopy measurements at the Institute of Physics at the University of Osnabrück.

I would like to thank **Prof. Dr. Dirk Enke**, **Maximilian Münzner** and **Alexander Grimm** for carrying out nitrogen sorption measurements at the Institute of Inorganic Chemistry at the University of Leipzig and for their support concerning the measurements.

I would like to thank **Jonas Klein** for carrying out measurements with the quartz micro balance in the Organic Chemistry at the University of Osnabrück.

I would like to thank **Dr. Markus Gallei** from the TU Darmstadt for providing me the PFS-*b*-P2VP material and **Hanna Hübner** for her support concerning this material.

The technicians of a work group are always very important people, they show you how it is done and support you with the best they can do. This is more than true for **Claudia Heß**, **Christine Schulz-Kölbel**, **Brigitte Hartmann-Azanza** and **Heinrich Tobergte**. Thank you so much!

Having great colleagues means looking forward to go to work every morning – at least most of the time. Thank you so much **Michael Philippi**, **Qaiser Ali Khan**, **Fernando Vázquez-Luna**, **Markus Geuß**, my former colleague **Anna Eichler-Volf** and my colleague from the biology department **Michael Holtmannspötter**. You made my days! Special thanks go to **Ruža Periz**, who became much more than a colleague, but a dear friend I would never want to miss. You are the Joey to my Chandler, and the Chandler to my inner Joey!



In addition, I would like to thank my parents **Pia** and **Dieter Schmidt**, who always believed in me and supported me in any way they could. In addition, I would like to thank my best friends **Simone Arnold** and **Thomas Held**, for always having my back.

Finally, I would like to thank **Sebastian Runge**, the love of my life. You are always there, not just when I need you, but always. Coming to Osnabrück and meeting you was the best thing that ever happened to me. I love you!

## **Ehrenwörtliche Erklärung**

Hiermit versichere ich, dass ich die vorliegende Arbeit selbstständig und ohne Benutzung anderer als der angegebenen Hilfsmittel angefertigt habe; die aus fremden Quellen direkt oder indirekt übernommenen Gedanken sind als solche kenntlich gemacht. Die Hilfeleistungen anderer Personen bei Messungen sind als solche gekennzeichnet und an entsprechender Stelle vermerkt. Weitere als die erwähnten Personen waren an der Erstellung dieser Arbeit nicht beteiligt. Es wurde keine Hilfe von Vermittlungs- oder Beratungsdiensten in Anspruch genommen. Die Arbeit wurde bisher weder im In- noch im Ausland in gleicher oder ähnlicher Form einer anderen Prüfungskommission vorgelegt und auch nicht veröffentlicht.

Osnabrück, den

Mercedes Schmidt





---

# Table of Contents

<b>1</b>	<b>Introduction</b>	<b>5</b>
<b>2</b>	<b>State of the art</b>	<b>8</b>
<b>2.1</b>	<b>Lithography</b>	<b>8</b>
2.1.1	Serial lithographic methods	8
2.1.2	Mask-based lithography	12
2.1.3	Maskless, parallel stamping processes	16
2.1.3.1	<i>Topographic structuring</i>	16
2.1.3.2	<i>Stamping including material transfer</i>	21
<b>2.2</b>	<b>Sol-gel synthesis and reinforcement strategies</b>	<b>27</b>
<b>3</b>	<b>Experimental</b>	<b>30</b>
<b>3.1</b>	<b>Materials and methods</b>	<b>30</b>
3.1.1	Methods and sample pretreatment	30
3.1.1.1	<i>Atomic force microscopy (AFM)</i>	30
3.1.1.2	<i>Confocal fluorescence microscopy/spectroscopy</i>	30
3.1.1.3	<i>Contact angle measurements</i>	30
3.1.1.4	<i>Dynamic light scattering (DLS)</i>	31
3.1.1.5	<i>Fluorescence spectroscopy</i>	31
3.1.1.6	<i>FT-IR spectroscopy</i>	31
3.1.1.7	<i>Nitrogen sorption measurements</i>	31
3.1.1.8	<i>Optically detected magnetic resonance (ODMR)</i>	31
3.1.1.9	<i>Quartz crystal microbalance</i>	32
3.1.1.10	<i>Scanning electron microscopy (SEM)</i>	32
3.1.1.11	<i>Other instruments</i>	33
3.1.1.12	<i>Size and shape analysis</i>	33
3.1.2	Chemicals	34
3.1.3	Materials	36
<b>3.2</b>	<b>Procedures</b>	<b>36</b>
3.2.1	General procedures and preparation	36

---

3.2.1.1	<i>Silanization of macroporous silicon templates</i> .....	36
3.2.1.2	<i>Silanization of substrate surfaces with different silanes</i> .....	36
3.2.2	Stamp syntheses .....	37
3.2.2.1	<i>Silica stamps – first generation</i> .....	37
3.2.2.2	<i>Silica stamps – second generation</i> .....	38
3.2.2.3	<i>Silica stamps – third generation</i> .....	38
3.2.3	Stamp holder and stamp preparation .....	39
3.2.4	Stamping procedures and subsequent functionalization .....	39
3.2.4.1	<i>Stamping of C<sub>60</sub> fullerenes from toluene onto FDTS-glass</i> .....	39
3.2.4.2	<i>Stamping of 1-dodecanethiol from ethanol onto gold-coated glass</i> .....	39
3.2.4.3	<i>Dewetting of polystyrene after stamping of 1-dodecanethiol from ethanol onto gold-coated glass</i> .....	40
3.2.4.4	<i>Stamping of nanodiamonds from isopropanol onto FDTS-glass</i> .....	40
3.2.4.5	<i>Functionalization of stamped nanodiamonds via click-chemistry with cyanine-3-DBCO</i> .....	41
3.2.4.6	<i>Stamping of Zeonex from toluene/chloroform onto FDTS-glass</i> .....	42
3.2.4.7	<i>Stamping of PS-b-P2VP from toluene/chloroform onto different functionalized substrates and subsequent swelling of the BCP</i> .....	42
3.2.4.8	<i>Stamping of PFS-b-P2VP from toluene/chloroform onto different substrates and subsequent growing of CNTs</i> .....	42
3.2.4.9	<i>Stamping of 17<math>\alpha</math>-ethinylestradiol (EE<sub>2</sub>) with subsequent redispersion and functionalization with fluorescent dye</i> .....	43
<b>4</b>	<b>Results and discussion .....</b>	<b>45</b>
<b>4.1</b>	<b>Capillary nanostamping with mesoporous silica stamps – stamp design .....</b>	<b>45</b>
4.1.1	Silica stamps – first generation.....	46
4.1.2	Silica stamps – second generation .....	48
4.1.3	Silica stamps – third generation.....	51
4.1.3.1	<i>Stamps with pore diameters of 31 nm</i> .....	51
4.1.3.2	<i>Stamps with pore diameters of 44 nm</i> .....	54
4.1.4	Stamping process .....	56
<b>4.2</b>	<b>Capillary nanostamping of selected model inks .....</b>	<b>60</b>

---

4.2.1	Meniscus confined particle growth – stamping of C <sub>60</sub> fullerenes from toluene onto hydrophobic glass.....	60
4.2.2	Self-limited spreading – stamping of 1-dodecanethiol from ethanol onto gold-coated glass .....	66
4.2.2.1	<i>Microscopic characterization</i> .....	66
4.2.2.2	<i>Image analysis</i> .....	67
4.2.2.3	<i>Structure formation model</i> .....	71
4.2.2.4	<i>Dewetting of polystyrene on 1-dodecanethiol stamped gold-coated glass slides</i> .....	72
4.2.3	Particulate inks – stamping of nanodiamonds from isopropanol onto hydrophobic glass .....	74
4.2.3.1	<i>Functionalization of stamped nanodiamonds with a diameter of 5 nm</i> .....	80
4.2.4	Stamping of Zeonex from toluene/chloroform onto hydrophobic glass.....	85
4.2.5	Stamping of PS- <i>b</i> -P2VP from toluene/chloroform onto differently functionalized glass with subsequent solvent treatment.....	89
4.2.5.1	<i>Contact angle measurements</i> .....	90
4.2.5.2	<i>Stamping onto hydroxyl-terminated glass</i> .....	91
4.2.5.3	<i>Stamping onto FDTS-functionalized glass</i> .....	95
4.2.5.4	<i>Stamping onto DMDCS-functionalized glass</i> .....	98
4.2.5.5	<i>Stamping onto ATAS-functionalized glass</i> .....	100
4.2.5.6	<i>Discussion of stamping of PS-<i>b</i>-P2VP and comparison of the impact of the differently functionalized substrates</i> .....	103
4.2.6	Stamping of PFS- <i>b</i> -P2VP from toluene/chloroform onto hydroxyl-terminated and FDTS-functionalized glass with subsequent pyrolysis.....	106
4.2.6.1	<i>Stamping of PFS-<i>b</i>-P2VP onto hydroxyl-terminated glass</i> .....	107
4.2.6.2	<i>Stamping of PFS-<i>b</i>-P2VP onto FDTS-functionalized glass</i> .....	109
4.2.6.3	<i>Pyrolysis of stamped PFS-<i>b</i>-P2VP spots</i> .....	112
4.2.6.4	<i>Growing of CNTs onto pyrolyzed PFS</i> .....	114
4.2.7	Active pharmaceutical ingredients – stamping of 17 $\alpha$ -ethinylestradiol (EE <sub>2</sub> ).....	118
4.2.7.1	<i>Stamping of EE<sub>2</sub> and analysis of obtained particles</i> .....	120
4.2.7.2	<i>Detachment of stamped EE<sub>2</sub> particles into aqueous dispersion</i> .....	122
4.2.7.3	<i>Click-chemical functionalization of EE<sub>2</sub> particles from dispersion</i> .....	125

## **5 Conclusion and outlook ..... 127**

---

<b>6</b>	<b>Appendix</b> .....	<b>131</b>
6.1	List of abbreviations .....	131
6.2	Publication list .....	133
6.2.1	Publications as first author .....	133
6.2.2	Publications as co-author .....	133
6.3	Curriculum vitae .....	135
<b>7</b>	<b>References</b> .....	<b>136</b>



## 1 Introduction

In the recent years of research and development, many approaches on generating nanostructures have been made. With the physical properties of materials in the nanometer size range, technological applications in the fields of e.g. electronics,<sup>[1]</sup> optoelectronics<sup>[2]</sup> and biological or chemical sensors<sup>[3]</sup> can be designed. For the generation of devices like displays,<sup>[4]</sup> lab-on-a-chip systems<sup>[5]</sup> or data storage,<sup>[6]</sup> a patterning of the nanomaterial is essential to obtain the desired functionality.

Many lithographic methods to pattern surfaces both by a mechanical manipulation of the surface or by printing functionalities in the form of particles or molecules have been developed and used in research. The different approaches to achieve the desired patterned substrate are various and imply respective advantages and disadvantages. This work is focusing on contact-lithographic methods. Examples for contact-lithographic methods are soft lithography and polymer-pen lithography. Firstly introduced by Whitesides and co-workers in 1998<sup>[7]</sup> and Mirkin and coworkers in 2008,<sup>[8]</sup> respectively, their applications range from patterning of complex polymer structures to degradation processes of enzymes in defined stamped regions.<sup>[9,10]</sup> Especially those two methods are widely used in research as they create patterns of molecules on counterpart substrates with high definition and a large variety of different materials and applications.

One of the main drawbacks of the previously mentioned methods is the lateral dimension of the obtained pattern. Due to limitations of stamps, materials and the methods themselves, feature sizes of arrays consisting of discrete spots in the sub-micrometer range remain challenging. Another factor in the state-of-the-art contact-lithographic methods is the *ex situ* adsorption of ink prior to the stamping procedure and thus, an uninterrupted flow of ink cannot be guaranteed. As the variety of imaginable inks is wide and the appropriate solvent often appears to be of organic nature, state-of-the-art contact-lithographic methods are unable to print these inks. The elastomeric polymer stamps used within contact-lithographic methods swell or dissolve in contact with organic solvents. Often, contact-lithographic methods require expensive equipment or defined conditions, e.g. high vacuum or a solvent-enriched humidity, and cannot be carried out in a simple and efficient way under ambient conditions.

In this work, a new approach to generate patterned structures with feature sizes in the sub-micrometer range and spot-to-spot distances in the one-micron range is presented. Stamps with an integrated, continuous pore system generate the patterns while the ink is supplied through the capillaries of the stamp. The method of capillary nanostamping

provides a simple and low-cost stamping procedure by the synthesis of spongy mesoporous silica stamps. Due to a continuous pore system within the stamp, the ink can be supplied continuously and even without a refilling system, the stamp itself serves as ink reservoir. This provides a continuous or intermittently ink supply for a stamping process with several stamping cycles without the need to refill the stamp. A new stamp or re-inking after one stamping cycle is not necessary. The stamping process is carried out manually by hand under ambient conditions. Due to the silica network, the stamps can be infiltrated with organic solvents.

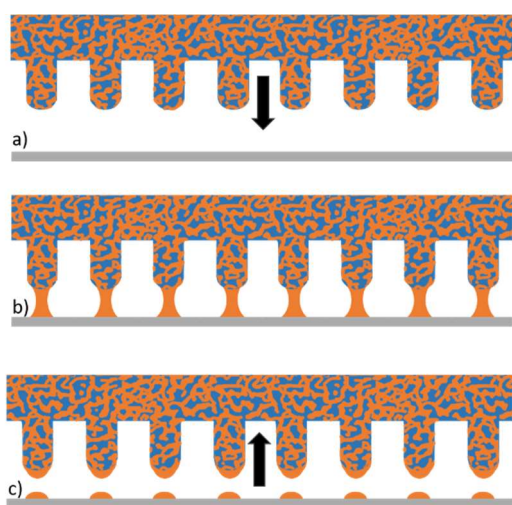


Figure 1. Illustration of the general stamping process. a) The mesoporous stamp (blue) is brought into contact with a counterpart substrate surface (grey). b) Capillary bridges of ink (orange) form between the contact elements of the stamp and the counterpart substrate surface. c) By removing the stamp from the substrate, droplets of ink are deposited on the substrate surface.

The procedure of capillary nanostamping is illustrated in Figure 1. A mesoporous silica stamp (blue) is infiltrated with ink (orange) and brought into contact with a counterpart substrate surface (grey, Figure 1a). Typically, the ink consists of a non-volatile component dissolved or dispersed in a volatile solvent. When the stamp is in close contact with the substrate surface, capillary bridges of solvent form. Within these capillary bridges, the ink is precipitated onto the substrate (Figure 1b). After a certain amount of time, the stamp is removed from the substrate and the ink forms liquid droplets on the surface (Figure 1c). After the volatile solvent evaporated, a pattern of the non-volatile ink component is generated.

The development of spongy mesoporous silica stamps for capillary nanostamping is presented in this work by demonstrating the progress from pure silica stamps in a typical well-known sol-gel synthesis to spongy and flexible silica stamps with a reduced network

bonding and hydrophobic internal residues. For the proof of concept of capillary nanostamping with spongy mesoporous silica stamps, several different inks are stamped. All inks are chosen with respect to a potential application and consist of a volatile organic solvent to proof the stability of the stamps against these solvents, and a non-volatile component, which remains on the substrate surface after precipitation and drying of the solvent. As ink, a dispersion of C<sub>60</sub> fullerenes in toluene is stamped onto perfluorinated glass slides. A solution of 1-dodecanethiol in ethanol is stamped onto a gold-coated glass with the outcome of a heterogeneous surface. As a model for nanoparticles, nanodiamonds dispersed in isopropanol are stamped and subsequently functionalized with a fluorescent dye in a click-reaction. A polymer and two different block copolymers dissolved in toluene/chloroform are stamped onto differently functionalized substrate surfaces to analyze the dependency of the nature of the substrate on the stamping results. In a final experiment, a solution of 17 $\alpha$ -ethinylestradiol in acetonitrile is stamped as a model for an active pharmaceutical ingredient and subsequently detached from the substrate surface to obtain a defined nanodispersion.

## 2 State of the art

### 2.1 Lithography

Lithographic methods have always been used to print on surfaces or to generate figures or patterns in a desired fashion. Reaching from a woodblock printing process in the ancient China, to the printing of single molecules onto surfaces, many different lithographic methods have been invented and enhanced over the years. As this work is based on the contact-lithographic method of a maskless, parallel stamping procedure, the methods discussed in the following sections are sorted towards this method. First, an overview of serial lithographic methods, as well as mask-based methods is given. Subsequently, maskless, parallel stamping processes are discussed in detail.

#### 2.1.1 Serial lithographic methods

In contrast to parallel stamping methods, where a large area of a desired pattern can be generated in a single stamping process, serial lithographic methods generate much smaller structured areas within similar time scales. In general, serial techniques imply a higher precision and therefore, smaller feature sizes can be achieved. In addition, the variety of obtained structures by serial lithography is independent from masks or pre-structures and thus, arbitrary patterns can be written. On the other hand, serial lithographic methods are working in a pixel-by-pixel manner and are normally time consuming and long-lasting procedures.

The serial lithographic methods with the highest resolution are the electron-beam (e-beam) and focused ion beam (FIB) lithography. In the e-beam lithography, an electron beam is focused on a substrate with electron-sensitive resist and generates patterns in a pixel-by-pixel fashion as shown in Figure 2. The FIB lithography works in a similar principle, but with cations – normally gallium – instead of electrons on arbitrary substrates. With FIB lithography, the substrate material is directly removed and thus, no photoresist is needed. These methods generate nanoscale patterns with a resolution of 5-20 nm, but have a very low throughput due to the pixel-by-pixel patterning. In addition, they have to be carried out under high vacuum and are time consuming and cost intensive. Therefore, the methods of e-beam or FIB lithography are normally used for the production of masks for other lithographic methods or the fabrication of nanoscale prototypes.<sup>[11,12]</sup>

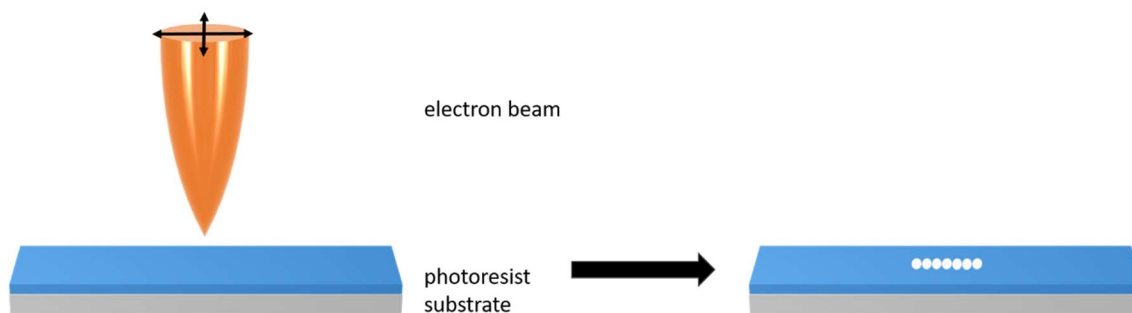


Figure 2. Illustration of maskless electron beam lithography. The electrons are focused on a substrate (grey) containing a photoresist (blue) pixel by pixel for the desired pattern, which results in holes in the photoresist.

Another serial lithographic method is the scanning probe lithography. For this, the tip of an atomic force microscope (AFM) is used to manipulate a substrate. It can be scratched, heated or oxidized. Mirkin *et al.*<sup>[13]</sup> described the dip pen nanolithography (DPN), where molecules adsorbed on the AFM tip are used to pattern the substrate. Figure 3 shows a schematic illustration of DPN, where the AFM tip is coated with molecules by immersion of the cantilever. During contact between the tip and the substrate, the adsorbed molecules are deposited onto the substrate surface by capillarity and local wetting.

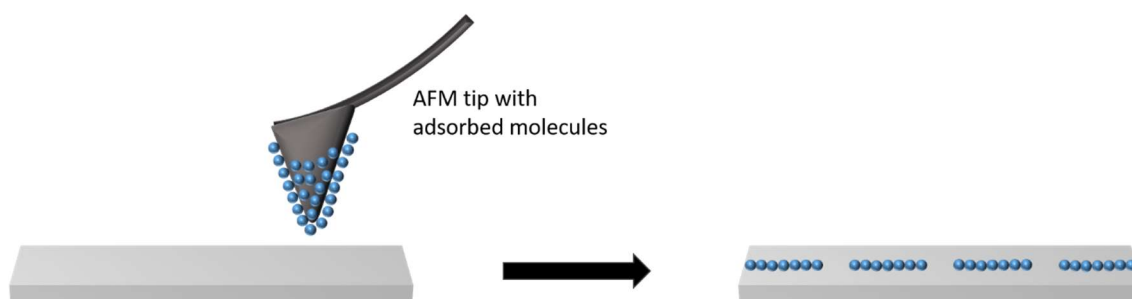


Figure 3. Illustration of dip pen nanolithography with adsorbed molecules (blue) on the AFM tip (black). Deposition of the particles on the substrate (grey) is performed by contact between the tip and the surface.

This method leads to precisely patterned surfaces and proceeds under ambient conditions. Nevertheless, only small areas can be patterned and the AFM tip has to be re-immersed with the molecules to be printed from time to time. Therefore, DPN is a time consuming method. Nowadays, DPN is used to create terabit-per-square-inch storage and has the potential to even work with a high number of AFM tips simultaneously on one surface.<sup>[6,14]</sup> The group of Schubert presented the manipulation of silicon wafer surfaces by silanization of the surface with octadecyl trichlorosilane and a local probe oxidation of the silane. In a subsequent reaction with quarternary ammonium salts, gold

nanoparticles could be adsorbed onto the patterned surface.<sup>[15]</sup> Chai *et al.* printed block copolymers from an aqueous solution with DPN.<sup>[16]</sup>

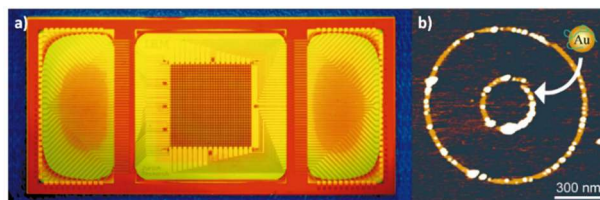


Figure 4. Examples of the method of dip pen nanolithography. a) A fabricated computer chip<sup>[14]</sup> and b) adsorbed gold nanoparticles on a functionalized patterned wafer.<sup>[15]</sup>

As a further development of DPN, the method of nanoscale dispensing (NADIS) uses the AFM tip as a dispenser for attoliter volume.<sup>[17]</sup> For NADIS, the AFM tip has a small opening at its apex generated with FIB lithography. The hole size can vary and ranges from a few tens of nanometers to the submicron range. NADIS can be performed with a standard AFM equipment under ambient conditions. As shown in Figure 5a, the top of the AFM tip serves as an ink reservoir with space for some 100's of femtoliters of ink. When the tip is brought into contact with the substrate surface, the ink is precipitated by capillarity.<sup>[17]</sup>

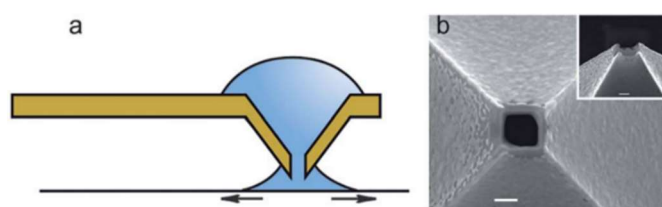


Figure 5. Illustration of the NADIS principle.<sup>[18]</sup> a) An AFM tip with a hole at the apex is loaded with liquid. When brought into contact with a substrate surface, the liquid is precipitated by capillarity. b) Electron microscopy image of the apex of a NADIS tip. The aperture amounted to 310 nm. The scale bar is 200 nm.

NADIS provides a method with a continuous ink flow. Although the ink reservoir appears to be small, one loading can be used for the dispensing of more than 1000 droplets.<sup>[17]</sup> Nevertheless, as the amount of ink in the reservoir is small, solvents with low evaporation rates (e.g. glycerol) have to be used to circumvent the ink from drying out. The obtained structure sizes range from 60 nm to  $\approx 1 \mu\text{m}$ .<sup>[19]</sup> The structure sizes can be influenced by a chemical modification of the substrate surface, where a hydrophilic surface provokes larger sizes and a hydrophobic surface smaller structure sizes. Another factor of influence is the chemical modification of the outer tip surface as shown in Figure 6. If the

AFM tip is hydrophobic (Figure 6a), the resulting structure sizes appear small. If the AFM tip is chemically modified (in this case by coating dodecanethiol onto the gold surface of the tip, Figure 6b), the sizes of the resulting structures appear larger.<sup>[19]</sup> In addition, the contact time between AFM tip and substrate surface can influence the size of the obtained structure. Nonetheless, after a certain contact time, an equilibrium state is reached and further contact has no longer influence in the structure size.

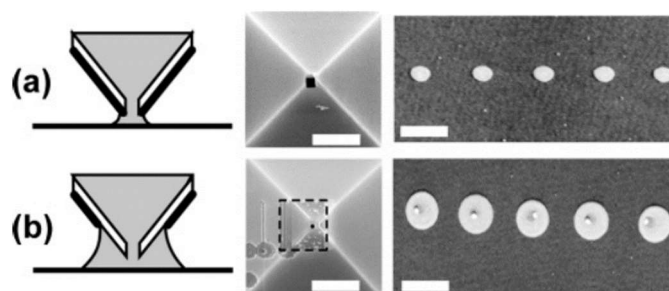


Figure 6. Differently functionalized NADIS tips and the belonging results after printing.<sup>[19]</sup> a) Hydrophobic tip with an aperture of 200 nm resulted in droplets with diameters of  $\approx 400$  nm. b) Hydrophobic-hydrophilic tip with an aperture of 80 nm and surroundings coated with dodecanethiol in the size of  $800 \times 800$  nm<sup>2</sup> resulted in droplets with diameters of  $\approx 1$   $\mu$ m.

An advantage of this method is the use under ambient conditions with standard AFM equipment. Only small amounts of ink are needed and a large variety of non-volatile ink components can be used. In addition, the ink reservoir guarantees a continuous ink supply and can be refilled without interruption of the precipitation process.<sup>[17]</sup> A disadvantage is the time needed for a large area of dispensed droplets, as one droplet needs about 0.5 s. The surface has to be chemically modified, as a bare SiO<sub>2</sub> surface results in an instantaneously total liquid transfer and ink spreading over the surface. In addition, only solvents with low evaporation rates can be used to circumvent the ink from drying out within the small ink reservoir.

Vengasandra *et al.*<sup>[20]</sup> deposited quantum dots in a micrometer size range with the method of NADIS. Another application of NADIS is presented by Deladi *et al.*<sup>[21]</sup> where two AFM tips are used, one represents the FIB-modified NADIS tip and the second one is used as a scanning tip. When the ink encounters the surface, it generates a chemical or mechanical modification whilst the second tip scans the ongoing alteration simultaneously.

### 2.1.2 Mask-based lithography

Another category of lithographic methods is the mask-based lithography. In this category, patterns are created by applying a mask onto a substrate surface. In general, the mask is defining the pattern, which in turn is created either by irradiation of a photoresist through the mask or by applying the mask directly in contact with the substrate. The pattern can consist of a material on top of the substrate or the substrate material itself, which is etched through the mask. In addition, a material can be precipitated through the mask. In either case, the mask has to be removed after the pattern is created and is destroyed in some methods.

The most common technique in the category of mask-based lithography is the photolithography, which is mainly used in the integrated circuit and semiconductor industry.<sup>[22]</sup> The operating principle (Figure 7) is to transfer a pattern onto a substrate by an etching process of a photoresist (a UV light polymerizable organic polymer), which is coated onto the substrate surface. In the pattern transfer step, the exposed area of the surface, which is not protected by the photoresist, is etched in a dry or wet etching process. The generally used technique of dry etching is achieved with plasma or reactive ion etching (RIE), which avoids undercutting of the photoresist. The wet etching procedure is obtained by e.g. KOH. After the etching process, the photoresist is removed and the desired structure is obtained on the substrate surface. While the photoresist is destroyed during the process, the photomask can be reused.

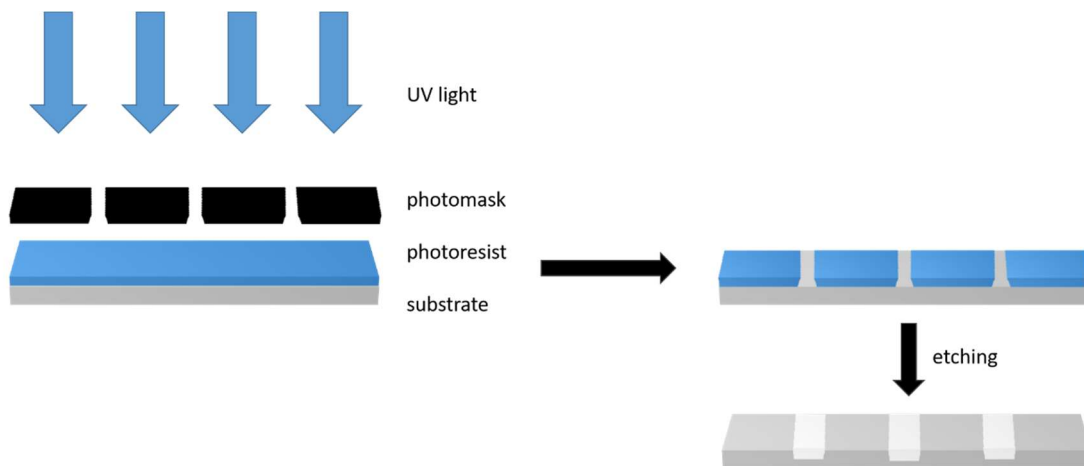


Figure 7. Photolithographic process. A substrate (grey) to be patterned is coated with a photoresist (blue), which resolves through UV light irradiation. A structured photomask (black) is put on top of the substrate, UV light resolves the photoresist and leaves the desired structure on the substrate surface. A subsequent etching procedure of the substrate generates a structure where the substrate is not protected by the photoresist. After the etching procedure, the photoresist is removed.



This technique is highly common and up to this day of great interest due to the high throughput and large variety of patterns to create.<sup>[23,24]</sup> Nevertheless, the most effort is put into minimizing the lateral dimensions of the pattern, which is still challenging. The resolution of the generated structures is limited by the wavelength of the used light. A deep ultraviolet (DUV) light from an excimer laser has wavelengths of 248 and 193 nm and allows a minimum feature size down to 50 nm.<sup>[25]</sup> Commonly, photolithography is used to create fabricated microstructures for further applications, such as electro oxidation of Si-wafers (Figure 8)<sup>[26]</sup> and synthesizing PDMS stamps.<sup>[27]</sup>

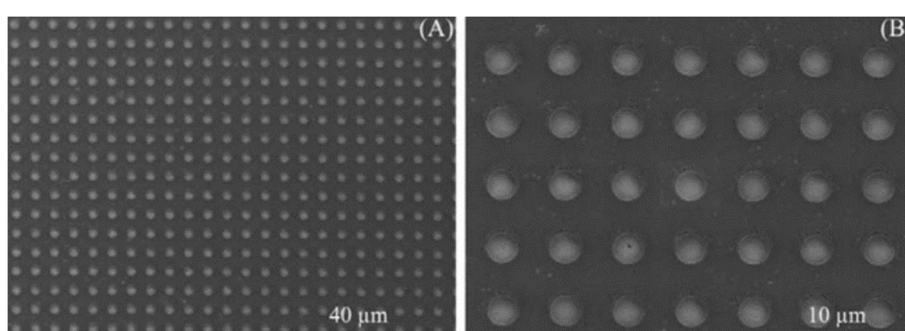


Figure 8. Example of a patterned silicon wafer using photolithography. A gold or silver layer is deposited onto the surface generated with photolithography and subsequently, a metal-catalyzed silicon etching generates the final pattern.<sup>[26]</sup>

Another mask-based method is the nanosphere lithography. In this method, a self-assembled monolayer of spherical nano- or microparticles (typical sphere sizes  $>100$  nm) on a substrate is used as a mask for the physical deposition of elements. After the deposition procedure, the particles are etched or washed away, and the desired element is patterned on the surface. For the basic nanosphere lithography, usually monodisperse polystyrene latex microparticles are deposited with spin coating or drop casting on a substrate surface. With the evaporation of the solvent, the microspheres form a self-assembled hexagonal packed monolayer on the substrate. By either thermal evaporation, e-beam deposition or pulsed laser deposition, normally a metallic material is deposited orthogonally to the surface.<sup>[28]</sup> After removing the microspheres from the substrate, a symmetric array of the deposited material is generated. The fabricated nanoparticles have a triangular shape with a  $P_{6mm}$  symmetry as shown in Figure 9.

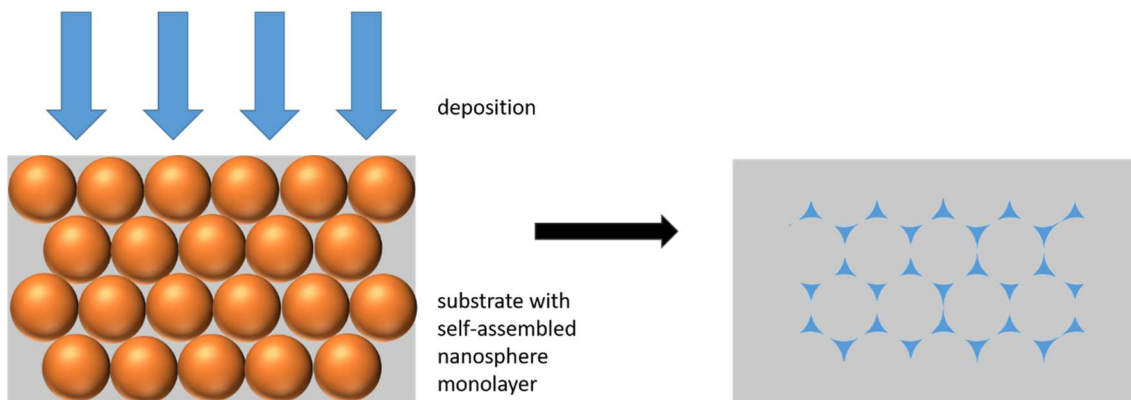


Figure 9. Illustration of nanosphere lithography with monolayered colloidal crystal mask (orange). Vapor deposition of a desired element results in triangularly shaped nanoparticles (blue) on the counterpart substrate (grey).

If the concentration of microspheres on the substrate surface is increased, the self-assembly of the microspheres forms hexagonally close-packed particles with more than one layer. With a second layer, every other hole is blocked, which leads to a lower density and a hexagonally arranged pattern of deposited spherical microparticles. If the higher concentration leads to three or more layers of microspheres, then a possible ABCABC packing results in full hole blocking, so no more material can be deposited onto the substrate surface.

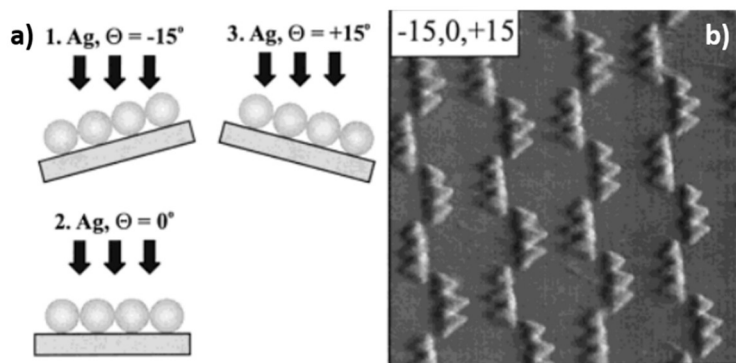


Figure 10. Example of shape variation by nanosphere lithography. a) The silver is deposited from three different angles to yield in the nanochain structure shown in b).<sup>[28]</sup>

The size of the deposited material can be tuned by increasing or decreasing the size of the microspheres. By other surface positions during the deposition, the particle shape can be tuned further, but is still limited to the shape of the microsphere holes. One example is shown in Figure 10. This technique produces parallel nanoparticles with a con-

trolled size, shape and interparticle spacing in an inexpensive way with a high throughput.<sup>[29]</sup> Nevertheless, the microspheres have to be chemically modified to avoid electrostatic interactions with the substrate surface and to obtain a homogeneous monolayer of microspheres. Typical defects as polydispersity and therefore occurring point or line defects or polycrystalline domains within the microspheres lead to typical domain sizes of 10-100  $\mu\text{m}^2$ . In addition, only a limited number of materials can be deposited, which are mostly inorganic metals and no organic particles can be fabricated with this method. In addition, the arrangement of the deposited material is limited by the symmetry of the microspheres. This leads to a main application in data storage, where single domain magnetic nanoparticles are needed.<sup>[28]</sup>

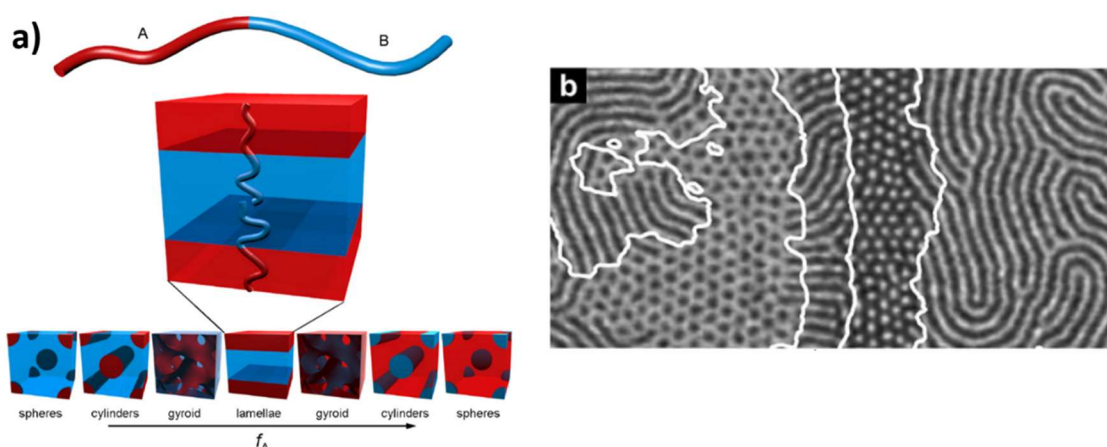


Figure 11. a) Illustration of thermodynamically stable diblock copolymer phases, where the two blocks, A and B, are simplified by a two-color chain. The self-organization of the blocks occurs in a way that the contact between the two immiscible blocks is minimized and an elongated chain conformation is avoided. The structure is primarily dependent on the relative volume fraction of the two blocks ( $f_A$ ).<sup>[30]</sup> b) Exemplary AFM image of different phases of a self-assembled BCP.<sup>[31]</sup>

Another method of mask-based lithography is the block copolymer (BCP) lithography. Here, a usually directed self-assembled BCP is used to generate a desired pattern on a substrate surface by microphase separation. Figure 11a shows different thermodynamically stable phases of a diblock copolymer. Dependent on the relative volume fraction ( $f_A$ ) of the single polymer, a minimized contact between the two immiscible blocks and the tendency to avoid entropic unfavorable elongated chain conformation, different microdomain structures can occur. Figure 11b shows an exemplary AFM image of different phases of a BCP coated on a substrate surface. In a directed self-assembly procedure, a specific phase can be generated.<sup>[32]</sup> Typically, this method is used for a further treatment with e.g. photolithographic procedures or to generate the negative BCP structure with other materials like silicon.<sup>[33]</sup> The feature sizes of the pattern are dependent on the

used BCPs and can be tuned within the range of the chain lengths. In a typical multiple-step procedure, where the BCP lithography is used as a mask for further treatment, the BCP is destroyed within the process.

Mask-based lithographic methods are normally based on the use of sacrificial masks or photoresists (for the method of photolithography, the photomask is reusable, but the photoresist is destroyed in the procedure) and therefore, for each process, a new mask or photoresist has to be generated. A mask-based lithographic procedure typically contains multiple steps and is a time consuming process.

### 2.1.3 Maskless, parallel stamping processes

Maskless, parallel stamping processes include both, stamping processes, where material is transferred, as well as methods for a topographic structuring. Although these methods are based on similar backgrounds and development steps, the following chapter is sorted correspondingly to the method of capillary nanostamping, which reflects a stamping method with material transfer.

#### 2.1.3.1 Topographic structuring

Techniques of producing topographic structured elastomeric polymers are well studied and used.<sup>[34]</sup> One example is the UV-imprint lithography. Here, a UV-curable polymer is structured by pouring or drop-dispensing it into a mold and curing it with UV irradiation. With this method, the resulting structured polymer can be hard or soft as reported by Yoo *et al.*<sup>[35]</sup> Another similar technique is the imprint lithography, where a hard mold is pressed into an elastomeric polymer, which is heated to a temperature above its glass transition temperature ( $T_g$ ) simultaneously.<sup>[36]</sup> Although the created shapes can reach sub-10 nm sizes, the imprinting lithographic process is limited. With imprint lithography in general, a large variety of surface structures can be created as shown in Figure 12.

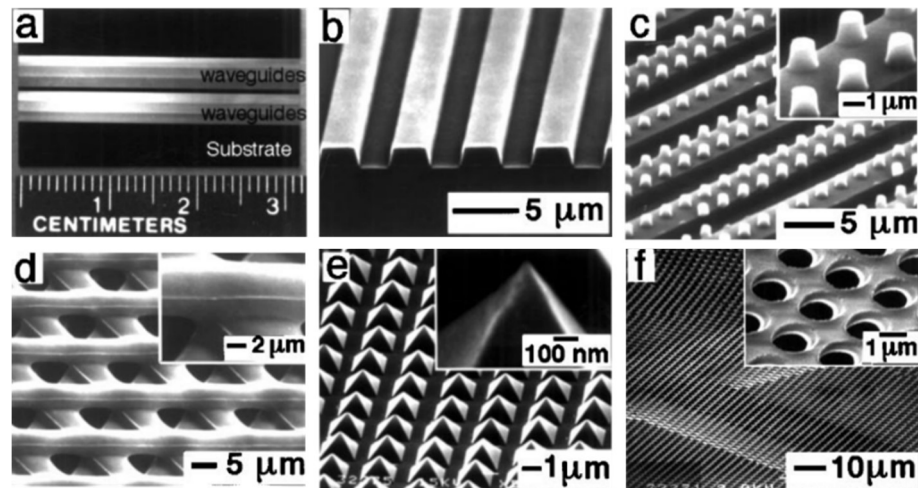


Figure 12. Example of polymeric microstructures fabricated with imprint lithography and microtransfer molding.<sup>[37]</sup>

Polydimethylsiloxane (PDMS) stamps can be used as molds, where the notches of the stamp serve as capillaries if put on a substrate surface. This is the principle of micromolding in capillaries (MIMIC), first published by Whitesides and co-workers in 1995.<sup>[38]</sup> The ink solution is poured at the open edges of the mold and is spontaneously filling the capillaries by capillary forces (Figure 13a).<sup>[39]</sup> The method is depending on the concentration of the solution, the size of the microchannels and the self-organizing properties of the solute, therefore the control of the experimental conditions is very important.<sup>[39]</sup> As the degree of wetting of the ink on the counterpart substrate plays an important role, concentration of ink, humidity and temperature have to be adjusted and controlled within the procedure. After the capillaries are completely filled (Figure 13b), Figure 13c and d show the control of the concentration of the solution and the related outcome. In the concentrated regime, the microchannels are filled up with solution while reaching supersaturation, which leads to a negative replica of the channels by the ink (Figure 13d). If the ink solution is diluted and the solvent starts to evaporate within the channels while reaching supersaturation, the ink accumulates on the boundaries of the channels and forms split lines or microstripes (Figure 13f).

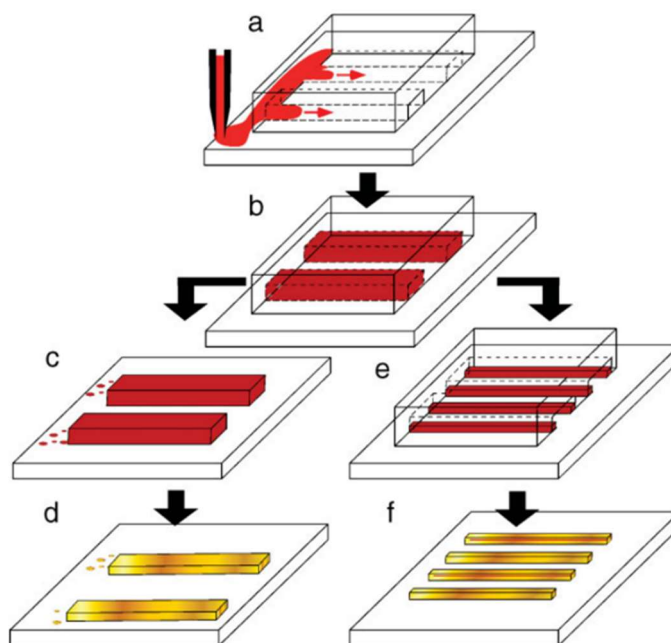


Figure 13. Schematic illustration of the principle of MIMIC.<sup>[39]</sup> a) A mold is placed onto a substrate surface and forms capillaries, the ink (red) is poured at the end of the capillaries and is sucked into the channels by capillarity. b) The mold is supersaturated with the ink. c) The pattern obtained by the concentrated regime is the negative replica of the mold. e) The pattern obtained by the dilute regime is dependent on the concentration and shows defects. d), f) After evaporation of the solvent.

Exemplary results of this principle are shown in Figure 14.<sup>[40]</sup> Here, the microchannels are filled with different solution volumes varying from filled up (100%, Figure 14a) to 25% filling (Figure 14d). The different outcomes can clearly be seen in the inserted AFM height profiles. When the microchannels are filled up 100%, the resulting structure is continuous (Figure 14a), while a 75% filling results in a structure showing defects and by the reduction to 50% filling, two separate lines are generated (Figure 14b and c). If the filling of the microchannels is reduced to 25%, randomly distributed particles are generated where the microchannels were applied onto the substrate surface (Figure 14d).

With MIMIC, possible applications are not widely spread due to several limitations of the method. Clearly, the mold has to consist of continuous channels and structures besides connected lines have to be obtained by subsequent dewetting, ripening or self-organization of the pattern. In addition, the solvent should be chosen so that a swelling of the mold is prevented. Some applications of MIMIC include the fabrication of a heterostructured field-effect transistor by using inorganic materials and a multistep procedure, published by Hu *et al.*<sup>[41]</sup> Cavalli *et al.* generated a pattern of magnetic nanoparticles in the sub- $\mu\text{m}$  size range with periodic features and a vertical solution of a monolayer by using MIMIC.<sup>[40]</sup>



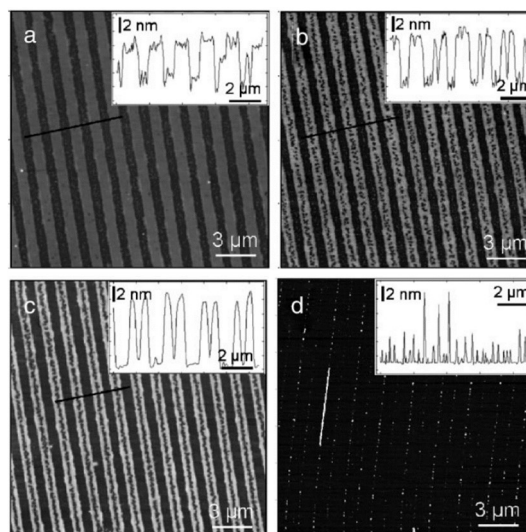


Figure 14. Exemplary results of the MIMIC principle showing different outcomes dependent on the degree of channel upfilling with ink solution.<sup>[40]</sup> a) 100%, b) 75%, c) 50%, d) 25% of the microchannels are filled with the ink solution. The insets show the AFM line scans with belonging heights of the obtained structures.

A larger variety of patterned structures can be fabricated with capillary force lithography. First presented by Suh *et al.* in 2001,<sup>[42]</sup> it combines nanoimprint lithography by molding a polymer melt, and soft lithography with the use of an elastomeric mold. The principle is the same as for MIMIC, the capillary force lithography uses masks with open ends and liquid polymers. A polymer is spin-coated onto a substrate, where an elastomeric PDMS mold is placed on top of the surface. Heating the spin-coated polymer to a temperature above  $T_g$  leads to a polymer melt with mobile polymer chains, which is filling up the voids of the mold driven by capillary forces.<sup>[43]</sup> After cooling to room temperature, the mold can be lift off and leaves a negative replica of polymer on the surface. Figure 15 shows the principle of capillary force lithography. If the polymer layer spin-coated onto the substrate is not thick enough to fill up the capillaries of the mold, menisci are formed on the edges of the capillaries and leave a double pattern due to a “molded dewetting” process (Figure 15b).<sup>[44]</sup>

The limitations of this method mostly originate from the mold, here the elastomeric behavior of PDMS influences the resolution. When the aspect ratio of the capillaries is too high, it causes stress originating from gravity, adhesion or capillary forces and results in collapse of the imprinted structures.<sup>[43]</sup> If the aspect ratio of the capillaries is too small, the recessed region will not be able to maintain its structure during stamping.<sup>[34]</sup> With PDMS as mold, the generation of sub-100 nm features is not possible and a stiffer material, such as polyurethane acrylate is used.<sup>[45]</sup> In general, the sizes of the generated patterns depend on the used mold material and this method is more suitable to generate large patterned structures.

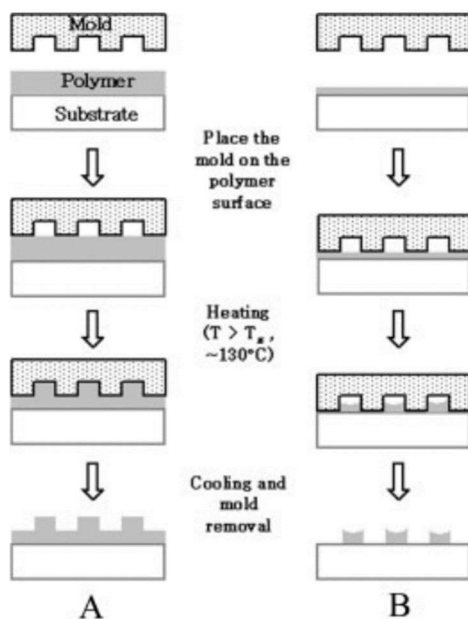


Figure 15. Illustration of capillary force lithography.<sup>[45]</sup> The mold (black dotted) is placed on a substrate (white) containing a spin-coated polymer film (grey), the polymer is heated to a temperature above  $T_g$  and starts to fill up the capillaries. After cooling down, the mold can be removed and dependent on the thickness of the polymer film, leaves a negative replica (A) or forms a meniscus within the capillaries (B).

With this method, Suh *et al.*<sup>[45]</sup> generated pillars up to 5  $\mu\text{m}$  in height and 80  $\mu\text{m}$  in line-and-space and even nanoparticles could be transferred, but only in a two-step procedure, where the nanoparticles were adsorbed onto the patterned polymer surface.<sup>[46]</sup> Another application of capillary force lithography is shown in Figure 16, where Moga *et al.* generated a flexible polymer with a microneedle array.<sup>[47]</sup> Other applications are found in the fields of biology<sup>[48]</sup> and the engineering of core-shell nanoparticles.<sup>[49]</sup>

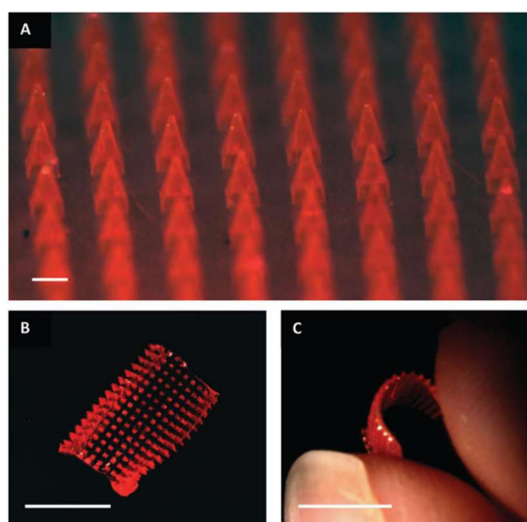


Figure 16. Example of capillary force lithography.<sup>[47]</sup> A flexible microneedle array produced with capillary force lithography. The scale bar in A is 200  $\mu\text{m}$ , scale bars in B and C are 1 cm.



### 2.1.3.2 Stamping including material transfer

The mostly used lithographic method related to maskless, parallel stamping is the micro-contact printing ( $\mu$ CP) as reviewed by Xia and Whitesides already in 1998.<sup>[7]</sup> As stamp, an elastomeric polymer – mostly PDMS – is produced by a soft lithographic process as illustrated in Figure 17.

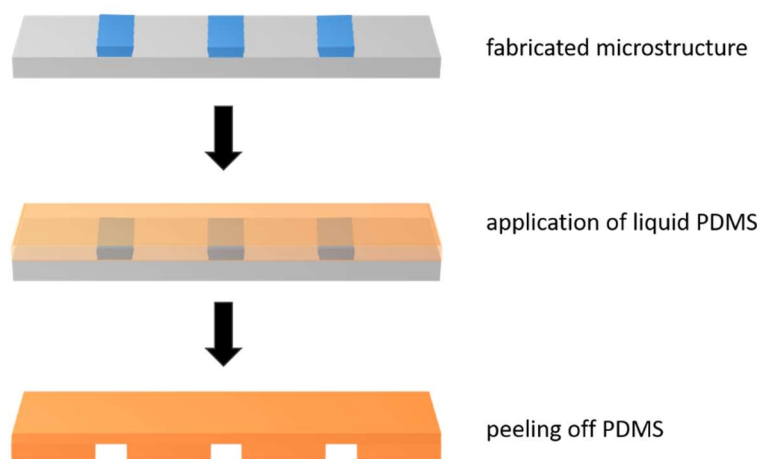


Figure 17. Illustration of the production process of PDMS stamps. A fabricated microstructure (e.g. by photolithography, grey-blue) is molded with an elastomeric PDMS precursor (orange). After curing of the PDMS, it can be peeled off and consists of the reverse structure of the molding template.

For this purpose, a microstructure in a desired shape and size is produced by e.g. photolithography or other lithographic methods. The polymer precursor is applied onto the mold; after curing and hardening, it can be peeled off and consists of the negative replica of the mold.

To use the obtained structured polymer as a stamp for  $\mu$ CP, it is e.g. immersed into a solution of molecules or particles to be transferred. After the adsorption process of the desired ink, the stamp is dried. Printing is carried out by pressing the PDMS stamp onto the counterpart surface, sometimes with the addition of e.g. a weight or UV light curing for a faster drying of the ink (see Figure 18).

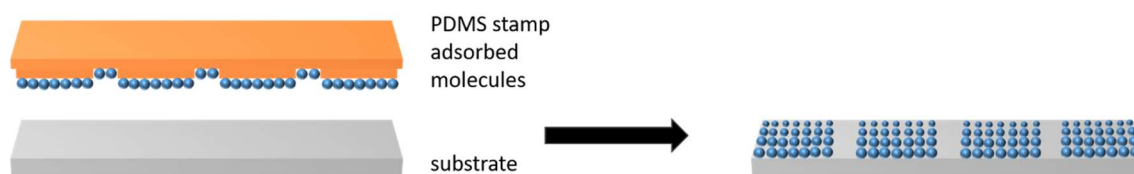


Figure 18. Process of microcontact printing ( $\mu$ CP) with PDMS stamps. The desired molecules or particles (blue) are adsorbed onto the PDMS surface (orange); after drying, the PDMS stamp is pressed onto a counterpart surface (grey). The molecules adsorbed on the contact elements are transferred onto the counterpart surface.

Microcontact printing is easily available, simple and low cost in fabrication of PDMS stamps; due to the softness of the stamps, curved substrate surfaces can be printed and even rolling stamp systems are made with great interest due to a wide range of industrial applications.<sup>[50]</sup> The drawback of this method is a normally long-lasting adsorption process of the molecules to be stamped onto the PDMS surface. In addition, the stamping often has to be performed under UV light irradiation or another catalyst for the certainty of the ink transfer. Moreover, due to a missing ink supplying system, commonly only one stamping cycle without deterioration of the quality of the stamped pattern can be carried out. Due to the PDMS, the stamps do not withstand a number of organic solvents, such as toluene or hexane. Swelling of the PDMS due to the organic solvent causes the structures to deform or rupture, therefore the single contact elements cannot be too small. In addition, the accuracy of the structure can vary over a large area due to the deformability of the PDMS and thus, a homogeneous pressure has to be applied during the stamping procedure. Another disadvantage of the  $\mu$ CP with PDMS stamps is the lateral dimension of the contact elements of only down to 3  $\mu$ m and the size reduction has remained challenging.<sup>[51]</sup> The elastomeric PDMS would cause the stamp's contact elements to collapse if the lateral dimension is too small. In addition, the aspect ratio of the contact elements is of importance. Figure 19a shows a PDMS stamp with optimal aspect ratio, which is important for the stamp design, as an aspect ratio of height to length ( $H/L$ )  $> 5$  leads to a lateral collapse of the single stamp elements, also called pairing, as shown in Figure 19b. If the aspect ratio of  $H/L < 0.5$ , the recessed structures begin to decline and sagging occurs, as shown in Figure 19c. For a stamp with feature sizes smaller than 500 nm, a stiff layer of hard PDMS has to be supported by a flexible layer of PDMS, which is generated in a four-step procedure containing electron beam (e-beam) lithography and the combination of hard and flexible PDMS.<sup>[34]</sup>

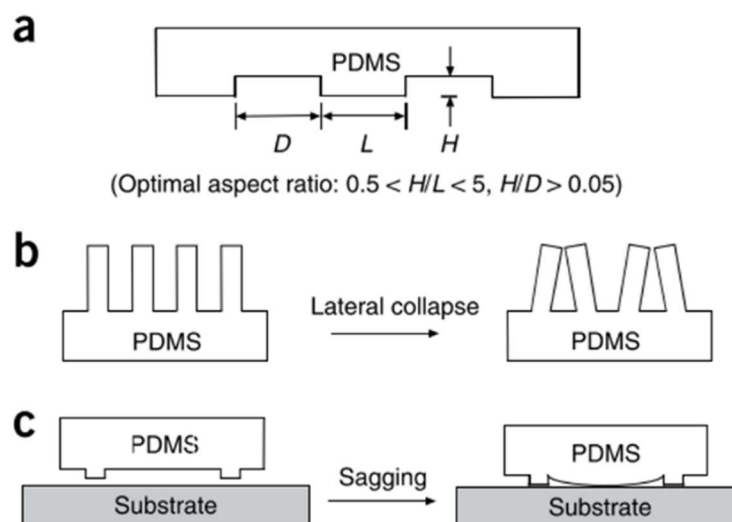


Figure 19. Possible problems occurring in the stamp design of PDMS stamps. a) PDMS stamp with optimal aspect ratio. b) If the aspect ratio  $H/L > 5$ , the relief structures collapse or pair. c) Sagging of recessed structures when the aspect ratio  $H/L < 0.5$ .<sup>[34]</sup>

Due to the hydrophobicity of PDMS, the stamp surface either has to be treated with ozone plasma or chemically modified, to make stamping of polar inks possible.<sup>[52]</sup> Nevertheless, surface modification opens a variety of usable inks with PDMS stamps. Therefore, stamping of biological polymers and DNA is carried out as well as stamping of initiators for polymer brushes to produce highly chemically active surfaces for further chemical modification.<sup>[53]</sup> As the PDMS is chemically affected during the ink adsorption process, where the PDMS is swollen; and the stamping procedure itself, where pressure is applied to the stamp, it is recommended to use a new stamp with each stamping process.<sup>[34]</sup>

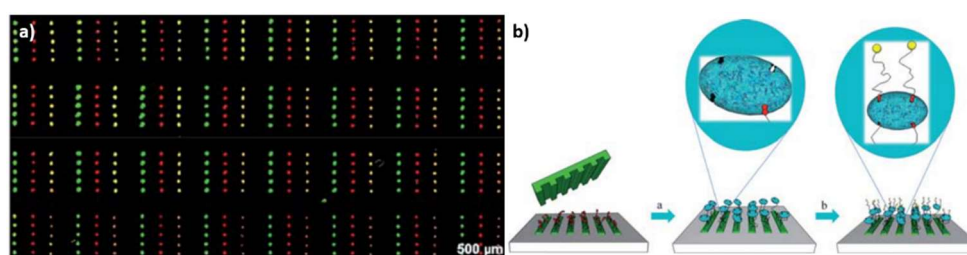


Figure 20. Examples of  $\mu$ CP with PDMS stamps. a) Printed DNA microarrays with coated PDMS stamps and b) printed biotin ligands for further biofunctionalization.<sup>[53]</sup>

Another way to create a patterned surface with the use of PDMS stamps is the particle transfer printing or lift-up soft lithography. In this method, colloidal particles – mostly monodisperse silica nanoparticles – are coated onto a substrate and form a uniform

monolayer or multiple layers.<sup>[54,55]</sup> A PDMS stamp with structured contact elements is brought into contact with the particles, normally under pressure or heating. Afterwards, the PDMS stamp is carefully peeled off the particle containing substrate and leaves the negative replica of its pattern on the substrate while the stamp adsorbs the particles of former contact.<sup>[56]</sup> In a second printing step, the adsorbed particles on the stamp can be printed onto another counterpart surface.

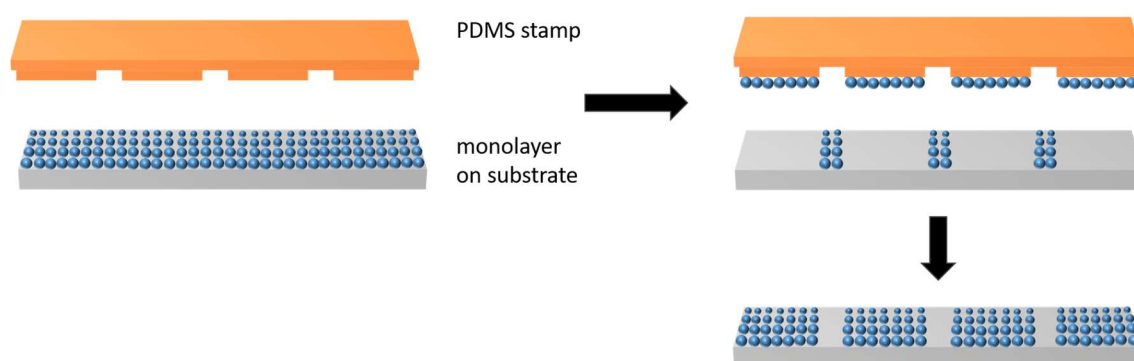


Figure 21. Schematic illustration of particle transfer printing. A monolayer of colloidal particles (blue) is applied on a substrate (grey), the PDMS stamp (orange) is brought into contact with the particles with simultaneous heating or pressure. The PDMS stamp is peeled off and contains the particles of former contact. The original substrate is left with the negative pattern of the PDMS stamp. Furthermore, the adsorbed particles on the PDMS stamp can be printed onto another counterpart surface in a second printing step.

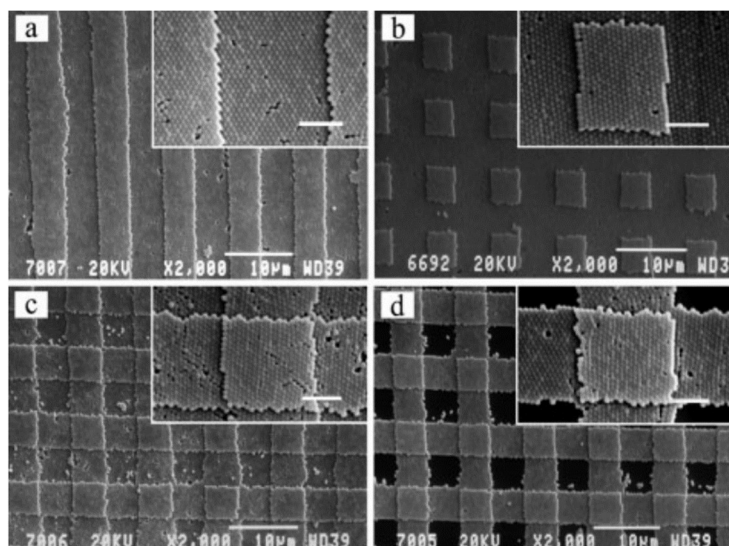


Figure 22. Example of the particle transfer printing process. Yao et al.<sup>[57]</sup> generated a 3D structure by the lift-up of colloidal silica nanoparticles from a multiple layered surface with a PDMS stamp with structured contact elements. All scale bars are 2 μm.

In Figure 22, an example of this particle transfer lithographic method is shown. By the lift-up of the upper layer of colloidal silica nanoparticles from a surface with multiple layers of particles, even 3D patterns could be created as reported by Yao *et al.*<sup>[57]</sup> This method generates 2D or 3D patterns of uniform particles, which can be further treated or functionalized. The patterns created by lift-up lithography are a few  $\mu\text{m}$  in size. When particles are used to pattern with lift-up lithography, the formation of precise edges is not possible as the obtained structures consist of nanospheres.

Another method within the category of parallel, maskless contact lithography is the polymer pen lithography. It was presented by Mirkin *et al.* in 2008<sup>[8]</sup> and is based on the combination of dip pen lithography (see chapter 2.1.1) with PDMS stamps. In the scanning probe-based polymer pen nanolithography, an array of elastomeric polymer tips is fabricated with prior lithographic methods. This array is then moved by a piezo scanner and, like in the common PDMS stamping method, desired molecules are adsorbed on the surface. With controlling of force of the tips and delivery time of the adsorbed molecules, patterns with spot sizes from 90 nm to over 10  $\mu\text{m}$  can be generated.<sup>[58]</sup> With this method, the group around Mirkin generated patterns of electronic circuits and protein nanoarrays.<sup>[59,60]</sup>

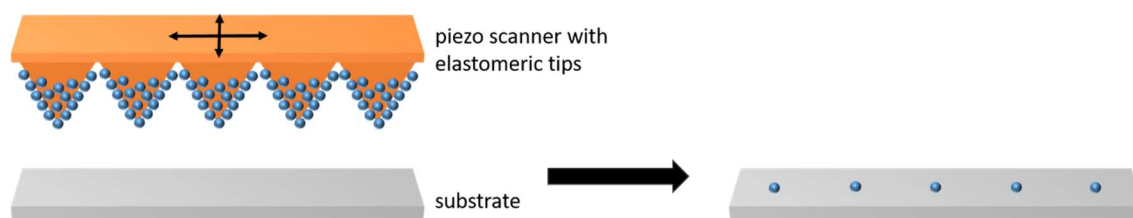


Figure 23. Illustration of polymer pen lithography. An array of pyramidal elastomeric tips (orange) is glued onto a glass slide, which is moved by a piezo scanner. When the tips are brought into contact with the substrate surface (grey), the adsorbed ink (blue) is dispensed onto the surface.

Although the typical contact element densities are some 100 per  $\text{mm}^2$ , the method of polymer pen lithography entails long-lasting preparation times including a time-consuming alignment process of the substrate prior to stamping, and requires a defined atmosphere. Furthermore, the single tips are large and have a minimal center-to-center distance of 10  $\mu\text{m}$ , which implies that printing of smaller sized patterns has to be done by displacing the stamp. The wait time between two printing steps is approximately around 15 minutes, during which the solvent moves onto the depleted pen tips. Additionally, the

relative positioning of the stamp between two contact cycles needs to be precisely adjusted using techniques (and time scales) of scanning probe microscopy. These factors result in ink loss throughout the stamped pattern and spot sizes with a high deviation as shown in Figure 24.<sup>[61]</sup> Within polymer pen lithography, the stamping procedure is carried out in a defined atmosphere containing evaporated solvent, which leads to a swelling of the PDMS. Therefore, lateral stamp element dimensions in a sub- $\mu\text{m}$  size range are impossible.

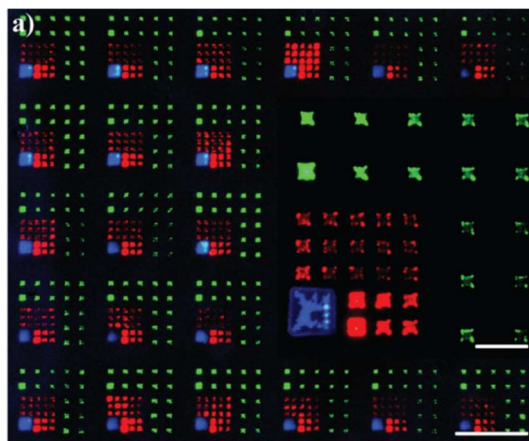


Figure 24. Example of an array of fluorescent molecules printed by polymer pen lithography.<sup>[61]</sup> The inset shows the magnification of the printed pattern with a scale bar of  $20\ \mu\text{m}$  (scale bar of big image equals  $100\ \mu\text{m}$ ). The spot sizes and accuracies vary significantly within the printing process.

The factor that all of the above presented methods have in common is that elastomeric PDMS is mainly used as stamp material. Elastomeric PDMS used for  $\mu\text{CP}$  is important for the conformal contact between stamp and counterpart surface, transfer molding and decal transfer.<sup>[34]</sup> But also, it is a source of technical problems as described above. The aspect ratio within the stamp design has to be within a certain range to obtain suitable stamps as described in Figure 19. A stamp with lateral dimensions below  $3\ \mu\text{m}$  remains challenging due to the elasticity of the PDMS, which causes the stamp's contact elements to collapse if the lateral dimension is too small. Before stamping, the surface of the stamp has to be modified due to its hydrophobicity and thus, the adsorption of an aqueous solution would be impossible when left untreated. The ink has to be adsorbed on the PDMS stamp, which is a long-lasting process and stamping is only possible under defined humidity and temperature conditions. The adsorbed ink can be precipitated within one stamping cycle and has to be repeatedly adsorbed for each additional stamping cycle. Pressure has to be applied during stamping and it is recommended to use a fresh stamp for each stamping cycle.<sup>[34]</sup>



## 2.2 Sol-gel synthesis and reinforcement strategies

The sol-gel chemistry provides a huge variety of materials to be synthesized. Its relevance up to this date is still high and working groups all around the world published almost 18,000 articles in 2018 alone (see Google Scholar). The processes of hydrolysis and condensation reactions of silica precursors in a catalytic (acidic or basic) medium are nowadays well understood and described in detail elsewhere.<sup>[62]</sup> The synthesis and conditions can be conveniently customized for each individual desire. Defined mesopore systems can be generated by introduction of structure directing agents within the synthesis to generate 2D or 3D pore structures in a large variety throughout the whole silica network.<sup>[63,64]</sup> Either particles or monolithic gels can be generated. After synthesis and aging of a monolith, the obtained hydrogel is typically dried. When the wet silica is dried under ambient conditions, the boundary between the liquid and the vapor phase causes the liquid to form menisci inside the pore channels. Hence, the Laplace pressure on the liquid-vapor interface induces stress within the wet gel. This stress causes the pore channels to collapse and the generated pore structure cannot be maintained after drying. This generates a dense structure with smaller pores compared to the wet gel, which is called xerogel.

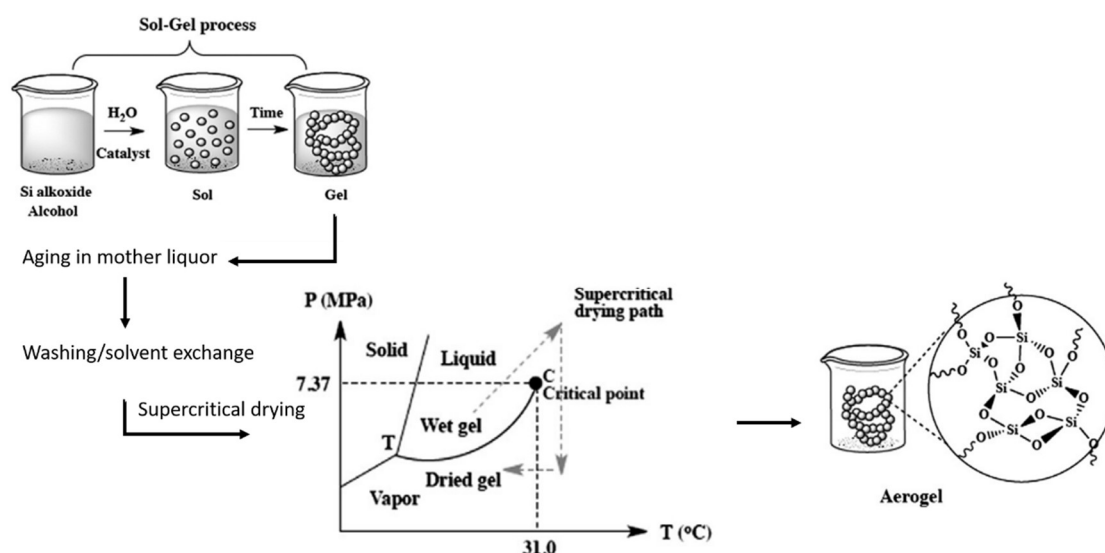


Figure 25. Schematic illustration of the sol-gel synthesis. By the supercritical drying procedure, an aerogel is generated consisting of the exact structure as the hydrogel where the liquid is replaced by air.<sup>[69]</sup>

The hydrogel can also be dried in a supercritical drying procedure with liquid CO<sub>2</sub>. The supercritical drying path is shown in Figure 25 within the phase diagram of CO<sub>2</sub>. Drying under supercritical conditions (high pressure, heat, dependent on solvent) prevents a

phase boundary between gas and liquid phases. In the state of a supercritical fluid, the densities of liquid phase and vapor phase become equal and the formation of menisci within the pores is prevented. With this method, the exact pore structure of the hydrogel can be conserved.<sup>[65]</sup> This leaves an aerogel with very low density and high surface area, high insulating properties and a withstanding of high temperatures at a light weight. Overall, sol-gel processes are of low cost and normally fast. The applications derive from sensors, catalysts, over storage media and thermal insulator to space applications.<sup>[66–68]</sup>

The mostly used silica precursor is tetraethylortho silicate (TEOS) and one of the most common silica materials is the mesoporous MCM-41 silica.<sup>[70,71]</sup> Babin *et al.*<sup>[72]</sup> produced silica monoliths consisting of MCM-41 material with control of macro- and mesoporosity. The as-synthesized macroporous monoliths using polyethylene oxide (PEO) as structure directing agent are hydrothermally post-treated with ammonia, which leads to a formation of disordered mesoporosity and stabilizes the network. Due to the basic post-treatment, a dissolution-precipitation process of the silica is induced which results in mesopores without changing the silica skeleton.

Pure inorganic silica gels are normally brittle and of poor mechanical stability. There are several different methods to reinforce pure silica for greater mechanical stability in the literature.<sup>[69]</sup> One method is to produce ORMOSILs (ORganically MODified Silica), where the co-gelation of the silica precursor with an organic polymer (such as PDMS) is induced. In this case, the compression of the silica is increased of up to 30%.<sup>[73]</sup> Another method is to mechanically reinforce the silica. Zhang *et al.* incorporated polypropylene fibers into the silica as supporting skeleton for the network.<sup>[73]</sup>

Another possibility of generating flexible or even spongy aerogels is the synthesis of silsequioxanes. Here, the precursor consists of less than four polymerizable functionalities, which leads to a less interconnected network with a higher flexibility. The molecular formula of silica changes from  $\text{SiO}_2$  to  $\text{RSiO}_{3/2}$  ( $\text{R} = \text{H, alkyl, aryl, alkoxy}$ ), this causes a reduction of free hydroxyl groups in the silica network and – dependent of the incorporated residue – a change to hydrophobic silica gels.<sup>[74,75]</sup> The group of Kanamori synthesized methylsilsequioxane materials by using methyltrimethoxy silane (MTMS, three dimensional network see Figure 26) as the silica source.<sup>[76]</sup> Due to less bonding within the silica network, they could determine a linear compression of up to 80% with a spring-back behavior of the gels to more than 95% of their original size.



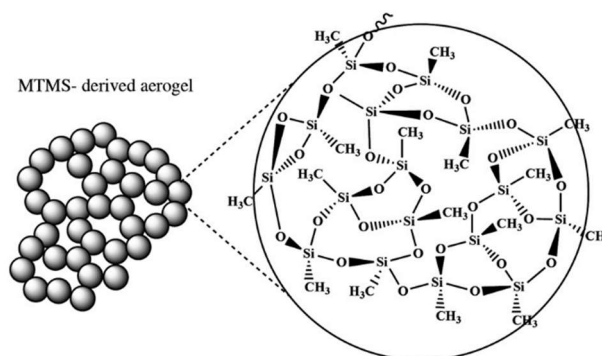


Figure 26. Three dimensional network structure of a sol-gel derived from the trifunctional precursor MTMS.<sup>[69]</sup>

As aerogels are prepared by pouring the liquid sol-gel into a polymeric container, the obtained shape of the aerogel is dependent on the container and can be chosen freely. To obtain a secondary structure on the outer surface of the aerogel, a template can be used and will be replicated by the sol-gel. Grimm *et al.*<sup>[77]</sup> achieved this secondary structure by pressing a nanorod array made from poly(methyl methacrylate) (PMMA) into the sol-gel with the outcome of mesoporous silica aerogels with macropores perpendicular to the surface. Figure 27 shows a schematic illustration of this synthesis.

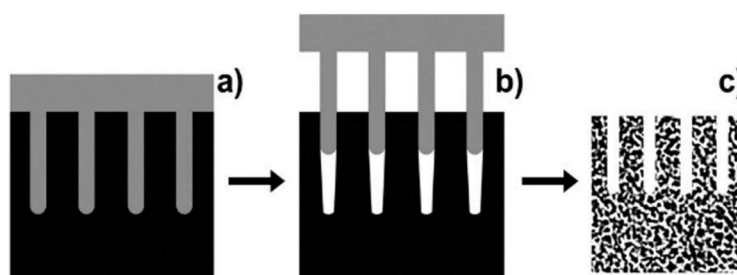


Figure 27. Illustration of the preparation of mesoporous silica aerogels with macropores as secondary structure. a) The PMMA nanorod array (grey) is applied to a sol-gel (black), b) the shrinkage of the gel presses out the nanorods. c) The aerogel after drying has both mesopores, as well as a lateral macroporous feature.<sup>[77]</sup>

Silica is an appropriate material to obtain structured monoliths with a defined porous network. With low costs and a large variety of possibly achievable network structures and pore sizes, it provides a great opportunity to use it as a material for lithographic patterning.

## 3 Experimental

### 3.1 Materials and methods

#### 3.1.1 Methods and sample pretreatment

In the following chapter, the different methods used in this work are described concerning technical information and sample pretreatment. The chapters are in alphabetical order.

##### *3.1.1.1 Atomic force microscopy (AFM)*

Atomic force microscope (AFM) measurements were carried out with a NT-MDT Ntegra device using gold-coated silicon cantilevers with a force constant of 0.003–0.13 N/m. For the scanning, both contact and tapping mode were used. The tapping mode was used for samples with movable particles (fullerenes, nanodiamonds), while the contact mode was used for all other experiments due to a higher resolution.

##### *3.1.1.2 Confocal fluorescence microscopy/spectroscopy*

Confocal fluorescence microscopy was used to identify nanodiamonds on the substrate surface. The beam path was directed into a spectrometer using mirrors, where locally integrative spectra could be obtained. Fluorescence spectra were recorded using an excitation laser with a wavelength of 520 nm, an optical power of 413  $\mu$ W and a CCD camera (DU401A-BV, 25  $\mu$ m slit, 600 l/mm grating) from Andor. Spectral resolution was achieved by means of spectrograph (MS 125 77400) from Oriel Instruments. The calibration of the optical detection instrument has been done with a mercury-vapor lamp. The spectra were obtained by an integration time of 1 second per spectrum and accumulation of 100 single spectra. Confocal fluorescence measurements were carried out by René Wiczorek in the Physics Department at the University Osnabrück.

##### *3.1.1.3 Contact angle measurements*

Contact angles were measured in the sessile drop mode at 22 °C and a humidity of 37% using a drop shape analyzer DSA100 by Krüss. To obtain the contact angle of ethanol on gold containing a layer of 1-dodecanethiol, the gold-coated glass slide was immersed into a solution of 2 mM 1-dodecanethiol in ethanol for 5 s. To obtain the contact angle of toluene/chloroform (1:3) on a PS- and P2VP-coated glass slide, 2.5 mg of the respective polymer was dissolved in 500  $\mu$ L of chloroform and drop-casted onto a glass slide.

#### 3.1.1.4 *Dynamic light scattering (DLS)*

Dynamic light scattering (DLS) was carried out to obtain hydrodynamic diameters. For DLS, a Zetasizer nanoseries S from Malvern with a laser at a wavelength of 633 nm, was used at an equilibrium temperature of 25 °C. For the measurements, each sample was measured 2x15 times.

#### 3.1.1.5 *Fluorescence spectroscopy*

Fluorescence spectroscopy was carried out with a Cary Eclipse Fluorescence Spectrometer from Agilent Technologies. Fluorescence spectra were edited with OriginLab and the single curves were smoothed with a FFT-filter.

#### 3.1.1.6 *FT-IR spectroscopy*

Fourier-transformation infrared spectroscopy (FT-IR) was measured with a UATR Two from Perkin Elmer in an attenuated total reflection (ATR) mode.

#### 3.1.1.7 *Nitrogen sorption measurements*

Nitrogen sorption measurements were performed with a Porotec Surfer device at 77 K on dried samples. Before any measurement, the samples were outgassed at 250 °C for 10 h. The nitrogen sorption measurements were carried out by Maximilian Münzner and Alexander Grimm at the University of Leipzig.

To obtain the pore size distribution, the adsorption branch of the BET isotherm was used with the method of Barrett, Joyner and Halenda (BJH).<sup>[78]</sup> For the analysis, the program ASiQwin from Quantachrome Instruments was used.

#### 3.1.1.8 *Optically detected magnetic resonance (ODMR)*

Optically detected magnetic resonance (ODMR) measurements were conducted in a home-built confocal microscope setup. A 520 nm digital modulated Diode Laser from Swabian Instruments was used for optical excitation (CW mode) such as initialization and readout (pulsed mode). The focusing of the laser beam as well as the collecting of the fluorescent light of the NV<sup>-</sup> center was achieved by an oil immersion objective (PLAPON 60XO; NA = 1.42) from Olympus. The emitted photons were guided through

a 25  $\mu\text{m}$  pinhole, detected with an avalanche photodiode (SPCM-AQRH-24) from Excelitas and, subsequently, counted either by a NI PCI-6236 counter card (National Instruments) or by a commercially available FPGA based counter from Swabian Instruments. The microwave was applied by means of a 30  $\mu\text{m}$  copper wire fed through a MW generator (APSIN 6010) from AnaPico and a downstream connected 42.3 dBm amplifier (AS0104-30/17) from Milmega. The experimental control was accomplished by using adapted Qudi software.<sup>[79]</sup> The following pulse scheme was used for  $T_1$  relaxation measurements: 3  $\mu\text{s}$  laser pulse – 2  $\mu\text{s}$  waiting time – incrementing of the control variable – repetition. ODMR measurements were carried out by René Wiczorek in the Physics Department at the University Osnabrück.

#### 3.1.1.9 Quartz crystal microbalance

To estimate the thicknesses of the coated titanium and gold layers, an AT-cut eQCM quartz having a defined area was coated with metal under the same conditions as the glass slides and weighed prior to and after metal deposition using a GAMRY eQCM 10 M quartz crystal microbalance. The quartz crystal microbalance analyses were carried out by Jonas Klein in the Organic Chemistry at the University Osnabrück.

#### 3.1.1.10 Scanning electron microscopy (SEM)

For scanning electron microscopy (SEM) analysis, a Zeiss Auriga system with additional energy dispersive X-ray spectroscopy (EDX) and focused-ion beam (FIB) system was used both with a secondary electron chamber detector (SESI), as well as with an in-lens detector. The main differences of these two detectors is the position in the SEM chamber. In general, if a sample is irradiated with an e-beam, the depth of penetration is dependent on the density of the material, atomic number of the elements within the material and the acceleration voltage. The penetrating electrons interact with the sample material and generate secondary electrons, which in turn can be detected with the SEM. The geometry of the detector in the SEM chamber defines, which secondary electrons each single detector mainly detects. The SESI detector is attached laterally tilted to the sample surface and collects SE1 and SE2 secondary electrons and backscattered electrons. The spatial arrangement of the SESI detector gives a side view of the sample and thus, a topographic image can be acquired. The in-lens detector is attached parallel to the sample surface above the objective lens. This ensures the collection of almost sole secondary electrons of type SE1, limits the collection of scattered electrons and enhances the signal to noise ratio significantly. The electrostatic field promotes a sample image with a

higher contrast and much more surface information compared to the SESI detector. Due to the geometry of the in-lens detector and the exclusion of SE2 and backscattered electrons, topographic information disappears. Prior to SEM analysis, the samples were attached to a conductive sample holder and coated with a conductive layer of platinum and iridium with a K575X Sputter Coater by Emitech. All samples were analyzed with an accelerating voltage of 3 keV.

#### 3.1.1.11 Other instruments

Sonication was carried out with a Sonorex RK 102 H sonicator from Bandelin at a frequency of 35 kHz. Critical point drying was carried out with a CPD300Auto manufactured by Leica. Prior to the drying procedure, the solvent was exchanged three times with ethanol. The samples were placed in a sample holder under a filling of ethanol. Within the drying procedure, the ethanol was exchanged by liquid CO<sub>2</sub> for 25 times. After heating to 42 °C and adjustment of the pressure to 80 bar, the CO<sub>2</sub> was evaporated and dry samples without any change of the porous structure were obtained. To obtain metal-coated glass slides (titanium and gold), chemical vapor deposition was carried out by thermal evaporation in a vacuum chamber at 10<sup>-4</sup> mbar using a Balzers BAE 120 evaporator. Cleaning and hydroxyl termination of substrate surfaces was carried out with O<sub>2</sub> (at a pressure of 5 mbar) or air plasma for 10 min using a Diener femto plasma cleaner. Spin Coating was carried out using a G3P-8 from Specialty Coating Systems. A diluted solution was spin coated with a frequency of 300-3000 rpm.

#### 3.1.1.12 Size and shape analysis

The size and shape analysis of the obtained stamped spots, micelles or particles were analyzed, if not mentioned otherwise, by evaluating corresponding SEM images with the program ImageJ. For binarization, the threshold was selected in a way that the sizes of the stamped spots did not change with changing brightness and contrast. Subsequent, particle analysis was carried out with ImageJ. The particle diameter  $d$  was calculated with OriginLab from the obtained area values  $A$  with the formula<sup>[80]</sup>

$$d = \sqrt{4 \cdot \frac{A}{\pi}} \quad (1)$$

The circularity and the aspect ratio of an object are geometric descriptors quantifying the deviation of the object's contour from that of an ideal circle, for which aspect ratio and circularity equal 1. The circularity was calculated with the formula<sup>[80]</sup>

$$C = \frac{4\pi \cdot A}{\text{perimeter}^2} \quad (2)$$

The aspect ratio was calculated with

$$AR = \frac{[\text{Major axis}]}{[\text{Minor axis}]} \quad (3)$$

### 3.1.2 Chemicals

Table 1. Register of used chemicals within this work. The indices of the polymers show the repeat unit

Chemical	Supplier	Purity	Pre-treatment
11-Bromoundecyltrichlorosilane	Gelest	95%	
17 $\alpha$ -Ethinylestradiol	Sigma-Aldrich	98%	
1-Dodecanethiol	AlfaAesar	98%	
1H,1H,2H,2H-Perfluorodecyltrichlorosilane (FDTs)	Abcr	97% (stabilized with copper)	
Acetic acid 10 mM	Merck	Puriss	
Acetonitrile	Sigma-Aldrich	ACS reagent, 99.5%	
C <sub>60</sub> Fullerenes	New Jersey Institute of Technology (Newark, USA)	C <sub>60</sub> :C <sub>70</sub> :higher fullerenes $\approx$ 78 wt%: 20 wt%: 2 wt%	99.9 wt% of C <sub>60</sub> by sublimation at $\approx$ 500 °C, chromatographic separation on activated charcoal/silica gel, preparative HPLC
Chloroform	Roth	For synthesis, >95%	
Cyanine-3-DBCO	Lumiprobe	95%	
Dimethyldichloro silane (DMDCS)	Merck	For synthesis	
Dimethylformamide (DMF)	Fluka	Purum, 98%	
Ethanol	Brekel AHK Alkoholhandel	Anhydrous, 100%	

Isopropanol	ORG Laborchemie	For analysis, 99.8%	
Methyltrimethoxy silane (MTMS)	Sigma-Aldrich	98%	
N-(2-aminoethyl)-2,2,4-trimethyl-1-aza-2-silacyclopentane (ATAS)	Gelest		
Nanodiamonds (NDs), 10 nm	Adámas	RT-DND detonation nanodiamonds, diameter: 10-13 ± 5 nm	Acid treatment by heating under reflux in a 1:1:1 volume ratio of sulfuric acid, perchloric acid and nitric acid
Nanodiamonds (NDs), 5 nm	Ray-Techniques Ltd.	RT-DND detonation nanodiamonds, diameter: 4-5 ± 3 nm	Acid treatment by heating under reflux in a 1:1:1 volume ratio of sulfuric acid, perchloric acid and nitric acid
n-Hexane	Fisher Chemicals	Analytical grade, 95%	
Nitric acid (64-66%)	Merck	Emplura	
PFS <sub>103</sub> -b-P2VP <sub>30</sub>	University Darmstadt		
Pluronic F127 (EO <sub>108</sub> PO <sub>70</sub> EO <sub>108</sub> )	Sigma-Aldrich		
Polyethylene glycol (PEG)	Sigma-Aldrich	M <sub>w</sub> = 8500-11500 g/mol	
Polystyrene (PS)	PSS Polymer	M <sub>w</sub> = 239000 g/mol, M <sub>n</sub> = 233000 g/mol, M <sub>w</sub> /M <sub>n</sub> = 1.03	
Polystyrene (PS)	Sigma-Aldrich	M <sub>w</sub> = 32000 g/mol, M <sub>n</sub> = 31000 g/mol, M <sub>w</sub> /M <sub>n</sub> = 1.02	
PS(27.7 kDa)-b-P2VP(4.3 kDa),	Polymer Source	M <sub>w</sub> /M <sub>n</sub> : 1.04	
Poly(2-vinylpyridine) (P2VP)	Sigma-Aldrich	M <sub>w</sub> = 37500 g/mol, M <sub>n</sub> = 35000 g/mol, M <sub>w</sub> /M <sub>n</sub> = 1.07	
Potassium ferrocyanide (II)	Alfa Aesar	98%	
Potassium ferrocyanide (III)	Alfa Aesar	98%	
Potassium hydroxide	Sigma-Aldrich	ACS, >95%	
Octanol	Merck		
Sodium azide	Merck	For synthesis, 99%	
Sodium thiosulfate pentahydrate	Alfa Aesar	ACS, 99.5-101%	

---

Sulfo-cyanine-3-azide	Lumiprobe	95%	
Sylgard 184	Dow Corning		
Tetraethyl orthosilicate (TEOS)	Sigma-Aldrich	Reagent grade, 98%	
Titanium tetrachloride	Fluka	Puriss, >99%	
Toluene	Fisher	Analytical reagent grade	
Toluene, anhydrous	AlfaAesar	99.8%	
Urea	Sigma-Aldrich	>98%	
Zeonex 330 R	Zeonex		

### 3.1.3 Materials

The polystyrene and polyethylene containers used for the syntheses, were obtained from Licefa. The stamp holder was made from stainless steel in the mechanical workshop at the University of Osnabrück. As glass substrates, standard microscopy slides with a thickness of 0.17 and 1 mm, respectively, were obtained from VWR International. The quartz substrate for the CNT growth was a standard ST cut purchased from Hoffman Materials. The dialysis tube was a Servapor, MWCO 12000-14000 from Serva with a pore diameter of approximately 2.5 nm.

## 3.2 Procedures

### 3.2.1 General procedures and preparation

#### 3.2.1.1 Silanization of macroporous silicon templates

Pieces of macroporous silicon (mSi) with areas of 2x2 cm<sup>2</sup> were silanized by immersion into a mixture of 500 µL dimethyldichloro silane (DMDCS) and 9.5 g *n*-hexane at 40 °C for 24 h. The silanized mSi was then rinsed with ethanol and dried in air.

#### 3.2.1.2 Silanization of substrate surfaces with different silanes

Prior to the stamping procedure, some of the glass substrates were silanized to achieve a surface with a certain hydrophilicity or hydrophobicity. Therefore, different silanes were



used to functionalize the substrates and obtain different functional groups as residues. The silanization procedures were kept equally throughout the whole work.

For the silanization with 1H,1H,2H,2H-perfluorodecyltrichlorosilane (FDTS), the glass slides were subjected to O<sub>2</sub> plasma for 10 min. The glass slides thus treated were then silanized with FDTS via vapor phase deposition. For this purpose, the glass slides were heated to 80 °C for 2 h in a sealed glass container in the presence of an excess of FDTS ( $\approx 2 \mu\text{L}$ ).

The silanization with dimethyldichloro silane (DMDCS) was carried out by immersing the plasma-cleaned glass slides into a 2 vol% solution of DMDCS in anhydrous toluene for 3 h at RT.

The silanization with N-(2-aminoethyl)-2,2,4-trimethyl-1-aza-2-silacyclopentane (ATAS) was carried out by immersing the plasma-cleaned glass slides into a 2 vol% solution of ATAS in toluene for 3 h at RT.

Prior to stamping, all silanized glass slides were washed with ethanol and dried in a nitrogen stream.

For the hydroxyl-terminated glass, the glass slides were used directly after the plasma treatment.

### 3.2.2 Stamp syntheses

#### 3.2.2.1 Silica stamps – first generation

The first generation of mesoporous silica stamps were synthesized according to Babin *et al.*<sup>[72]</sup> 1.69 g polyethylene glycol (PEG) were mixed with 16 g deionized water and 1.37 g nitric acid in an Erlenmeyer flask and vigorously stirred for 30 min at 0 °C. Then, 13.4 mL tetraethyl orthosilicate (TEOS) was quickly added and stirring at 0 °C was continued for 30 min. Silanized mSi located in a polystyrene container was coated with the sol. The container was tightly sealed, and the sol was allowed to age for 3 days at 40 °C. The obtained silica monoliths were neutralized with deionized water for 5 times within 24 h at room temperature to remove residual surfactant and chemicals. After the washing water reached a pH of at least 4-5, the monoliths were immersed in 40 mL of 0.1 N ammonia at 80 °C for 24 h. The obtained mesoporous monoliths were again washed with water 2 times. The water was replaced by ethanol and the ethanol was in turn replaced with fresh ethanol for two more times within 24 h.

### 3.2.2.2 Silica stamps – second generation

For the second generation of mesoporous silica stamps, the previously described synthesis procedure was supplemented by the incorporation of Ti-atoms into the silica network. Therefore, a synthesis procedure according to Schäfer *et al.*<sup>[81]</sup> was adapted. 1.69 g PEG were mixed with 16 g deionized water and 1.37 g nitric acid in an Erlenmeyer flask and vigorously stirred for 30 min at 0 °C. Then, 13.4 mL TEOS and 0.1 mL titanium tetrachloride were quickly added, and stirring was continued at 0 °C for 30 min. Silanized mSi located in a polystyrene container was coated with the sol. The container was tightly sealed, and the sol was allowed to age for 3 days at 40 °C. The obtained mesoporous silica stamps were neutralized with deionized water for 5 times within 24 h at room temperature to remove residual surfactant and chemicals. The water was replaced by ethanol and the ethanol was in turn replaced with fresh ethanol for two more times within 24 h.

### 3.2.2.3 Silica stamps – third generation

#### 3.2.2.3.1 Stamps with pore diameters of 31 nm

For the synthesis of the third generation of mesoporous silica stamps, a synthesis approach reported by Kanamori *et al.*<sup>[76]</sup> was used. Therefore, 14 g of 10 mM aqueous acetic acid solution was mixed with 2.2 g Pluronic F127 and 1 g urea in an Erlenmeyer flask and vigorously stirred for 30 min at room temperature. Then, 9.97 mL methyltrimethoxy silane (MTMS) were quickly added and stirring was continued for 30 min. Silanized mSi located in a polystyrene container was coated with the sol thus obtained. The container was tightly sealed, and the sol was allowed to age for 4 d at 60 °C. The obtained silica monoliths were neutralized with deionized water for 1 d at 60 °C to remove residual surfactant and chemicals. The water was replaced by ethanol, which was in turn replaced by fresh ethanol for two more times within 24 h.

#### 3.2.2.3.2 Stamps with pore diameters of 44 nm

For the synthesis of third generation mesoporous silica stamps with larger pores, the procedure from Kanamori *et al.*<sup>[76]</sup> was used with different quantities of chemicals. Therefore, 10 g of 10 mM aqueous acetic acid solution was mixed with 1 g Pluronic F127 and 0.5 g urea in an Erlenmeyer flask and vigorously stirred for 30 min at room temperature. Then, 4.98 mL MTMS were added quickly and stirring was continued for 30 min. Silanized mSi located in a polystyrene container was coated with the sol thus obtained.

The container was tightly sealed, and the sol was allowed to age for 4 d at 60 °C. The obtained silica monoliths were neutralized with deionized water for 1 d at 60 °C to remove residual surfactant and chemicals. The water was replaced by ethanol, which was in turn replaced by fresh ethanol for two more times within 24 h.

### 3.2.3 Stamp holder and stamp preparation

As stamp holder a stainless steel cylinder with a height of 4.5 cm, a diameter of 2 cm, a mass of  $\approx 27$  g and a flat cylinder base was used. An elastomeric PDMS film with a thickness of 3 mm was prepared using Sylgard 184 formulation. Base and PDMS prepolymer were mixed at a ratio of 1:9, stirred for 10 min, and poured into a polyethylene mold. The mixture was then allowed to cure for 1 week at room temperature. Using double-sided adhesive tape, the elastomeric PDMS film was glued onto the flat cylinder base of the stamp holder. The mesoporous silica stamps were loaded with ink as described in the sections below. Excess ink on the surfaces of the mesoporous silica stamps was removed with tissue. Then, the mesoporous silica stamps were fixated on the PDMS films with double-sided adhesive tape. The mesoporous silica stamps mounted on the stamp holders were manually brought into contact with glass slides modified as described above.

### 3.2.4 Stamping procedures and subsequent functionalization

#### 3.2.4.1 Stamping of $C_{60}$ fullerenes from toluene onto FDTS-glass

Fullerene nanoparticles were stamped on 0.17 mm thick glass slides silanized with FDTS. The dry mesoporous silica stamps were infiltrated from the non-structured side with a solution of 1 mg  $C_{60}$  per 1 mL toluene and then brought into contact with the FDTS-modified glass slides for 5 s.

#### 3.2.4.2 Stamping of 1-dodecanethiol from ethanol onto gold-coated glass

1-Dodecanethiol was stamped onto 1 mm thick glass slides. Prior to stamping, the glass slides were coated with titanium and gold by thermal evaporation. At first, a 5 nm thick titanium layer was deposited followed by the deposition of a 30 nm thick gold layer. Before stamping, the metal-coated glass slides were rinsed with ethanol and dried in an

argon flow. The ethanol-wet mesoporous silica stamps (pore diameter of 31 nm) were infiltrated by immersion into an ethanolic 2 mM 1-dodecanethiol solution for 5 min and then brought into contact with the gold-coated glass slides for 1 s.

To increase the contrast of stamped 1-dodecanethiol spots for SEM analysis, the unprotected part of the gold layer was thinned to 10 nm by a cyanide etching process reported elsewhere.<sup>[82]</sup> For this purpose, the stamped gold-coated glass slides were immersed in a solution containing sodium thiosulfate, potassium ferrocyanide (III), potassium ferrocyanide (II), potassium hydroxide and octanol at a molar ratio of 1:0.1:0.01:10:0.02 for 6 min at room temperature. Subsequently, the substrates were rinsed with water as well as with ethanol and dried in an argon flow.

#### *3.2.4.3 Dewetting of polystyrene after stamping of 1-dodecanethiol from ethanol onto gold-coated glass*

For the dewetting of polystyrene (PS) from the as-stamped 1-dodecanethiol dots on gold-coated glass (here, the etching procedure has not been carried out), 10  $\mu$ L of solutions of PS in chloroform (0.5 and 0.05 wt%, respectively) were spin coated onto gold-coated glass slides modified with arrays of 1-dodecanethiol dots at 3000 rpm for 30 s. To evaluate the thickness of the PS films, the solutions were spin-coated under exactly the same conditions onto glass slides without gold coating. The step height of scratches in the PS films were measured with AFM. The PS films covering the gold-coated glass slides patterned with arrays of 1-dodecanethiol dots were first kept at 80 °C, a temperature at which PS is vitreous, for 24 h to remove residual solvent. Then, the samples were heated to 170 °C, a temperature well above  $T_g$  of PS, for 30 min to enable dewetting.

#### *3.2.4.4 Stamping of nanodiamonds from isopropanol onto FDTs-glass*

Nanodiamonds (NDs) with a mean size of 10 nm were stamped on 0.17 mm thick glass slides silanized with FDTs. The NDs were bought in a stabilized solution of 1 mg/mL NDs in water and salt. As the used stamps were hydrophobic, the aqueous ND dispersion needed to be exchanged by an organic solvent prior to stamping. Therefore, 1 mL of NDs were centrifuged and washed with 1 mL of water one time and with 1 mL of isopropanol two times. After washing, the dispersion was diluted 1:100 to obtain an ink solution with a concentration of 10  $\mu$ g/mL NDs. The dry mesoporous silica stamps (pore diameter 31 nm) were infiltrated from the non-structured side with ink solution and then brought into contact with the FDTs-modified glass slides for 5 s.

### 3.2.4.5 Functionalization of stamped nanodiamonds via click-chemistry with cyanine-3-DBCO

NDs with an average size of 5 nm were wet-chemically modified to obtain click-chemistry-accessible NDs containing azide residues on the surface. The wet chemical procedures were performed similar to different reported synthesis strategies.<sup>[83–85]</sup> To obtain NDs-OH, the hydroxylation protocol was conducted according to Krueger *et al.*<sup>[86]</sup> For this purpose, 500 mg of acid treated detonation NDs were used. After the reaction, a washing procedure including subsequent steps of deionized water rinsing and centrifugation (5 x) was carried out. The NDs-OH were then silanized with 11-bromoundecyltrichlorosilane by adding 50 mg of NDs-OH and 10 mL of anhydrous toluene in a flask under argon and sonicated for 30 min. 250  $\mu$ L of 11-bromoundecyltrichlorosilan was added to the dispersion and stirred overnight at RT. To separate the product of bromide-functional NDs (NDs-Br) from unreacted 11-bromoundecyltrichlorosilane, the reaction mixture was centrifuged and redispersed with toluene for five times. After the last washing cycle, the solvent was decanted and the NDs-Br were dried for 2 h at 60 °C. The silanized NDs-Br were then added with 10 mL of dimethylformamide (DMF) and a spatula tip of sodium azide ( $\text{NaN}_3$ ) in a flask, sonicated for 5 min and stirred overnight at 60 °C under reflux. The obtained NDs- $\text{N}_3$  were washed by centrifugation and redispersion with water for two times and with isopropanol for two times. The isopropanol is decanted and the NDs- $\text{N}_3$  were dried for 24 h at 60 °C. After drying, a dispersion of 1 mg/mL of ND- $\text{N}_3$  in isopropanol was made and used as ink solution.

Azide-functionalized NDs (NDs- $\text{N}_3$ ) were stamped on 0.17 mm thick glass slides. The ethanol-wet mesoporous silica stamps (pore diameter of 31 nm) were infiltrated with a solution of 1 mg NDs- $\text{N}_3$  per 1 mL isopropanol and then brought into contact with the glass slides for 5 s.

For the click-reaction with cyanine-3-DBCO, the glass slides were fixated into a holder and 1 mL of a 1  $\mu$ M cyanine-3-DBCO solution in isopropanol was added. The holder was covered with aluminum foil and the reaction took place for 30 min at RT. Afterwards, the glass slide was carefully washed with isopropanol and dried in air.

To confirm the successful click-reaction, the NDs- $\text{N}_3$  were also functionalized with dye in a flask. For this purpose, the dried NDs- $\text{N}_3$  from the previous reaction (functionalization with azide) were added with 20 mL of isopropanol in a flask and sonicated for 30 min. Then, 20  $\mu$ L of a 1 mM solution of cyanine-3-DBCO in isopropanol was added to obtain a total dye concentration of 1  $\mu$ M. The reaction was stirred for 30 min at RT and subsequently washed by centrifugation and redispersion with isopropanol.

#### 3.2.4.6 *Stamping of Zeonex from toluene/chloroform onto FDTs-glass*

Zeonex was stamped as-received on 0.17 mm thick glass slides silanized with FDTs. The ethanol-wet mesoporous silica stamps (pore diameter of 31 nm) were immersed into a solution of toluene and chloroform (1:3) for 1 d. The ink consisted of 125  $\mu$ L of a 100 mg/mL Zeonex in toluene solution, 125  $\mu$ L toluene and 750  $\mu$ L chloroform, which amounted to a total concentration of Zeonex of 12.5 mg/mL within the ink. After the immersion of the stamps into the solvent of the ink, the stamps were immersed into the ink for 2 h. For stamping, the stamps were brought into contact with the FDTs-modified glass slides for 5 s.

#### 3.2.4.7 *Stamping of PS-*b*-P2VP from toluene/chloroform onto different functionalized substrates and subsequent swelling of the BCP*

The polystyrene-*block*-poly(2-vinylpyridine) (PS-*b*-P2VP) was stamped onto 0.17 mm thick glass slides silanized with FDTs, DMDCS and ATAS, or hydroxyl-terminated, respectively. The ethanol-wet mesoporous silica stamps (pore diameter of 44 nm) were immersed into a solution of toluene and chloroform (1:3) for 1 d. As ink, a solution of PS-*b*-P2VP in toluene/chloroform (1:3) was prepared with a total concentration of 2.5 mg/mL of PS-*b*-P2VP within the ink. After the immersion of the stamps into the solvent of the ink, the stamps were immersed into the ink for 2 h. For stamping, the stamps were brought into contact with the silanized and hydroxyl-terminated glass slides for 5 s.

For the swelling of PS-*b*-P2VP, the glass slides were immersed into ethanol subsequent to stamping and kept at 60 °C for 1 h. After retrieval, the ethanol evaporated at air and the glass slides could be analyzed.<sup>[87]</sup>

#### 3.2.4.8 *Stamping of PFS-*b*-P2VP from toluene/chloroform onto different substrates and subsequent growing of CNTs*

The polyferrocenyl(dimethylsilane)-*block*-poly(2-vinylpyridine) (PFS-*b*-P2VP) was stamped onto 1 mm thick glass slides silanized with FDTs, or hydroxyl-terminated, respectively. The ethanol-wet mesoporous silica stamps (pore diameter of 44 nm) were immersed into a solution of toluene and chloroform (1:3) for 1 d. As ink, a solution of PFS-*b*-P2VP in toluene/chloroform (1:3) was made with a total concentration of 2.5 mg/mL of PFS-*b*-P2VP within the ink. After the immersion of the stamps into the solvent of the ink, the stamps were immersed into the ink for 2 h. For stamping, the

stamps were brought into contact with the silanized and hydroxyl-terminated glass slides for 5 s.

The calcination process was carried out with stamped PFS-*b*-P2VP on FDTS-functionalized quartz substrates at 900 °C under a constant flow of argon (1.5 sccm, quality 4.6). The heating rate amounted to 40-41 °C/min and thus, after 22 min, a temperature of 900 °C was reached. Subsequently, the furnace was turned off and the samples cooled down to room temperature with no further support.

Carbon nanotube (CNT) growth using chemical vapor deposition was carried out by stamping PFS-*b*-P2VP onto a FDTS-functionalized quartz substrate. The samples were heated in a tube furnace to 900 °C under constant flow of argon (1.5 sccm, quality 4.6). The heating rate amounted to 40-41 °C/min and thus, after 22 min, a temperature of 900 °C was reached. CNTs were grown applying CH<sub>4</sub> (quality 2.5, flow 0.52 sccm) and H<sub>2</sub> (quality 5.0, flow 0.70 sccm) for 10 minutes. The samples were cooled down under argon flow. Mainly single-walled and double-walled CNTs with respect to the growth temperature were expected.<sup>[88]</sup>

#### 3.2.4.9 *Stamping of 17 $\alpha$ -ethinylestradiol (EE<sub>2</sub>) with subsequent redispersion and functionalization with fluorescent dye*

17 $\alpha$ -Ethinylestradiol (EE<sub>2</sub>) was stamped as-received on 0.17 mm thick glass slides silanized with FDTS. Prior to stamping, the ethanol-wet silica stamps (pore diameter of 31 nm) were immersed in acetonitrile (ACN) for 12 h and subsequently a solution of 50 mM of ethinyl estradiol in ACN for 2 h. The mesoporous silica stamps immersed in solution of EE<sub>2</sub> in ACN were then brought in contact with the FDTS-modified glass slides for 5 s.

For the detachment of the stamped EE<sub>2</sub> particles, the FDTS-functionalized substrate was placed in a glass container including 2 mL of water in a way, that the stamped EE<sub>2</sub> particles were facing the water. The glass container was sonicated for 2 h at 50 °C.

For the click reaction of the redispersed EE<sub>2</sub> particles, 5  $\mu$ L of a 1 mM sulfo-cyanine-3-azide solution in water were added to the obtained 2 mL of water dispersion (total concentration of 2.5  $\mu$ M of dye). The solution was slowly stirred at RT for 2 h. The reaction solution was washed in a dialysis tube with 1 L of water for 5 d, which was then replaced with fresh water for 1 d.

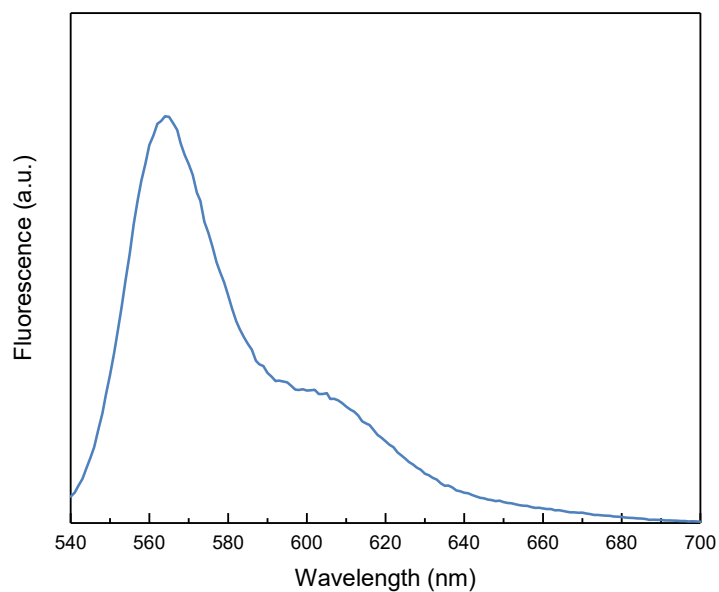


*Figure 28. Fluorescence spectrum of 1 mM sulfo-cyanine-3-azide in H<sub>2</sub>O with an absorption wavelength of 530 nm. The emission maximum is at 563 nm and a shoulder at 600 nm is visible.*



---

## 4 Results and discussion

### 4.1 Capillary nanostamping with mesoporous silica stamps – stamp design

Conventional lithographic methods, specifically stamping or printing to generate patterns of particles or molecules on counterpart surfaces are discussed in section 2.1 (see page 8). The advantages and disadvantages of each method were compiled within the discussion of these methods. One trait all of these methods have in common is the limitation of ink supply, as the stamping process with solid stamps only allows the transfer of molecules adsorbed on the stamp surface, whereby continuously stamping is not possible.

To overcome this disadvantage and generate a stamping method with high throughput, fast cycle times and a continuous ink supply, porous stamps were made. For the successful development of a capillary stamping procedure, several requirements have to be fulfilled.

- As many possible inks and particles are dissolved or dispersed in **organic solvents**, the stability against these solvents should be ensured. Therefore, silica was chosen as stamp material, as it is chemically inert against organic solvents.
- The porous stamp should have a continuous pore system with a relatively **narrow pore size distribution** to allow for a continuous ink flow throughout the whole stamp. A broad pore size distribution would be accompanied by different Laplace pressures within larger and smaller pores on the stamps' surfaces, which could lead to stress of the silica network. This factor is important for the infiltration of dry stamps.
- As the solid stamp is used to print on usually flat and inflexible surfaces, the **surface** to encounter the counterpart substrate should be **flat**.
- To withstand the stamping procedure and to obtain the best possible results, the stamp should be **flexible** to a certain extent and **mechanically stable** at the same time.
- To generate patterns of ink on the substrate surface, the stamp needs to have **ordered contact elements** on its flat top surface.

A silica gel is fabricated by pouring a sol-gel into a mold to reproduce the shape of the mold. Although the gel undergoes a certain shrinkage during aging, the mold could consist of any structure or shape and is equally replicated. To create structured contact elements on top of the silica aerogel, a silanized macroporous silicon wafer (mSi), as de-

scribed in chapter 3.2.1.1 (see page 36), was used as mold. The mSi contained hexagonal arrays of macropores with a center-to-center distance of  $1.5\ \mu\text{m}$ , as shown in Figure 29a, and a macropore depth of 600 nm. The diameter of the macropores amounted to 900 nm at their openings and to 600 nm at their bottoms as shown in Figure 29b. The sol was poured into a polypropylene container with the porous mSi on the bottom. After the aging procedure, the silica gel consists of a bulk in manageable size for manual operation, with contact elements on the top surface in the sub- $\mu\text{m}$  size range.

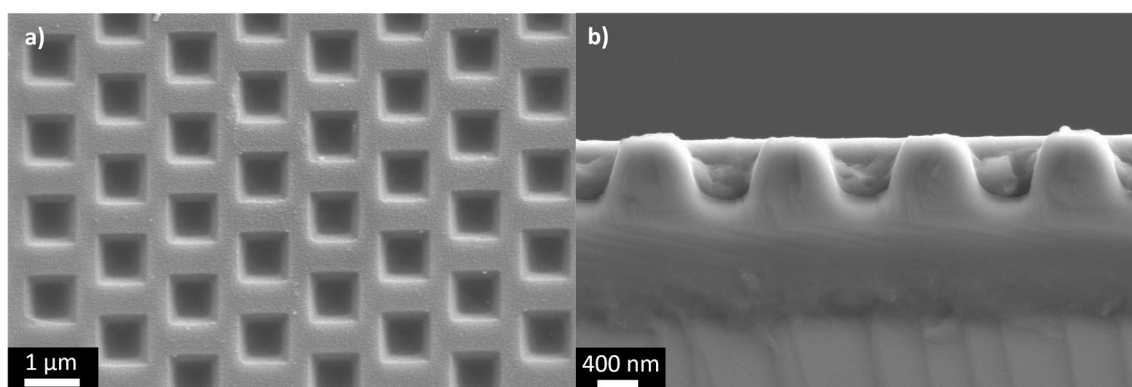


Figure 29. SEM images of macroporous silicon (mSi) with hexagonally arranged pores. a) Top and b) side view of the mSi pores with a center-to-center distance of  $1.5\ \mu\text{m}$  and a depth of 600 nm. The pore size at the pore openings is 900 nm and 600 nm at the pore bottoms. The images were taken with a SESI detector.

#### 4.1.1 Silica stamps – first generation

As first attempt, stamps consisting of pure silica were made in a procedure described in chapter 3.2.2.1 (see page 37) following procedures reported by Babin *et al.*<sup>[72]</sup> Here, tetraethyl orthosilicate (TEOS) was used as silica precursor, which is the “classical” tetra functional silica source. Polyethylene glycol (PEO) was used as structure directing agent to generate macropores, and a treatment with ammonia hydroxide ( $\text{NH}_4\text{OH}$ ) after aging was used to rearrange the pore structure into a mesoporous system. After synthesis, the stamps were dried in a supercritical drying process with liquid  $\text{CO}_2$  to prevent pore collapse. The synthesis of monoliths based on the well-known MCM-41 material resulted in monolithic aerogels in the size of  $2 \times 2\ \text{cm}^2$ , consisting of a flat surface with ordered contact elements on top. The dried stamps were white and opaque. The SEM image in Figure 30a shows the bulk structure of the stamp, where the porosity is clearly visible. Figure 30b shows the hexagonally arranged contact elements on top of the silica stamp. The single contact elements were  $490 \pm 22\ \text{nm}$  in diameter and the distance between the single contact elements resulted in  $0.9\ \mu\text{m}$ . An overview of the stamp surface (Figure

30c) shows a flat top surface with well-ordered contact elements. During aging, the silica network is formed by participation of single particles to generate a network. This leads to an overall shrinkage of the silica. In comparison to the mSi templates, the finished silica stamps underwent a lateral shrinkage of 20-40%.

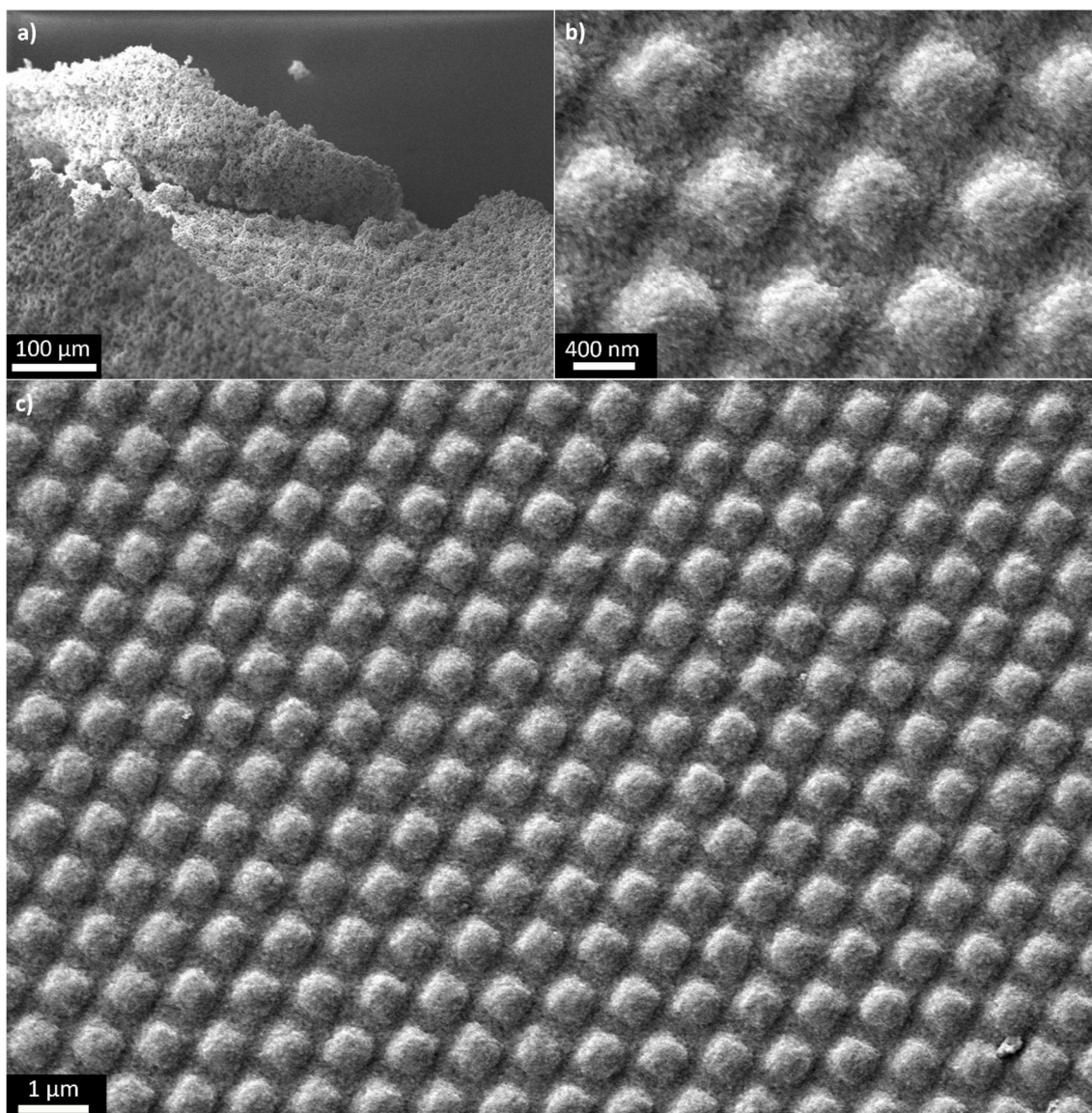


Figure 30. SEM images of first-generation silica stamps. a) View of the porous bulk material, b) magnification of structured stamp elements and c) overview of the topographically patterned stamp surface. The images were taken with a SESI detector.

Nitrogen sorption analysis of the synthesized silica material is shown in Figure 31. The BET isotherm in Figure 31a displays a variety of a type IV isotherm with a H1 hysteresis,<sup>[89]</sup> which stands in good agreement with the literature.<sup>[72]</sup> The BET specific surface area is 233 m<sup>2</sup>/g (overview of all nitrogen sorption data see Table 2 on page 56), the isotherm shows a narrow hysteresis, which indicates a uniform pore size distribution.

The ammonia hydrothermal treatment induces the formation of a mesoporous system into the macroporous monoliths without changing the overall system.<sup>[72]</sup> The pore size distribution is relatively narrow and shows pore sizes between 13-19 nm with a mean pore diameter of 15 nm (see Table 2, page 56).

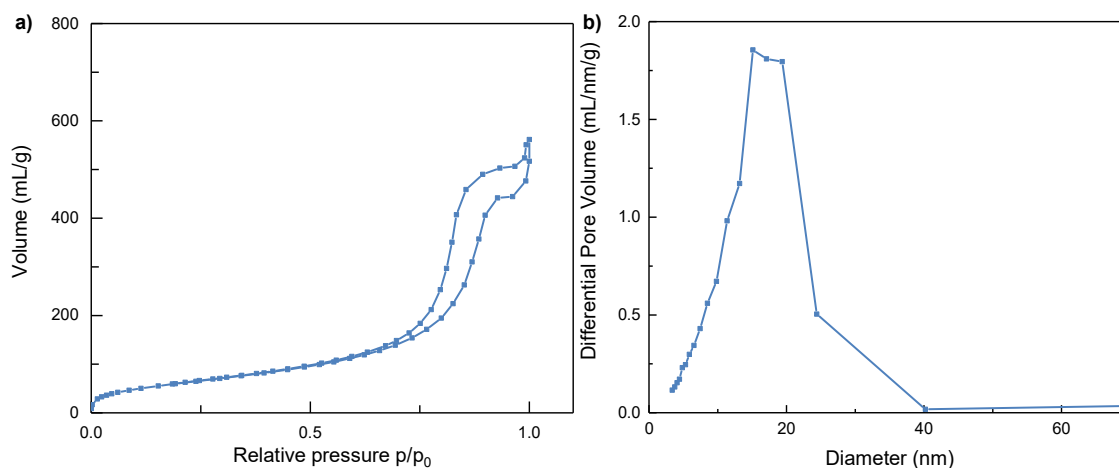


Figure 31. Nitrogen sorption measurements of silica stamps of the first generation. a) The BET isotherm is a variety of a type IV isotherm with a H1 hysteresis.<sup>[89]</sup> b) The pore size distribution is calculated with the BJH theory from the adsorption branch of the BET isotherm. It shows a relatively narrow peak at 15 nm.

The generation of silica stamps consisting of pure silica was successful, but revealed several disadvantages originating from pure silica. Although the top surface resulted to be flat, the monoliths in total were very brittle and mechanically unstable. The infiltration with ink resulted almost every time in breaking of the stamp. Therefore, this stamp generation was not suitable for a mechanical stamping process and could not be used for stamping.

#### 4.1.2 Silica stamps – second generation

As pure silica was not suitable for stamp production, a reinforcement strategy was developed. The methods discussed in section 2.1.3.2 (see page 21) all have in common, that they change the silica network by the introduction of either chemically reactive molecules or pore structure changing fibers. The requirements of the silica stamps for a successful application in a stamping procedure do not allow chemically active residues within the silica network, as they could react with the ink to be stamped. Therefore, these methods are not compatible with the requirements for the stamps.

To strengthen the silica network without causing a chemical interaction between silica and the used inks, Ti-atoms were introduced into the silica network, as titanium is known to build SiO<sub>2</sub>-similar materials.<sup>[90–93]</sup> Following the procedures reported by Schäfer *et al.*,<sup>[81]</sup> the silica network derived by the previously used synthesis was incorporated with Ti-atoms by addition of TiCl<sub>4</sub> to the synthesis mixture. The resulting Si<sub>1-n</sub>Ti<sub>n</sub>O<sub>2</sub> (with n<1, a total implementation of Ti-atoms would yield in Si<sub>0.98</sub>Ti<sub>0.02</sub>O<sub>2</sub>) stamps were much harder than the first generation and did not break as easy. The dried stamps were white opaque. The SEM image in Figure 32a shows the porous network of the bulk material, while Figure 32b shows the topographically patterned surface. The single contact elements are more defined compared to the first-generation stamps and with 342 ± 32 nm also smaller in top diameter. Determining the distance between the single contact elements is difficult in this case due to the high surface waviness. If measured on a spot with uniform ordered contact elements as shown within the orange square in Figure 32c, the center-to-center distance between the single contact elements amounted to 1.0 µm. In comparison to the mSi templates, the finished silica stamps underwent a lateral shrinkage of 32-43%. Figure 32c shows clearly the disadvantage of these stamps – a high waviness and therefore no hexagonally ordered structure on the surface of the stamp. This waviness prevents parts of the contact elements from touching the counterpart substrate during stamping, which leads to a non-promising stamping process.



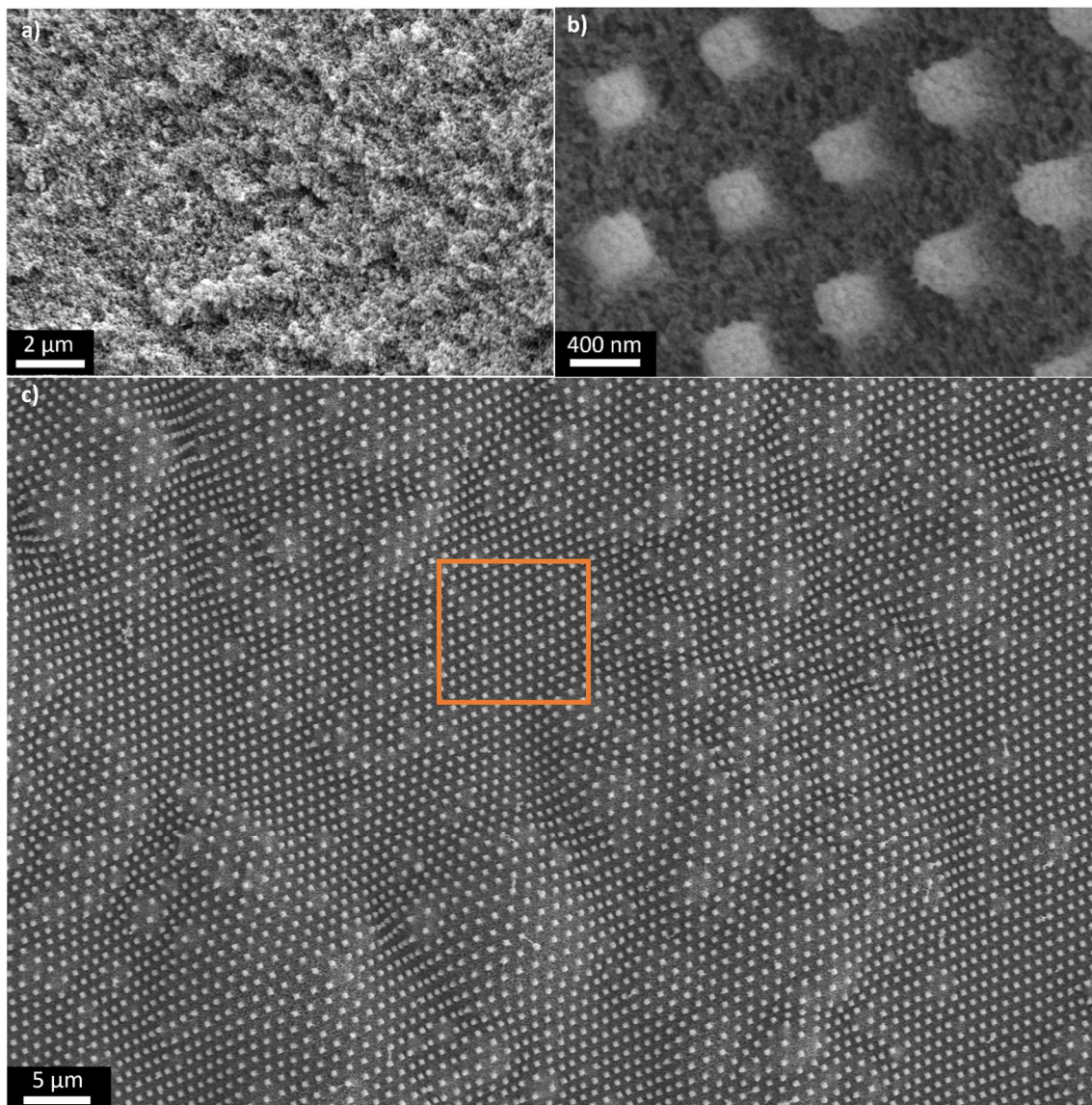


Figure 32. SEM images of second-generation silica stamps. a) View of the porous bulk material, b) magnification of stamp elements and c) overview of the topographically patterned stamp surface. The distance between single stamp elements was calculated within the area of the orange square. Images were taken with a SESI detector.

The BET surface area amounted to  $330 \text{ m}^2/\text{g}$  with a mean pore volume of  $2.2 \text{ mL/g}$ , which increased compared to the first-generation stamps, as shown in Table 2 (see page 56). Nevertheless, the pore size distribution (see Figure 33b) does not show uniform pore sizes, but a broad peak from 20-60 nm. A porous network with different pore sizes, which could cause different flow rates within different pore channel sizes. This could in turn lead to a possible retention of an ink consisting of nanoparticles or molecules with high intermolecular interactions thus, presumably cannot provide a continuous ink flow throughout the whole network.

Although the mechanical properties were improved by introducing titanium into the silica network, the stamps of the second generation could not be used for the stamping process. As the mechanical strength was improved by hardening the network, the stamps became tough to handle. Apart from their waviness, they were not suitable for mechanical grinding and broke easily under stress or ink infiltration.

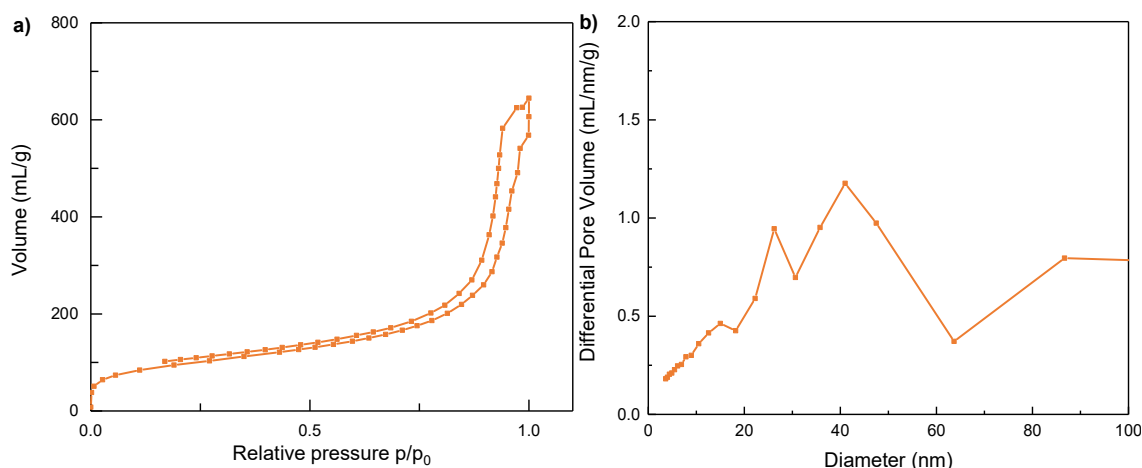


Figure 33. Nitrogen sorption measurements of silica stamps of the second generation. a) The BET isotherm is of type IV with a H1 hysteresis. b) The pore size distribution is calculated with the BJH theory from the adsorption branch of the BET isotherm. It shows a wide peak from 20-60 nm.

### 4.1.3 Silica stamps – third generation

#### 4.1.3.1 Stamps with pore diameters of 31 nm

The mechanical reinforcement and the introduction of Ti-atoms into the network did not result in a suitable stamp material. As an alternative route to the common sol-gel synthesis with tetra functional silica precursors, a silsequioxane was synthesized using a trifunctional precursor as introduced in section 2.1.3.2 (see page 21). The silica stamps were synthesized in a procedure described in chapter 3.2.2.3.1 (see page 38). According to Kanamori *et al.*,<sup>[76]</sup> methyltrimethoxysilane (MTMS) was used as silica precursor, resulting in a  $\text{SiMeO}_{3/2}$  stamp. The mild reaction conditions and the increasing pH during aging due to the added urea ensured the prevention of a macroscopic phase separation and promote gelation of the network. After the synthesis, the stamps were again dried *via* critical point drying with liquid  $\text{CO}_2$  and resulted in fully transparent monoliths. The SEM image in Figure 34a shows the porous network, while Figure 34c shows the highly uniform and flat top surface with hexagonally arranged contact elements with a diameter of  $459 \pm 22$  nm and a distance between the single elements of 1.1  $\mu\text{m}$ . This reflects a



lateral shrinkage of 24-26% in comparison to the mSi template, which is much less compared to the first- and second-generation silica stamps. Figure 34b shows the magnification of a single stamp element, where the porous structure is clearly visible both on the top surface of the contact element, and within the bulk silica on the bottom of the contact element.

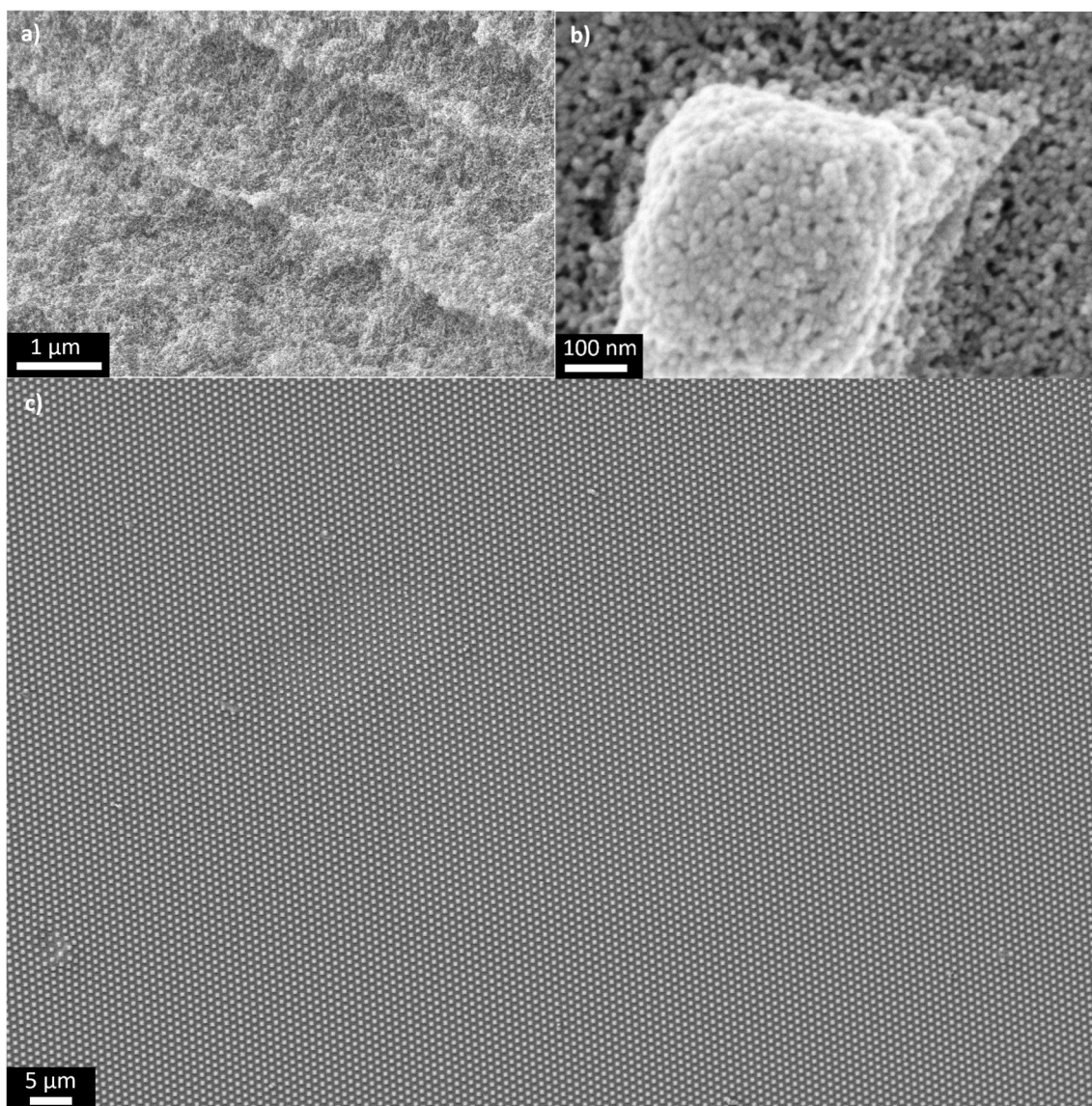


Figure 34. SEM images of third-generation silica stamps. a) View of the porous bulk material, b) magnification of a single contact element and c) overview of the topographically patterned stamp surface. Images were taken with a SESI detector.

The SEM image in Figure 35a shows the side view of a silica stamp. It can be seen that the stamp consists of a bulk silica network and ordered contact elements on the flat top surface of the stamp. The length of the contact elements amounted to 450 nm. The silica network is interconnected not only in the bulk, but also throughout the contact elements,



which guarantees an unimpeded ink flow. Figure 35b shows a photograph of a dried silica stamp. The typical sizes amounted to  $5 \times 5 \times 3 \text{ mm}^3$ .

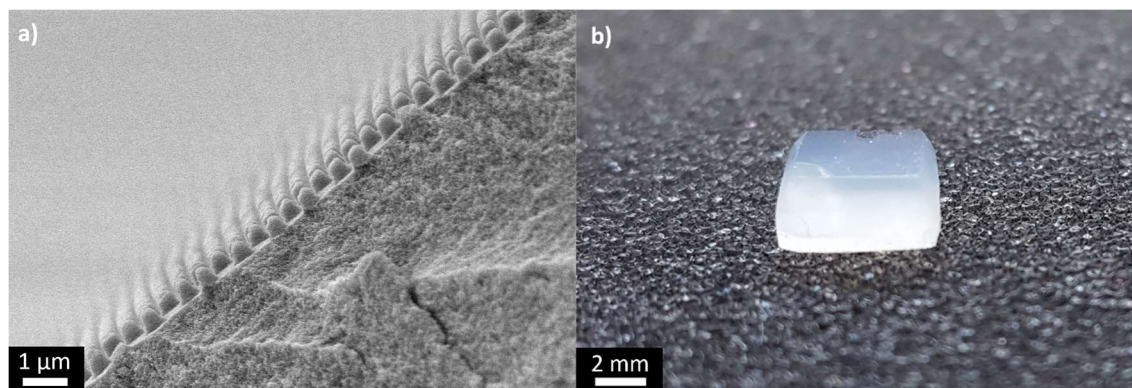


Figure 35. a) SEM image of the side view of a silica stamp. The stamp is synthesized as a bulk silica with a topographically structured top surface. The stamp elements have a top diameter of 459 nm and a length of 450 nm. The image was taken with a SESI detector. b) Photograph of a dried silica stamp in a typical dimension of  $5 \times 5 \times 3 \text{ mm}^3$ .

Nitrogen sorption measurements revealed a BET surface area of  $530 \text{ m}^2/\text{g}$  (shown in Table 2, page 56), which is noticeably higher than the surface areas of the first- and second-generation stamps. The shape of the nitrogen sorption isotherm shown in Figure 36a could be assigned to a type IV isotherm with a H1 hysteresis loop. Here, the steep and narrow H1 hysteresis loop indicates that the necks and the nodes of the mesopore system are uniform in size and highly interconnected.<sup>[94]</sup> By contrast, a mesopore system consisting of narrow necks and wider nodes would yield a H2 hysteresis loop.<sup>[95]</sup> The pore size distribution (Figure 36b) shows a narrow peak at 31 nm and a total pore volume of  $2.2 \text{ mL/g}$  (Table 2), which suggests that an empty mesoporous silica stamp with a mass of  $\approx 90 \text{ mg}$  may absorb  $\approx 200 \text{ }\mu\text{L}$  ink. The results of the nitrogen sorption measurements obtained here are in line with results reported by Yun *et al.*,<sup>[96]</sup> who synthesized silica microspheres using MTMS as a silica precursor.

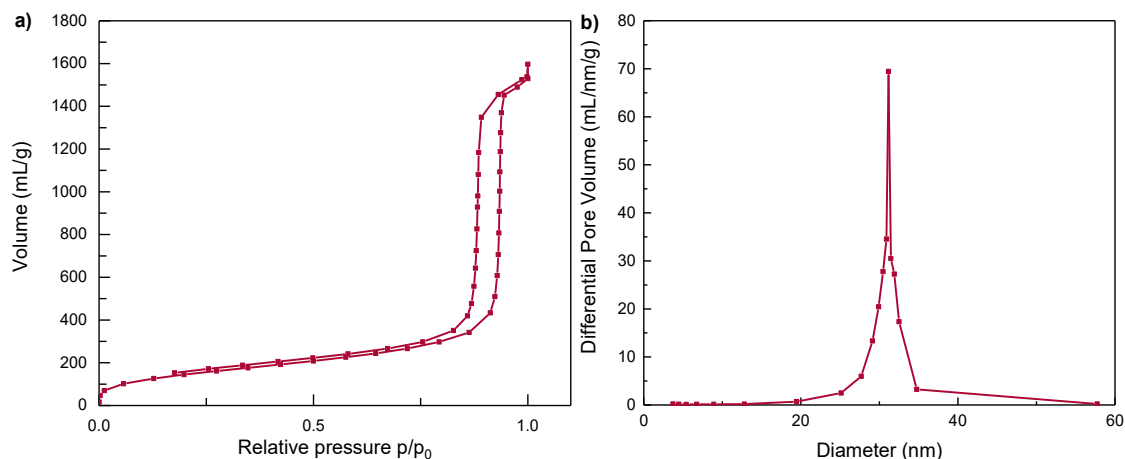


Figure 36. Nitrogen sorption measurements of silica stamps of the third generation. a) The BET isotherm is of type IV with a H1 hysteresis. b) The pore size distribution is calculated with the BJH theory from the adsorption branch of the BET isotherm. It shows a narrow peak at 31 nm.

#### 4.1.3.2 Stamps with pore diameters of 44 nm

To create the same stamps but with larger pores, the quantities of chemicals within the sol solution were varied whilst the procedure and pre-treatment conditions were kept equally. The synthesis procedure is described in chapter 3.2.2.3.2 (see page 38). The SEM image in Figure 37 shows the surface structure containing contact elements. The pores are clearly visible both in the contact elements as well as in the bulk silica. For verification of the larger pore sizes, only SEM is not suitable as the small difference between 31 and 44 nm will not be visible in this method. Therefore, nitrogen sorption measurements were taken as shown in Figure 38 and summarized in Table 2 (see page 56). The specific surface area amounted to 465 m<sup>2</sup>/g, which is less than for the same stamps with smaller pores, which is due to a decreasing surface area with increasing pore sizes. The BET isotherm shown in Figure 38a shows a type IV isotherm with a H1 hysteresis loop, which could not be fully obtained due to technical problems during measurements. Nevertheless, this result is comparable to the same stamps with smaller pores. The pore size distribution (Figure 38b) shows a relatively narrow peak at 40-48 nm and a total pore volume of 2.4 mL/g (Table 2), which is again due to larger pores. Compared to the same stamps with smaller pores, an empty stamp with larger pores and a mass of  $\approx 90$  mg may absorb  $\approx 215$   $\mu$ L ink.

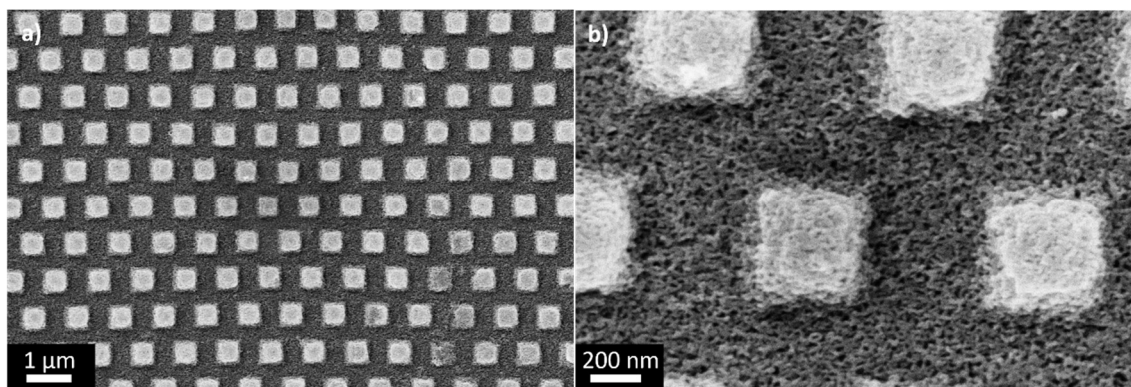


Figure 37. SEM images of third-generation silica stamps synthesized to obtain larger pore sizes with a) overview of larger area and b) magnification. The pore structure is well visible both in the contact elements as well as in the bulk silica. The images were taken with an in-lens detector for a higher contrast.

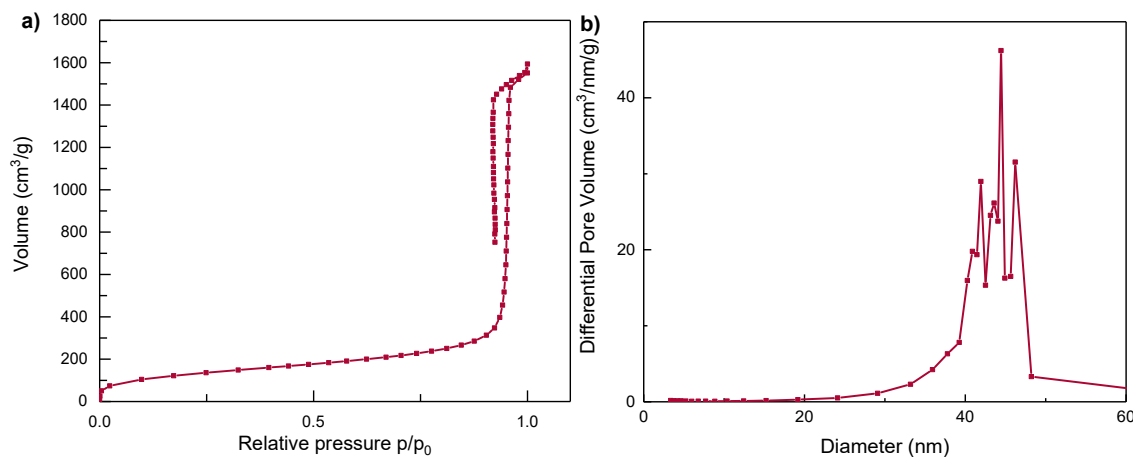


Figure 38. Nitrogen sorption measurements of silica stamps of the third generation. a) The BET isotherm is of type IV with a H1 hysteresis. The measurement interrupted at desorption due to a high surface area and technical problems during the procedure. Nevertheless, as the calculation of the pore size is referred to the adsorption branch of the isotherm, it remained valid to calculate. b) The pore size distribution is calculated with the BJH theory from the adsorption branch of the BET isotherm. It shows a relatively narrow peak at 40-48 nm.

The third generation of silica stamps consisting of a silica network with methyl residues resulted in a more flexible silica network compared to a TEOS-derived silica material. Due to less interconnection in the silica network and the reduction of the hydroxyl group density on the silica surface, the stamps of the third generation became mechanically resilient and hydrophobic. The stamps could be ground with abrasive paper to obtain a form appropriate to the stamping procedure. Also the edges on the structured side of the stamp (referred to as top side) were ground so that air bubbles caused during the aging process could be removed. The BET isotherm reflects a pore system without any constrictions and therefore, no pore blocking effects can occur when infiltrating the stamp with ink. The top surface of the stamps is flat and when turned in sunlight, interference

colors caused by the regular arrangement of the contact elements could be seen. These stamps fulfill the entire requirements for a successful stamping process.

The comparison of all three stamp generations shows clearly that the silsequioxane is the most promising material for a stamp design. Therefore, further stamping experiments were all carried out with the third-generation stamps.

*Table 2. Comparison of nitrogen sorption data of different stamp generations.  $S_{BET}$  is the specific surface area calculated from the BET isotherm;  $C$  is the BET constant (empirical constant for quantification of the attractive adsorbent-adsorbate interactions); the mean pore diameter and the specific pore volume were calculated from the adsorption branch of the BET isotherm.*

Stamp generation	$S_{BET}$ (m <sup>2</sup> /g)	$C$	Mean pore diameter (nm)	Specific pore volume (mL/g)
1 <sup>st</sup>	233	44	15	0.87
2 <sup>nd</sup>	330	80	27	2.2
3 <sup>rd</sup> , smaller pores	534	61	31	2.2
3 <sup>rd</sup> , larger pores	465	72	44	2.4

#### 4.1.4 Stamping process

In this entire work, the silica stamps of the third generation were used in a manual stamping procedure under ambient conditions. The respective pore diameters of the used stamps are specified in each chapter. To manage the stamping process, a stamp holder was made of stainless steel as shown in Figure 39. As the stamping process is a contact lithographic method and the stamps consist of a material not as flexible as e.g. a polymer, attention has to be taken when the contact elements of the stamp come in contact with the counterpart surface. Although the silica network is flexible and to some extent robust, the single stamp elements are still in the sub- $\mu\text{m}$  size range and can break easily when sheared on a hard surface. Therefore, an elastomeric PDMS layer is applied between stamp holder and stamp, which increases the flexibility and softens the stamp-substrate interaction.

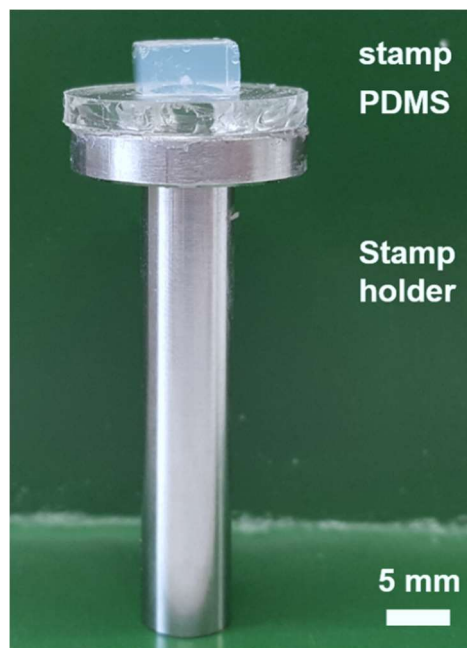


Figure 39. Stamp holder for manual stamping processes. The stamp holder consists of stainless steel, on top is an elastomeric PDMS layer glued to the stamp holder to soften the contact between stamp and counterpart surface. The stamp (in this case a dry stamp of the third generation) is glued on top of the PDMS layer. The stamp holder is held and brought into contact with a surface to be patterned manually by hand.

The stamp holder is operated by hand by bringing the stamp surface in contact with the counterpart substrate. Figure 1 (see page 6) illustrates a general stamping procedure. The mesoporous stamp (blue) infiltrated with ink (orange) is brought into contact with a surface to be patterned (grey). When the distance between stamp and substrate is small enough, liquid bridges form between the contact elements of the stamp and the counterpart surface. By removing the stamp from the surface, the liquid bridges rupture and leave droplets of ink on the surface.

The stamping procedure consists of several adjustable factors. As mentioned before, the stamps were ground before gluing them onto the stamp holder. This grinding procedure has two reasons. As the sol is poured into the mold for aging, a meniscus is formed during the aging process, which leads to a concave backside surface. If the stamp was glued to the holder on these edges only, it would not withstand the stamping process. Therefore, the backside of the stamps was ground to form a flat surface to provide a larger area for gluing. The second reason for grinding is to compensate possible imbalances in the height of the stamps due to aging processes. To avoid air bubbles and small edges on the structured surface side of the stamp, the top edges were also ground, which is visible in Figure 35b (see page 53).

The dry stamps were infiltrated from the backside (unstructured side), which verifies that the ink supplied from the backside permeates through the stamps' mesopore system to



the tips of the contact elements, as shown in Figure 40. This proves the principle of a capillary process. Within this work, the stamps were used both dry and wet and infiltrated with ink as described in each chapter. After infiltration, the stamps were kept wet throughout their entire lifetime; this has the advantage of circumventing the drying procedure and reduces the stress for the stamps. Therefore, the stamps were kept in ethanol until used and immersed in the desired ink for a certain time. In general, the stamps should be prevented from drying out after the infiltration with ink, as the fragile silica structure breaks due to capillary forces. In addition, the expansion during the conversion of a dissolved to a solid molecule caused by a possible crystallization of ink can lead to breakage.



*Figure 40. Photographs of the imbibition process of a silica stamp with ink (in this case a solution of  $C_{60}$  in toluene). The stamp is located on a glass slide with the structured stamp side facing upwards. The dried silica stamp is opaque and colorless. The infiltration occurs from the backside of the stamp by dropping the stamp solution onto the glass slide. The fully infiltrated stamp appears pink transparent.*

When the stamp is brought into contact with the counterpart surface, both pressure and contact time can be varied. Several attempts to systematically measure the expended pressure during stamping did not reveal meaningful results. This is due to the fact that stamping is performed by hand and therefore, measuring the pressure is not only dependent on the individual operator but also not reproducibly applicable. Nevertheless, the pressure tests showed that the applied pressure during stamping in the range of additional 30-100 g per stamp did not produce good results and also broke the single contact elements as shown in Figure 41. Hence, stamping was performed by bringing the stamp slightly into contact with the substrate surface.

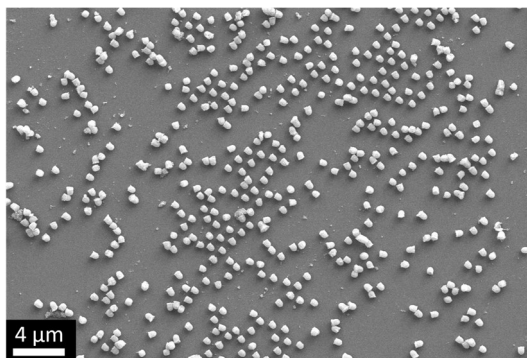


Figure 41. SEM image of exemplary stamping with additionally applied pressure. The single stamp elements broke off the stamp and could be found on the surface. The image was taken with a SESI detector.

The contact time between stamp and counterpart surface was 5 s, if not specified otherwise. This contact time was long enough for an enrichment of the non-volatile ink components in the ink menisci between the stamp's contact elements and the counterpart surface. A longer contact time did not result in well ordered stamped spots, as the manual stamping process can cause shear effects due to slight movement of the stamp holder. Also, for volatile organic solvents as chloroform or toluene, the contact time should be rather short to prevent the stamp from running dry.

The throughput of this capillary stamping method varies with different inks and different solvents. In general, several stamping cycles could be performed with almost every ink type as discussed later in this section. The bulk material of the stamp serves as ink reservoir and carries approximately 200 and 215  $\mu\text{L}$  of ink for stamps with mean pore sizes of 31 and 44 nm, respectively. Thus, the contact elements will be automatically refilled through the capillaries. Nevertheless, if the volatile ink component (solvent) has a high evaporation rate or is used throughout several stamping cycles, the stamp could be refilled with ink by simply applying a small amount of ink either on the backside or on the side walls of the stamp. This represents a capillary nanostamping process with short cycle times and a high throughput with self-refilling and manual refilling possibilities.

## 4.2 Capillary nanostamping of selected model inks

In the following chapter, the stamping process with different inks is described. As the method of capillary nanostamping with spongy mesoporous silica stamps was firstly developed, a proof of the stamping principle had to be carried out. Therefore, different kinds of model inks were stamped and investigated in their behavior as ink and within the stamping process. Every used ink consisted of a volatile component (solvent), which evaporated after or during the stamping process, and a non-volatile component, which remained on the substrate surface after the solvent evaporated.

Three possible ink precipitation processes are presumably possible. First, a stamping process, where the volatile ink component evaporates during stamping and enables an enrichment of the non-volatile ink component within the meniscus between the stamp's contact elements and the substrate surface. Second, a stamping process, where the non-volatile ink component has a high affinity to the surface, which would cause ink spreading. Third, particulate ink, which would undergo a size separation process since the stamps also act as filters to withhold larger aggregates. In addition, the dependency of different surface functionalities on the stamping results were investigated.

### 4.2.1 Meniscus confined particle growth – stamping of C<sub>60</sub> fullerenes from toluene onto hydrophobic glass

Fullerenes are of great interest, more precisely, C<sub>60</sub> is a model for endohedral fullerenes.<sup>[97]</sup> Moreover, C<sub>60</sub> is being considered as one of the best electron acceptors for organic solar cells.<sup>[98]</sup> Morphology design via controlled assembly of C<sub>60</sub> may pave the way for efficient phase-separated donor/acceptor systems.<sup>[99]</sup> However, while C<sub>60</sub> nanoparticles have gained significant interest,<sup>[100]</sup> controlled assembly of fullerenes<sup>[101]</sup> has remained challenging.

C<sub>60</sub> molecules have a high affinity to each other and crystallize in different morphologies when the solvent is evaporating. The drying conditions determine the crystal structure of the obtained C<sub>60</sub> particles, e.g. C<sub>60</sub> needles in controlled sizes can be obtained.<sup>[102]</sup> C<sub>60</sub> is a molecule by definition, but the formed agglomerates or crystals can be designated as nanoparticles.

The conditions of the stamping process of C<sub>60</sub> from toluene can be found in chapter 3.2.4.1 (see page 39). As stamps, the third-generation silica stamps with an average pore diameter of 31 nm were used. The substrate was functionalized with FDTS to obtain



a reduced surface wettability to thermodynamically prevent ink spreading. Therefore, the contact angle of toluene on FDTS-functionalized glass amounted to  $\approx 71^\circ$ . As illustrated in Figure 42, it is reasonable to assume that liquid bridges form as soon as the stamp approaches the counterpart surface between the contact elements of the stamp and the FDTS-functionalized glass. As the contact time lasted 5 s, additional ink was drawn into the liquid bridges by solvent evaporation (Figure 42b). This is due to the silica stamp, which serves as ink reservoir and draws the contained ink to flow through the network towards the counterpart substrate. As toluene is evaporating,  $C_{60}$  could be enriched within the liquid bridges and crystallized into nanoparticles. When the stamp was retracted from the substrate surface, ordered arrays of  $C_{60}$  nanoparticles remained on the surface (Figure 42c).

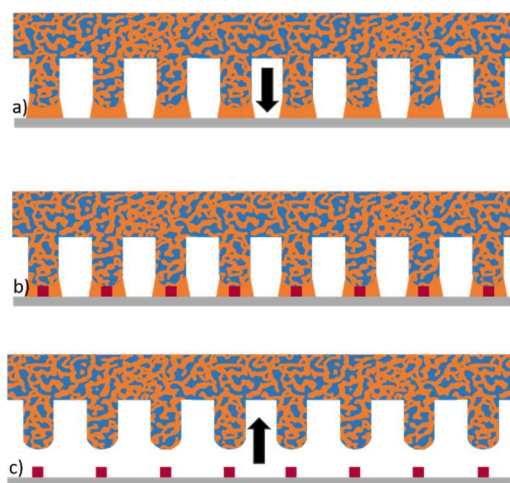


Figure 42. Illustration of a stamping process with  $C_{60}$  as ink. a) When the silica stamp (blue) filled with ink (orange) is brought into contact with a counterpart surface (grey), liquid bridges form when the stamp is close enough to the surface. b) As  $C_{60}$  (red) in toluene is stamped onto a hydrophobic substrate, the ink only partially wets the surface. The evaporation of the solvent draws additional ink into the liquid bridges and  $C_{60}$  enriches and crystallizes into nanoparticles. c) After detachment of the stamp, the  $C_{60}$  nanoparticles remain at the former positions of the contact elements.

SEM images of the obtained fullerene nanoparticles were taken either with a secondary electron chamber detector (SESI) or with an in-lens detector. The SESI detector is attached laterally tilted to the sample surface and collects SE1 and SE2 secondary electrons from the surface and a few nanometers below the surface of the sample. As it sees the sample from the side, a topographic image can be acquired. The in-lens detector is attached parallel to the sample surface above the objective lens, this ensures the collection of solely secondary electrons of type SE1 and enhances the signal to noise ratio significantly. The electrostatic field promotes a sample image with a higher contrast and

much more surface information compared to the SESI detector. Due to the geometry of the in-lens detector, topographic information disappears.

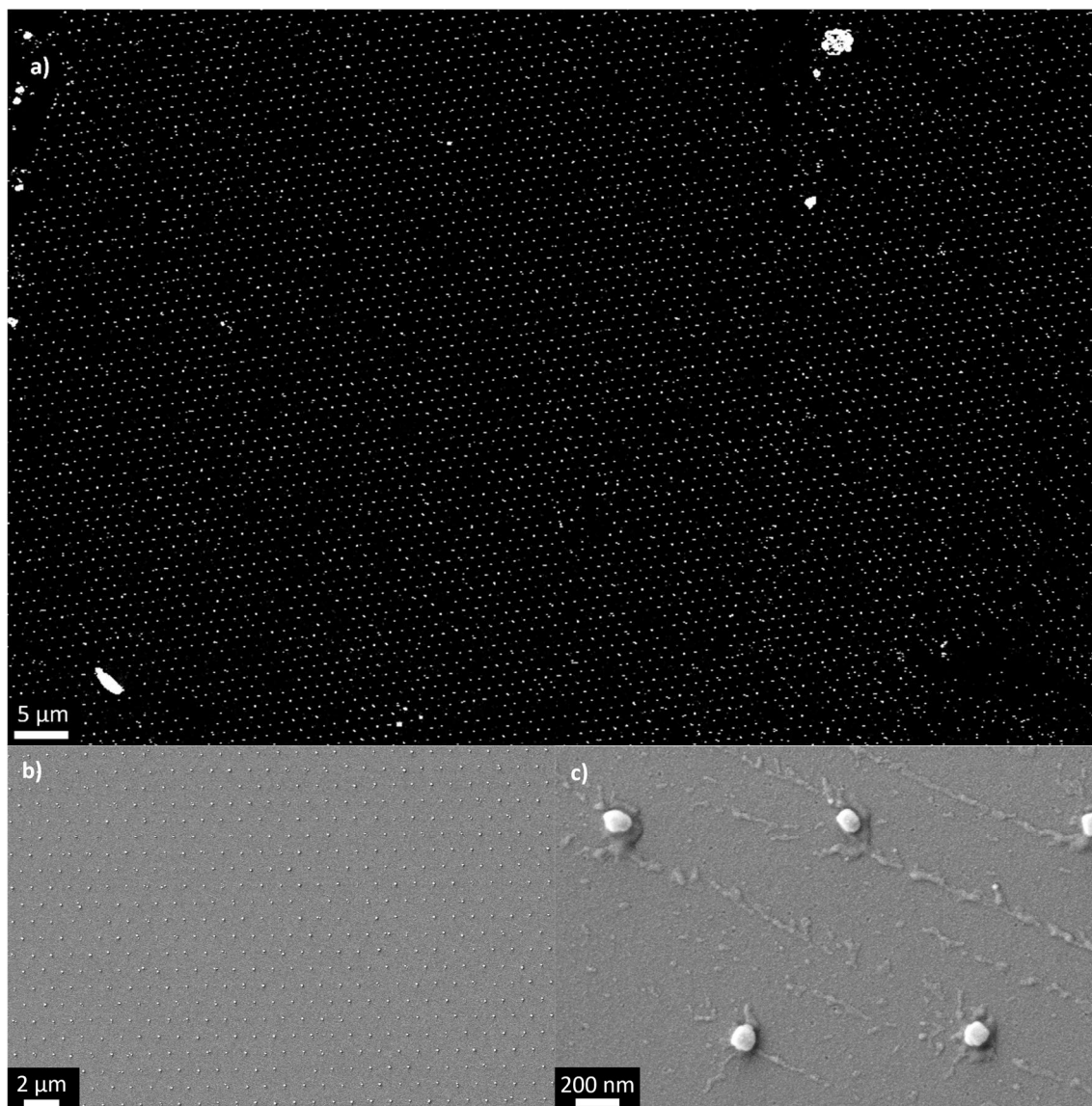


Figure 43. SEM images of stamped  $C_{60}$  particles. a) The hexagonally arranged  $C_{60}$  particles show a high uniformity over a large area. Image acquired with an in-lens detector. b) Magnification of array of  $C_{60}$  nanoparticles. c) The higher magnification of the particles shows that the  $C_{60}$  has crystallized and formed particles on the substrate. Images b) and c) were acquired with a SESI detector.

Figure 43 shows the results of the stamped fullerene nanoparticles. The SEM images acquired with the in-lens detector show the stamped fullerene nanoparticles as bright spots due to low work functions, while the glass surrounding appears dark due to a high work function, as shown in Figure 43a. The hexagonally arranged arrays of  $C_{60}$  nanoparticles have a long-range order and show few defects. The SESI detector shows topographic structures with less contrast than the in-lens detector as shown in Figure 43b

and c. Both are magnifications of the large area, in Figure 43b the order of the stamped particles can clearly be seen, while Figure 43c with the highest magnification shows the crystallized rectangular nanoparticles consisting of fullerenes. Analysis of the obtained particles was carried out according to chapter 3.1.1.12 (see page 33). The evaluation of Figure 43b resulted in 713 analyzed particles with a diameter of  $123 \pm 22$  nm, a circularity of  $0.98 \pm 0.06$ , an average aspect ratio of  $1.37 \pm 0.27$  (see Figure 44) and a center-to-center distance between neighboring particles of  $1.1 \mu\text{m}$ .

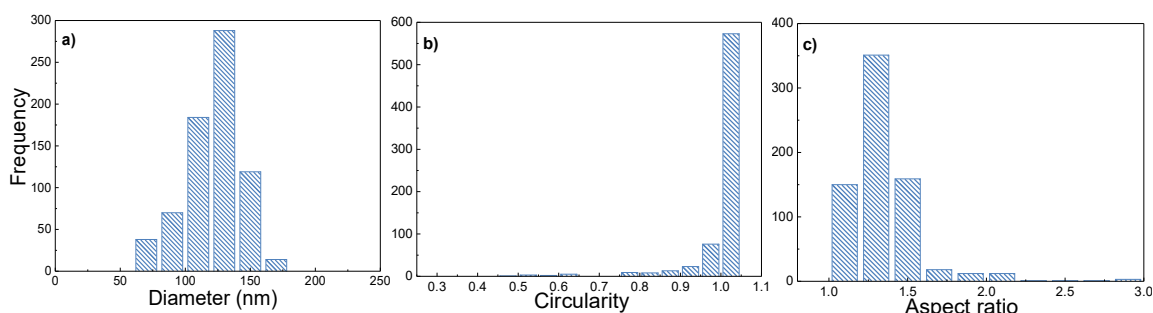


Figure 44. Histograms of 713 analyzed stamped  $C_{60}$  particles showing a) the diameters, b) the circularities and c) the aspect ratios of the  $C_{60}$  particles.

An AFM image was obtained to analyze the particle height as shown in Figure 45, the average height of the  $C_{60}$  particles amounted to 50-70 nm. The challenge in obtaining a qualitatively good AFM image is to select a scanning mode, where the AFM tip is not in physical contact with the fullerene nanoparticles, therefore the so-called tapping mode or non-contact mode was used. Nevertheless, the AFM tip can still drag single particles along the substrate and precipitate these again on a different spot. In addition, AFM is a very sensitive method and shows smallest particles, which would not be of interest in analysis methods as e.g. SEM.

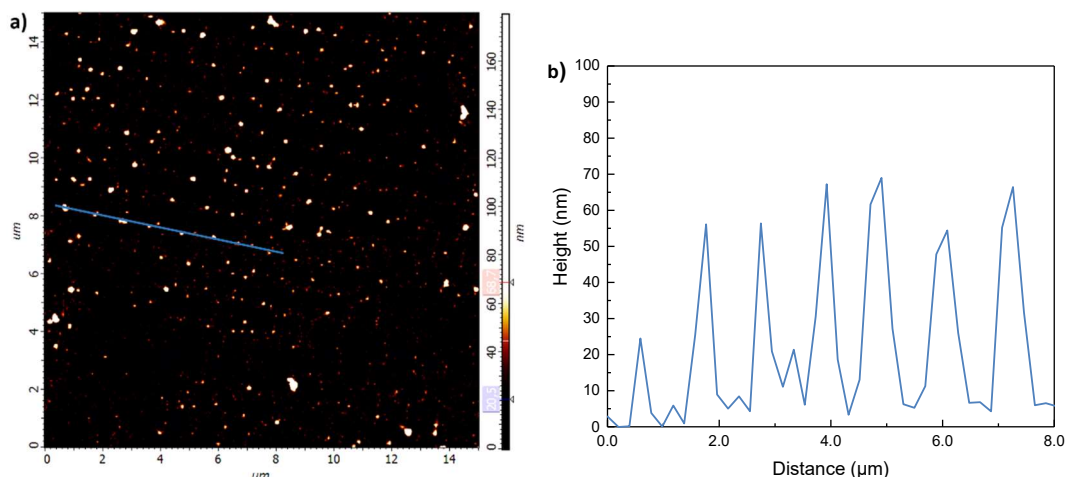


Figure 45. a) AFM image of stamped  $C_{60}$  particles and b) height profile of blue line. The average height of the  $C_{60}$  particles amounted to 50-70 nm.

Within the process of stamping fullerenes onto FDTs-functionalized glass slides, the stamps were used at least two times without changing the outcome of the pattern. As toluene is a volatile solvent, which evaporates quickly under ambient conditions, the stamp was refilled after 2-3 stamping cycles. As the stamping process lasted 5 s, evaporation of toluene results in the enrichment of the fullerenes within the meniscus between the contact elements and the substrate surface. The ink is refilled from the non-structured side or onto the side walls of the stamp and thus, a continuous stamping process was carried out. Additionally, the ink could be washed out of the stamp. To this end, the infiltrated stamp was immersed in toluene, which was replaced by fresh toluene after two hours. After five washing cycles, the stamps were fully transparent again. The nitrogen sorption analysis shows a full recovery of the mesopores and a maintaining pore system (see Figure 46). The slight changes in pore sizes and pore volume is because the analysis could not be carried out with the same stamp. Therefore, a slight variation between the single stamps is possible.

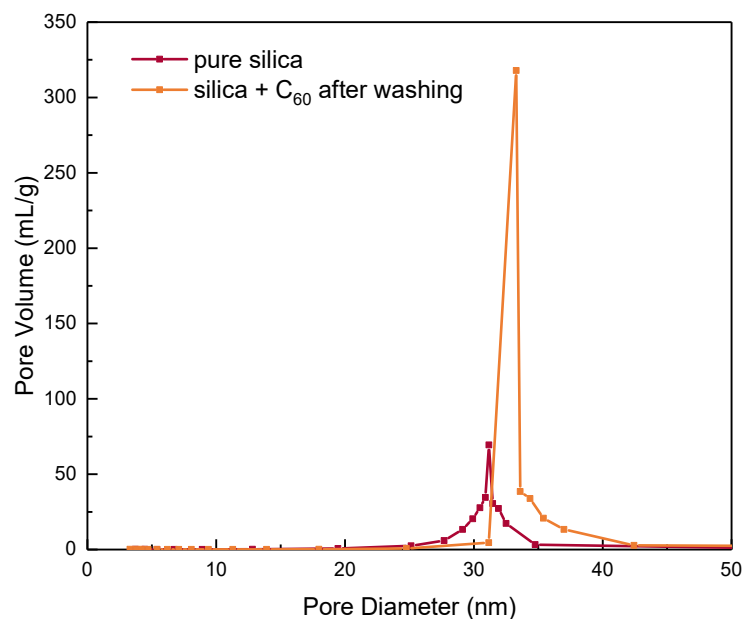


Figure 46. Nitrogen sorption analysis of silica stamps prior and subsequent to infiltration with ink and washing of the stamp. The pore size distribution calculated with the BJH method from the adsorption branch of the BET isotherm. The red curve shows a pure silica stamp, the orange curve shows a washed silica stamp, which has been infiltrated with C<sub>60</sub>/toluene and washed with toluene.

Although dry stamps were used and infiltrated for the described stamping process, a drying out of the already infiltrated stamp should be avoided. Nevertheless, every new stamping process was carried out with new stamps. Although the stamps can outlast a long time when infiltrated with ink, the fullerenes tend to aggregate when stored in a solution and interactions between the pores and the fullerene aggregates could lead to pore blocking or breakage of the stamp. Hence, a dispersion of fullerenes in toluene was freshly made and a new stamp was used every time stamping experiments were carried out.

C<sub>60</sub> fullerenes from toluene could be stamped on perfluorinated glass slides and resulted in defined particles of regular sizes and shapes in a hexagonally arranged order. The particle sizes were smaller compared to the contact elements of the stamp, which is due to the crystallization of the fullerenes on the substrate surface.

When fullerenes dispersed in toluene as solvent are used as ink, attention has to be taken of preventing the stamp from drying out. Therefore, refilling of the infiltrated stamp with ink is possible to keep the continuous stamping process running.



## 4.2.2 Self-limited spreading – stamping of 1-dodecanethiol from ethanol onto gold-coated glass

The strong affinity of thiols with gold surfaces<sup>[103]</sup> was utilized to develop a stamping process of 1-dodecanethiol on gold-coated glass slides. 1-Dodecanethiol is a representative of the broad variety of functional thiols used for the generation of chemically patterned surfaces.<sup>[104]</sup>

### 4.2.2.1 Microscopic characterization

The conditions of the stamping process of 1-dodecanethiol from ethanol can be found in chapter 3.2.4.2 (see page 39). As stamps, the third-generation silica stamps with an average pore diameter of 31 nm were used. The glass slides were coated with titanium and gold, respectively, by physical vapor deposition. The titanium layer ensures the adhesion of the gold layer on the surface. The thicknesses of the layers, determined with a quartz crystal microbalance (as described in chapter 3.1.1, page 30), amounted to 5 and 30 nm for titanium and gold, respectively.

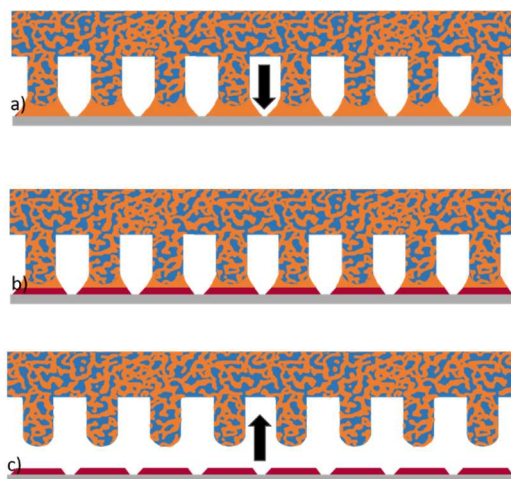


Figure 47. Illustration of a stamping process with 1-dodecanethiol as ink. a) The ethanolic 1-dodecanethiol solution (orange) is stamped onto a gold-coated glass slide (grey). b) Submicron dots of 1-dodecanethiol (red) are formed at the positions of the contact elements by adsorption of 1-dodecanethiol onto the gold surface. c) After detachment of the silica stamp, a chemically patterned surface is obtained.

The general schematic illustration of the stamping process of inks, where both, the non-volatile ink component and the solvent, have a high affinity to the surface to be stamped, is shown in Figure 47. The contact elements close to the substrate surface form capillary bridges, whereby the non-volatile component of the ink (in this case the 1-dodecanethiol)

is transported to the substrate surface (Figure 47a). When the stamp is retracted from the substrate and the volatile component of the ink (in this case ethanol) has evaporated, spots of the non-volatile ink component remain where the contact elements encountered the substrate surface (Figure 47c).

#### 4.2.2.2 *Image analysis*

After stamping of 1-dodecanethiol, the unprotected part of the gold layer was partially etched as described in chapter 3.2.4.2 (see page 39), to create a higher topographic contrast, which allowed the identification of the 1-dodecanethiol spots with SEM analysis. The images in Figure 48 show the outcome of the SEM analysis. The dots of stamped 1-dodecanethiol are clearly visible as well as the hexagonal order. Figure 48a shows a large area with an even larger area obtained as shown in Figure 49. Figure 48b shows a detail of Figure 48a, but was taken with an in-lens detector. The areas with 1-dodecanethiol have a high work function and hence appear dark, whereas the gold appears bright. The differences between the SESI and the in-lens detector can be seen clearly in the images in Figure 48a and b. The SESI detector gives a topographic information, where the stamped 1-dodecanethiol spots and the surroundings appear to be on a different height level. With the in-lens detector, the height information vanishes completely, while the material contrast increases significantly. While the SESI detector shows both structures, spots and surroundings, in the same grey, the in-lens detector differentiates between higher and lower work function, which leads to black 1-dodecanethiol spots and bright gold surroundings.

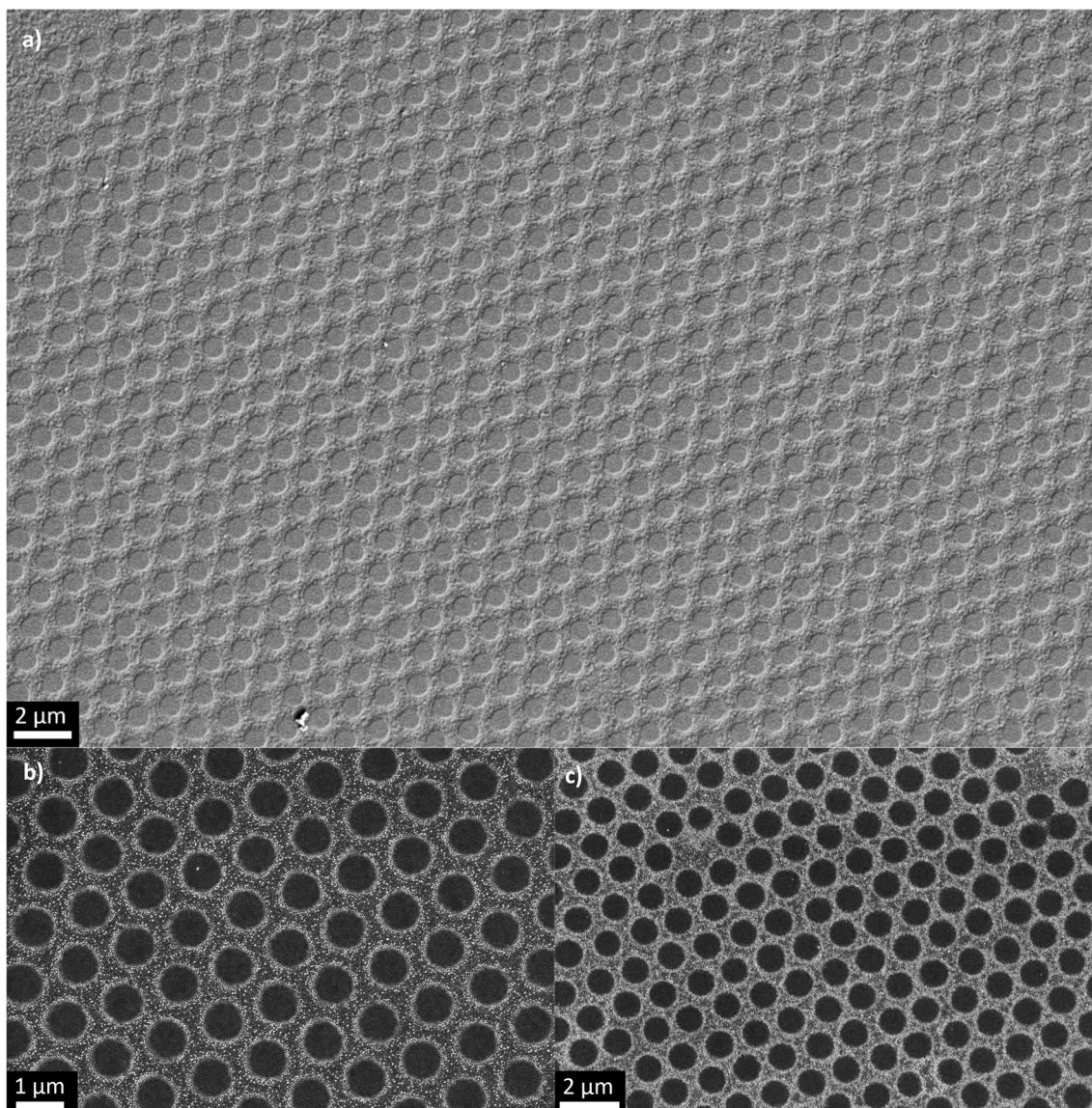


Figure 48. SEM images of hexagonally arranged arrays of 1-dodecanethiol dots generated by stamping on gold-coated glass slides after partial etching of the gold. The 1-dodecanethiol serves as protection for the gold, therefore on the stamped dots, the gold could not be etched away. a) Overview of large stamped area. b) Detail of a), but taken with an in-lens detector. The areas with 1-dodecanethiol have a high work function and hence appear dark, whereas the remained gold appears bright. c) Stamped dots prepared in the 10<sup>th</sup> successive stamping cycle without refilling of the stamp. Image a) acquired with a SESI detector, images b) and c) acquired with an in-lens detector.



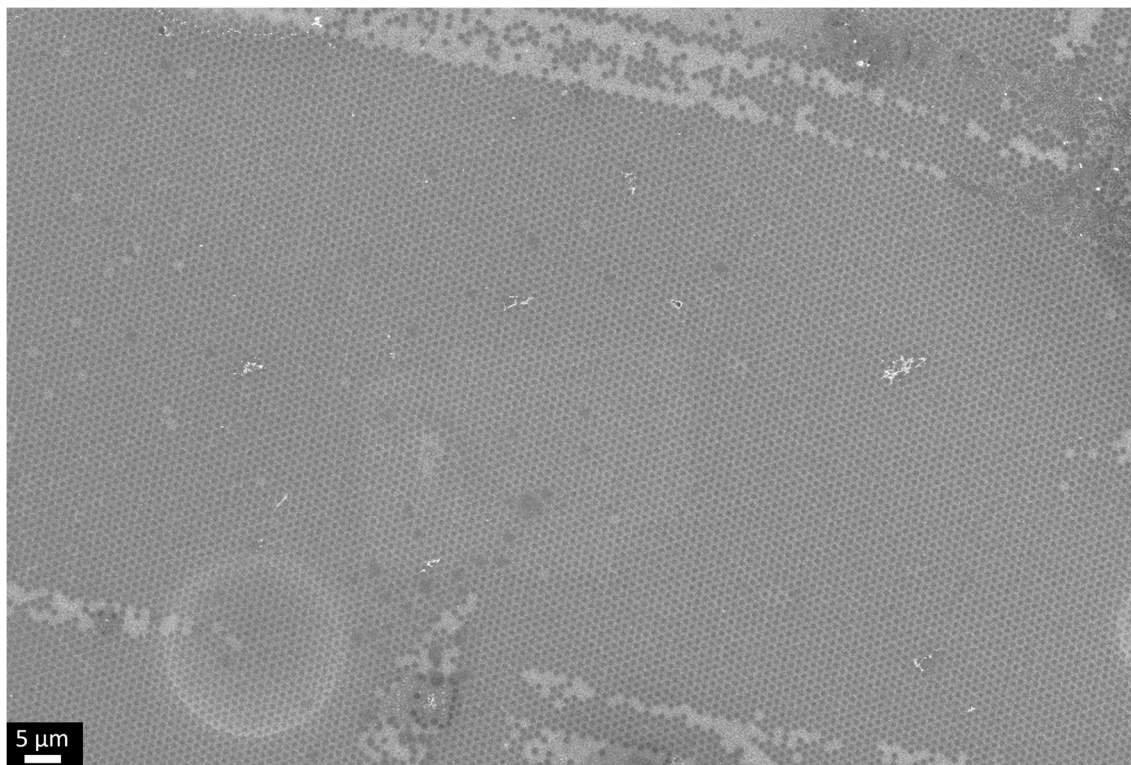


Figure 49. SEM image acquired with a SESI detector of a large overview area of 1-dodecanethiol dots stamped on a gold-coated substrate with subsequent partially etching of the unprotected gold layer.

One SEM image (see Figure 50) was binarized for a more precise analysis of the single dots according to chapter 3.1.1.12 (see page 33). The analysis resulted in 1304 dots with an average diameter of  $757 \pm 25$  nm and a distance of 1.2 μm between the single dots. For the evaluated 1-dodecanethiol dots, the obtained average circularity is  $0.94 \pm 0.03$  and the average aspect ratio is  $1.09 \pm 0.04$  (Figure 51). The slight deviations from ideal circular shape may be rationalized by slight shear during stamping or by aberration.

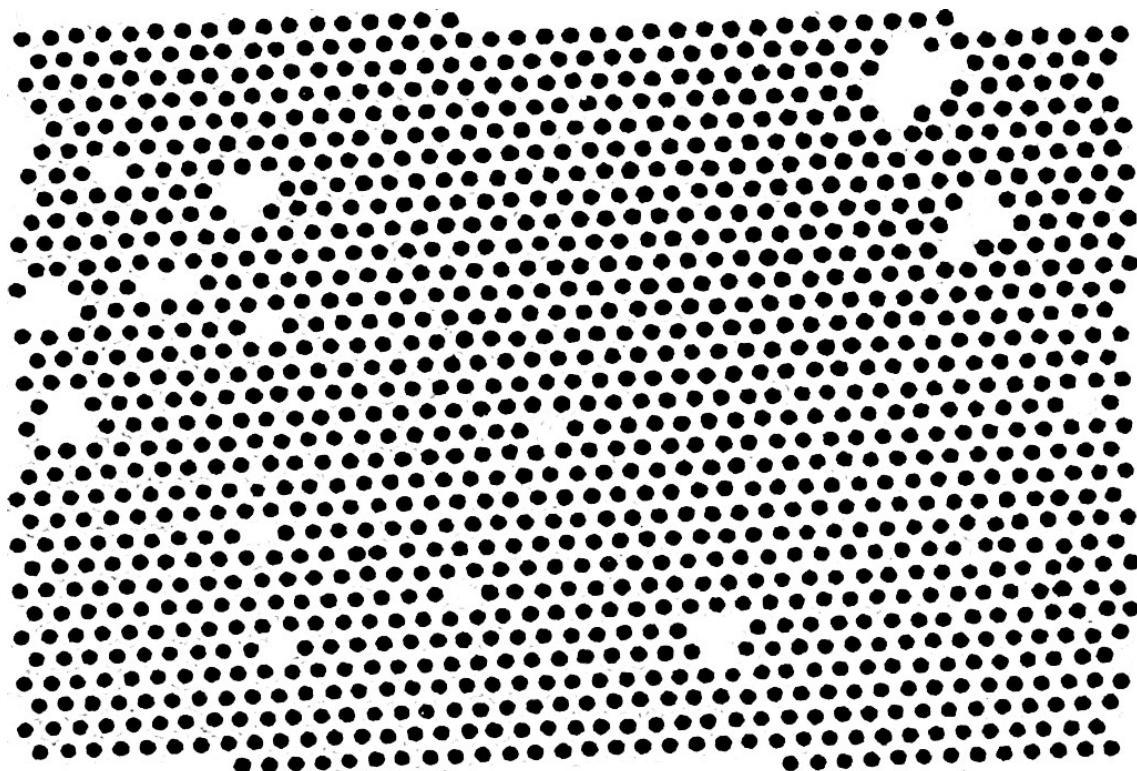


Figure 50. Binarized SEM image of stamped 1-dodecanethiol dots on gold-coated glass.

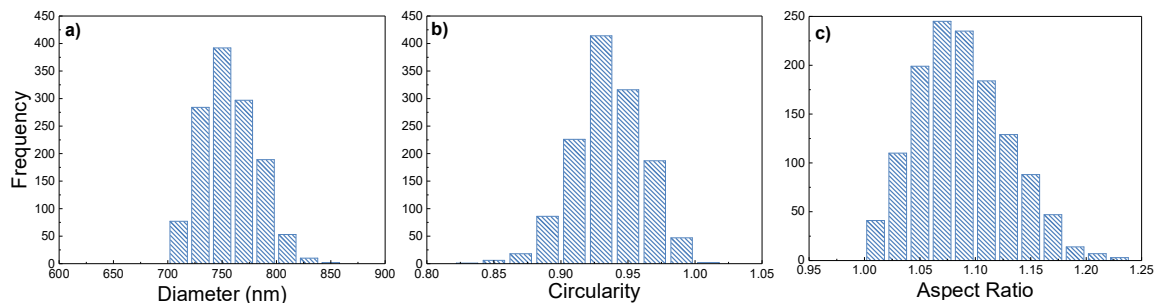


Figure 51. Histograms of 1304 analyzed stamped 1-dodecanethiol dots (see Figure 50) showing a) the diameters, b) the circularities and c) the aspect ratios of the 1-dodencanethiol dots.

The peak-to-valley height of the 1-dodecanethiol dots and their partially etched gold surroundings amounted to 15-20 nm as measured with AFM using the contact mode and extracting a line profile of the measured data. AFM image with inserted line and related line scan are shown in Figure 52.

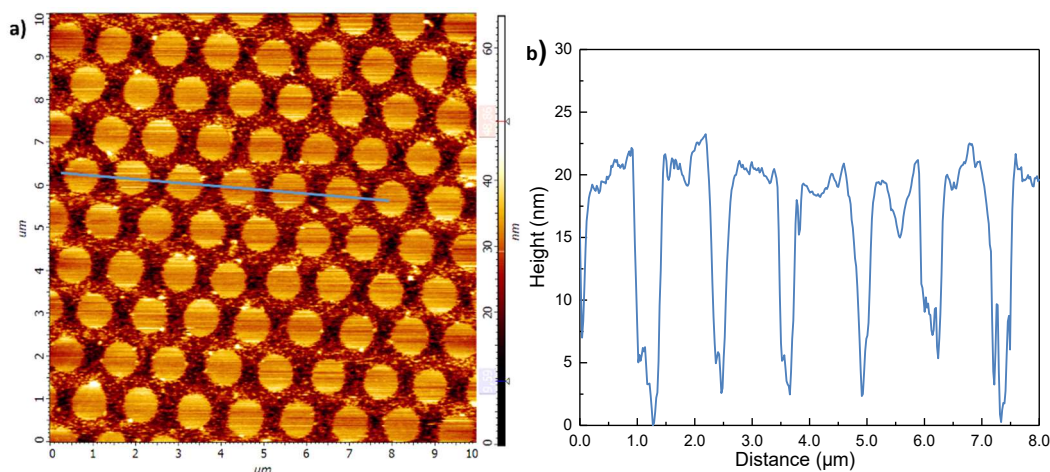


Figure 52. a) AFM image of 1-dodecanethiol stamped on gold-coated glass with subsequent etching of unprotected gold layer and b) height profile of blue line. The average peak-to-valley height between the 1-dodecanethiol dots and their gold surroundings amounted to 15-20 nm.

#### 4.2.2.3 Structure formation model

The stamped 1-dodecanethiol dots had a larger diameter than the contact elements. In fact, the mean diameter of the 1-dodecanethiol dots is by a factor of 1.75 larger than the diameter of the contact elements of the stamps. It is remarkable that discrete sub-micron 1-dodecanethiol dots were obtained despite the fact that macroscopic ethanol drops spread on the gold-coated glass slides. The contact angle of ethanol on gold is  $0^\circ$ , which should lead to ink spreading. Nevertheless, dots of 1-dodecanethiol on gold could be obtained.

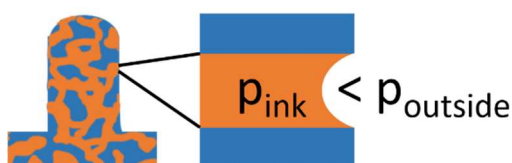


Figure 53. Illustration showing a concave meniscus formed by ink (orange) at a mesopore opening of a silica stamp (blue). The pressure of the ink  $p_{ink}$  is smaller than the air pressure  $p_{outside}$ . The pressure difference across the meniscus is the Laplace pressure.

This outcome may be rationalized as follows. The ink is drawn out of the contact elements of the stamp by van der Waals interactions between ink and gold-coated glass slide. However, the entire surface of the stamp exhibits mesopore openings where the ink forms concave menisci. Because of the concave curvature of the menisci, the ink pressure  $p_{ink}$  is lower than the air pressure outside the stamp  $p_{outside}$  (see Figure 53). The pressure drop across the menisci with

$$\Delta p = p_{outside} - p_{ink} \quad (4)$$

is referred to as Laplace pressure,<sup>[105]</sup> which counteracts the attractive van der Waals forces between ink and gold-coated glass slide. Therefore, it is reasonable to assume that the Laplace pressure within the open mesopores in the silica stamps impedes spreading of ethanol on the gold-coated glass substrates. On the other hand, if a gold-coated glass slide is immersed into a solution of 2 mM 1-dodecanethiol in ethanol for 5 s, the contact angle of ethanol on this glass slide increases to  $\approx 34^\circ$ . Hence, the adsorption of 1-dodecanethiol on the gold-coated glass substrate itself in the course of capillary nanostamping may suppress ink spreading.

Stamping of 1-dodecanethiol was carried out up to 10 times before re-infiltration of the stamp as shown in Figure 48c. As the stamping process only lasts  $\approx 1$  s, multiple stamping cycles without refilling were possible. Due to the ink reservoir within the stamp, a continuous stamping procedure can be achieved. The number of cycles is mostly dependent on the nature of the used ink.

1-Dodecanethiol dissolved in ethanol could be stamped onto gold-coated glass with the outcome of regular, round dots of sizes larger than the contact elements of the stamp. Although ethanol spreads on gold surfaces, an overall ink spreading did not occur, as the mesoporous contact elements serve as counteracting part due to the occurring Laplace pressure. Furthermore, the changing surface properties due to the adsorption of 1-dodecanethiol on the substrate, prevents further ink spreading.

In general, a continuous stamping mode could be achieved by creating an ink storage out of the silica network. When 1-dodecanethiol was used as ink, up to 10 stamping cycles could be carried out without deformation or changes in the pattern obtained.

#### 4.2.2.4 *Dewetting of polystyrene on 1-dodecanethiol stamped gold-coated glass slides*

Stamping of 1-dodecanethiol results in a heterogeneous substrate surface, where the created pattern consists of areas of different chemical properties. Chemically heterogeneous surfaces have gained significant interest in research.<sup>[106]</sup> Surface patterns of areas with chemically different properties template the dewetting of polymeric liquids deposited on the chemically heterogeneous surfaces.<sup>[107,108]</sup> Therefore, a dewetting experiment with polystyrene (PS) as well-characterized model liquid was carried out.<sup>[109,110]</sup>



Solutions of 0.5 and 0.05 wt% of PS in chloroform, respectively, were spin-coated onto the gold-coated glass slides patterned with 1-dodecanethiol dots. Subsequently, the samples were heated to 170 °C for 30 min, a temperature above the glass transition temperature ( $T_g$ ) of PS. The exact procedure is described in chapter 3.2.4.3 (see page 40). PS selectively wets gold because the polarizability of gold is higher than that of 1-dodecanethiol. Thus, the attractive London dispersion interactions between PS and gold are stronger than between PS and 1-dodecanethiol.

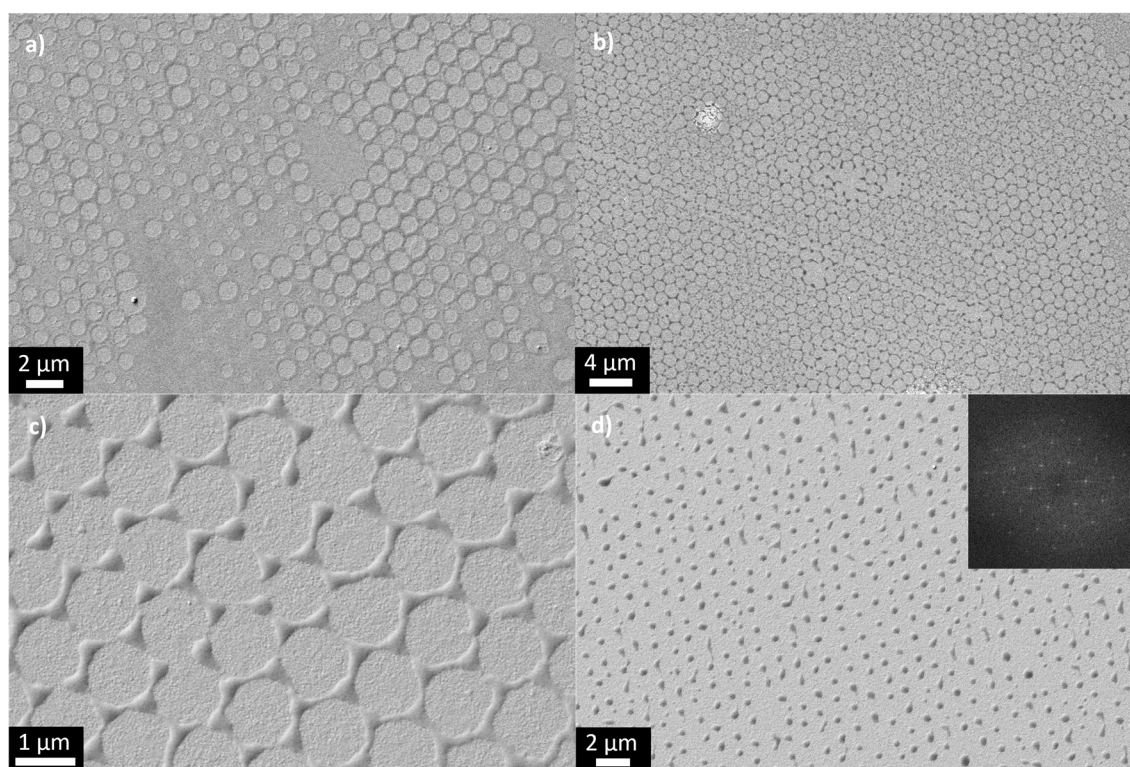


Figure 54. Dewetting process of PS on a gold-coated glass slide modified by stamping of 1-dodecanethiol dots. a) The dewetting process starts with the building of round holes where the 1-dodecanethiol dots were stamped and continues by b), c) forming a honeycomb structure around the dots and d) finally ends in creating single PS dots in triangular spaces located in the gaps between three adjacent 1-dodecanethiol dots. The inset of d) shows the FFT analysis, where the hexagonal order is clearly visible. All SEM images were acquired with a SESI detector.

The dewetting velocities slightly varied in different sample regions so that snapshots of different wetting stages could be taken as seen in Figure 54. In some parts, a continuous PS film still exists (Figure 54a). Also seen, however, are circular holes in the PS film at the positions of 1-dodecanethiol dots. Many of these holes have smaller areas than the 1-dodecanethiol dots, suggesting that dewetting is initiated by nucleation of holes in the PS film at positions where the PS film covers 1-dodecanethiol dots. Dewetting then proceeds by growth of the holes and formation of thickened PS rims surrounding the growing holes (Figure 54b). The thickened rims move outwards until they impinge on each other

in areas where gold is exposed to the PS. As a result, the PS leaves the 1-dodecanethiol dots blank and forms a honeycomb pattern that coincides with the exposed gold surface separating the discrete 1-dodecanethiol dots (Figure 54c). The honeycomb pattern further decomposes into discrete triangular PS nanoparticles located in the gaps between three adjacent 1-dodecanethiol dots. Eventually, ordered arrays of PS nanoparticles were obtained. The obviously patterned structure is shown in Figure 54d, where the inset shows the FFT analysis, and thus the hexagonal order, of the acquired image.

The heterogeneous surface obtained with stamping of 1-dodecanethiol dots onto gold-coated glass could be used in a dewetting application. It was shown that PS spin-coated onto the heterogeneous surface with subsequent heating to a temperature above  $T_g$  of PS resulted in triangularly shaped dots of PS arranged on the unmodified gold-coated area of the surface. This opens the opportunity to create heterogeneous substrates consisting of discrete dots and remaining surroundings with different properties regarding e.g. wettability or adhesion.

#### 4.2.3 Particulate inks – stamping of nanodiamonds from isopropanol onto hydrophobic glass

Nanodiamonds (NDs) are widely used in a wide range of research. Biologists have found the advantages of NDs as robust, fluorescent emitters with applications in biolabeling while NDs can be introduced into the cells without toxic effects.<sup>[111–113]</sup> Physicists are working on understanding and controlling the electronic properties of lattice impurities within the nanodiamonds.<sup>[114]</sup> The mostly investigated defect is the nitrogen-vacancy (NV) defect, which has magnetic properties and shows quantum behavior. The detection of electron paramagnetic resonance (EPR) from a single NV defect was reported by Gruber *et al.* in 1997.<sup>[115]</sup> These characteristics make nanodiamonds predestined as sensors to monitor electric or magnetic fields with high sensitivity.<sup>[116–118]</sup> For that means, many attempts on patterning nanodiamonds for spatially resolved sensors onto a desired substrate were made.<sup>[119–121]</sup> All of these patterning experiments were long-lasting and time-consuming procedures with many synthesis steps resulting in ND spots with diameter sizes of 300 nm up to tens of micrometers.

Using the method of capillary nanostamping, nanodiamonds were stamped from dispersion onto glass and investigated with SEM, confocal fluorescence microscopy and optically detected magnetic resonance (ODMR). The exact stamping conditions can be found in chapter 3.2.4.4 (see page 40). As stamps, the third-generation silica stamps with an average pore diameter of 31 nm were used. Nanodiamonds with average sizes of 10 nm were stamped from a dispersion in isopropanol with a concentration of 10  $\mu\text{g}/\text{mL}$  onto FDTS-functionalized glass to prevent ink spreading (contact angle of isopropanol on FDTS-functionalized glass  $\approx 45^\circ$ ). For the stamping of NDs from isopropanol, dry stamps were infiltrated from the non-structured backside. The dispersion of NDs in isopropanol is not stabilized and thus, the NDs rapidly start to aggregate. To prevent the precipitation of larger aggregates of NDs on the substrate surface, the silica stamp was additionally used as a filter. The stamping process of NDs in isopropanol as ink follows the procedure described in Figure 55. Bigger aggregates of NDs are rejected by the stamp due to a larger size compared to the stamp's pore size (Figure 55a). During stamping, the non-volatile ink component is enabled to enrich within the meniscus between contact element and substrate surface (Figure 55b). After evaporation of the solvent, small aggregates of NDs are left at the former positions of the contact elements (Figure 55c).

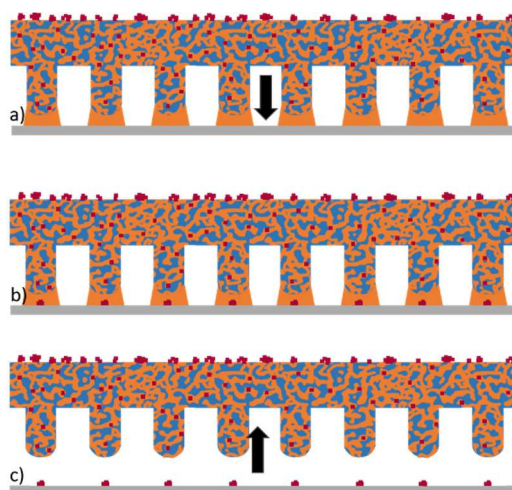


Figure 55. Illustration of a stamping process with particulate inks, which tend to aggregate, e.g. nanodiamonds. a) When the silica stamp (blue) filled with ink (orange) is infiltrated with nanodiamonds (red), bigger aggregates are rejected by the stamp, as larger particles cannot pass through the pore system. When the infiltrated stamp is brought into contact with a counterpart surface (grey), liquid bridges are formed. b) As the NDs in isopropanol are stamped onto a hydrophobic substrate, the ink only partially wets the surface. The evaporation of the solvent draws additional ink into the liquid bridges and the NDs enrich and crystallize into small aggregates. c) After detachment of the stamp, the NDs remain at the former positions of the contact elements.



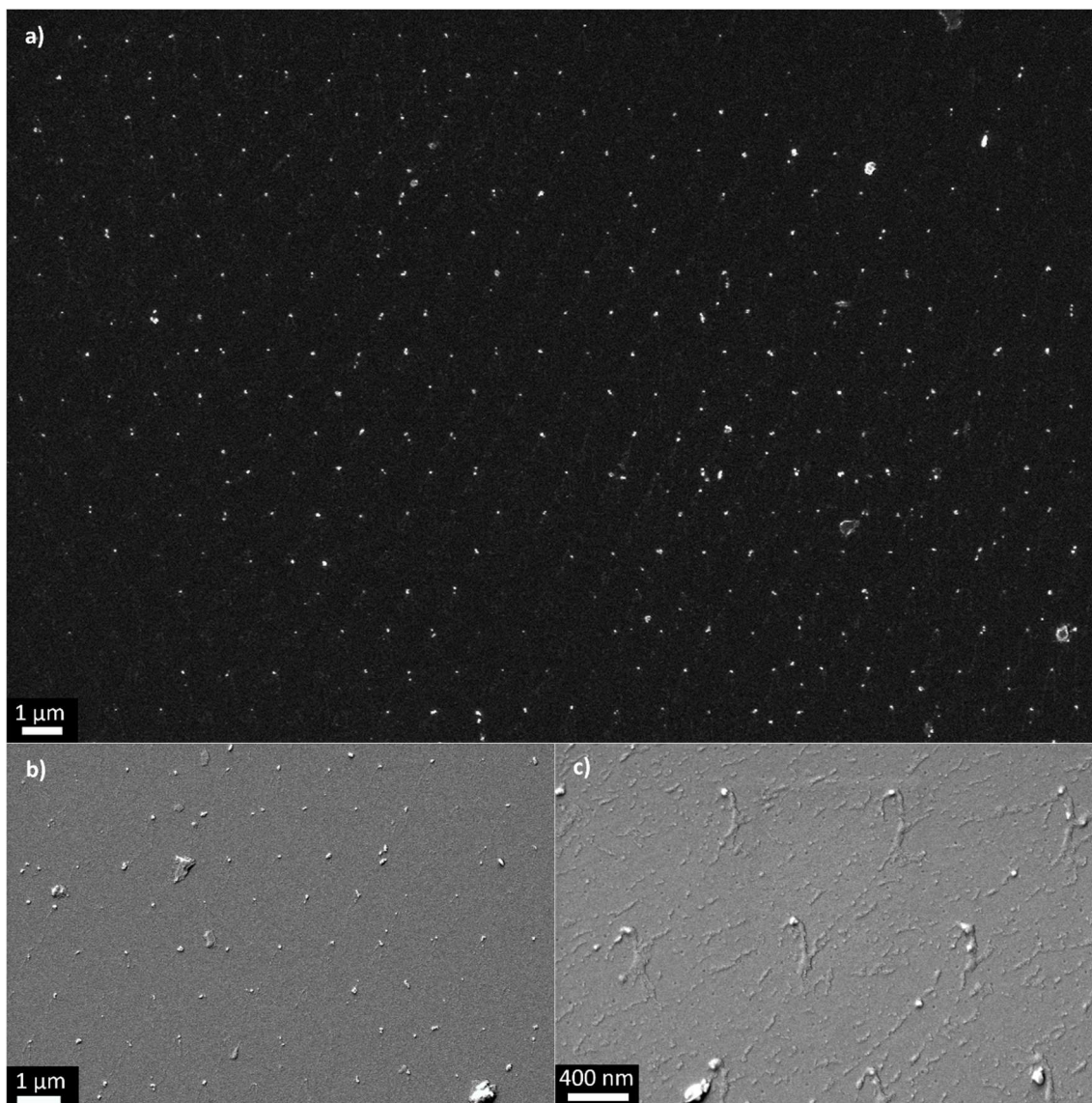


Figure 56. SEM images of stamped NDs on FDTD-functionalized glass. a) Overview of larger area. The NDs are hexagonally arranged. b), c) Magnifications of stamped particles. From image c) it is assumable that only 1-4 NDs were precipitated per spot. Image a) was taken with an in-lens detector, images b) and c) were taken with a SESI detector.

The SEM image in Figure 56a shows the overview of a larger area of precipitated NDs on the substrate surface. The hexagonal order is visible, although the overall area is not highly clean. The magnification in Figure 56b illustrates the accumulation of larger aggregates of NDs on some spots. Although the dry stamps were infiltrated from the non-structured side to prevent the precipitation of larger aggregates, a total avoidance was not successful. Bigger particles and larger aggregates may have been transferred over the edges of the stamp onto the substrate. In addition, some parts of the stamp's contact elements presumably broke during stamping and were precipitated on the surface. In some regions, as seen in Figure 56c, only a very small amount of NDs was precipitated onto the substrate. In this case, it is assumable, that only 1-4 NDs were stamped per



spot. If compared to any state-of-the-art literature, where NDs were used to obtain an ordered pattern on a substrate, the diameter of the obtained spots ranges from 100 nm<sup>[120]</sup> to 30  $\mu\text{m}$ ,<sup>[121]</sup> which is significant larger than the ND spots obtained by capillary nanostamping. Analysis of the obtained ND aggregates was carried out according to chapter 3.1.1.12 (see page 33). The analysis of the SEM images resulted in 334 aggregates with a particle-to-particle distance of 1.1  $\mu\text{m}$ , an average diameter of  $43 \pm 24$  nm, a circularity of  $0.90 \pm 0.16$ , and an average aspect ratio of  $1.55 \pm 0.50$  (see Figure 57).

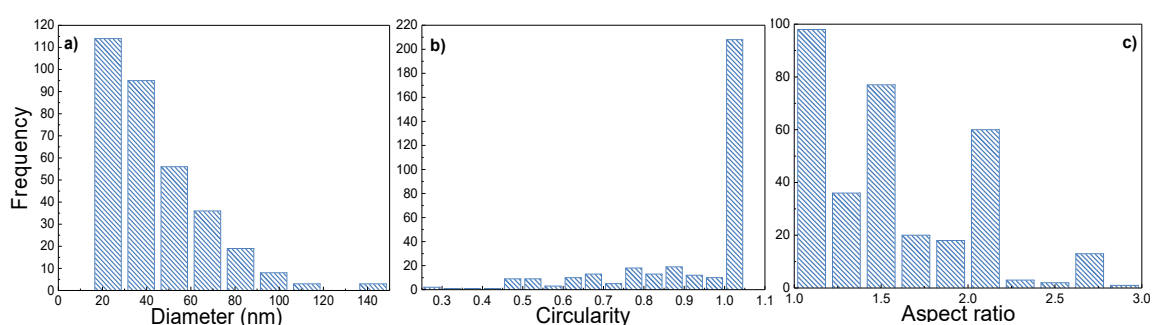


Figure 57. Histograms of 334 analyzed stamped ND aggregates showing a) the diameters, b) the circularities and c) the aspect ratios of the ND aggregates.

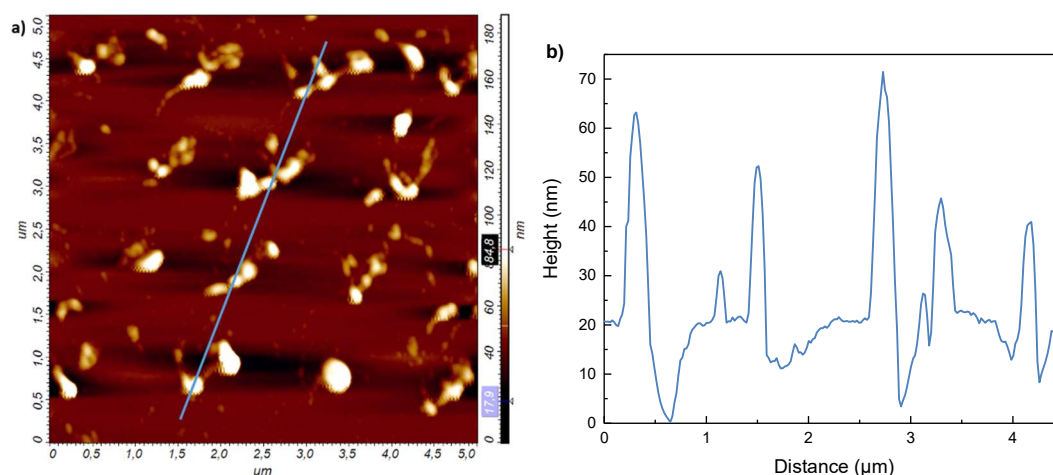


Figure 58. a) AFM image of stamped NDs on FDTs-functionalized glass. b) The line scan shows the height of the stamped ND aggregates. The height of the aggregates amounted to 10-50 nm.

AFM analysis turned out to be quite delicate, as the nanodiamonds interact with the AFM tip and were pulled away by the tip. The obtained AFM image shown in Figure 58a resulted in a height of 10-50 nm (Figure 58b).

To prove the presence of stamped NDs on the substrate surface, the detection of the characteristic response of diamond-hosted  $\text{NV}^-$  centers was measured with ODMR and  $T_1$ -relaxation by René Wiczorek in the Physics Department of the University of Osna-brück.<sup>[122]</sup> The zero-field splitting  $D$  is the energy difference between spin sublevels in the absence of external magnetic fields. It originates from the triplet spin ground state of the  $\text{NV}^-$  center, which further splits into three spin sublevels once a magnetic field is applied.<sup>[114]</sup> Characteristic values for  $D$  within  $\text{NV}^-$  centers in nanodiamonds are  $D=2.87 \text{ GHz}$  for the ground state and  $D=1.42 \text{ GHz}$  for the excited state.<sup>[123]</sup> Further, the transition rate between the different sublevels is given by the  $T_1$  relaxation time, which is typically in the millisecond range at room temperature and can be influenced by applying a magnetic field, which makes nanodiamonds excellent sensors for magnetic fields.<sup>[124]</sup>

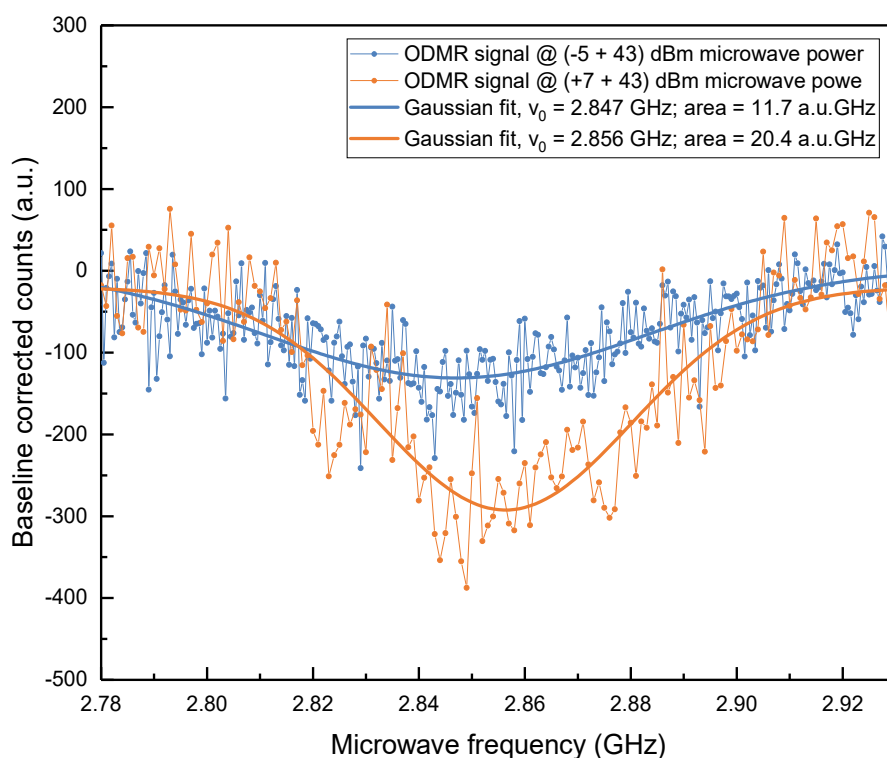


Figure 59. ODMR measurement of nanodiamonds stamped onto FDTs-functionalized glass at two different microwave power settings. The microwave power was set to -5 dBm amplified by 43 dBm (blue curve), and 7 dBm amplified by 43 dBm (orange curve). The results were fit with a Gaussian model and resulted to  $D=2.856$  and  $D=2.847 \text{ GHz}$  for a microwave power of -5 and 7 dBm, respectively. The integration of the Gaussian fit gives an area of 11.7 and 20.4 a.u.·GHz for a microwave power of -5 and 7 dBm, respectively.

The results of the ODMR measurements are shown in Figure 59. The stamped NDs were measured with a microwave power of -5 and 7 dBm amplified by 43 dBm, and resulted in the blue and orange curves, respectively. The obtained data were approximated by a single Gaussian model, which amounted to  $D=2.856$  and  $D=2.847 \text{ GHz}$  for a microwave

power of -5 and 7 dBm, respectively. The slight difference of the single center resonance frequencies is due to thermal background conditions and the deviation from the typical zero magnetic field resonance at room temperature may be due to crystal strain, which is typically observed for small nanodiamonds.<sup>[123]</sup> The integration of the Gaussian fit results in an area of 11.7 and 20.4 a.u.·GHz for a microwave power of -5 and 7 dBm, respectively. Within these measurements, no fine structure could be monitored, which is traced back to power broadening. Nevertheless, the data was taken below the saturation limit and an increasing microwave power led to enhanced signal areas as expected.<sup>[125]</sup>

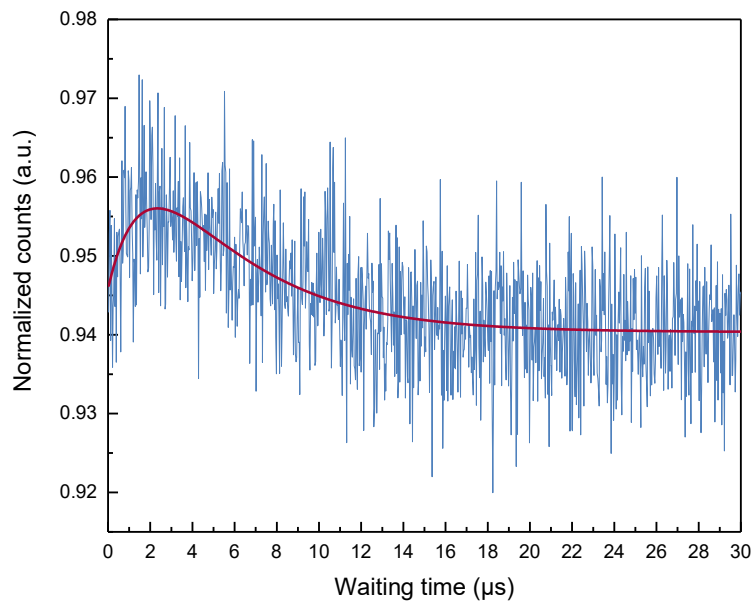


Figure 60.  $T_1$  relaxation time measurement. The blue data was fit with a double exponential model according to Tetienne *et al.*<sup>[126]</sup> with (5) and amounted to  $T_1=1.8 \mu\text{s}$ .

The typical spin relaxation is obtained with the  $T_1$  measurement shown in Figure 60. Therefore, the data was fit to a double exponential model according to Tetienne *et al.*<sup>[126]</sup> with

$$I(\tau) = I(\infty) \left[ 1 - C_m e^{-\frac{\tau}{T_m}} + C_1 e^{-\frac{\tau}{T_1}} \right] \quad (5)$$

The obtained relaxation time amounted to  $T_1=1.8 \mu\text{s}$ . These measurements reflect a proof of stamped nanodiamonds on the substrate surface.

Stamping of nanodiamonds with an average size of 10 nm from dispersion with the method of capillary nanostamping with mesoporous silica stamps resulted in hexagonally

ordered spots in the 40 nm size range, which corresponds to 1-4 nanodiamonds per spot. These results show the capability of capillary nanostamping with a particulate ink and present a new way of generating ordered arrays of a few nanodiamonds per spot. The used NDs had an amount of NV<sup>-</sup> centers of 6%, although fluorescence microscopy analysis was carried out, it did not result in sufficient images due to a relatively low chance of the presence of NV<sup>-</sup> centers within 1-4 nanodiamonds per spot. With a higher quality of NV<sup>-</sup> centers within the nanodiamonds, these measurements would supplement the presented results.

#### 4.2.3.1 *Functionalization of stamped nanodiamonds with a diameter of 5 nm*

The modification of surfaces to control their behavior and availability for chemical reactions is of great interest. Nevertheless, a direct functionalization of a surface in a defined order is difficult due to steric hindrances and long-lasting functionalization procedures. As click chemistry is easily available, fast and offers a whole range of possibilities, it becomes more and more interesting for surface functionalization.<sup>[127–129]</sup> The combination of click chemistry and  $\mu$ CP allows a controlled surface functionalization in a desired pattern.<sup>[130–132]</sup> Nevertheless, if the surface should be patterned with larger structures, e.g. proteins or large bio-molecules, a direct printing process would become difficult. NDs provide an outer surface consisting of a variety of organic residues, which can be reduced or oxidized as desired.<sup>[83]</sup> To combine these methods, click-available NDs were stamped onto a substrate surface in a capillary nanostamping procedure. A subsequent click reaction was carried out to show the accessibility of the as-stamped particles on the surface for further chemistry.

The exact synthesis procedures can be found in chapter 3.2.4.5 (see page 41). As stamps, the third-generation silica stamps with an average pore diameter of 31 nm were used. For the functionalization, NDs with an average size of 5 nm were used. Prior to stamping of NDs, a functionalization towards click-availability was carried out. Therefore, the as-received NDs were functionalized according to Figure 61. Raw nanodiamonds have a variety of surface residues, ranging from hydroxyl-groups to carboxyl or ketone residues.<sup>[86]</sup> To generate a homogeneous surface with equally available residues for further synthesis, the surface residues of the as-received NDs were reduced with  $\text{BH}_3 \cdot \text{THF}$  to obtain a mostly hydroxyl-terminated surface of NDs (Figure 61a). With this easily available surface residues, a further synthesis with a silane was carried out (Figure 61b) to generate a bromo-residue, which again is available for a variety of further functionalization. In the next step, the NDs were converted to become click-accessible by the reaction

of the bromo-residue with sodium azide (Figure 61c). The obtained ND-N<sub>3</sub> could then be stamped and provided a suitable reaction partner for click chemistry.

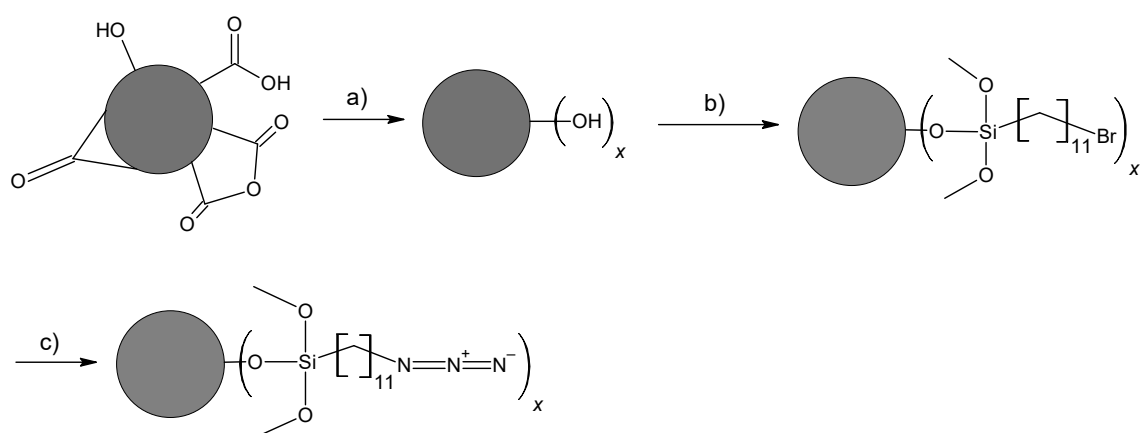


Figure 61. Reaction scheme of functionalization of NDs. a) The as-received NDs were reduced with  $\text{BH}_3\cdot\text{THF}$  to receive hydroxyl residues on the surface. b) In a second step, the surface was silanized with 11-bromo-undecyltrichlorosilane for a bromo-functionalization, which then reacted with c) sodium azide to generate an azide residue on the ND surface.

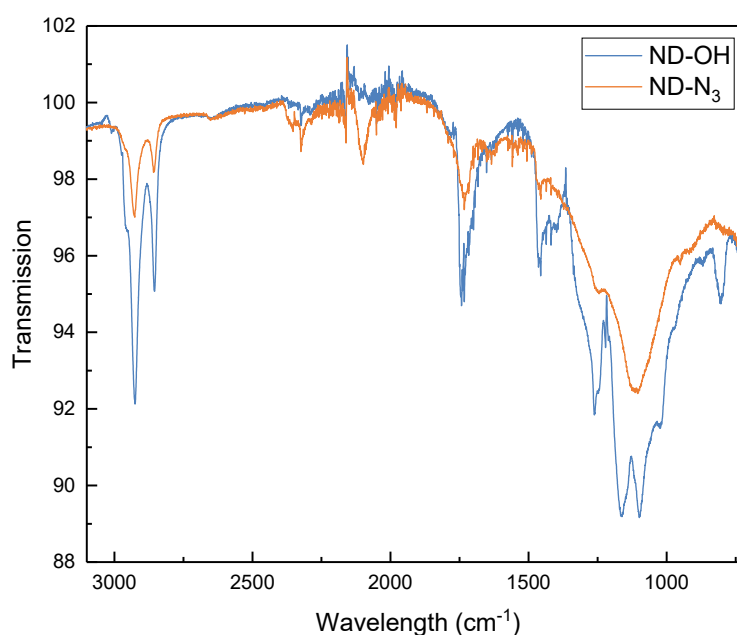


Figure 62. FT-IR spectra of NDs after reduction (blue) and functionalization with  $\text{NaN}_3$  (orange), respectively. At a wavenumber of  $2100\text{ cm}^{-1}$ , the specific azido band is shown in the orange spectrum.

As the functionalization of NDs prior to stamping was carried out with a dispersion of diamonds in a flask, the obtained outcome could be analyzed with Fourier-transformation infrared spectroscopy (FT-IR) as shown in Figure 62. The silica band overlaps with the ND band, which makes the silanized intermediate product ND-Br difficult to analyze.

Whereas after the reaction with sodium azide, the azide band is clearly visible at a wavelength of  $2100\text{ cm}^{-1}$ , proving the successful reaction of ND-Br with sodium azide.

A dispersion of 1 mg ND- $\text{N}_3$  in 1 mL isopropanol was stamped onto glass with a subsequent click reaction with cyanine-3-DBCO forming a triazole ring of the triple bond within DBCO and the azide residue on the NDs according to Figure 63.

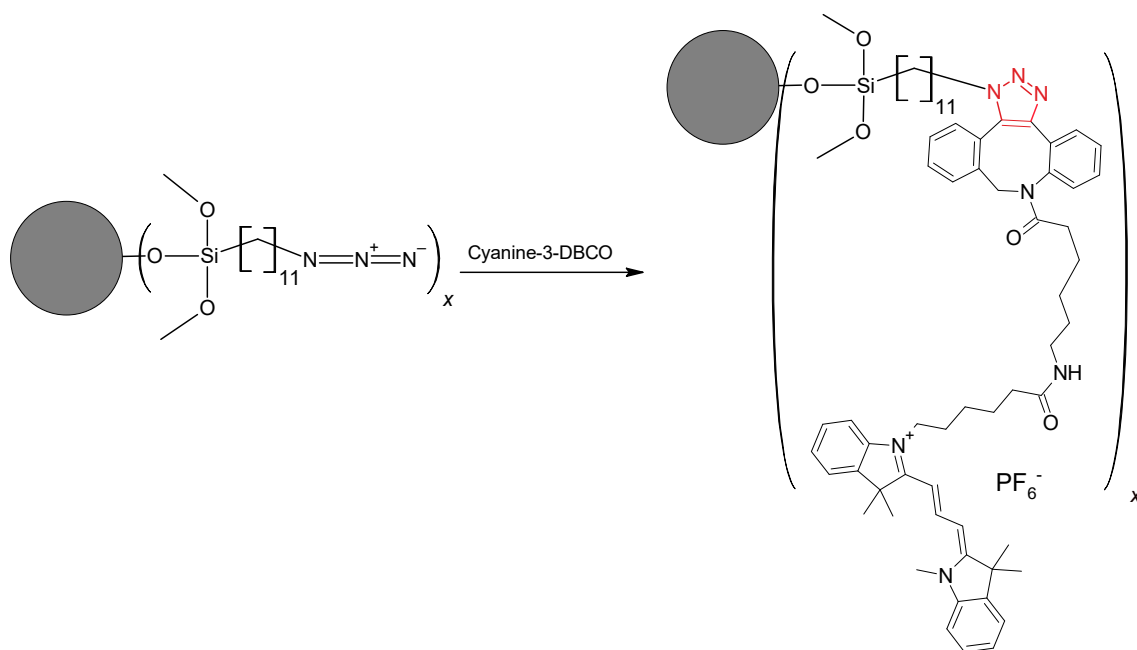


Figure 63. Reaction scheme of copper-free click reaction with stamped ND- $\text{N}_3$ . The triple bond and the azide residue have formed a triazole ring (red).

The SEM images in Figure 64 show the results of the stamped NDs subsequent to the click reaction. Although the areas of ordered particles are smaller compared to previous stamping results, still in some regions, the hexagonal order is retained after the click reaction. This can be due to the washing procedure after the click reaction, which may have caused the nanodiamonds to move around the surface. The surface tension of the water drop and the curvature of the drop on the outer edges of the substrate could have driven the nanodiamonds towards the edges of the substrate. This mechanism was presumably driven by the Marangoni effect or the coffee-ring effect.<sup>[133,134]</sup> To obtain a higher degree of order within larger areas, a possible immobilization of the nanodiamonds onto the surface could be carried out. The size and shape analysis is shown in the histograms in Figure 65. Analysis of the obtained ND aggregates was carried out according to chapter 3.1.1.12 (see page 33). The analysis of 527 stamped ND aggregates after click reaction amounted to a mean diameter of  $134 \pm 49\text{ nm}$ , a circularity of  $0.85 \pm 0.17$ , and an



average aspect ratio of  $1.55 \pm 0.54$ . The particle-to-particle distance amounted to  $1.1 \mu\text{m}$ . The diameters of the obtained ND aggregates stamped from a dispersion of 5 nm NDs amounted to a larger size compared to the 10 nm NDs stamped in the previous chapter. This can be due to a higher particle mobility with decreasing size within the pore system. The smaller particles presumably move faster and do not get bogged down in the pore system as easy as the bigger particles and thus, can undergo an enrichment process during stamping.

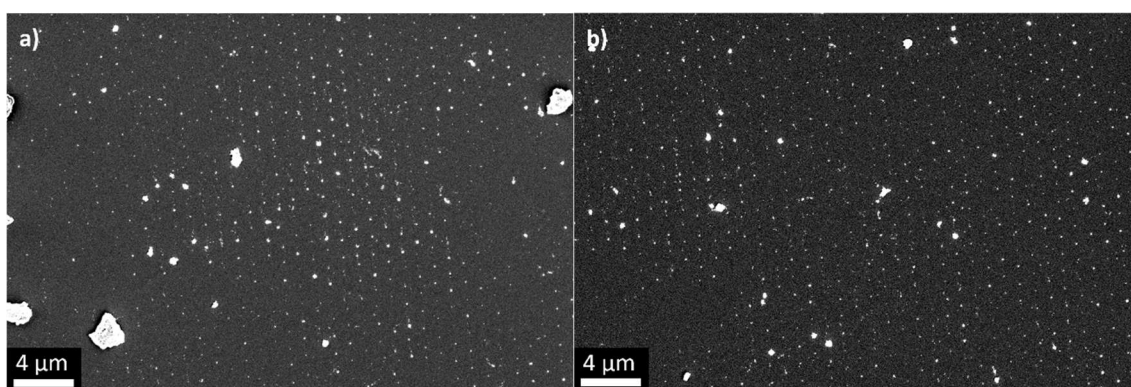


Figure 64. SEM images of stamped ND-N<sub>3</sub> subsequent to the click reaction with cyanine-3-DBCO. Although the hexagonally arranged NDs are not visible over a large area anymore, still NDs are on the substrate surface and can be found ordered in some areas. Images were taken with an in-lens detector.

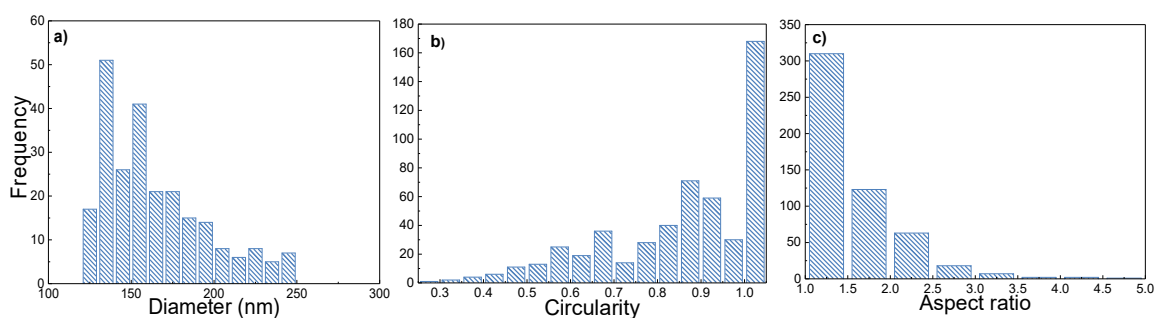


Figure 65. Histograms of 527 analyzed stamped ND aggregates showing a) the diameters, b) the circularities and c) the aspect ratios of the ND aggregates.

To confirm the success of the click reaction of the ND-N<sub>3</sub> with cyanine-3-DBCO, fluorescence spectra of the stamping results and drop-casted ND nanodispersions were recorded with a confocal fluorescence microscope as shown in Figure 66 (see description in chapter 3.1.1.2, page 30). After the functionalized NDs were localized with confocal fluorescence microscopy, the beam path was directed into a spectrometer to obtain locally integrative spectra of the NDs. For a comparison of stamped NDs and NDs within nanodispersion, a dispersion of NDs was functionalized with dye *via* click-chemistry to

obtain a larger amount of dye-functionalized NDs for analysis. 200  $\mu\text{L}$  of a 1 mg/mL dye-functionalized ND nanodispersion was drop-casted onto a glass substrate and analyzed likewise to the stamped NDs. The red curve in Figure 66 shows the fluorescence spectrum of the functionalized ND dispersion. The band at 570 nm and a shoulder at 610 nm are specific for the cyanine-3-dye as shown in Figure 28 (see page 44). The orange curve shows the measurement of stamped NDs subsequent to the click reaction with cyanine-3-DBCO. Although with less intensity, the specific band and shoulder of cyanine-3 are clearly visible. This confirms the successful reaction of stamped nanodiamonds with a fluorescent dye *via* click chemistry on the substrate surface.

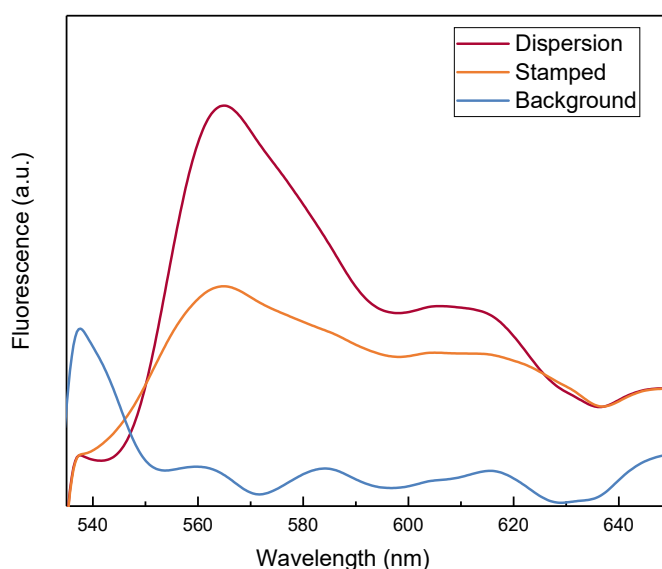


Figure 66. Fluorescence spectra of NDs after click reaction with cyanine-3-DBCO. The confocal fluorescence microscope had a laser stimulation at 530 nm. The blue curve shows the measurement of the background of the glass slide, the red curve shows the measurement of the nanodispersion of ND- $\text{N}_3$  clicked with cyanine-3-DBCO. The band at 570 nm and a shoulder at 610 nm are specific for the cyanine-3-dye. The orange curve shows the measurement of stamped NDs subsequent to the click reaction with cyanine-3-DBCO. Although with less intensity, the specific band and shoulder of cyanine-3 are visible.

Although the NDs were “clicked” with the cyanine-3-DBCO and the confocal fluorescence microscopy results show the successful reaction in the spectra in Figure 66, fluorescence images of the dye-functionalized NDs could not show the same order as the SEM images in Figure 64. This is due to several factors, first, the substrate surface was not clean enough after the click reaction. This means that not only on the stamped spot sizes, but also in between these spots, some particles, presumably dye-functionalized, could be observed in the SEM images (Figure 64). As the resolution limit of the fluorescence microscope amounted to 600-700 nm, these disruptive particles could not be differentiated in the fluorescence images as they could be differentiated in the SEM images. Second,

as not every single ND is functionalized with the same amount of dye molecules, the signal intensity varies and a high quality of dye and therefore, a high signal intensity could lead to extinction of adjacent lower quality of dye on the NDs.

Nevertheless, the results of this experiment give a good orientation of possible applications of NDs. Stamping of NDs with the method of capillary nanostamping results in hexagonally ordered NDs with a diameter smaller than in state-of-the-art literature presented.<sup>[121]</sup> With a functionalization of the NDs towards a click-accessible surface, a combination of stamping of NDs and subsequent reaction applicability of the ND-structured surface in an ordered pattern becomes possible.

#### 4.2.4 Stamping of Zeonex from toluene/chloroform onto hydrophobic glass

Silica is inert against most organic solvents, which opens the possibility of using polymers as ink, which mostly dissolve in organic solvents. Zeonex is a commercially available cyclo olefin polymer (COP) with a structural formula shown in Figure 67. The physical properties of Zeonex include a refractive index of 1.51,<sup>[135]</sup> which is similar to the refractive indices of optical glasses (1.46-1.85) as quartz, crown or flint glass, which are used for optical components like lenses, prisms or mirrors.<sup>[136]</sup> It has a high transparency and high transmittance in the visible and near-infrared range, a low water absorption and a high molding precision.<sup>[135]</sup> Therefore, Zeonex is used as material for lenses, thin-film transistors and optical fibers.<sup>[137,138]</sup> With upcoming applications within these fields, an exemplary attempt of stamping of Zeonex was made.

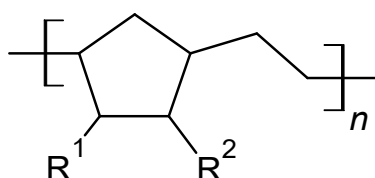


Figure 67. Structural formula of COP.

The conditions of the stamping procedure of Zeonex from toluene/chloroform can be found in chapter 3.2.4.6 (see page 42). As stamps, the third-generation silica stamps with an average pore diameter of 31 nm were used. The substrate was functionalized with FDTs to obtain a hydrophobic surface to thermodynamically prevent ink spreading.

Therefore, the contact angle of toluene/chloroform on FDTS-functionalized glass amounted to  $\approx 55^\circ$ . It is assumable that the stamping process of Zeonex on FDTS-functionalized glass can be compared to the stamping process of  $C_{60}$  and thus corresponds to meniscus confined particle growth (see Figure 42, page 61). The SEM images shown in Figure 68 and Figure 69 show the outcome of stamping of Zeonex. The Zeonex forms small, uniform particles on the substrate surface over a large area, which is confirmed by the FFT analysis shown in the inset of Figure 68. Analysis of the obtained particles was carried out according to chapter 3.1.1.12 (see page 33). The analysis of 289 particles resulted in a particle-to-particle distance of  $1.4 \mu\text{m}$ , an average particle diameter of  $91 \pm 16 \text{ nm}$ , an average circularity of  $0.77 \pm 0.18$  and an average aspect ratio of  $1.53 \pm 0.37$  as shown in Figure 70. The analysis with AFM shown in Figure 71 confirms the hexagonal order as well as the particle shape and sizes. The height determined with the AFM line scan (blue line in Figure 71b) amounted to a particle height of 25-30 nm.

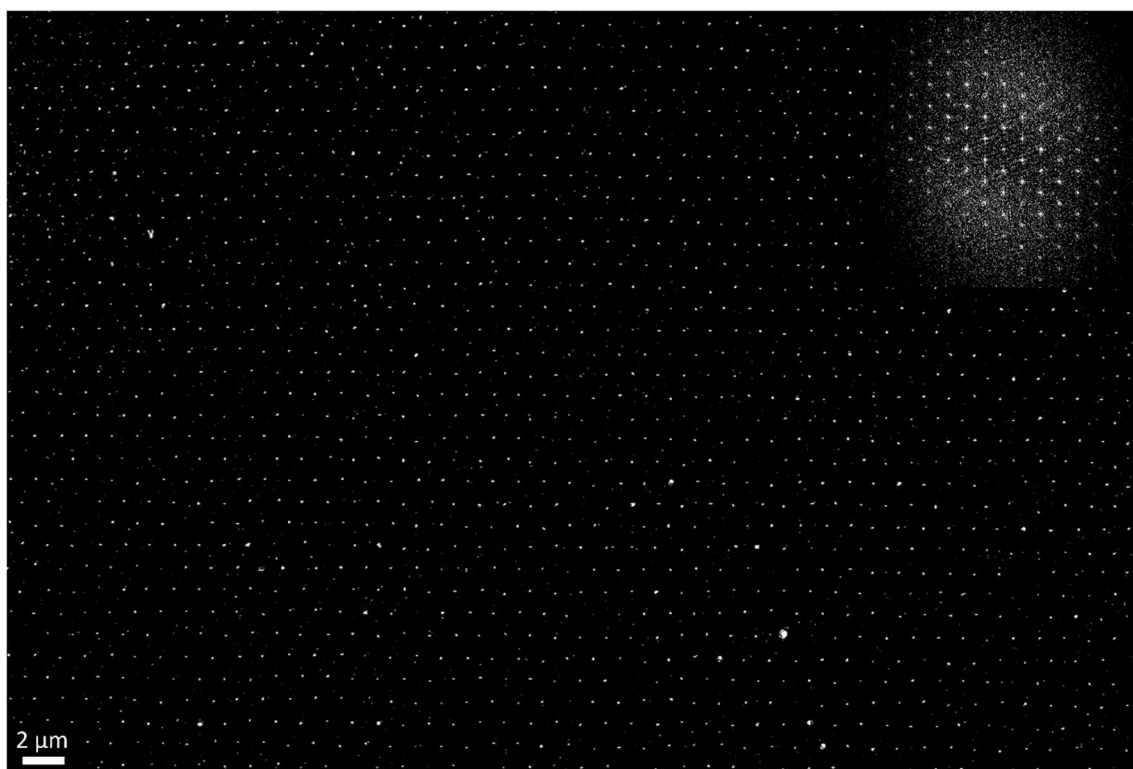


Figure 68. SEM image of stamped Zeonex particles on a FDTS-functionalized substrate. The overview image shows the hexagonal arrangement of the particles. The inset shows a FFT analysis, where the hexagonal pattern is significant. The image was acquired with an in-lens detector.

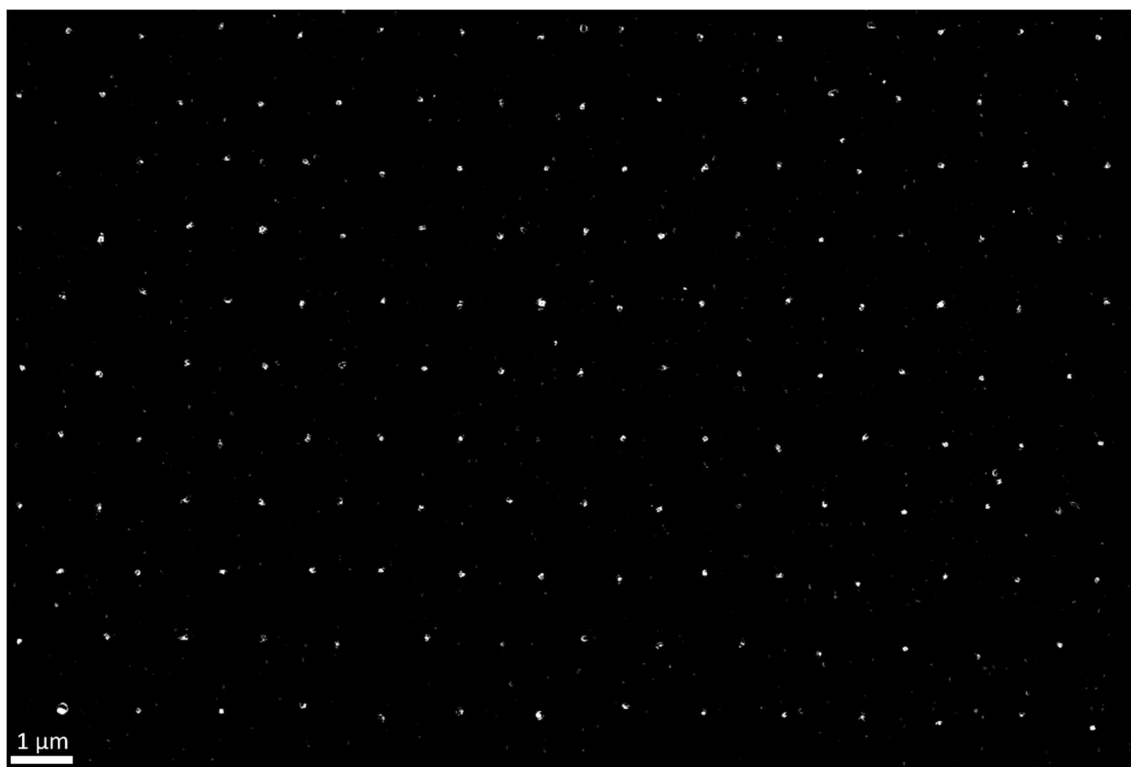


Figure 69. SEM image of stamped Zeonex particles. Magnification of Figure 68. The particles are not perfectly round in shape. The image was acquired with an in-lens detector.

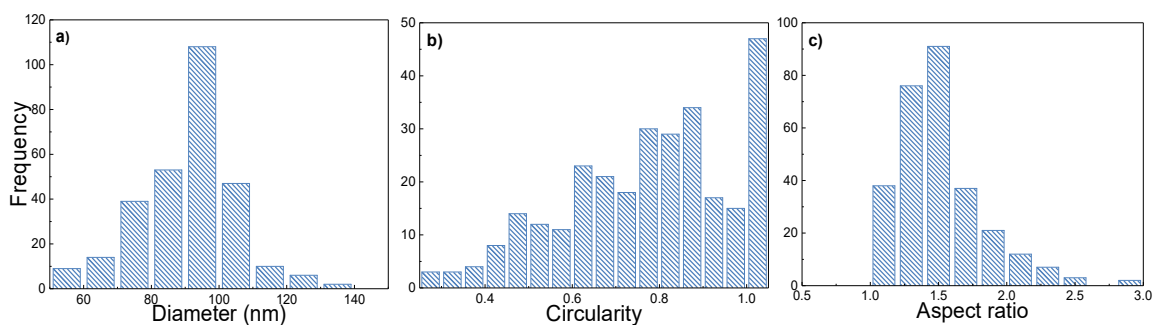


Figure 70. Histograms of 289 analyzed stamped Zeonex particles showing a) the diameters, b) the circularities and c) the aspect ratios of the Zeonex particles.



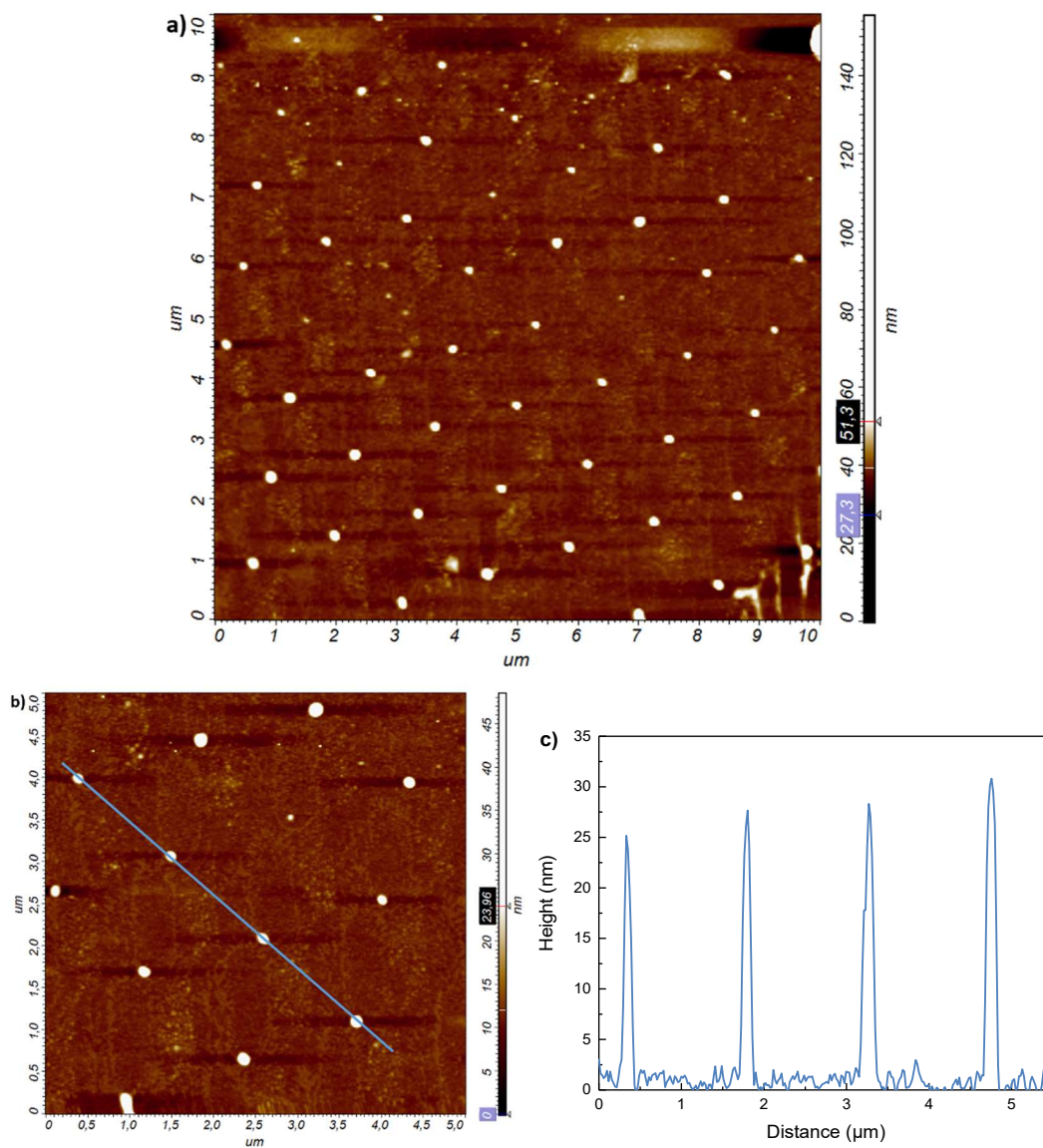


Figure 71. AFM images of stamped Zeonex particles on FDTS-functionalized glass. a) The overview shows highly ordered particles of uniform sizes and shape. b) Magnification of a). c) Line-scan of blue line in b). The average height of the Zeonex particles amounted to 25-30 nm.

The stamping procedure of Zeonex from toluene/chloroform onto FDTS-functionalized glass was successful and promises surfaces patterned over a large area with uniform Zeonex particles serving as e.g. lenses. Further experiments for the development of possible applications were not performed within this work.



#### 4.2.5 Stamping of PS-*b*-P2VP from toluene/chloroform onto differently functionalized glass with subsequent solvent treatment

Block copolymers (BCPs) are macromolecules consisting of two or more blocks of different polymers that are covalently connected to each other. As the single blocks are normally immiscible, a microphase separation occurs and leads to ordered nanoscopic domain structures with a defined morphology (see Figure 11, page 15). The nature of the nanoscopic domain structure is determined by the volume fractions of the blocks, the degree of compatibility between the blocks and the tendency of the blocks to adopt coiled conformations associated with high conformational entropy.<sup>[139]</sup> The nanoscopic self-assembly and the material characteristics itself make BCPs highly attractive for applications in the fields of nanolithography,<sup>[140]</sup> drug delivery,<sup>[141,142]</sup> organic photovoltaics (OPVs)<sup>[143]</sup> and organic light emitting diodes (OLEDs).<sup>[144]</sup> Polystyrene-*block*-poly(2-vinylpyridine) (PS-*b*-P2VP, Figure 72), consisting of the two blocks polystyrene (PS) and poly(2-vinylpyridine) (P2VP), is used e.g. for the immobilization of gold nanoparticles.<sup>[145–147]</sup> Although BCPs have the affinity to undergo a self-assemble, the phase separation periods depend on the polymer chain lengths and are normally in the size range of a few tens of nanometers. BCPs can be patterned on substrate surfaces with common lithographic methods. Mirkin and coworkers used the method of dip-pen nanolithography to deposit poly ethylenglycol-*block*-poly(2-vinylpyridine) (PEO-*b*-P2VP),<sup>[148]</sup> polypyrrole and poly(aniline sulfonic acid) from aqueous solution.<sup>[149]</sup> Nevertheless, lithographic deposition of BCPs, which dissolve in organic solvents, could not be carried out with state-of-the-art methods. Therefore, BCPs dissolved in organic solvents were stamped in a capillary nanostamping procedure with spongy mesoporous silica stamps from a solution of toluene/chloroform. In the following chapter, PS-*b*-P2VP was stamped by capillary nanostamping and subjected to swelling-induced morphology reconstruction by solvent treatment.

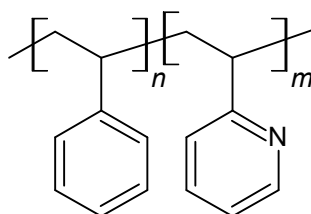
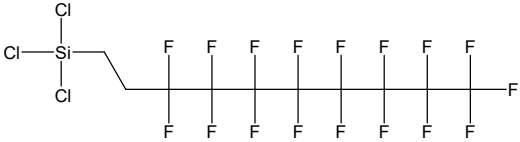
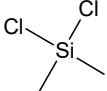
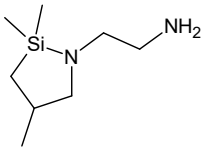


Figure 72. Structural formula of PS-*b*-P2VP. The polystyrene block has  $n$  repeat units, while the poly(2-vinylpyridine) block has  $m$  repeat units.

#### 4.2.5.1 Contact angle measurements

Contact angle measurements were carried out to understand the wettability behavior of the solvent on the differently functionalized glass slides. The procedures can be found in the chapters 3.1.1.3 (see page 30) and 3.2.1.2 (see page 36). The results of the contact angle measurements of the volatile solvent toluene/chloroform (1:3) on the differently functionalized glass slides are shown in Table 3 and Figure 73. The contact angle amounted to  $\approx 55^\circ$  for FDTS-functionalized glass (Figure 73a), which is less compared to the contact angle of pure toluene on FDTS-functionalized glass, which amounted to  $\approx 71^\circ$ , as analyzed in chapter 4.2.1 (see page 60). Nevertheless, the surface still shows a partial wettability and thus, discrete droplets can be formed and will be stable on the surface. The contact angle on DMDCS-functionalized glass amounted to  $\approx 18^\circ$  (Figure 73b), which represents a higher wettability of the solvent on the surface. The contact angles on hydroxyl-terminated and ATAS-functionalized glass amounted to  $0^\circ$  (Figure 73c, picture representatively for both surfaces), which eventually causes total ink spreading.

Table 3. Overview of different surface functionalization with structural formula and residual group on the substrate surfaces, and contact angle measurements of toluene/chloroform (1:3) on the surfaces at  $22^\circ\text{C}$  and a humidity of 37%.

Functionalization	Structural formula	Residual group on surface	Contact angle of solvent ( $^\circ$ )
OH	$(\text{SiO}_2)_n\text{-OH}$	-OH	0
FDTS		$-(\text{CF}_2)_7\text{-CF}_3$	$\approx 55$
DMDCS		-CH <sub>3</sub>	$\approx 18$
ATAS		-NH <sub>2</sub>	0

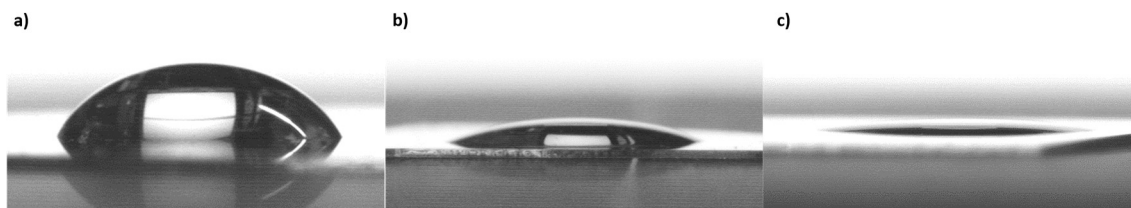


Figure 73. Contact angle measurements of toluene/chloroform (1:3) on glass slides functionalized with a) FDS, b) DMDCS and c) ATAS-silane or hydroxyl-terminated. The contact angles amounted to 55°, 18° and 0°, respectively.

#### 4.2.5.2 Stamping onto hydroxyl-terminated glass

Stamping procedure, ink preparation and further information about the ink are described in chapter 3.2.4.7 (see page 42). As stamps, the third-generation silica stamps with an average pore diameter of 44 nm were used. The results of stamping of PS-*b*-P2VP onto hydroxyl-terminated glass are shown in Figure 74. The PS-*b*-P2VP formed spots in a hexagonally arranged pattern with interconnection between the single spots. Although the contact angle of toluene/chloroform on hydroxyl-terminated glass amounted to 0° (see Figure 73), stamping of PS-*b*-P2VP from toluene/chloroform onto hydroxyl-terminated glass yielded in discrete spots and the expected ink spreading did not occur. This phenomenon was observed before in chapter 3.2.4.2 (see page 39) with stamping of 1-dodecanethiol onto gold-coated glass, which proceeded according to Figure 47 (see page 66). In this stamping procedure, a similar process ensured the generation of discrete spots. As shown in Figure 75, the contact angle of toluene/chloroform increased from 0° on hydroxyl-terminated glass to ≈32-34° after immersion of the glass slide into solutions of 2.5 mg/mL P2VP and PS in toluene/chloroform. This change in surface wettability in conjunction with the mesopores of the stamp, where the Laplace pressure counteracts the attractive van der Waals forces between ink and substrate surface, ensured the formation of polymer spots.

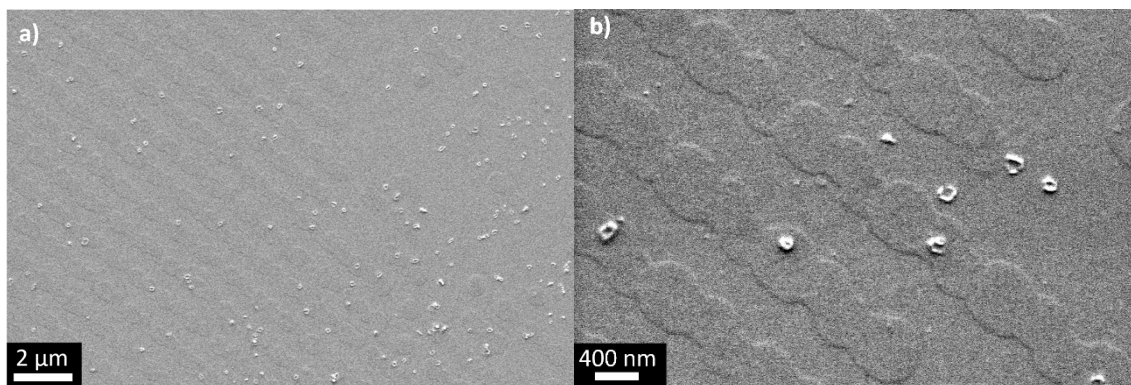


Figure 74. SEM images of stamped PS-*b*-P2VP on hydroxyl-terminated glass. a) Overview and b) magnification. The block copolymer has formed spots in a hexagonal order. The spots are interconnected with each other. The images were taken with a SESI detector.

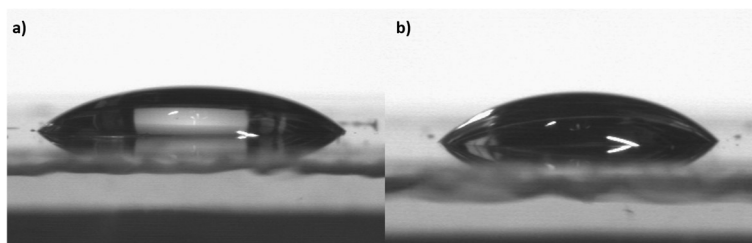


Figure 75. Contact angle measurements of toluene/chloroform on hydroxyl-terminated glass after immersion of the glass into solutions of 2.5 mg/mL a) P2VP and b) PS in toluene/chloroform. The contact angle amounted to a)  $\approx 32^\circ$  and b)  $\approx 34^\circ$ . After adsorption of the first monolayer of P2VP and PS, respectively, the plain glass is not determining anymore.

Since polystyrene and poly(2-vinylpyridine) do not show any contrast in the SEM, a solvent treatment was carried out according to chapter 3.2.4.7 (see page 42).<sup>[87]</sup> In this process, the poly(2-vinylpyridine) was selectively swollen with ethanol, while polystyrene remains glassy. After the removal of the glass slides from the ethanol, the P2VP relaxed into the coiled state so that pores formed in place of the previously swollen P2VP domains. After swelling, the P2VP blocks are exposed and accessible for further functionalization. Figure 76 shows the results of the stamped PS-*b*-P2VP on hydroxyl-terminated glass after solvent treatment. In Figure 76a, a large area of stamped PS-*b*-P2VP structures is shown, the PS-*b*-P2VP structures are hexagonally ordered over the whole area. Figure 76b and c show magnifications of a few and one single PS-*b*-P2VP spots, respectively. Due to the reconstruction of the morphology of the stamped PS-*b*-P2VP spots during the treatment, a porous structure has formed.



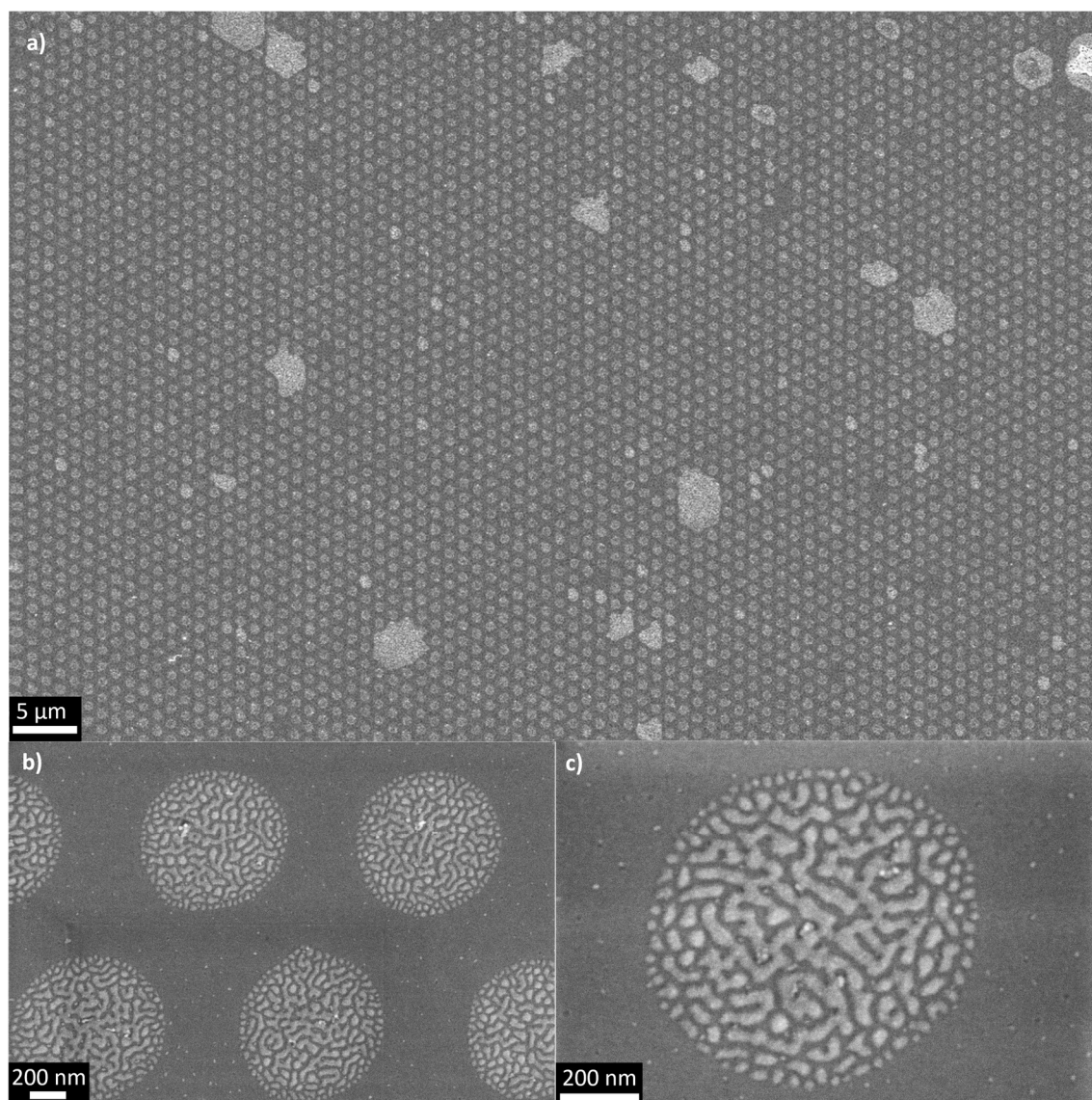


Figure 76. SEM images of stamped PS-*b*-P2VP on hydroxyl-terminated glass after solvent treatment in EtOH at 60 °C for 1 h. a) Overview of larger area of stamped spots and b, c) magnifications. The stamping resulted in porous spots with a diameter of  $730 \pm 24$  nm, consisting of PS-*b*-P2VP in a hexagonal order. c) A single spot shows the visible porous structure of the PS-*b*-P2VP due to the morphology reconstruction during solvent treatment. All images were taken with an in-lens detector.

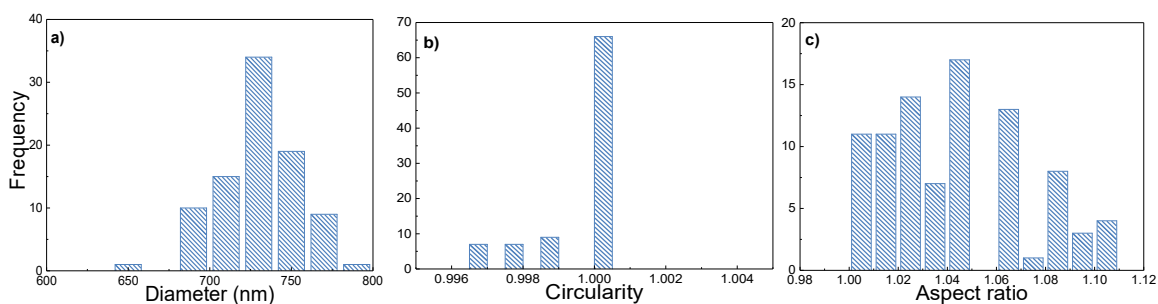


Figure 77. Histograms of 89 analyzed stamped PS-*b*-P2VP spots on hydroxyl-terminated glass after solvent treatment. Showing a) the diameters, b) the circularities and c) the aspect ratios of the PS-*b*-P2VP spots.

The SEM images were analyzed concerning diameter, circularity and aspect ratio of the stamped PS-*b*-P2VP spots according to chapter 3.1.1.12 (see page 33). Figure 77 shows histograms of 89 analyzed spots, which had an average center-to-center distance of 1.3  $\mu\text{m}$ , a mean diameter of  $730 \pm 24$  nm, a circularity of  $1.00 \pm 0.01$  and an average aspect ratio of  $1.04 \pm 0.04$ . AFM analysis (see Figure 78) resulted in a spot height of 2-5 nm.

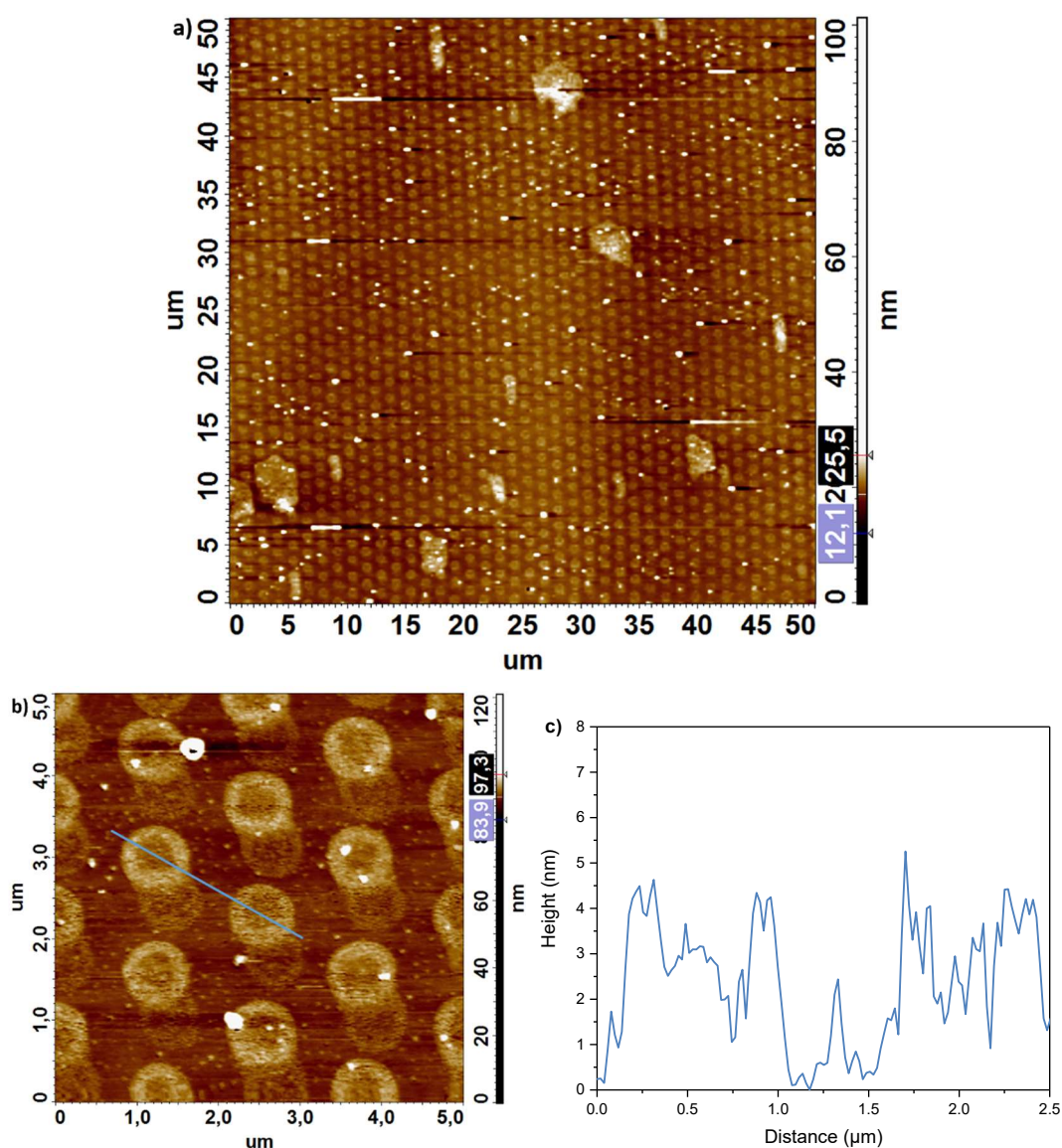


Figure 78. AFM images of stamped PS-*b*-P2VP on hydroxyl-terminated glass after solvent treatment in EtOH at 60  $^{\circ}\text{C}$  for 1 h. a) Overview area and b) magnification. c) The line scan of the blue line shows clearly that the obtained structures are not even particles but formed large spots with pores. The height of the blue line scan shows heights within the polymer spots of 2-5 nm.



#### 4.2.5.3 Stamping onto FDTS-functionalized glass

The stamping of PS-*b*-P2VP onto FDTS-functionalized glass was carried out according to chapter 3.2.4.7 (see page 42) and obtained the following results shown in Figure 79 to Figure 82. As stamps, the third-generation silica stamps with an average pore diameter of 44 nm were used. The SEM images shown in Figure 79 were obtained prior to the swelling procedure. Here, similar to stamping onto hydroxyl-terminated glass, large polymer spots are hexagonally ordered over a large area. A difference is though, that the stamped spots are not throughout connected, but already formed separate smaller structures, which can be due to a limited wettability of the PS-*b*-P2VP on the FDTS-functionalized surface and a higher cohesion of PS-*b*-P2VP compared to the interaction of PS-*b*-P2VP with FDTS. As the solvent evaporates after the stamping procedure, a dewetting process of the polymer occurs and leads to separated small particles within the stamped spots. The larger particle within each stamped spot (Figure 79b) presumably shows the spot, where the contact elements of the stamp encountered the substrate surface.

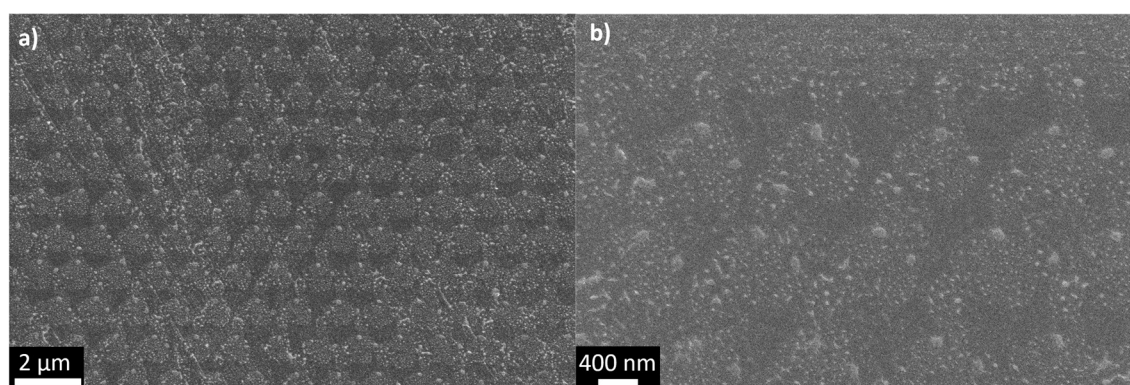


Figure 79. SEM images of stamped PS-*b*-P2VP on FDTS-functionalized glass without solvent treatment. A) Overview area and b) magnification. The block copolymer has formed large spots in a hexagonally arranged order. Within the stamped spots, a dewetting process of the polymer occurred and yielded single smaller particles. Images were taken with an in-lens detector.

After solvent treatment and thus morphology reconstruction of the PS-*b*-P2VP, small particles were obtained as shown in Figure 80. The hexagonal pattern is visible over a large area (Figure 80a) and when magnified (Figure 80c), a small non-porous island with several smaller polymer particles can be seen.

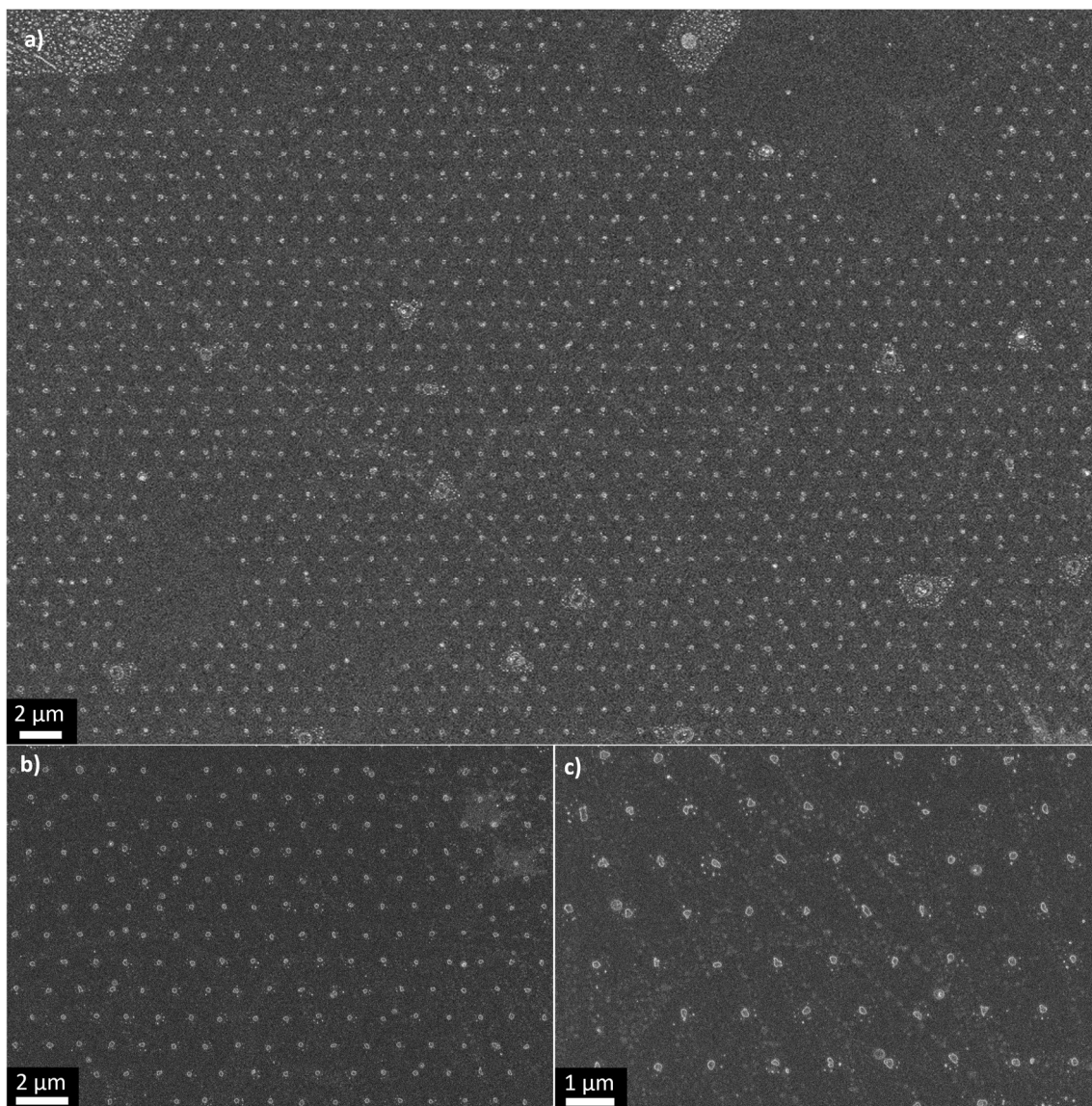


Figure 80. SEM images of stamped PS-b-P2VP on FDTD-functionalized glass after solvent treatment in EtOH at 60 °C for 1 h. a) Large area overview and b), c) magnifications of stamped particles. The stamping results in discrete particles consisting of PS-b-P2VP in a hexagonal order. All images were taken with an in-lens detector.

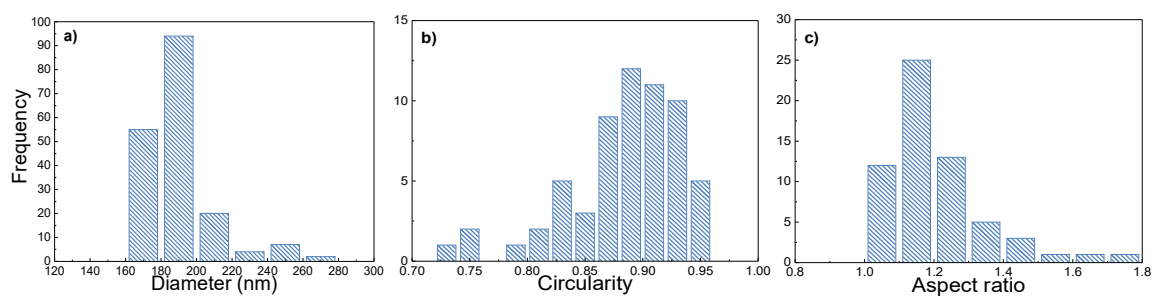


Figure 81. Histograms of 183 analyzed stamped PS-b-P2VP particles on FDTD-functionalized glass after solvent treatment. Showing a) the diameters, b) the circularities and c) the aspect ratios of the PS-b-P2VP particles.



The SEM images were analyzed concerning diameter, circularity and aspect ratio of the stamped spots according to chapter 3.1.1.12 (see page 33). Figure 81 shows histograms of 183 analyzed spots, which resulted in a particle-to-particle distance of  $1.3\ \mu\text{m}$ , a mean diameter of  $191 \pm 21\ \text{nm}$ , a circularity of  $0.88 \pm 0.05$  and an average aspect ratio of  $1.20 \pm 0.14$ . AFM analysis (see Figure 82) resulted in a spot height of 20-60 nm.

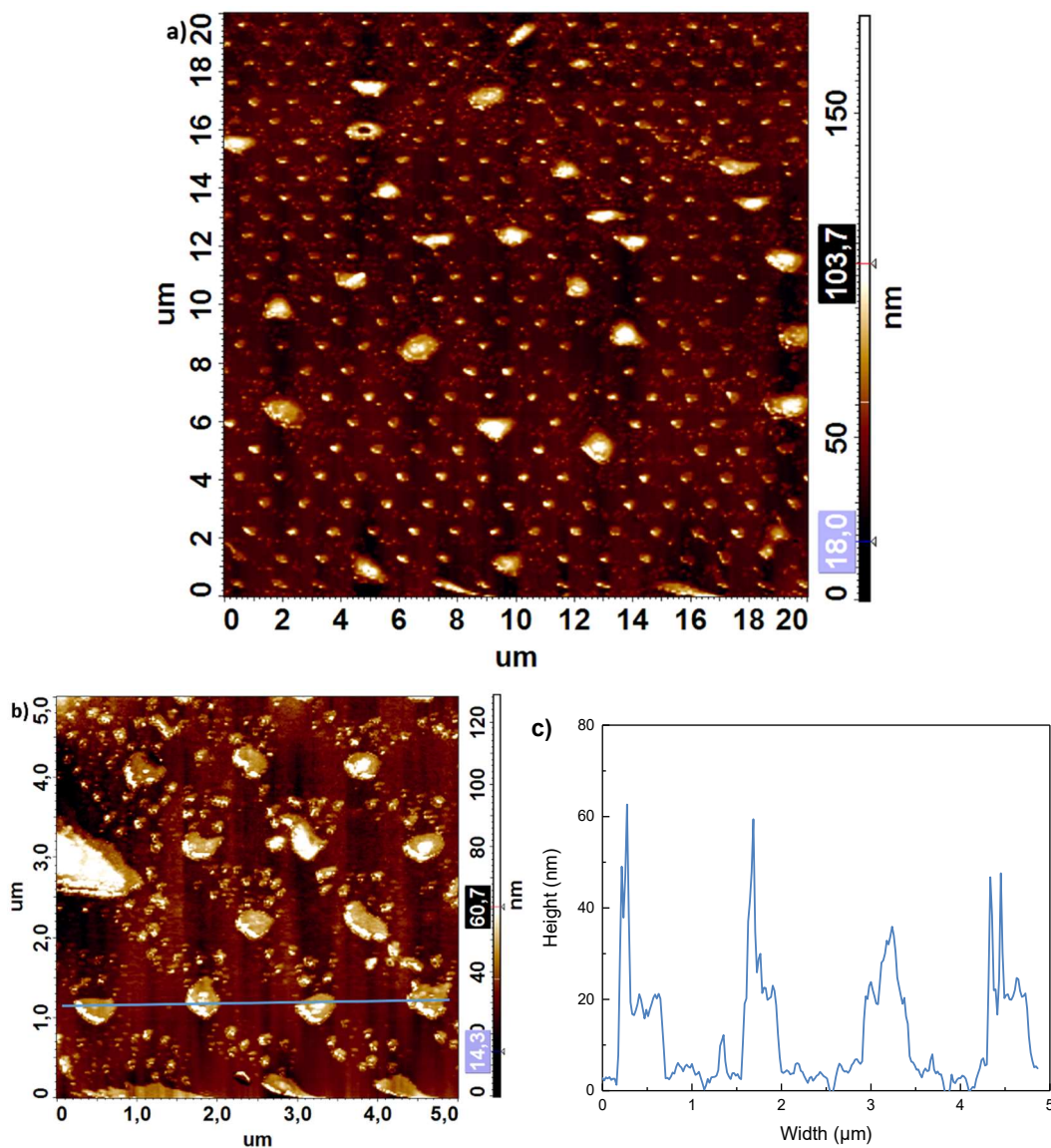


Figure 82. AFM images of stamped PS-*b*-P2VP on FDTS-functionalized glass after solvent treatment in EtOH at 60 °C for 1 h. a) Overview of large area and b) magnification. c) The line scan of the blue line shows a structure height of 20-60 nm.

#### 4.2.5.4 Stamping onto DMDCS-functionalized glass

The stamping onto DMDCS-functionalized glass was carried out according to chapter 3.2.4.7 (see page 42). As stamps, the third-generation silica stamps with an average pore diameter of 44 nm were used. The stamping resulted in a continuous polymer layer with no visible obtained structure as shown in Figure 83.

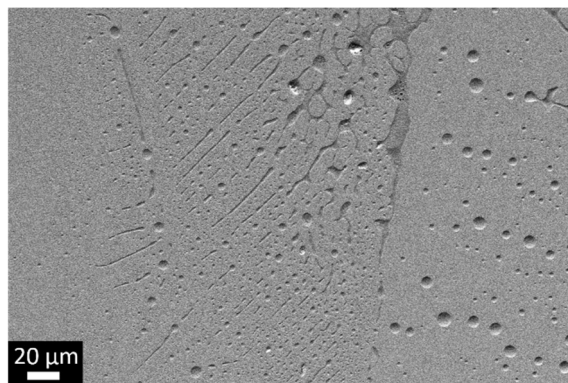


Figure 83. SEM image of stamped PS-*b*-P2VP on DMDCS-functionalized glass without solvent treatment. The pattern is not visible. Either a continuous polymer layer has formed or the stamping process did not work out. The image was taken with a SESI detector.

Subsequent to the solvent treatment, a small patterned area could be found as shown in Figure 84. In this case, no large area with the typical hexagonal pattern could be obtained (Figure 84a) and even the small structured area shows a large variety of stamped structures concerning size and shape. From the magnification in Figure 84b, it is visible that the stamped PS-*b*-P2VP has formed structures with multiple height levels, which is called “terracing”.<sup>[30]</sup>

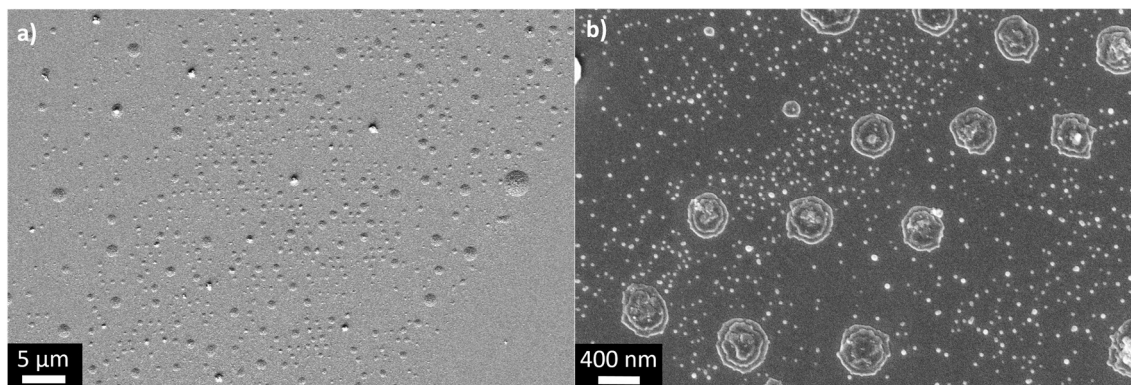


Figure 84. SEM images of stamped PS-*b*-P2VP on DMDCS-functionalized glass after solvent treatment in EtOH at 60 °C for 1 h. The results show a short-range order of hexagonally arranged particles on the surface. At closer look, the particles formed small hills with bigger bottoms and smaller heights. The sizes of the particles show a large variety. Image a) was taken with a SESI detector, b) was taken with an in-lens detector.

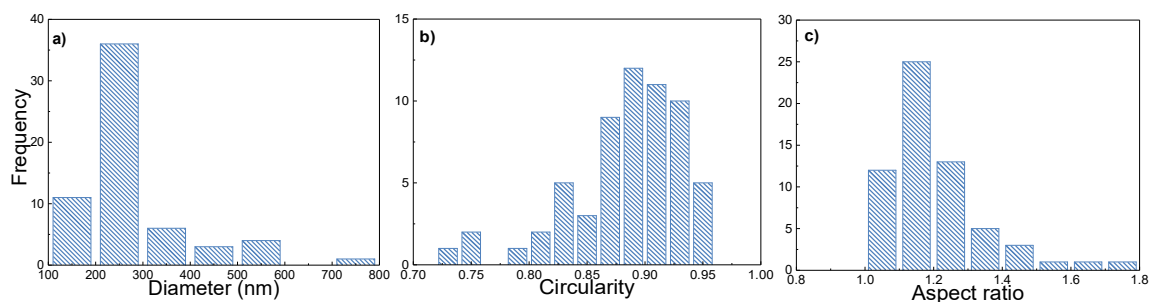


Figure 85. Histograms of 61 analyzed stamped PS-*b*-P2VP particles on DMDCS-functionalized glass after solvent treatment showing a) the diameters, b) the circularities and c) the aspect ratios of the PS-*b*-P2VP particles.

Small ordered areas and large varieties in size and shape led to an imprecise analysis of only 61 obtained particles, which resulted in a particle-to-particle distance of 1.0  $\mu\text{m}$ , a mean diameter of  $282 \pm 111$  nm, a circularity of  $0.88 \pm 0.05$  and an average aspect ratio of  $1.20 \pm 0.14$  (Figure 85). The AFM analysis in Figure 86a confirms the weak order, while Figure 86b shows the different height levels. The line analysis of the single obtained particle (Figure 86c) yields in three height levels, a ground level at a height of 15 nm, a second level at a total height of 20 nm and a top level at a total height of 30 nm. This terracing behavior occurred presumably within an asymmetric wetting of the ink on the substrate.<sup>[30]</sup> The peak up to 80 nm can be due to tip-sample interactions during scanning or indicate higher edges on the top level of the single particle, which have been investigated before for specific conditions.<sup>[150]</sup> The shape of these particles are similar to printed lipid structures obtained with dip-pen nanolithography (DPN).<sup>[151]</sup>

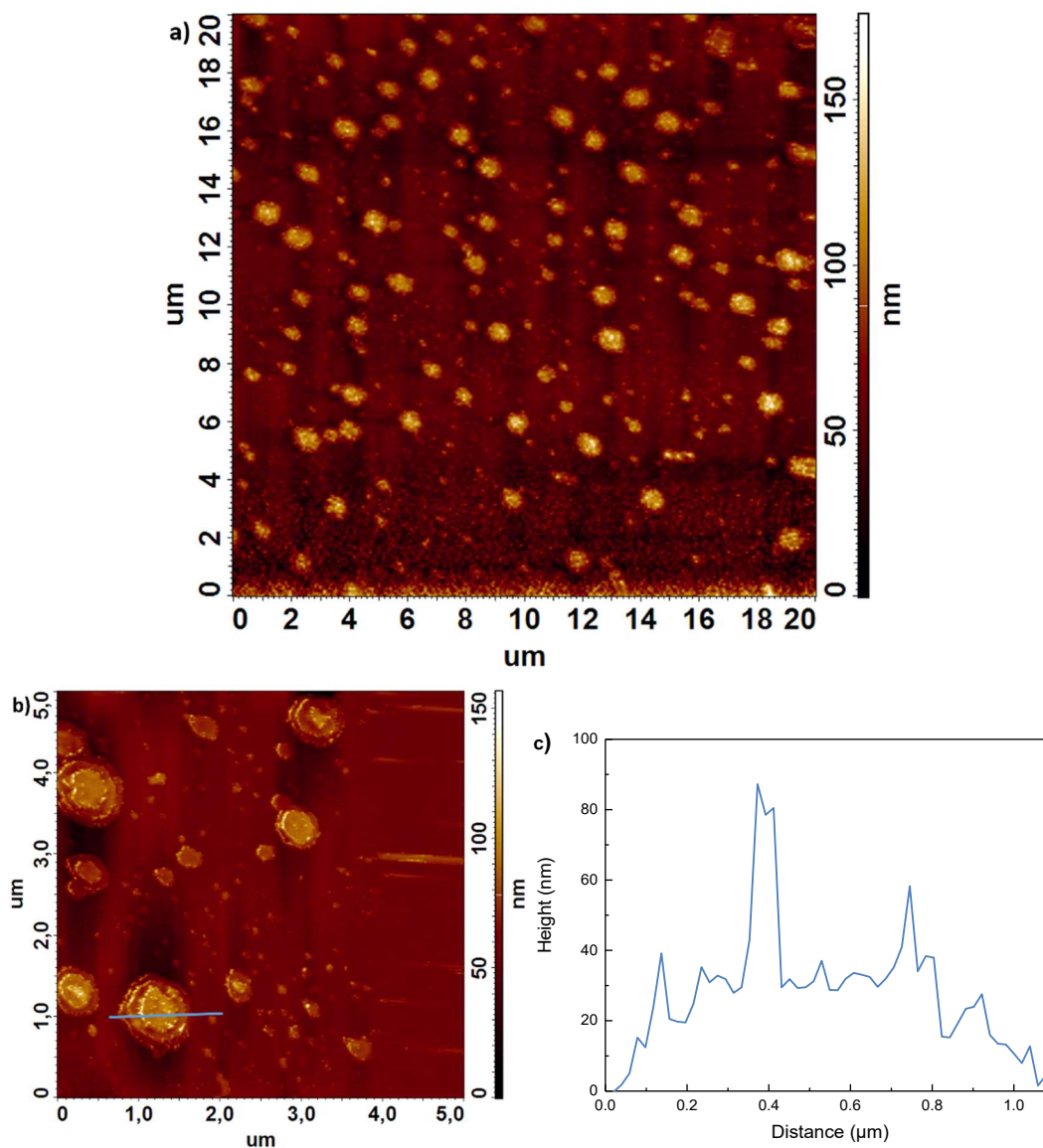


Figure 86. AFM images of stamped PS-*b*-P2VP on DMDCS-functionalized glass after solvent treatment in EtOH at 60 °C for 1 h. a) Overview of large area and b) magnification. c) The line scan of the blue line shows the height of one single stamped polymer particle. The particle consists of three height levels, the first is at 15 nm, the second at 20 nm and the third level has a height of up to 80 nm with a plateau at 30 nm.

#### 4.2.5.5 Stamping onto ATAS-functionalized glass

The stamping onto ATAS-functionalized glass was carried out according to chapter 3.2.4.7 (see page 42). As stamps, the third-generation silica stamps with an average pore diameter of 44 nm were used. The stamping resulted in a continuous polymer layer with no visible obtained structure as shown in Figure 87.



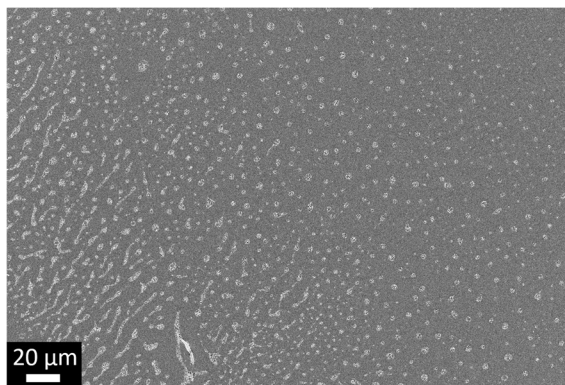


Figure 87. SEM image of stamped PS-*b*-P2VP on ATAS-functionalized glass without solvent treatment. The pattern is not visible. Either a continuous polymer layer has formed or the stamping process did not work out. The image was taken with a SESI detector.

The results of stamping with subsequent solvent treatment can be seen in Figure 88. As shown in Figure 88a, PS-*b*-P2VP particles are hexagonally ordered over a large area. The magnification (Figure 88b) shows some single defects within the ordering, which can be explained by single defects of contact elements within the stamp. Figure 88c shows roundly shaped particles without any porous structure.

The analysis of 205 stamped particles resulted in a particle-to-particle distance of 1.1  $\mu\text{m}$ , a mean diameter of  $143 \pm 18$  nm, a circularity of  $0.89 \pm 0.15$  and an average aspect ratio of  $1.45 \pm 0.28$  as shown in Figure 89. The AFM analysis was difficult due to low adhesion between the stamped PS-*b*-P2VP particles and the ATAS-functionalized surface and did not reveal the long range order. Nonetheless, two single particles could be measured concerning their height as shown in Figure 90a. The height analysis (Figure 90b) amounted to a total height of 25 nm.

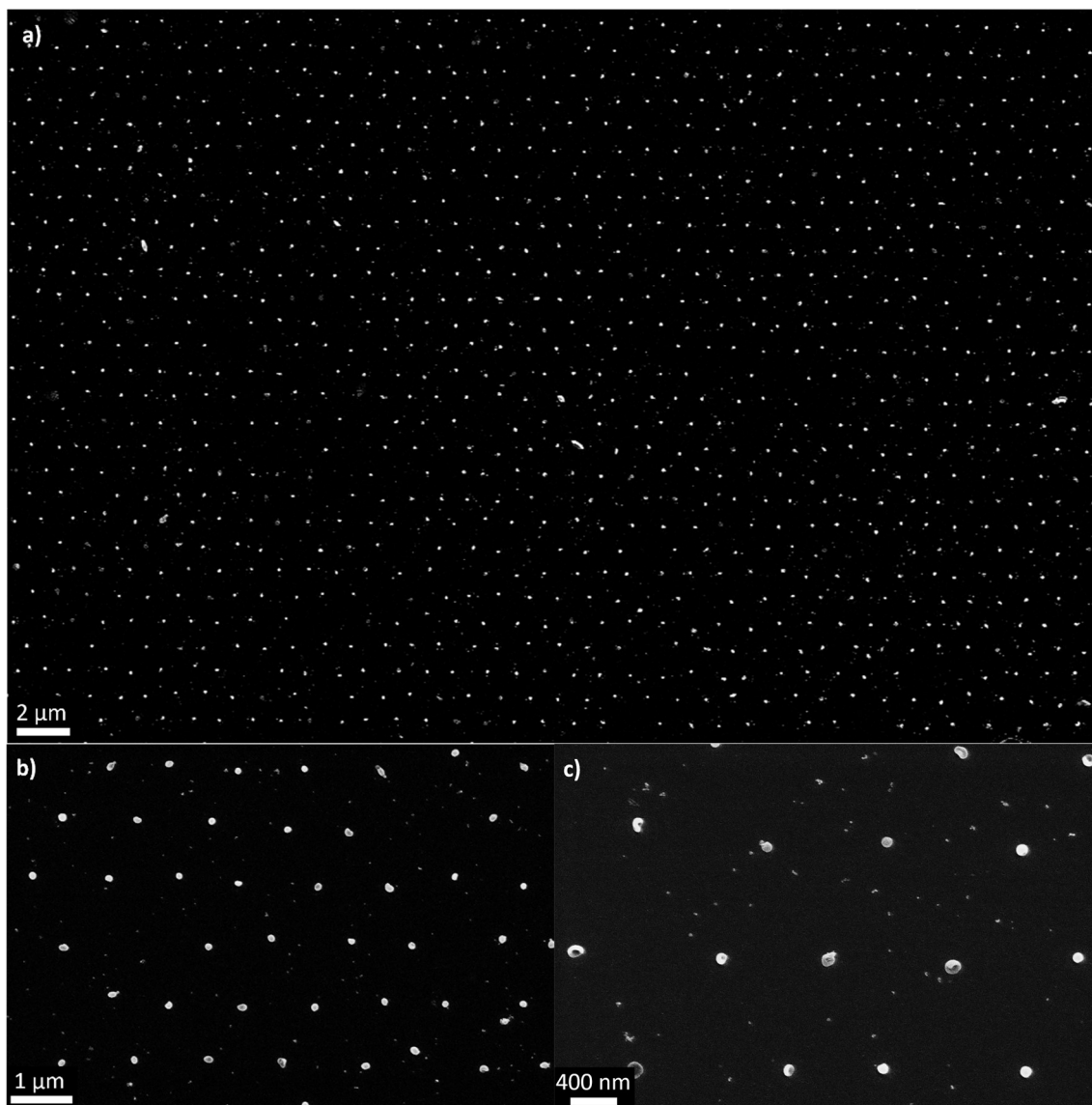


Figure 88. SEM images of stamped PS-*b*-P2VP on ATAS-functionalized glass after solvent treatment in EtOH at 60 °C for 1 h. a) Large area overview and b), c) magnifications of stamped particles. The stamping resulted in discrete particles consisting of PS-*b*-P2VP in a hexagonal order. All images were taken with an *in-lens* detector.

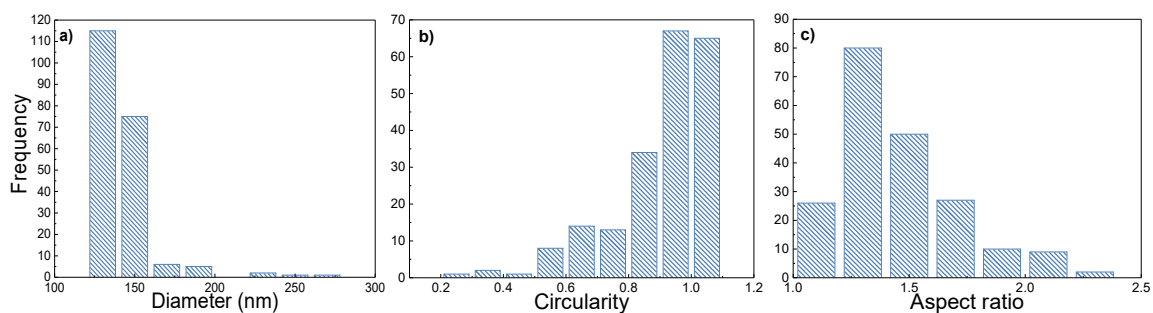


Figure 89. Histograms of 205 analyzed stamped PS-*b*-P2VP particles on ATAS-functionalized glass after solvent treatment. Showing a) the diameters, b) the circularities and c) the aspect ratios of the PS-*b*-P2VP particles.

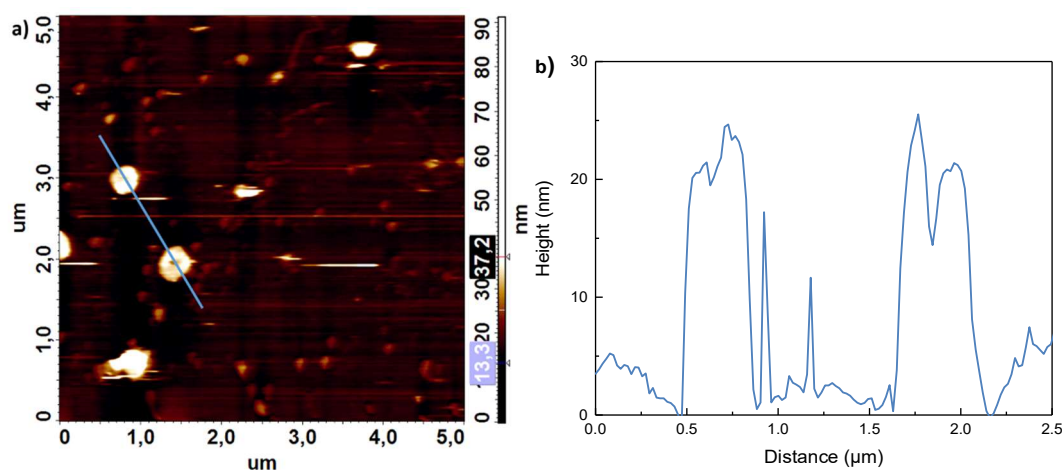


Figure 90. a) AFM image of stamped PS-*b*-P2VP on ATAS-functionalized glass after solvent treatment in EtOH at 60 °C for 1 h. b) The line scan shows the height of two stamped polymer particles. The height of the particles amounted to 20-25 nm. The AFM analysis was difficult due to low adhesion between the stamped PS-*b*-P2VP particles and the ATAS-functionalized surface.

#### 4.2.5.6 Discussion of stamping of PS-*b*-P2VP and comparison of the impact of the differently functionalized substrates

Table 4 gives an overview of all data of stamped PS-*b*-P2VP onto differently functionalized substrate surfaces and summarizes analyzed PS-*b*-P2VP particle diameters and heights. The comparison of the mean diameters is shown in Figure 91.

A comparison of stamped PS-*b*-P2VP onto hydroxyl-terminated glass prior and subsequent to the solvent treatment shows that the spot sizes became significant smaller and the spots did not remain interconnected subsequent to the solvent treatment (comparison of Figure 74 and Figure 76). As the solvent treatment proceeds in EtOH at 60 °C for 1 h, the polymer became mobile in a certain way and presumably formed discrete, porous spots. The disjoining pressure<sup>[152,153]</sup> forces the wide-spread polymer to contract, which is supported by the cohesion of the intramolecular interaction of the polymer. Nevertheless, due to acidic hydroxyl groups on the substrate surface, the nitrogen residue within the P2VP presumably formed hydrogen bonds with the substrate and a high mobility of the polymer is prevented. As a result, large spots with a small height were formed during the solvent treatment.

A comparison of stamped PS-*b*-P2VP onto FDTS-functionalized glass prior and subsequent to the solvent treatment shows a decreasing particle size (comparison of Figure 79 and Figure 80). Stamping of PS-*b*-P2VP onto FDTS-functionalized glass resulted in non-interconnected spots, where a dewetting process formed small particles. Within the solvent treatment of the stamped PS-*b*-P2VP on FDTS-functionalized glass, the polymer became mobile. As the interaction between polymer and substrate surface is weak, the

mobility of the polymer increased compared to the stamped PS-*b*-P2VP on hydroxyl-terminated glass. During the solvent treatment, surface diffusion of the polymer and a possible process similar to the Ostwald ripening formed one large PS-*b*-P2VP particle per initial contact between the stamp's contact elements and the FDTs-modified surface.<sup>[154,155]</sup> Although the size of the stamped polymer spots is large, normally one big polymer particle has formed after solvent treatment. Skaug *et al.*<sup>[156]</sup> observed the diffusion process of a molecule on a substrate and concluded that intermitted hopping could occur while the polymer is mobile on the substrate surface. Nevertheless, it is visible that some smaller particles have formed around the big particle (see Figure 80c, Figure 82b). The interruption of the solvent treatment could be a reason for this observation.

Stamping of PS-*b*-P2VP onto DMDCS-functionalized glass did not result in any patterned structures (see Figure 83, page 98). The results of stamping PS-*b*-P2VP onto DMDCS-functionalized glass after solvent treatment show non-porous particles as observed before on the FDTs-functionalized substrate. As the overall results are of weak order and similarity, a structure building mechanism is difficult to define. The interaction between the methyl residues on the substrate surface and the stamped PS-*b*-P2VP is presumably weak and thus, the mobility of the PS-*b*-P2VP during solvent treatment is high. The observed terracing behavior can occur, when one block of the BCP preferentially wets the surface and one block of the BCP preferentially wets the interface. The selective wetting is then driven by the minimization of the surface energy.<sup>[30]</sup> A minimal order within the observed terracing behavior is achieved after the solvent treatment in comparison to the results prior to swelling, where no structure at all is visible. Nevertheless, the results of stamping of PS-*b*-P2VP onto DMDCS-functionalized glass are poor compared to the stamping results when hydroxyl-terminated or FDTs-functionalized glass is used as substrate.

Stamping of PS-*b*-P2VP onto ATAS-functionalized glass resulted in a polymer layer throughout the hole surface area (see Figure 87, page 101). When compared to the results of stamping of PS-*b*-P2VP onto hydroxyl-terminated glass, the hexagonally ordered arrays could not be observed. This is presumably due to a reduced interaction between PS-*b*-P2VP and the ATAS-modified surface compared to the occurring hydrogen bridge bonding between PS-*b*-P2VP and the hydroxyl-terminated surface. After solvent treatment of the polymer, discrete particles with a narrow size range have formed over a large area of the surface. During the silanization of the glass with ATAS, the bond between silicon and nitrogen breaks and the ring opens (structural formula see Table 3).<sup>[157,158]</sup> This leads to a long chain, which could either stand up on the substrate surface or collapse and lay on the surface, where the latter is presumably the preferred option.

Although hydrogen bonding can occur between the amino residues and the PS-*b*-P2VP, the collapsing of the amino-containing chain causes a decrease in accessibility of amino groups. This weak interaction between surface residues and PS-*b*-P2VP increases the mobility of the polymer during the solvent treatment and thus, discrete particles can form at the former positions of the stamp's contact elements. The mechanism of the particle formation is presumably similar to the mechanism of stamped PS-*b*-P2VP on FDTS-functionalized glass after solvent treatment and thus follows surface diffusion and Ostwald ripening processes.<sup>[154,155]</sup>

*Table 4. Summary of all results of stamping of PS-*b*-P2VP onto differently functionalized substrate surfaces after solvent treatment. Showing the contact angles of toluene/chloroform (1:3) on the differently functionalized glass slides, the mean particle sizes of the stamped polymer analyzed with SEM and the particle heights analyzed with AFM.*

Functionalization	Functional group	Contact angle of solvent (°)	Mean particle size (SEM, nm)	Particle height (AFM, nm)
OH	-OH	0	730 ± 24	2-5
FDTS	-(CF <sub>2</sub> ) <sub>7</sub> -CF <sub>3</sub>	≈55	191 ± 21	20-60
DMDCS	-CH <sub>3</sub>	≈18	282 ± 111	40
ATAS	-NH <sub>2</sub>	0	143 ± 18	20-25

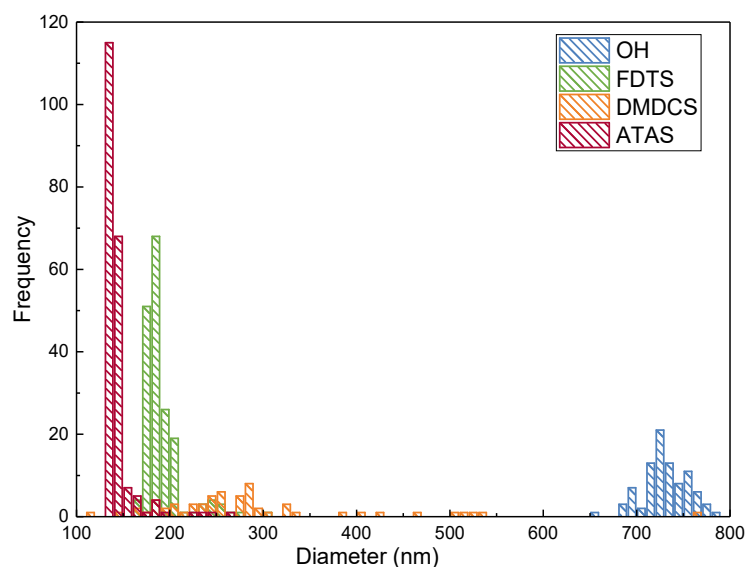


*Figure 91. Diameter analysis of all stamped samples on differently functionalized substrate surfaces after solvent treatment. The smallest particles were obtained by stamping on ATAS-functionalized glass. Also small non-porous particles were obtained by stamping onto FDTS-functionalized glass. A large variety of sizes and no long-range order were obtained when stamped onto DMDCS-functionalized glass. Large and porous spots could be obtained by stamping of PS-*b*-P2VP onto hydroxyl-terminated glass.*

In general, stamping of PS-*b*-P2VP worked and solvent treatment resulted in the formation of either porous or solid BCP structures, size and shape of which depended on the nature of the substrate. The interaction of PS-*b*-P2VP with the surface residues on the substrate surface is the main factor to influence particle size, height and shape. During the solvent treatment, the PS-*b*-P2VP becomes mobile in a certain way, which is also dependent on the interaction with the surface residues. This mobility of the polymer leads to a particle formation during solvent treatment, where the positions of the particles correspond to the former position of the stamp's contact elements. Overall, the solvent treatment plays an important role in the particle formation. Nevertheless, stamping of the PS-*b*-P2VP influences the positions of the particles to form during solvent treatment.

After the solvent treatment, the P2VP is exposed and the free electrons of the nitrogen are available for further chemistry. This can be used for different applications as atomic layer deposition (ALD) of semiconductors<sup>[159]</sup> or the immobilization of gold nanoparticles.<sup>[145, 146]</sup>

#### **4.2.6 Stamping of PFS-*b*-P2VP from toluene/chloroform onto hydroxyl-terminated and FDTs-functionalized glass with subsequent pyrolysis**

Block copolymers containing poly(ferrocenylsilanes) (PFS) can be used in a wide application range. As shown in Figure 92, the PFS block consists of repeat units that contain a ferrocenyl and an organosilane (in this case a dimethylsilane) group. Therefore, BCPs consisting of a PFS block can be used for redox-active gels<sup>[160]</sup> or plasma and electron beam etch resist.<sup>[161]</sup> The PFS block within a BCP is mostly immiscible with other organic or inorganic blocks and thus, a nanostructured material is formed by self-assembly of the BCP with periodic iron rich domains and varied morphologies.<sup>[162]</sup> As stamping of PS-*b*-P2VP from organic solution resulted in highly ordered arrays of BCPs on differently functionalized substrate surfaces (see chapter 4.2.5, page 89), the highly interesting polyferrocenyl(dimethylsilane)-*block*-poly(2-vinylpyridine) (PFS-*b*-P2VP) was also stamped in a capillary nanostamping procedure.



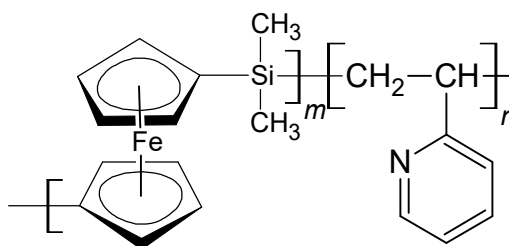


Figure 92. Structural formula of the used derivative of PFS-*b*-P2VP containing two methyl residues bound to the Si-atom. The poly(ferrocenyldimethylsilane) block has *m* repeat units, while the poly(2-vinylpyridine) block has *n* repeat units.

#### 4.2.6.1 Stamping of PFS-*b*-P2VP onto hydroxyl-terminated glass

The procedure of stamping of PFS-*b*-P2VP onto hydroxyl-terminated glass can be found in chapter 3.2.4.8 (see page 42). As stamps, the third-generation silica stamps with an average pore diameter of 44 nm were used. Stamping of PFS-*b*-P2VP onto hydroxyl-terminated glass resulted in discrete spots with a visible porous structure as shown in Figure 93. The overview of a large stamped area in Figure 93a shows the hexagonal pattern. Magnifications in Figure 93b and c illustrate the porous structure and furthermore presumably show a certain degree of shearing during the stamping process.

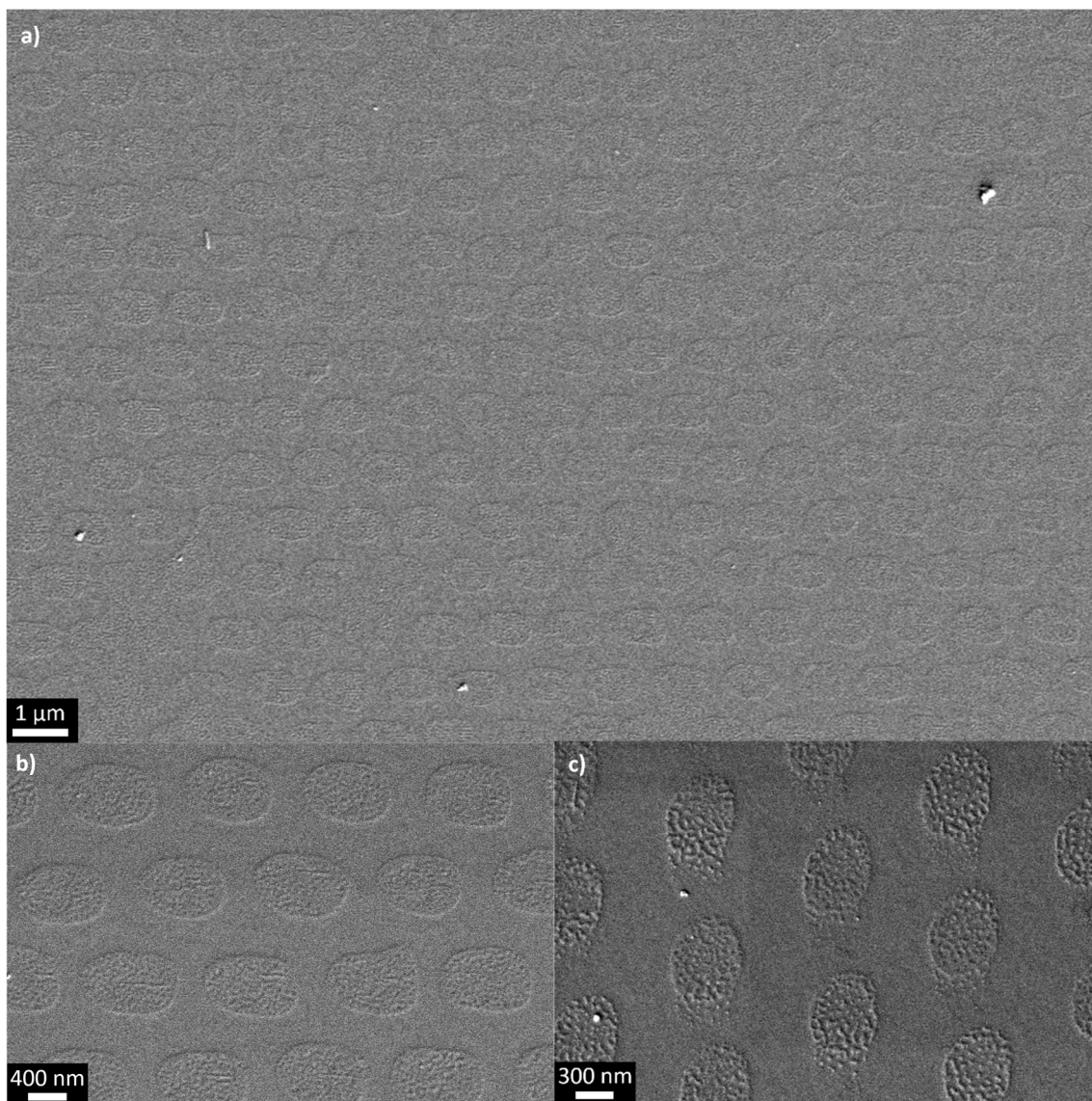


Figure 93. SEM images of stamped PFS-*b*-P2VP onto hydroxyl-terminated glass. a) Large area overview of stamped spots, b),c) magnification of the spots. The PFS-*b*-P2VP has formed porous structures. All images were taken with a SESI detector.

The structures obtained by AFM measurements in Figure 94a were used for size and shape analysis according to chapter 3.1.1.12 (see page 33). The histograms in Figure 95 illustrate the analysis of 44 particles with a center-to-center distance of 1.3 μm, a mean diameter of  $571 \pm 41$  nm, a circularity of  $1.00 \pm 0.01$  and an average aspect ratio of  $1.06 \pm 0.06$ . The line scan in Figure 94b shows the height of the spots marked in Figure 94a, which amounted to 1-1.5 nm.

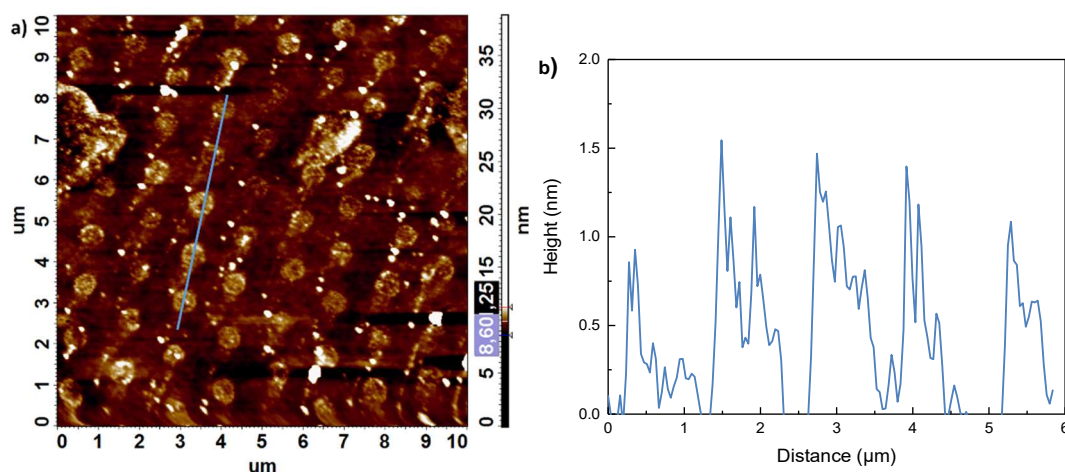


Figure 94. a) AFM image of stamped PFS-*b*-P2VP onto hydroxyl-terminated glass. b) Line scan of the blue line in a), the average height of the spots amounted to 1-1.5 nm.

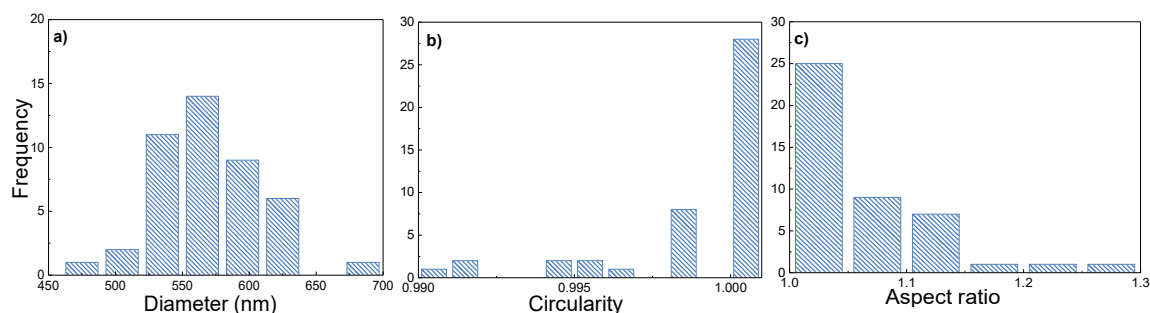


Figure 95. Histograms of 44 analyzed stamped PFS-*b*-P2VP spots on hydroxyl-terminated glass showing a) the diameters, b) the circularities and c) the aspect ratios of the PFS-*b*-P2VP spots.

The stamping of the PFS-*b*-P2VP onto hydroxyl-terminated glass resulted in discrete spots showing a porous structure without ink spreading. These results can be compared to the stamping of PS-*b*-P2VP onto hydroxyl-terminated glass subsequent to the solvent treatment (see chapter 4.2.5.2, page 91).

#### 4.2.6.2 Stamping of PFS-*b*-P2VP onto FDTS-functionalized glass

The procedure of stamping PFS-*b*-P2VP onto FDTS-functionalized glass can be found in chapter 3.2.4.8 (see page 42). As stamps, the third-generation silica stamps with an average pore diameter of 44 nm were used. Stamping of PFS-*b*-P2VP onto FDTS-functionalized glass resulted in discrete, porous spots as shown in Figure 96. The overview of a large stamped area in Figure 96a shows the hexagonal pattern. The magnification in Figure 96c shows a phenomenon, where within some of the structures, the pores are visible and within others, the polymer is allocated all over the stamped spot. This can be



due to the FDTS-functionalization, which causes a reduced wettability of the ink on the substrate and thus, encourages a possible polymer enrichment during stamping. This phenomenon was not visible within stamping of PFS-*b*-P2VP onto hydroxyl-terminated glass.

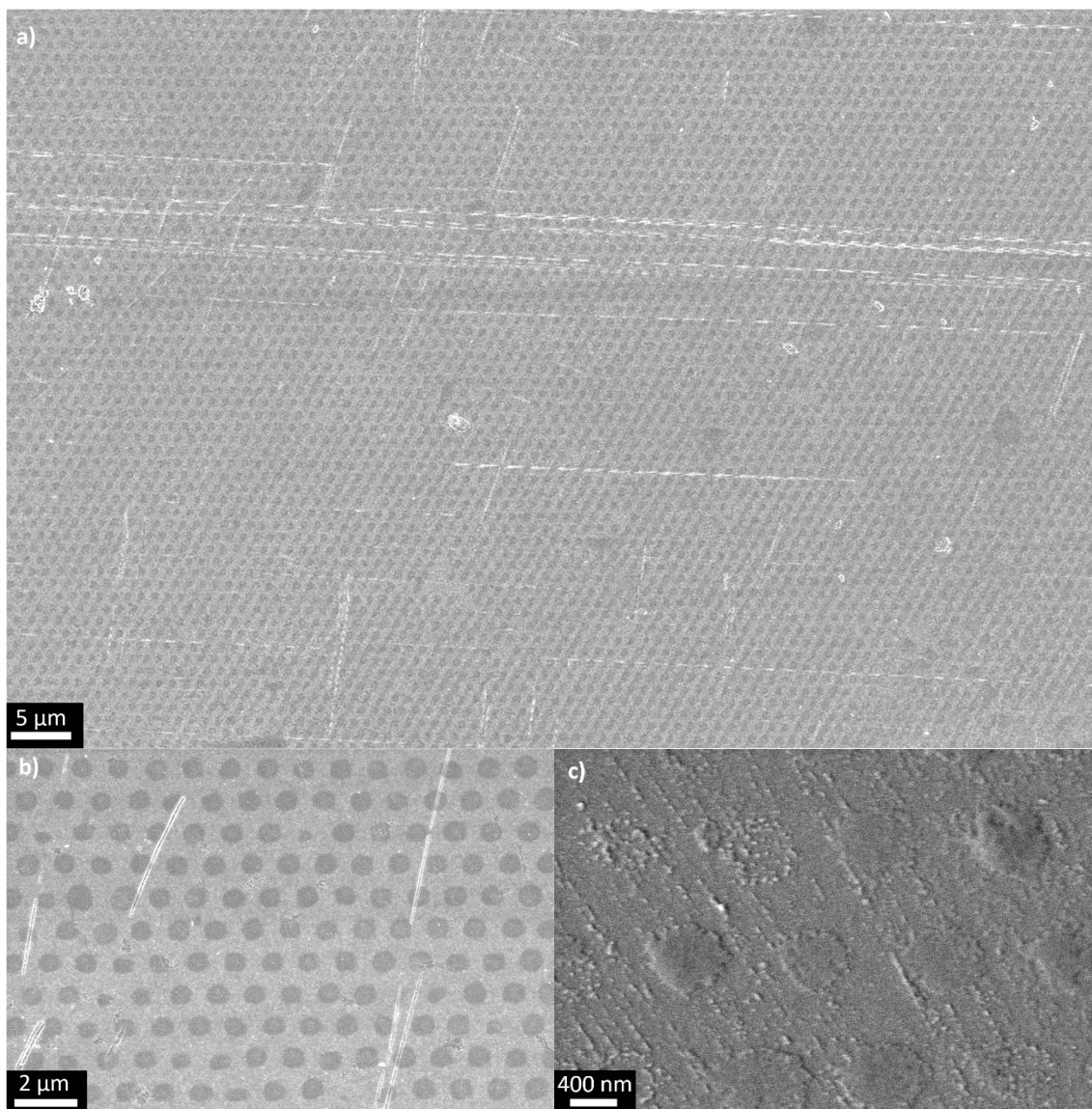


Figure 96. SEM images of stamped PFS-*b*-P2VP onto FDTS-functionalized glass. a) Large area overview of stamped structures, b) magnification of the spots. c) shows a phenomenon, which did not occur when stamped onto hydroxyl-terminated glass. The upper left spots are still forming porous structures, while the rest of the spots are filled with polymer. Images a) and b) were taken with an in-lens detector, image c) was taken with a SESI detector. The white lines are scratches in the glass substrate.

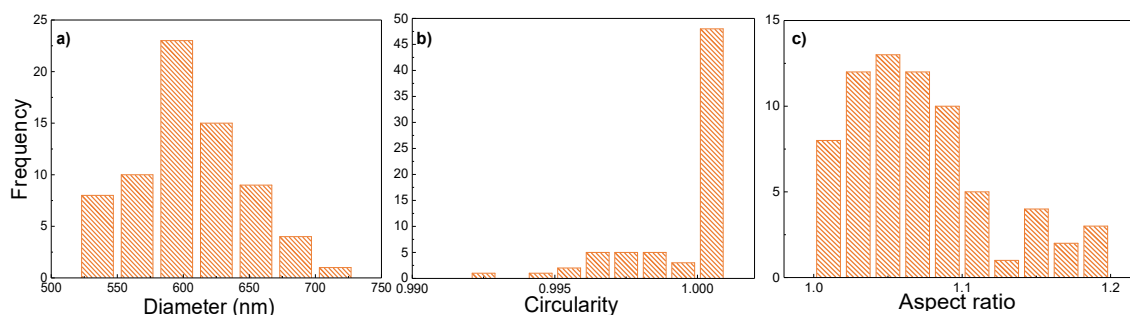


Figure 97. Histograms of 70 analyzed stamped PFS-*b*-P2VP spots on FDTS-functionalized glass showing a) the diameters, b) the circularities and c) the aspect ratios of the PFS-*b*-P2VP spots.

Analysis of the obtained particles was carried out according to chapter 3.1.1.12 (see page 33). The SEM images were analyzed and resulted in 70 stamped spots with sizes and shapes as shown in the histograms in Figure 97. The analysis revealed a center-to-center distance of the stamped spots of  $1.3 \mu\text{m}$ , a mean diameter of  $606 \pm 42 \text{ nm}$ , a circularity of  $1.00 \pm 0.01$  and an average aspect ratio of  $1.07 \pm 0.04$ . The AFM image in Figure 98a illustrates the height of the spots, which amounted to 2-5 nm as shown in Figure 98b. The height differences of 1-3 nm between the stamped PFS-*b*-P2VP on hydroxyl-terminated and FDTS-functionalized glass strengthens the assumption of different wettability behaviors of toluene/chloroform on the individual substrates. As toluene/chloroform has a high evaporation rate and additional ink is supplied through the stamp, the PFS-*b*-P2VP undergoes a certain degree of enrichment on the substrate surface during stamping.

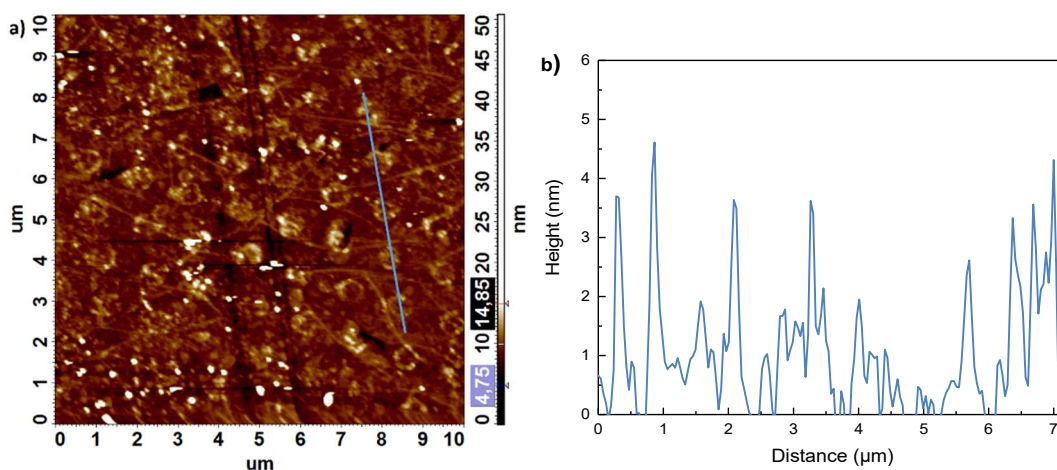


Figure 98. a) AFM image of stamped PFS-*b*-P2VP onto FDTS-functionalized glass. b) Line scan of the blue line in a), the spots have an average height of 2-4 nm.

The stamping procedures of PFS-*b*-P2VP on both substrates, hydroxyl-terminated and FDTS-functionalized, respectively, resulted in discrete porous spots or an enrichment of polymer within the stamped spots, dependent on the wettability of the solvent on the substrate surface. This second example of a block copolymer used as ink proves the capability of the method of capillary nanostamping with spongy mesoporous silica stamps as a good method to obtain hexagonally arranged discrete spots dependent on the surface functionality and nature of the polymer. In general, this method could be used to achieve patterned functional surfaces with desired block copolymers for further applications.

#### 4.2.6.3 Pyrolysis of stamped PFS-*b*-P2VP spots

A characteristic of PFS-containing BCPs is their ability to transform into ceramics after pyrolysis.<sup>[163]</sup> When poly(ferrocenylsilanes) are pyrolyzed, a ceramic consisting of Fe/Si/C with magnetic characteristics dependent on temperature and atmosphere during pyrolysis is obtained.<sup>[164]</sup> Therefore, PFS-*b*-P2VP was stamped onto FDTS-functionalized quartz substrates and pyrolyzed at 900 °C in an argon atmosphere as described in section 3.2.4.8 (see page 42).

The quartz substrate was silanized with FDTS, as the smooth quartz surface did not yield sufficient results when left untreated. During pyrolysis, the organic block is burned, while the PFS block is forming a ceramic structure. Therefore, after pyrolysis, solely ceramic particles are left. In Figure 99, SEM images of the pyrolyzed and thus, ceramic structures are shown. The diameters of 108 ceramic particles after pyrolysis amounted to  $90 \pm 37$  nm (see histogram in Figure 100). The height analyzed with AFM resulted in a height of 5-6 nm after pyrolysis (see Figure 101b).

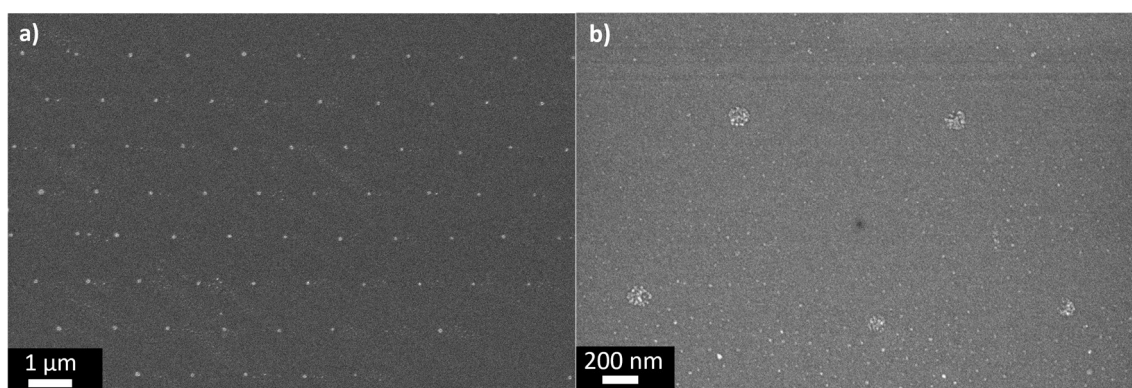


Figure 99. SEM images of ceramic particles after pyrolysis at 900 °C under a constant argon flow. a) Overview area and b) magnification of single ceramic particles. Images were taken with an in-lens detector.



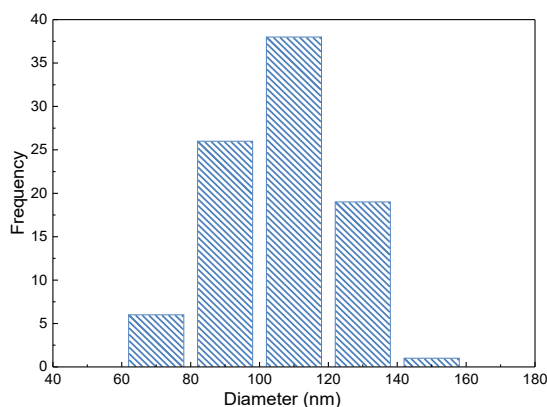


Figure 100. Histogram showing the diameters of 108 analyzed ceramic particles after pyrolysis.

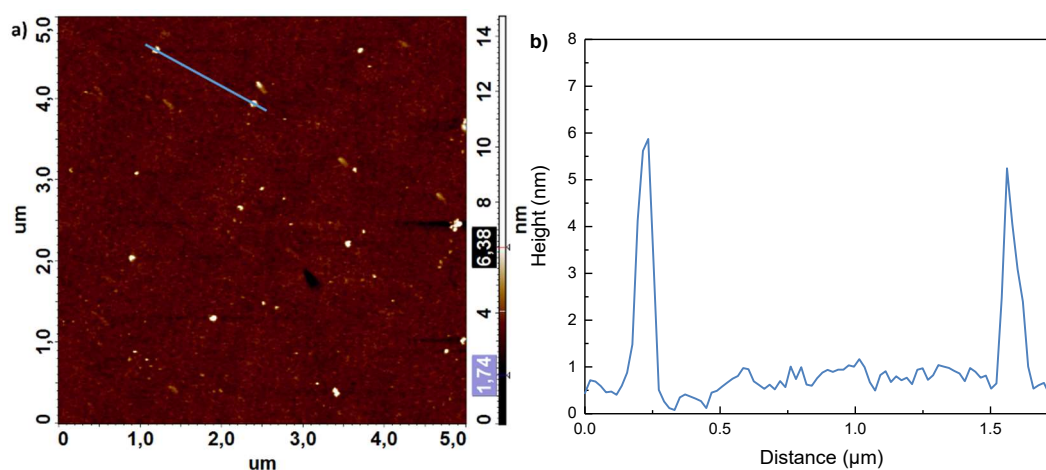


Figure 101. a) AFM image of ceramic particles on FDTS-functionalized quartz subsequent to pyrolysis. b) Line scan of the blue line in a) shows a height of 5-6 nm.

One can see a clear difference between the stamped PFS-*b*-P2VP particles on FDTS-functionalized glass and the ceramic particles on FDTS-functionalized quartz after pyrolysis. The diameter of the stamped PFS-*b*-P2VP particles prior to the pyrolysis amounted to  $606 \pm 42$  nm (see Figure 97), while the diameter of the pyrolyzed ceramic particles decreased to  $90 \pm 37$  nm (see Figure 100). This decreasing particle size has several reasons. First, the polymer becomes mobile during heating, where the disjoining pressure<sup>[152,153]</sup> forces the wide-spread polymer to contract, which is supported by the cohesion of the intramolecular interaction of the polymer. Second, with higher temperature, the organic parts of the polymer are burned and the iron, silicon and carbon formed a ceramic structure and thus, the diameters decrease. Another observation subsequent to pyrolysis is the formation of small particles, which are spread over the substrate surface (see Figure 99b and Figure 101a). Due to a particle size shrinkage of  $\approx 500$  nm during pyrolysis, it seems plausible that the mobility of the polymer during pyrolysis is not high

enough to form one single polymer particle. Therefore, several smaller ceramic particles are formed on the substrate surface.

#### 4.2.6.4 *Growing of CNTs onto pyrolyzed PFS*

Ceramic structures obtained from PFS-containing block copolymers are known as a good catalyst for the growth of carbon nanotubes (CNTs).<sup>[165,166]</sup> For this application, ordered structures were made in a complex photolithographic process as a catalyst for the growth of patterned CNTs.<sup>[167,168]</sup> Capillary nanostamping was used in an explorative experiment to stamp PFS-*b*-P2VP particles, which undergo a pyrolysis procedure and form ceramic particles, with the application as a catalyst for the subsequent growth of CNTs.

In a one-step synthesis procedure, the as-stamped PFS-*b*-P2VP was converted into a ceramic by a pyrolysis procedure at 900 °C in an argon atmosphere with subsequent growing of CNTs according to chapter 3.2.4.8 (see page 42). As stamps, the third-generation silica stamps with an average pore diameter of 44 nm were used. For this experiment, the PFS-*b*-P2VP was stamped onto FDS-functionalized quartz. The SEM images of the resulting ceramic particles are shown in Figure 102. The hexagonal arrangement is still intact after the procedure and a small amount of CNTs were grown on the surface. The magnification in Figure 102c shows the CNTs as long lines with a small diameter.

The diameters of 147 ceramic particles obtained from pyrolysis and CNT growth amounted to  $148 \pm 22$  nm (see histogram in Figure 103). The AFM analysis resulted in ceramic particles with a height of 17-22 nm after pyrolysis and CNT growth (see Figure 105c and green line in a). The SEM images in Figure 102 show the same phenomenon as observed before with the ceramic particles after pyrolysis. Smaller ceramic particles were formed during pyrolysis and seem to have formed a honeycomb-like pattern around the larger ceramic particles. Also noteworthy from these results is the form of the obtained ceramic particles after pyrolysis and CNT growth. In Figure 102b and c, it is clearly visible that every single particle has a brighter spot on one side, where the work function of the material is lower than for the rest of the spot. As the stamped PFS-*b*-P2VP was treated with methane and hydrogen during pyrolysis, a possible enrichment of carbon on these spots could have happened.

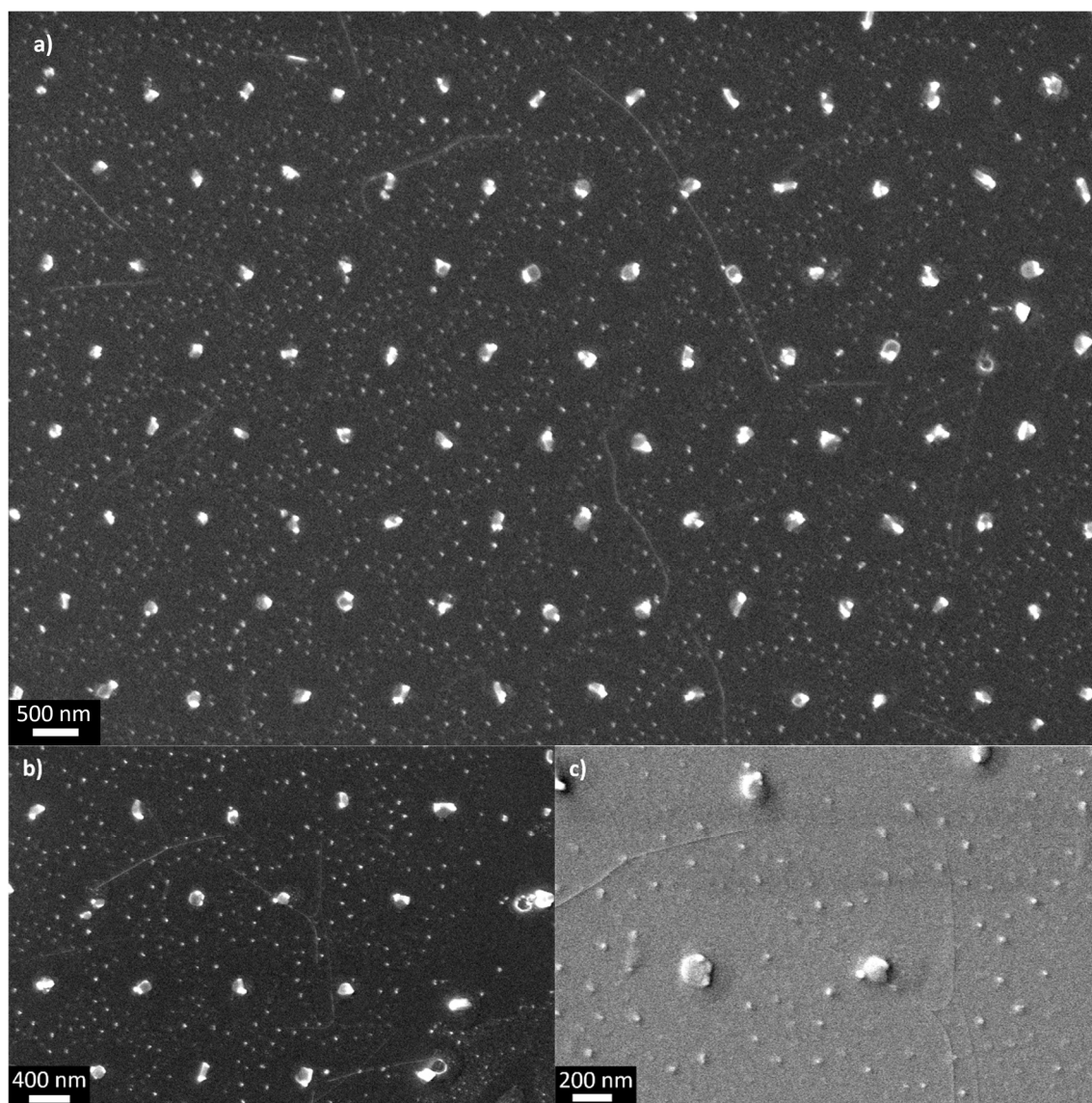


Figure 102. SEM images of stamped ceramic particles after pyrolysis and growing of CNTs. a), b) The stamped and pyrolyzed ceramic particles on quartz are hexagonally ordered over a large surface area. c) The magnification of b) shows the grown CNTs as long lines with small diameters. Images a) and b) were taken with an in-lens detector, image c) was taken with a SESI detector.

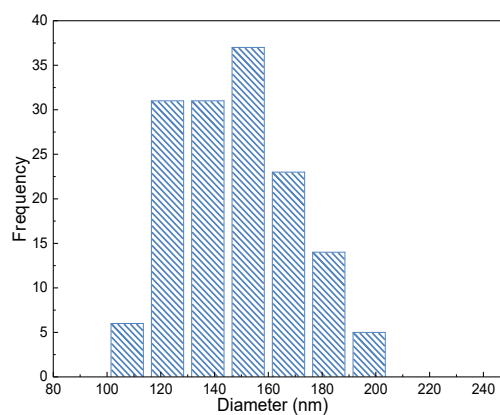


Figure 103. Histogram showing the diameters of 147 analyzed ceramic particles after pyrolysis and CNT growth.

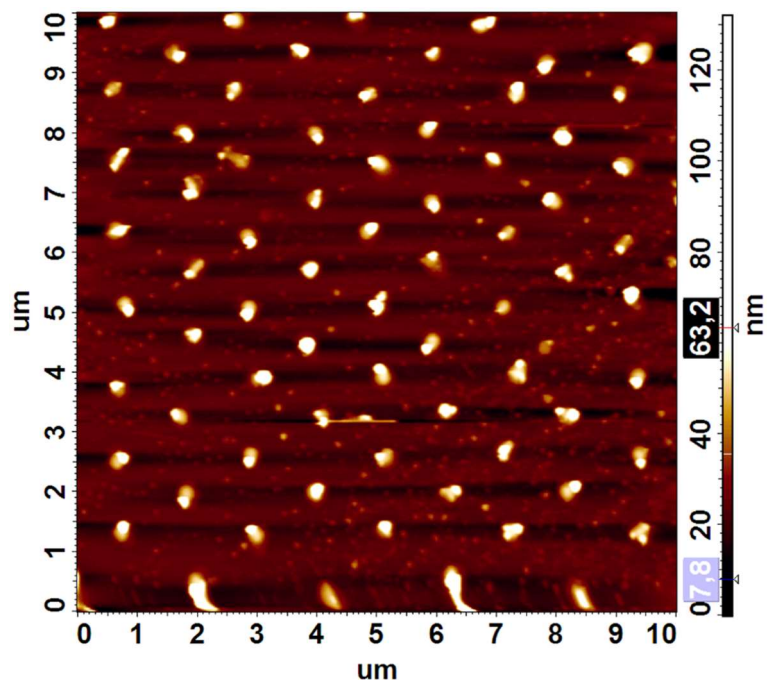


Figure 104. AFM overview image of ceramic particles on quartz subsequent to pyrolysis and growing of CNTs. The hexagonal order remained visible after pyrolysis and CNT growth.

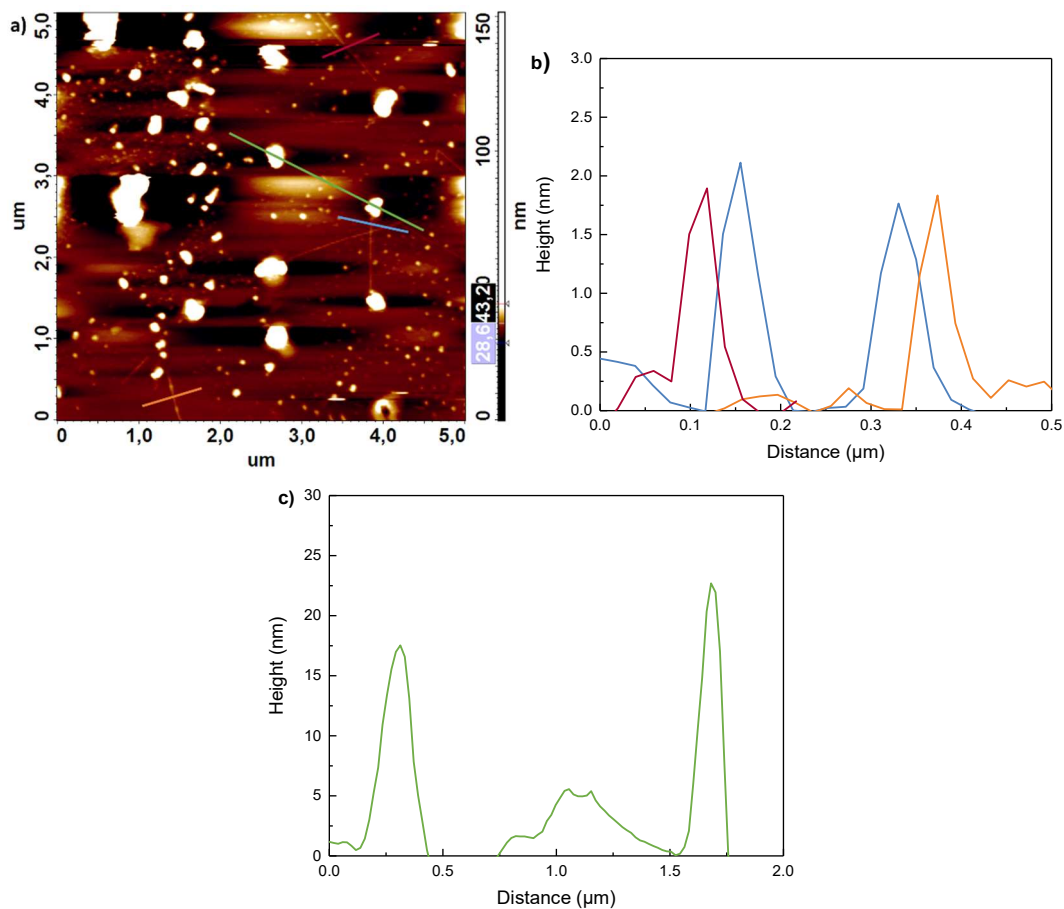


Figure 105. a) AFM image of ceramic particles on quartz subsequent to pyrolysis and growing of CNTs. b) Line scans of the single lines in a) show the single CNTs with a height of approximately 2 nm. c) The green line shows the height analysis of ceramic particles and amounted to 17-22 nm.



The grown CNTs were analyzed with AFM. The AFM analysis shows a larger area in Figure 104, whereas the height analysis of the ceramic particles and the CNTs was carried out with Figure 105a due to a higher precision with higher magnification. Figure 105a shows the grown CNTs with a height of approximately 2 nm as shown in Figure 105b (blue, orange and red line). Within this size range, it can be assumable that the growing of CNTs led to single- or double-walled CNTs.<sup>[168]</sup> Nevertheless, it is also visible that the CNTs did not grow from the larger ceramic particles, but seem to have grown from the smaller ceramic particles surrounding the larger ceramic particles. This seems logical, as a good catalyst for the growth of CNTs is supposed to be in the same size range.<sup>[166]</sup> Therefore, although the CNT growth worked on the ceramic particles, the sizes of the resulting ceramic particles after pyrolysis should be further decreased for an improvement as a catalyst.

When the results of the ceramic particles after pyrolysis and pyrolysis with additional CNT growth are compared, both, the particle sizes and the heights increased. In detail, the ceramic particles after pyrolysis show a diameter of  $90 \pm 37$  nm and a height of 5-6 nm, which increased after pyrolysis with additional CNT growth, to a diameter size of  $148 \pm 22$  nm and a height of 17-22 nm. Therefore, it is presumable, that with the CNT growth, a graphitic sheet is formed around the ceramic particles, as this is supposed to be the competing reaction to the CNT growth.<sup>[169]</sup> This could also be the explanation for the bright spots visible in the SEM images of the ceramic particles after pyrolysis and CNT growth.

In principal, ceramic particles obtained by pyrolysis of stamped PFS-*b*-P2VP spots, can be used as a catalyst for the growth of CNTs. Even though only a small amount of CNTs were grown onto the stamped substrate, this could become a potential usage for this block copolymer. To produce highly dense CNTs on the substrate surfaces patterned with ceramic particles, the reaction conditions of the CNT growth should be optimized, as well as the ceramic particle size, which should be decreased significantly. Nevertheless, the optimization of these results could be an improvement to previous methods, where the patterning was carried out by a complicated and time consuming photolithographic process and the pyrolysis and growing of CNTs was done in a two-step procedure.<sup>[166]</sup>



When compared to the former chapter 4.2.5 (see page 89), it is possible to achieve an altered formation of the single BCPs either by a solvent treatment, or by pyrolysis. Both methods lead to smaller, denser particles compared to the particles prior to the solvent treatment or pyrolysis procedures. Whereby the properties of the surface play a significant role. What should be kept in mind is that, in the latter chapter, the smaller ceramic particles are obtained by burning of the organic parts within the PFS-*b*-P2VP and therefore, the obtained structure became smaller after the pyrolysis. The solvent treatment of PS-*b*-P2VP does not provoke an extinction of a polymer component. Nevertheless, a certain degree of movement of the polymer is provided by both methods and therefore, smaller and denser particles were formed.

#### 4.2.7 Active pharmaceutical ingredients – stamping of 17 $\alpha$ -ethinylestradiol (EE<sub>2</sub>)

A significant proportion of the active pharmaceutical ingredients (APIs) in the market or under development suffers from poor water solubility and, consequently, low bioavailability that impedes their clinical use.<sup>[99,170,171]</sup> Poor water solubility of APIs has become a major challenge in the drug development process as APIs with poor water solubility are difficult to formulate by conventional methods.<sup>[172]</sup> To overcome this problem, engineering approaches such as pH adjustment and salt-form selection, polymorphism management, and cocrystallization, formulations containing surfactants and cyclodextrins, lipid-based formulations and amorphous solid dispersions have been investigated,<sup>[173]</sup> as well as hot melt extrusion<sup>[174]</sup> and 3D printing.<sup>[175,176]</sup> Particle size reduction to the sub-micron range significantly increases the specific API surface area and has, therefore, been considered as a particularly promising strategy to enhance solubility and bioavailability of poorly water-soluble APIs as compared to conventional dosage forms.<sup>[172]</sup> Apart from oral administration, nanocrystals of poorly water-soluble APIs are also suitable for transdermal delivery, for example of cosmeceuticals and in the therapy of skin diseases.<sup>[177]</sup> Besides nanoscale API carriers formed, for example, from polymers or liposomes,<sup>[178,179]</sup> “cargo-free” nanomedicines consisting of the APIs themselves without new excipients have attracted significant attention.<sup>[177]</sup> Nanoparticles of poorly water-soluble APIs<sup>[172,177,180–182]</sup> have predominantly been obtained by nanoprecipitation-based approaches<sup>[99]</sup> and *via* mechanical milling.<sup>[183]</sup> Nanodispersions containing poorly water-soluble API nanoparticles are versatile delivery systems for oral, dermal, ocular, parenteral and pulmonary administration routes.<sup>[184]</sup>

Despite the advantages of nanoparticulate APIs, it has remained challenging to form nanoparticles of poorly water-soluble APIs in a well-defined way with a narrow size distribution.<sup>[180]</sup> Therefore, poorly water-soluble APIs, in detail the estrogen 17 $\alpha$ -ethinylestradiol (EE<sub>2</sub>), was stamped by capillary nanostamping according to the mechanism in Figure 106. The silica stamps are filled with a solution of the poorly water-soluble EE<sub>2</sub> in a suitable organic solvent, in this case acetonitrile (ACN, Figure 106a). When the silica stamp approaches the perfluorinated glass surface, liquid bridges of the EE<sub>2</sub> solution form at the positions of the stamp's contact elements. As the ACN evaporates, more solution is drawn into the liquid bridges, where the EE<sub>2</sub> enriches and eventually precipitates (Figure 106b). After retraction of the silica stamp, nanoparticles of EE<sub>2</sub> remain on the perfluorinated glass surface at the former position of the stamp's contact elements (Figure 106c). Since the contact elements are uniform in size and shape, the formed nanoparticles have similar sizes. Eventually, the nanoparticles of EE<sub>2</sub> are transferred to aqueous colloidal nanodispersions by sonication (Figure 106d).

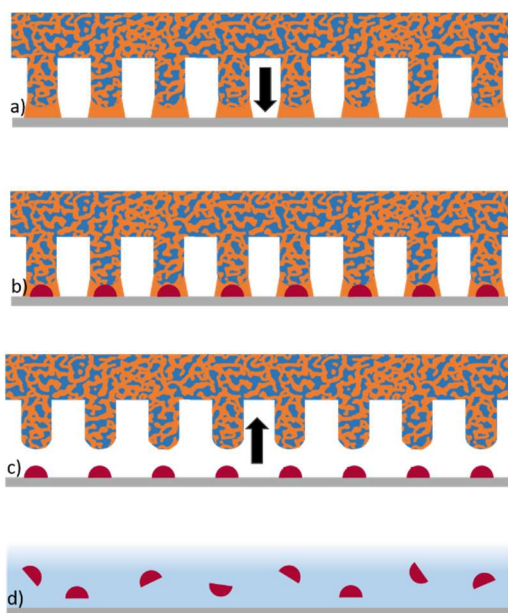


Figure 106. Production of poorly water-soluble EE<sub>2</sub> nanoparticles by capillary nanostamping. a) The silica stamp (blue) is filled with a solution of the poorly water-soluble EE<sub>2</sub> in ACN (orange). b) Upon approach of the ink-filled silica stamp to the FDTS-functionalized glass slide (grey), liquid ink bridges form between the contact elements of the silica stamp and the glass slide. c) Solvent evaporation drives additional EE<sub>2</sub> into the liquid bridges so that solid EE<sub>2</sub> particles form. d) After stamp retraction, EE<sub>2</sub> nanoparticles remain on the glass slides. The poorly water-soluble EE<sub>2</sub> nanoparticles are transferred to aqueous colloidal nanodispersions by sonication.

#### 4.2.7.1 Stamping of $EE_2$ and analysis of obtained particles

The conditions of the stamping process of  $EE_2$  from ACN solution can be found in chapter 3.2.4.9 (see page 43). As stamps, the third-generation silica stamps with an average pore diameter of 31 nm were used. The substrate was functionalized with FDTs to obtain a hydrophobic surface to thermodynamically prevent ink spreading. The contact angle of ACN on FDTs-functionalized glass amounted to  $\approx 70^\circ$ . The SEM images in Figure 107 show the outcome of the stamping of  $EE_2$ . The  $EE_2$  forms small, uniform particles on the substrate surface over a large area. Nevertheless, small deviations from the perfect hexagonal order can be observed, which can be due to the high contact angle of ACN on the FDTs-functionalized substrate. During the stamping process, dissolved  $EE_2$  in ACN is precipitated through the contact elements of the stamp onto the substrate surface. As the ACN is evaporating,  $EE_2$  particles form by the movement of single molecules to one discrete spot, where an accumulation of molecules forms the final particle. The mobility of the single molecules within the ink droplet is dependent on the nature of the substrate surface, where weak interactions between the surface residues and the molecules within the non-volatile ink component promotes a high mobility.

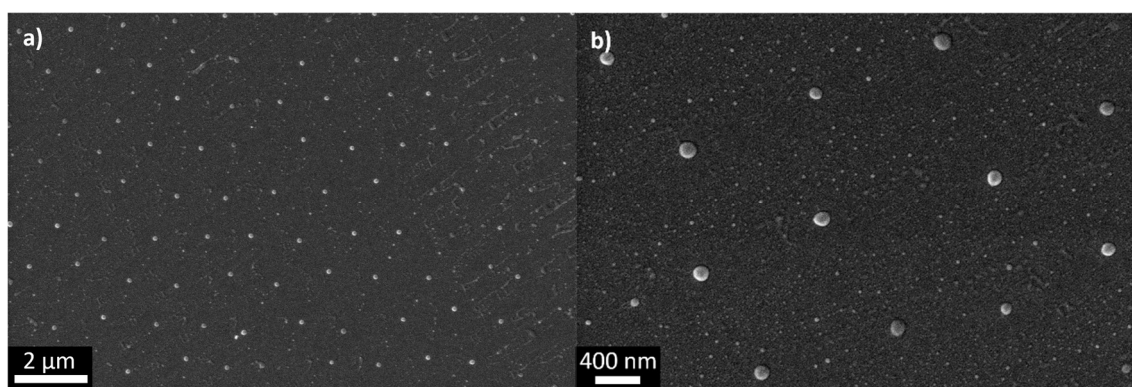


Figure 107. SEM images of stamped  $EE_2$  particles on FDTs-functionalized glass. The particles are hexagonally arranged. a) Overview of larger area and b) magnification of the particles. Although the pattern has slight deviations from a perfect hexagonal order, the particles are uniform in sizes and shape and the overall order is visible. Images were taken with an in-lens detector.

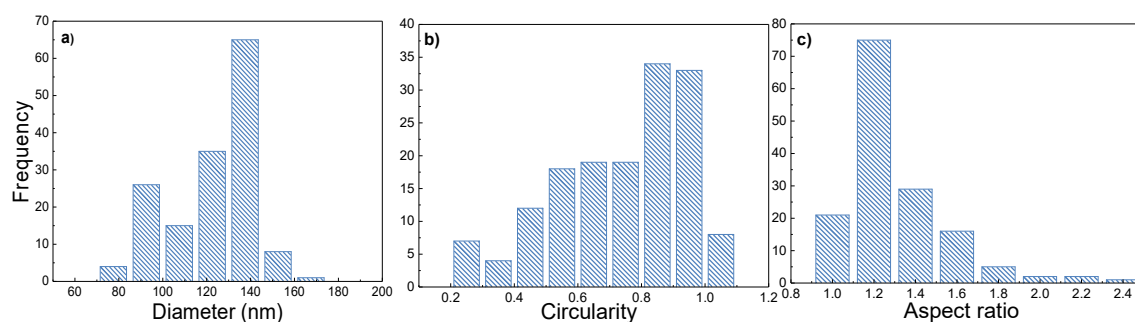


Figure 108. Histograms of 154 analyzed stamped  $EE_2$  particles on FDTs-functionalized glass showing a) the diameters, b) the circularities and c) the aspect ratios of the  $EE_2$  particles.

Analysis of the obtained particles was carried out according to chapter 3.1.1.12 (see page 33). The analysis of 154 particles amounted to a particle-to-particle distance of  $1.3\ \mu\text{m}$ , an average particle diameter of  $123 \pm 19\ \text{nm}$ , an average circularity of  $0.73 \pm 0.21$  and an average aspect ratio of  $1.33 \pm 0.31$  as shown in Figure 108. The analysis with AFM shown in Figure 109 confirms the hexagonal order as well as the particle shape and sizes. The height determined with the AFM line scan (blue line in Figure 109b) amounted to a particle height of 10-12 nm. Thus, the  $\text{EE}_2$  nanoparticles had a disk-like shape, which is advantageous for the administration of poorly water-soluble drugs in that the specific surface of discs is larger than that of spheres.

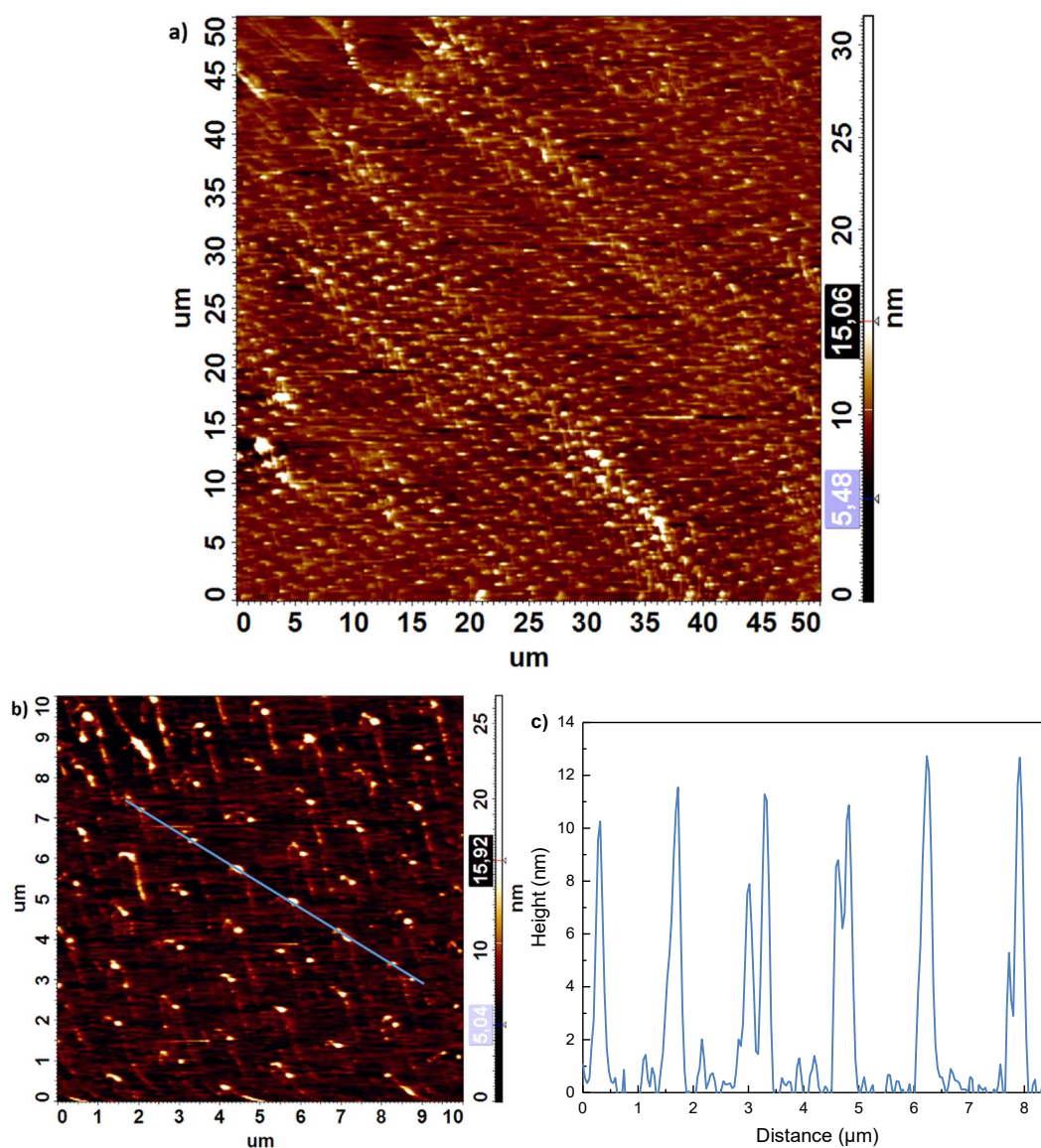


Figure 109. AFM analysis of stamped  $\text{EE}_2$  particles. a) Overview of large area. b) The magnification of a) shows the hexagonal order of the particles in detail. c) A line scan of the blue line in b) shows an average height of the particles of 10-12 nm.

#### 4.2.7.2 Detachment of stamped EE<sub>2</sub> particles into aqueous dispersion

Subsequent to stamping of EE<sub>2</sub> onto FDTS-functionalized glass, the particles were dispersed into an aqueous solution by sonication. The theoretical concentration of the dispersed EE<sub>2</sub> particles can be calculated as followed. It is assumed that the EE<sub>2</sub> nanoparticles generated by the stamping process constitute a defect-free hexagonal lattice with a lattice constant of 1.3 μm. A hexagon with an edge length of 1.3 μm corresponding to the lattice constant of the EE<sub>2</sub> nanoparticle array has one EE<sub>2</sub> nanoparticle in the middle of the hexagon plus one EE<sub>2</sub> nanoparticle located on each of its six corners. However, since each of the 6 EE<sub>2</sub> nanoparticles on the edges touch overall three hexagons, only 1/3 of each EE<sub>2</sub> nanoparticle can be assigned to the considered hexagon. The area  $A$  can be calculated with an equilateral hexagon with a side length  $a$ , which is reflected by the particle-to-particle distance and amounted to 1.3 μm (mean distance). Therefore, the area is<sup>[80]</sup>

$$A = \frac{3}{2} \cdot a^2 \cdot \sqrt{3} = 4.39 \mu\text{m}^2 \quad (6)$$

As every hexagon has an amount of  $P = 1 + 6 \cdot \frac{1}{3} = 3$  particles, and the total stamped area  $A_{tot}$ , which consists of 10 times 5x5 mm<sup>2</sup> spots, amounts to  $A_{tot} = 250,000,000 \mu\text{m}^2$ , the total amount of stamped particles amounts to

$$P_{tot} = \frac{A_{tot}}{A} \cdot 3 = 170,842,825 \approx 170 \text{ millions} \quad (7)$$

The stamped particles have the shape of a spherical cap with a height  $h$  of 11 nm and a segmental radius  $a$  of 62 nm, the spherical radius  $r$  can be calculated with<sup>[80]</sup>

$$a = \sqrt{h \cdot (2r - h)} \quad (8)$$

and amounts to 175 nm. From that, the spherical volume can be calculated with<sup>[80]</sup>

$$V = \frac{\pi}{3} \cdot h^2 \cdot (3r - h) = 65,129 \text{ nm}^3 \quad (9)$$

Therefore, the volume of all stamped particles amounts to  $V_{tot} = 1.11 \cdot 10^{13} \text{ nm}^3$ . With a density of EE<sub>2</sub> of  $\delta = 1.21 \frac{\text{g}}{\text{cm}^3}$ ,<sup>[185]</sup> the total mass of EE<sub>2</sub> within the dispersion results in 0.013 μg or 13 ng. Therefore, the EE<sub>2</sub> concentration within the dispersion amounted to 0.02 nmol/mL or 7 ng/mL.



The EE<sub>2</sub> nanoparticle dispersions were investigated by dynamic light scattering (DLS) measurements (Table 5). Standard DLS evaluation procedures are only valid for dispersions of spherical particles. Because of the non-spherical shape of the EE<sub>2</sub> nanoparticles, only “apparent” hydrodynamic diameters were accessible. However, DLS measurements may yield information on the stability of the EE<sub>2</sub> nanoparticle dispersions. As the polydispersity index (PDI) is > 0.5 for each measurement, the Z-average number was not taken into account. Therefore, only the apparent diameter and its alteration were considered. Directly after the preparation of the aqueous EE<sub>2</sub> particle dispersion, the apparent diameter according to DLS measurements amounted to ≈70 nm (see Table 5). After one hour, the DLS measurements still show apparent diameters in the same range. Two hours after the dispersion was prepared, the particles began to aggregate, which is visible in the increasing diameter of 116-194 nm. After 20 hours, the particle sizes increased significantly and reached an apparent diameter of ≈300 nm. After one day, the dispersion was redispersed by sonication for one hour and again measured with DLS. Here it is visible, that the original particle sizes of 60-80 nm could be obtained again. The freshly dispersed EE<sub>2</sub> particles were stable without aggregation for at least one hour, whereby a sonication procedure for one more hour ensured a dispersion stability for 24 hours. If considered that the dispersion was not stabilized with any techniques at all, the stability of pure EE<sub>2</sub> particles in an aqueous solution amounted to last long enough for a possible application in a medical field. For long-lasting dispersion stabilities, several work groups have used surfactants,<sup>[186,187]</sup> an emulsification-evaporation method<sup>[188]</sup> or a high-gravity process with subsequent spray-drying of the particles to stabilize the dispersion.<sup>[189]</sup>

Table 5. Mean diameters with standard deviations and number percentages of particle populations of DLS measurements on aqueous EE<sub>2</sub> nanoparticle dispersions after different storage times. Before each measurement, the dispersion was sonicated for 10 min. The number reflects the absolute percentage of measured particles. After 24 h, the dispersion was sonicated for 1 h.

Storage time (h)	Sonication treatment (min)	Peak 1		Peak 2	
		Apparent diameter (nm)	Percentage particles	Apparent diameter (nm)	Percentage particles
0	10	301 ± 78	3.1	69 ± 18	96.9
0	10	268 ± 67	4.7	71 ± 12	95.3
1	10	289 ± 54	2.2	68 ± 10	97.8
1	10	315 ± 62	1.6	63 ± 9	98.4
2	10	317 ± 85	11.6	116 ± 30	88.4
2	10	--	--	194 ± 94	100
20	10	296 ± 54	100	--	--
20	10	310 ± 51	100	--	--
24	60	302 ± 64	1.2	61 ± 10	98.8
24	60	273 ± 47	7.1	88 ± 13	92.9

The SEM image in Figure 110 shows the stamped EE<sub>2</sub> particles after detachment from the substrate and dispersion into aqueous solution, which were drop-casted onto a glass slide and dried in air for SEM analysis. It is visible that the EE<sub>2</sub> remained in discrete particles and did not dissolve within the dispersion in water. If the EE<sub>2</sub> would have dissolved in water, an overall EE<sub>2</sub> film on the substrate surface would have occurred.

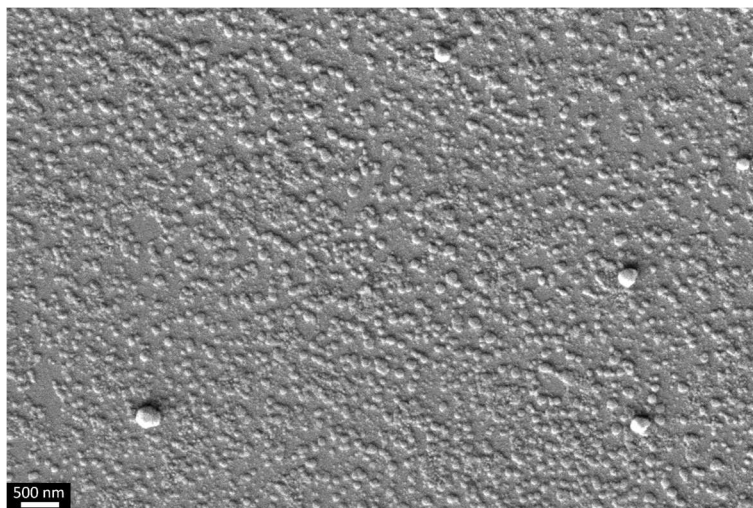


Figure 110. SEM image of stamped  $EE_2$  particles, which were detached from the substrate and redispersed in water. It is visible that the  $EE_2$  particles are still intact and did not dissolve in water. The SEM image was taken with a SESI detector.

#### 4.2.7.3 Click-chemical functionalization of $EE_2$ particles from dispersion

$EE_2$  molecules possess terminal triple bonds accessible for functionalization. For an exemplary functionalization, the dye sulfo-cyanine-3-azide was coupled to  $EE_2$  nanoparticles dispersed in water *via* a copper-free click reaction according to chapter 3.2.4.9 (see page 43). The  $EE_2$  nanoparticles have a density similar to water and thus, could not be separated by centrifugation. Therefore, the excess of dye had to be washed out by dialysis. For this purpose, the reaction mixture was washed in a dialysis tube for 7 days to remove excess dye. The dialysis was continued until the repeatedly exchanged water at the other side of the semipermeable membrane did no longer show traces of dye fluorescence. The reaction mixture of containing the dye-modified  $EE_2$  nanoparticles turned from pink to colorless during dialysis.

The fluorescence spectra after click reaction and dialysis give evidence of a successful functionalization of  $EE_2$  particles. The orange curve shows the pure  $EE_2$  nanoparticles dispersed in water prior to the click reaction. Here, no significant fluorescence signal is visible. The red curve shows the reaction mixture after click-chemical coupling of sulfo-cyanine-3-azide to the  $EE_2$  nanoparticles dispersed in water followed by removal of excess dye by dialysis. The band at 563 nm and the shoulder at 600 nm are characteristic for the cyanine-3 dye as shown in Figure 28 (see page 44).

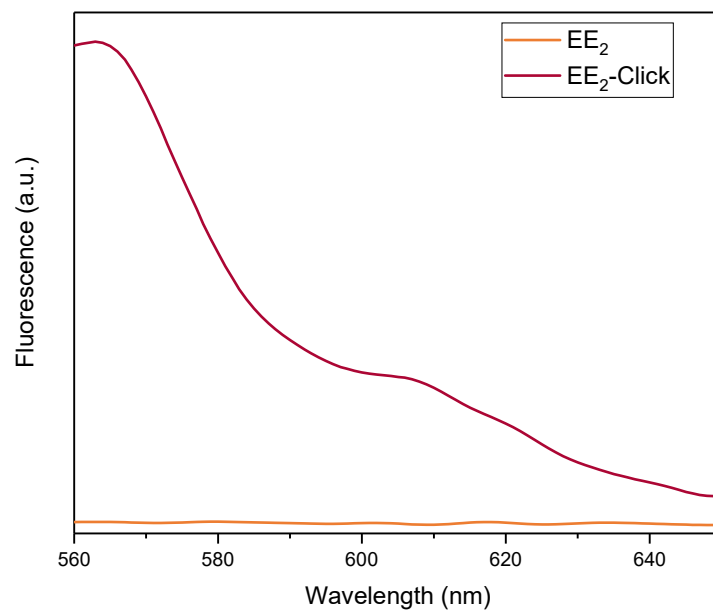


Figure 111. Fluorescence spectra prior and subsequent to click reaction of EE<sub>2</sub> particle dispersion with sulfo-cyanine-3-azide. The orange curve shows the pure EE<sub>2</sub> particles prior to the click reaction. Here, no significant fluorescence signal is visible. The red curve shows the reaction mixture after dialysis and washing of excess dye. The band at 563 nm and the shoulder at 600 nm are characteristic for the cyanine-3 dye as shown in Figure 28.

Stamping of EE<sub>2</sub> resulted in small, uniform particles in a hexagonal pattern over a large surface area. After detachment of the EE<sub>2</sub> particles from the substrate and dispersion into aqueous solution, the dispersion stability was measured with DLS and remained unchanged for one hour, whereas within 24 hours, the original obtained particle sizes could be recovered by sonication. The EE<sub>2</sub> particles do not dissolve in water and remain particulate even after re-precipitation on a substrate surface. The successful copper-free click reaction with the fluorescent dye sulfo-cyanine-3-azide shows the remaining accessibility of the EE<sub>2</sub> particles within aqueous solution.

## 5 Conclusion and outlook

The method of capillary nanostamping with spongy mesoporous silica stamps was developed and carried out within this work. Typical disadvantages of commonly used state-of-the-art methods are large sizes of the obtained stamped structures, the limitation of water as solvent, a non-continuous stamping procedure and defined temperature, humidity or vacuum conditions during stamping. To overcome these disadvantages, mesoporous silica stamps were synthesized in a sol-gel process. The spongy mesoporous silica stamps withstand the contact with organic solvents and provide a large variety of usable inks. The pore system of the stamp serves as ink reservoir due to the porous network of the silica. Therefore, the stamp can be used in a continuous stamping procedure without the need of refilling the stamp or can be refilled through the pore system without significant interruption of the stamping process. The infiltration with ink and the stamping process itself are non-complicated, inexpensive procedures and can be performed under ambient conditions manually by hand.

The development of silica stamps resulted in spongy, flexible silica stamps with a high mechanical stability, due to a less interconnectivity of the silica within the network. The generation of a manual stamping procedure under ambient conditions was carried out by creating a stamp holder with an elastomeric PDMS layer between the stamp holder and the stamp.

To proof the method of capillary nanostamping with spongy mesoporous silica stamps, several different model inks with regard to a possible application were used in a stamping process.

C<sub>60</sub> fullerenes serve as a model for endohedral fullerenes and were stamped from toluene onto FDTS-functionalized glass with dry stamps. The stamping resulted in hexagonally ordered C<sub>60</sub> particles with diameters of  $123 \pm 22$  nm and a height of 50-70 nm over a large surface area. The precipitation process during stamping followed a mechanism, where the non-volatile ink component was enriched during stamping within the meniscus between the stamp's contact elements and the substrate surface. As the volatile solvent evaporates during stamping, more ink is driven through the capillaries onto the substrate surface. The non-volatile ink component enriched during stamping, and due to a higher affinity to itself than to the substrate surface, formed small, discrete particles of C<sub>60</sub> fullerenes.

1-Dodecanethiol is a model for functional thiols, which was stamped in a self-limited spreading process from ethanol onto gold-coated substrate surfaces. The ink consisting



of 1-dodecanethiol in ethanol had a high affinity to the gold-coated surface and thus, ink spreading was expectable. Nevertheless, full ink spreading was prevented as the contact angle of ethanol changed from  $0^\circ$  on pure gold to  $34^\circ$  on a layer of 1-dodecanethiol. The stamped spots had a diameter of  $757 \pm 25$  nm with a height of 15-20 nm. As application, the created heterogeneous surface was used in a dewetting experiment. The dewetting process of polystyrene began by the formation of holes on the spots, where the 1-dodecanethiol was stamped as the polystyrene selectively wets the gold; proceeded by forming honeycomb-shaped structures of polystyrene around the stamped spots, and finally continued until single polystyrene dots appeared in the gaps between adjacent 1-dodecanethiol spots.

Nanodiamonds were stamped to analyze particulate inks within capillary nanostamping. Nanodiamonds with sizes of 10 nm were stamped from isopropanol onto FDTs-functionalized glass. For this purpose, dry stamps were used and infiltrated from the backside to prevent larger aggregates of nanodiamonds to precipitate onto the substrate surface, as nanodiamonds in isopropanol do not maintain a stable dispersion. The stamping resulted in hexagonally arranged nanodiamond-clusters with diameters of  $43 \pm 25$  nm and a height of 30-50 nm, which indicates only a few nanodiamonds per spot. ODMR and  $T_1$  relaxation measurements were carried out to successfully prove the existence of NV-centers within the stamped nanodiamonds. As nanodiamonds are applicable for further functionalization, a copper-free click reaction was carried out with nanodiamonds with sizes of 5 nm and cyanine-3-DBCO. Here, the nanodiamonds were functionalized to obtain azide residues on the nanodiamond surface and subsequently stamped onto a substrate. The click reaction was carried out with the stamped nanodiamond-clusters to obtain a functionalized substrate surface. The successful click reaction could be proven by fluorescence spectroscopy of the stamped and functionalized nanodiamond-clusters.

A commercially available cyclo olefin polymer, Zeonex, was stamped from toluene/chloroform onto FDTs-functionalized glass and yielded highly uniform particles with diameters of  $91 \pm 16$  nm and a height of 25-30 nm. This material is mainly used to generate lenses, which could be used to create patterned surfaces of a lens material. The stamping of Zeonex followed the precipitation process of ink with higher affinity to itself than to the substrate and proved the applicability of stamping of polymers with capillary nanostamping.

Block copolymers are mostly soluble in organic solvents, which makes it difficult to print with state-of-the-art methods. Capillary nanostamping with spongy mesoporous silica stamps is a good method to generate surfaces patterned with block copolymers. PS-*b*-

P2VP was chosen for its capability of solvent-induced morphology reorganization. A solution of PS-*b*-P2VP in toluene/chloroform was stamped onto four differently functionalized substrate surfaces and subsequently, a solvent treatment with ethanol was carried out. Hydroxyl-terminated, FDTS-, ATAS-, and DMDCS-functionalized surfaces were used as substrates and resulted in structures with diameters between 140 and 730 nm, dependent on the surface properties. Stamping and subsequent solvent treatment of PS-*b*-P2VP on hydroxyl-terminated glass amounted to porous structures, where the PS-*b*-P2VP underwent a morphology reorganization. While the PS block remained glassy, the P2VP block became mobile and formed a layer around the PS block, exposing the morphology formed on the substrate surface. The interactions between the silane-functionalized substrates and the PS-*b*-P2VP were weaker than for the hydroxyl-terminated substrate. Therefore, the mobility of the PS-*b*-P2VP increased during solvent treatment. As a result non-porous, smaller and denser particles were formed. Stamping of PS-*b*-P2VP onto FDTS- and ATAS-functionalized substrates resulted in well-ordered and small particles. From stamping of PS-*b*-P2VP onto DMDCS-functionalized substrates, only a small ordered area with larger particles showing terracing behavior, could be obtained.

PFS-*b*-P2VP was stamped from toluene/chloroform onto hydroxyl-terminated and FDTS-functionalized glass. The stamping resulted in structures with diameters of  $571 \pm 41$  nm and  $606 \pm 42$  nm for hydroxyl-terminated and FDTS-functionalized glass, respectively. PFS-*b*-P2VP was stamped onto FDTS-functionalized quartz and pyrolyzed, resulting in ceramic particles with significantly decreased sizes of  $90 \pm 37$  nm. This was used to create structured ceramic particles for the growth of carbon nanotubes.

17 $\alpha$ -Ethinylestradiol was used as a model molecule for poorly water-soluble drugs, which are difficult in formulation and clinical efficiency. 17 $\alpha$ -Ethinylestradiol was stamped from acetonitrile onto FDTS-functionalized glass and resulted in hexagonally arranged discrete particles with diameters of  $123 \pm 19$  nm and a height of 10-12 nm. A detachment by sonication was carried out to obtain a dispersion of 17 $\alpha$ -ethinylestradiol particles in aqueous solution. The solution was stable for one hour without any additional stabilization and remained particulate even after re-precipitation. To proof the remaining accessibility of the terminal triple bond of 17 $\alpha$ -ethinylestradiol within the particles, a copper-free click reaction with sulfo-cyanine-3-azide was carried out successfully.

In total, seven different model inks were successfully stamped with spongy mesoporous silica stamps in a capillary nanostamping procedure under ambient conditions. This proves not only the applicability of this method, but also the flexibility in the ink selection. Particulate inks, dissolved molecular inks, as well as polymeric ink solutions could be transferred into hexagonally ordered arrays onto counterpart substrate surfaces. The

method of capillary nanostamping with spongy mesoporous silica stamps was developed and proven to work. It provides a new lithographic method and can be used in a manual stamping procedure under ambient conditions. Neither temperature, nor humidity have to be defined. The stamps can be used dry or can be kept wet after the synthesis for a variety of different stamping approaches and the simultaneous use of the stamp's pore system as a size filter for particulate inks. The synthesis of the stamps is easy, cost inexpensive and relatively fast. With variable stamp sizes, large surface areas in the mm size range can be patterned with obtaining structures down to  $\approx 40$  nm in size in one stamping cycle. The stamp's bulk structure serves as ink reservoir and ensures a continuous stamping process of up to 10 cycle times without the need of refilling. When kept within the ink, the stamp can be used for several weeks in an unlimited number of stamping cycles.

In the future, a huge variety of ink systems and their individual applications could be stamped and used as e.g. sensors, to generate heterogeneous surfaces or for further chemical modifications.

## 6 Appendix

### 6.1 List of abbreviations

The following abbreviations are used in this work.

$\mu$ CP	Microcontact printing
2D	Two dimensional
3D	Three dimensional
AFM	Atomic Force Microscopy
API	Active pharmaceutical ingredient
ATAS	N-(2-aminoethyl)-2,2,4-trimethyl-1-aza-2-silacyclopentane
BET	Brunauer-Emmett-Teller
$\text{BH}_3 \cdot \text{THF}$	Borane–tetrahydrofuran
BJH	Barret, Joyner and Halenda
CNT	Carbon nanotube
$\text{CO}_2$	Carbon Dioxide
COP	Cyclo olefin polymer
CPD	Critical Point Drying
DBCO	Dibenzocyclooctyne
DLS	Dynamic Light Scattering
DMDCS	Dimethyldichloro silane
DMF	Dimethylformamide
DNA	Deoxyribonucleic acid
DPN	Dip pen nanolithography
DUV	Deep ultraviolet
EDX	Energy dispersive X-ray spectroscopy
$\text{EE}_2$	Ethinylestradiol
e.g.	For example
FDTS	1H,1H,2H,2H-Perfluorodecyltrichlorosilane
FIB	Focused Ion Beam
H/L	Height/Length

HPLC	High-performance liquid chromatography
KOH	Potassium hydroxide
$M_n$	Average molecular mass by number
$M_w$	Average molecular mass by weight
MCM-41	Mobile Composition of Mater No. 41
MIMIC	Micromolding in Capillaries
mSi	Macroporous Silicon
MTMS	Methyltrimethoxy silane
NADIS	Nanoscale dispensing
$\text{NaN}_3$	Sodium azide
ND	Nanodiamond
$\text{NH}_4\text{OH}$	Ammonia hydroxide
ODMR	Optically Detected Magnetic Resonance
OLED	Organic light emitting diode
OPV	Organic photovoltaic
ORMOSIL	Organically modified silica
PDMS	Polydimethylsiloxane
PDI	Polydispersity index
PEO/PEG	Polyethylene oxide/glycol
PFS- <i>b</i> -P2VP	Polyferrocenyl(dimethylsilane)-block-poly(2-vinylpyridine)
PMMA	Poly(methyl methacrylate)
PS	Polystyrene
PS- <i>b</i> -P2VP	Polystyrene-block-poly(2-vinylpyridine)
RIE	Reactive ion etching
SEM	Scanning Electron Microscopy
SESI	Secondary electron chamber detector (SEM)
TEOS	Tetraethyl orthosilicate
$T_g$	Glass Transition Temperature
$\text{TiCl}_4$	Titanium tetrachloride
UV-Vis	Ultraviolet visible (spectroscopy)



## 6.2 Publication list

Parts of this work were published according to the following references.

### 6.2.1 Publications as first author

Mercedes Schmidt, Michael Philippi, Maximilian Münzner, Johannes M. Stangl, René Wieczorek, Wolfgang Harneit, Klaus Müller-Buschbaum, Dirk Enke, Martin Steinhart, *Capillary Nanostamping with spongy mesoporous silica stamps*, **Adv. Funct. Mater.** **2018**, **28**, **1800700**, DOI: 10.1002/adfm.201800700.

See chapters 4.1 (page 45), 4.2.1 (page 60) and 4.2.2 (page 66).

Mercedes Schmidt, Martin Steinhart, *Forming water-insoluble drugs to discrete nanoparticles by capillary nanostamping*, in preparation, 2019.

See chapter 4.2.7 (page 118).

Mercedes Schmidt, Gririraj Manoharan, René Wieczorek, Michael Philippi, Hanna Hübner, Markus Gallei, Wolfgang Harneit, Carola Meyer, Martin Steinhart, *Capillary nanostamping of block copolymers* (preliminary title), in preparation, 2019.

See chapters 4.2.5 (page 89) and 4.2.6 (page 106).

Mercedes Schmidt, René Wieczorek, Wolfgang Harneit, Martin Steinhart, *Capillary nanostamping of nanodiamonds* (preliminary title), in preparation, 2019.

See chapter 4.2.3 (page 74).

### 6.2.2 Publications as co-author

M. Philippi, C. You, C. Richter, M. Schmidt, D. Liße, J. Piehler, M. Steinhart, *Close-Packed Silane Nanodot Arrays by Capillary Nanostamping Coupled with Heterocyclic Silane Click Chemistry*, in preparation, 2019.

H. Schäfer, K. Küpper, M. Schmidt, K. Müller-Buschbaum, J. Stangl, D. Daum, M. Steinhart, C. Schulz-Kölbel, W. Han, J. Wollschläger, U. Krupp, P. Hou, X. Liu, *Steel-based electrocatalysts for efficient and durable oxygen evolution in acidic media*, **Catal. Sci. Technol.**, **2018**, **8**, **2104-2116**, DOI: 10.1039/c7cy02194a.

H. Schäfer, K. Küpper, K. Müller-Buschbaum, D. Daum, M. Steinhart, J. Wollschläger, U. Krupp, M. Schmidt, W. Han, J. Stangl, *Electro-oxidation of a cobalt based steel in*

*LiOH: a non-noble metal based electro-catalyst suitable for durable water-splitting in an acidic milieu*, **Nanoscale**, **2017**, **9**, **17829-17838**, DOI: 10.1039/c7nr06527b.

H. Schäfer, D. M. Chevrier, K. Kuepper, P. Zhang, J. Wollschlaeger, D. Daum, M. Steinhart, C. Heß, U. Krupp, K. Müller-Buschbaum, J. Stangl, M. Schmidt, *X<sub>20</sub>CoCrWMo<sub>10-9</sub>/Co<sub>3</sub>O<sub>4</sub>: a metal-ceramic composite with unique efficiency values for water-splitting in the neutral regime*, **Energy Environ. Sci.**, **2016**, **9**, **2609-2622**, DOI: 10.1039/c6ee01304j.

H. Schäfer, D. M. Chevrier, P. Zhang, J. Stangl, K. Müller-Buschbaum, J. D. Hardege, K. Kuepper, J. Wollschläger, U. Krupp, S. Dühnen, M. Steinhart, L. Walder, S. Sadaf, M. Schmidt, *Electro-Oxidation of Ni<sub>42</sub> Steel: A Highly Active Bifunctional Electrocatalyst*, **Adv. Funct. Mater.** **2016**, **26**, **6402-6417**, DOI: 10.1002/adfm.201601581.

### 6.3 Curriculum vitae

- 10/15 - 05/19      **University Osnabrück**  
Department of Chemistry – Physical Chemistry  
**PhD in Chemistry**  
Dissertation: „Capillary nanostamping with spongy mesoporous silica stamps“
- 10/11 - 03/14      **University Ulm**  
Department of Chemistry  
**M.Sc. Chemistry**  
Master program with specialization in Inorganic, Analytical and Organic Chemistry  
  
Master's thesis: „Detailed evaluation of adsorption processes on mesoporous materials“  
  
Graduation: **Master of Science**
- 10/07 - 09/11      **University Ulm**  
Department of Chemistry  
**B.Sc. Chemistry**  
Scientific program in the fields of Chemistry, Physics, Mathematics with specialization in Analytical and Inorganic Chemistry  
  
Bachelor's thesis: „Click-chemistry-based functionalization of nanostructured silica materials“  
  
Graduation: **Bachelor of Science**
- 1996 - 2005      **Dietrich-Bonhoeffer-Gymnasium Metzingen**  
Graduation: **General matriculation standard**

## 7 References

- [1] S. R. Forrest, "The Path to Ubiquitous and Low-Cost Organic Electronic Appliances on Plastic," *Nature* **2004**, 428, 911.
- [2] B. A. Yamashita, T. Hayashi, "Organic Molecular Beam Deposition of Metallophthalocyanines for Opto-Electronics Applications," *Adv. Mater* **1996**, 8, 791.
- [3] Y. Dong, C. Shannon, "Heterogeneous Immunosensing Using Antigen and Antibody Monolayers on Gold Surfaces with Electrochemical and Scanning Probe Detection," *Anal. Chem.* **2000**, 72, 2371.
- [4] H. E. Maes, C. Claeys, R. Mertens, A. Campitelli, C. Van Hoof, J. De Boeck, "Trends in Microelectronics, Optical Detectors, and Biosensors," *Adv. Eng. Mater.* **2001**, 3, 781.
- [5] B. Schwarz, P. Reininger, D. Ristanic, H. Detz, A. M. Andrews, W. Schrenk, G. Strasser, "Monolithically Integrated Mid-Infrared Lab-on-a-Chip Using Plasmonic and Quantum Cascade Structures," *Nat. Commun.* **2014**, 5:4085, 1.
- [6] E. B. Cooper, S. R. Manalis, H. Fang, H. Dai, K. Matsumoto, S. C. Minne, T. Hunt, C. F. Quate, "Terabit-per-Square-Inch Data Storage with the Atomic Force Microscope," *Appl. Phys. Lett.* **1999**, 75, 3566.
- [7] Y. Xia, G. M. Whitesides, "Soft Lithography," *Annu. Rev. Mater. Sci.* **1998**, 28, 153.
- [8] F. Huo, Z. Zheng, G. Zheng, L. R. Giam, H. Zhang, C. A. Mirkin, "Polymer Pen Lithography," *Science* **2008**, 321, 1658.
- [9] Z. Xie, C. Chen, X. Zhou, T. Gao, D. Liu, Q. Miao, Z. Zheng, "Massively Parallel Patterning of Complex 2D and 3D Functional Polymer Brushes by Polymer Pen Lithography," *ACS Appl. Mater. Interfaces* **2014**, 6, 11955.
- [10] M. Ganesh, J. Nachman, Z. Mao, A. Lyons, M. Rafailovich, R. Gross, "Patterned Enzymatic Degradation of Poly( $\epsilon$ -Caprolactone) by High-Affinity Microcontact Printing and Polymer Pen Lithography," *Biomacromolecules* **2013**, 14, 2470.
- [11] C. Vieu, F. Carcenac, A. Pepin, Y. Chen, M. Mejias, A. Lebib, L. Manin-Ferlazzo, L. Couraud, H. Launois, "Electron Beam Lithography - Resolution Limits and Applications," *Appl. Surf. Sci.* **2000**, 164, 111.
- [12] S. Reyntjens, R. Puers, "A Review of Focused Ion Beam Applications in Microsystems Technology," *J. Micromechanics Microengineering* **2001**, 11, 287.
- [13] R. D. Piner, J. Zhu, F. Xu, S. H. Hong, C. A. Mirkin, "'Dip-Pen' Nanolithography," *Science* **1999**, 283, 661.

- 
- [14] P. Vettiger, M. Despont, U. Drechsler, U. Dürig, W. Häberle, M. I. Lutwyche, H. E. Rothuizen, R. Stutz, R. Widmer, G. K. Binnig, "The 'Millipede' - More than One Thousand Tips for Future AFM Data Storage," *IBM J. Res. Dev.* **2000**, *44*, 323.
- [15] D. Wouters, U. S. Schubert, "Constructive Nanolithography and Nanochemistry: Local Probe Oxidation and Chemical Modification," *Langmuir* **2003**, *19*, 9033.
- [16] J. Chai, F. Huo, Z. Zheng, L. R. Giam, W. Shim, C. A. Mirkin, "Scanning Probe Block Copolymer Lithography," *Proc. Natl. Acad. Sci. U.S.A.* **2010**, *107*, 20202.
- [17] A. Meister, M. Liley, J. Brugger, R. Pugin, H. Heinzelmann, "Nanodispenser for Attoliter Volume Deposition Using Atomic Force Microscopy Probes Modified by Focused-Ion-Beam Milling," *Appl. Phys. Lett.* **2004**, *85*, 6260.
- [18] L. Fabie, T. Ondarcuhu, L. Fabi, T. Ondarc, "Writing with Liquid Using a Nanodispenser: Spreading Dynamics at the Sub-Micron Scale," *Soft Matter* **2012**, *8*, 4995.
- [19] A. Fang, E. Dujardin, T. Ondarcuhu, "Control of Droplet Size in Liquid Nanodispersing," *Nano Lett.* **2006**, *6*, 2368.
- [20] S. G. Vengasandra, M. Lynch, J. T. Xu, E. Henderson, "Microfluidic Ultramicroscale Deposition and Patterning of Quantum Dots," *Nanotechnology* **2005**, *16*, 2052.
- [21] S. Deladi, J. W. Berenschot, N. R. Tas, G. J. M. Krijnen, J. H. de Boer, M. J. de Boer, M. C. Elwenspoek, "Fabrication of Micromachined Fountain Pen with in Situ Characterization Possibility of Nanoscale Surface Modification," *J. Micromech. Microeng.* **2005**, *15*, 528.
- [22] R. F. Pease, S. Y. Chou, "Lithography and Other Patterning Techniques for Future Electronics," *Proc. IEEE* **2008**, *96*, 248.
- [23] J. Sun, N. M. Litchinitser, "Toward Practical, Subwavelength, Visible-Light Photolithography with Hyperlens," *ACS Nano* **2018**, *12*, 542.
- [24] K. Brower, A. K. White, P. M. Fordyce, "Multi-Step Variable Height Photolithography for Valved Multilayer Microfluidic Devices," *J. Vis. Exp.* **2017**, 55276.
- [25] K. Jain, C. G. Willson, B. J. Lin, "Ultrafast Deep UV Lithography with Excimer Lasers," *IEEE Electron Device Lett.* **1982**, *3*, 1981.
- [26] K. Q. Peng, X. Wang, X. Wu, S. T. Lee, "Fabrication and Photovoltaic Property of Ordered Macroporous Silicon," *Appl. Phys. Lett.* **2009**, *95*, 93.
- [27] D. Qin, Y. Xia, G. M. Whitesides, "Rapid Prototyping of Complex Structures with Feature Sizes Larger than 20 Mm," *Adv. Mater* **1996**, *8*, 917.
-

- [28] C. L. Haynes, R. P. Van Duyne, "Nanosphere Lithography: A Versatile Nanofabrication Tool for Studies of Size-Dependent Nanoparticle Optics," *J. Phys. Chem. B* **2001**, *105*, 5599.
- [29] J. C. Hulteen, R. P. Van Duyne, "Nanosphere Lithography: A Materials General Fabrication Process for Periodic Particle Array Surfaces," *J. Vac. Sci. Technol. A Vacuum, Surfaces, Film.* **1995**, *13*, 1553.
- [30] S. B. Darling, "Directing the Self-Assembly of Block Copolymers," *Prog. Polym. Sci.* **2007**, *32*, 1152.
- [31] A. Knoll, A. Horvat, K. S. Lyakhova, G. Krausch, G. J. A. Sevink, A. V Zvelindovsky, R. Magerle, "Phase Behavior in Thin Films of Cylinder-Forming Block Copolymers," *Phys. Rev. Lett.* **2002**, *89*, 1.
- [32] S. Jeong, J. Y. Kim, B. H. Kim, H. Moon, S. O. Kim, "Directed Self-Assembly of Block Copolymers for next Generation Nanolithography," *Mater. Today* **2013**, *16*, 468.
- [33] L. Wan, R. Ruiz, H. Gao, K. C. Patel, T. R. Albrecht, "The Limits of Lamellae-Forming PS-b-PMMA Block Copolymers for Lithography," *ACS Nano* **2015**, *9*, 7506.
- [34] D. Qin, Y. Xia, G. M. Whitesides, "Soft Lithography for Micro- and Nanoscale Patterning," *Nat. Protoc.* **2010**, *5*, 491.
- [35] P. J. Yoo, S. Choi, J. H. Kim, D. Suh, S. J. Baek, T. W. Kim, H. H. Lee, "Unconventional Patterning with A Modulus-Tunable Mold: From Imprinting to Microcontact Printing," *Chem. Mater.* **2004**, *16*, 5000.
- [36] S. Y. Chou, P. R. Krauss, "Imprint Lithography with Sub-10nm Feature Size and High Throughput," *Microelectron. Eng.* **1997**, *35*, 237.
- [37] Y. N. Xia, G. M. Whitesides, "Soft Lithography," *Angew. Chem. Int. Ed.* **1998**, *28*, 550.
- [38] E. Kim, Y. Xia, G. M. Whitesides, "Polymer Microstructures Formed by Moulding in Capillaries," *Nature* **1995**, *376*, 581.
- [39] M. Cavallini, C. Albonetti, F. Biscarini, "Nanopatterning Soluble Multifunctional Materials by Unconventional Wet Lithography," *Adv. Mater* **2009**, *21*, 1043.
- [40] M. Cavallini, E. Bystrenova, M. Timko, M. Koneracka, V. Zavisova, P. Kopcansky, "Multiple-Length-Scale Patterning of Magnetic Nanoparticles by Stamp Assisted Deposition," *J. Phys. Condens. Matter Condens. Matter* **2008**, *20*, 204144.
- [41] J. Hu, R. G. Beck, T. Deng, R. M. Westervelt, K. D. Maranowski, A. C. Gossard, G. M. Whitesides, "Using Soft Lithography to Fabricate GaAs/AlGaAs Heterostructure Field Effect Transistors," *Appl. Phys. Lett.* **1997**, *71*, 2020.



- 
- [42] K. Y. Suh, Y. S. Kim, H. H. Lee, "Capillary Force Lithography," *Adv. Mater.* **2001**, *13*, 1386.
- [43] D. Ho, J. Zou, B. Zdyrko, K. S. Iyer, I. Luzinov, "Capillary Force Lithography: The Versatility of This Facile Approach in Developing Nanoscale Applications," *Nanoscale* **2015**, *7*, 401.
- [44] H. L. Zhang, D. G. Bucknall, A. Dupuis, "Uniform Nanoscopic Polystyrene Patterns Produced from a Microscopic Mold," *Nano Lett.* **2004**, *4*, 1513.
- [45] K. Y. Suh, H. H. Lee, "Capillary Force Lithography: Large-Area Patterning, Self-Organization, and Anisotropic Dewetting," *Adv. Funct. Mater.* **2002**, *12*, 405.
- [46] B. Zdyrko, M. K. Kinnan, G. Chumanov, I. Luzinov, "Fabrication of Optically Active Flexible Polymer Films with Embedded Chain-like Arrays of Silver Nanoparticles," *Chem. Commun.* **2008**, 1284.
- [47] K. A. Moga, L. R. Bickford, R. D. Geil, S. S. Dunn, A. A. Pandya, Y. Wang, J. H. Fain, C. F. Archuleta, A. T. O'Neill, J. M. DeSimone, "Rapidly-Dissolvable Microneedle Patches via a Highly Scalable and Reproducible Soft Lithography Approach," *Adv. Mater.* **2013**, *25*, 5060.
- [48] D. H. Kim, P. Kim, I. Song, J. M. Cha, S. H. Lee, B. Kim, K. Y. Suh, "Guided Three-Dimensional Growth of Functional Cardiomyocytes on Polyethylene Glycol Nanostructures," *Langmuir* **2006**, *22*, 5419.
- [49] J. M. Jung, F. Stellacci, H. T. Jung, "Generation of Various Complex Patterned Structures from a Single Ellipsoidal Dot Prepattern by Capillary Force Lithography," *Adv. Mater.* **2007**, *19*, 4392.
- [50] N. Kooy, K. Mohamed, L. T. Pin, O. S. Guan, "A Review of Roll-to-Roll Nanoimprint Lithography," *Nanoscale Res. Lett.* **2014**, *9*, 320.
- [51] A. del Campo, E. Arzt, "Fabrication Approaches for Generating Complex Micro- and Nanopatterns on Polymeric Surfaces," *Chem. Rev.* **2008**, *108*, 911.
- [52] A. Perl, D. N. Reinhoudt, J. Huskens, "Microcontact Printing: Limitations and Achievements," *Adv. Mater.* **2009**, *21*, 2257.
- [53] T. Kaufmann, B. J. Ravoo, "Stamps, Inks and Substrates: Polymers in Microcontact Printing," *Polym. Chem.* **2010**, *1*, 371.
- [54] X. Y. Ling, I. Y. Phang, D. N. Reinhoudt, G. J. Vancso, J. Huskens, "Transfer-Printing and Host-Guest Properties of 3D Supramolecular Particle Structures," *ACS Appl. Mater. Interfaces* **2009**, *1*, 960.
-

- [55] A. Carlson, A. M. Bowen, Y. Huang, R. G. Nuzzo, J. A. Rogers, "Transfer Printing Techniques for Materials Assembly and Micro/Nanodevice Fabrication," *Adv. Mater.* **2012**, *24*, 5284.
- [56] H. Wu, L. Wu, X. Zhou, B. Liu, B. Zheng, "Patterning Hydrophobic Surfaces by Negative Microcontact Printing and Its Applications," *Small* **2018**, *1802128*, 1.
- [57] J. Yao, X. Yan, G. Lu, K. Zhang, X. Chen, L. Jiang, B. Yang, "Patterning Colloidal Crystals by Lift-up Soft Lithography," *Adv. Mater.* **2004**, *16*, 81.
- [58] A. B. Braunschweig, F. Huo, C. A. Mirkin, "Molecular Printing," *Nat. Chem.* **2009**, *1*, 353.
- [59] S. W. Chung, D. S. Ginger, M. W. Morales, Z. Zhang, V. Chandrasekhar, M. A. Ratner, C. A. Mirkin, "Top-down Meets Bottom-up: Dip-Pen Nanolithography and DNA-Directed Assembly of Nanoscale Electrical Circuits," *Small* **2005**, *1*, 64.
- [60] K. Salaita, Y. Wang, C. A. Mirkin, "Applications of Dip-Pen Nanolithography," *Nat. Nanotechnol.* **2007**, *2*, 145.
- [61] F. Brinkmann, M. Hirtz, A. M. Greiner, M. Weschenfelder, B. Waterkotte, M. Bastmeyer, H. Fuchs, "Interdigitated Multicolored Bioink Micropatterns by Multiplexed Polymer Pen Lithography," *Small* **2013**, *9*, 3266.
- [62] C. J. Brinker, G. W. Scherer, "Sol-Gel Science," Academic Press, Inc., **1990**.
- [63] V. Alfredsson, M. W. Anderson, "Structure of MCM-48 Revealed by Transmission Electron Microscopy," *Chem. Mater.* **1996**, *8*, 1141.
- [64] Q. Cai, W.-Y. Lin, F.-S. Xiao, W.-Q. Pang, X.-H. Chen, B.-S. Zou, "The Preparation of Highly Ordered MCM-41 with Extremely Low Surfactant Concentration," *Microporous Mesoporous Mater.* **1999**, *32*, 1.
- [65] M. J. van Bommel, A. B. de Haan, "Drying of Silica Gels with Supercritical Carbon Dioxide," *J. Mater. Sci.* **1994**, *29*, 943.
- [66] J. L. Rousset, A. Boukenter, B. Champagnon, J. Dumas, E. Duval, J. F. Quinson, J. Serughetti, "Granular Structure and Fractal Domains of Silica Aerogels," *J. Phys. Condens. Matter* **1990**, *2*, 8445.
- [67] G. M. Pajonk, T. Manzalji, "Synthesis of Acrylonitrile from Propylene and Nitric Oxide Mixtures on PbO<sub>2</sub>-ZrO<sub>2</sub> Aerogel Catalysts," *Catal. Letters* **1993**, *21*, 361.
- [68] J. L. Gurav, I.-K. Jung, H.-H. Park, E. S. Kang, D. Y. Nadargi, "Silica Aerogel: Synthesis and Applications," *J. Nanomater.* **2010**, *2010*, 1.
- [69] H. Maleki, L. Duraes, A. Portugal, "An Overview on Silica Aerogels Synthesis and

- Different Mechanical Reinforcing Strategies,” *J. Non. Cryst. Solids* **2014**, *385*, 55.
- [70] A. Zukal, M. Thommes, J. Čejka, “Synthesis of Highly Ordered MCM-41 Silica with Spherical Particles,” *Microporous Mesoporous Mater.* **2007**, *104*, 52.
- [71] N. Hüsing, U. Schubert, “Aerogele - Luftige Materialien. Chemie, Struktur Und Eigenschaften,” *Angew. Chemie* **1998**, *110*, 22.
- [72] J. Babin, J. Iapichella, B. Lefevre, C. Biolley, J.-P. Bellat, F. Fajula, A. Galarneau, “MCM-41 Silica Monoliths with Independent Control of Meso- and Macroporosity,” *New J. Chem.* **2007**, *31*, 1.
- [73] Z. Zhang, J. Shen, X. Ni, G. Wu, B. Zhou, M. Yang, X. Gu, M. Qian, Y. Wu, “Hydrophobic Silica Aerogels Strengthened with Nonwoven Fibers,” *J. Macromol. Sci. Part A* **2006**, *43*, 1663.
- [74] A. V. Rao, M. M. Kulkarni, G. M. Pajonk, D. P. Amalnerkar, T. Seth, “Synthesis and Characterization of Hydrophobic Silica Aerogels Using Trimethylethoxysilane as a Co-Precursor,” *J. Sol-Gel Sci. Technol.* **2003**, *27*, 103.
- [75] M. Ochoa, L. Durães, A. M. Beja, A. Portugal, “Study of the Suitability of Silica Based Xerogels Synthesized Using Ethyltrimethoxysilane and/or Methyltrimethoxysilane Precursors for Aerospace Applications,” *J. Sol-Gel Sci. Technol.* **2012**, *61*, 151.
- [76] K. Kanamori, M. Aizawa, K. Nakanishi, T. Hanada, “New Transparent Methylsilsesquioxane Aerogels and Xerogels with Improved Mechanical Properties,” *Adv. Mater.* **2007**, *19*, 1589.
- [77] S. Grimm, A. Lange, D. Enke, M. Steinhart, J. M. Chem, S. Grimm, A. Lange, M. Steinhart, D. Enke, M. Steinhart, “Imprinting Macropore Arrays into Mesoporous Silica Monoliths,” *J. Mater. Chem.* **2012**, *22*, 9490.
- [78] E. P. Barrett, L. G. Joyner, P. P. Halenda, “The Determination of Pore Volume and Area Distributions in Porous Substances. I. Computations from Nitrogen Isotherms,” *J. Am. Chem. Soc.* **1951**, *73*, 373.
- [79] J. M. Binder, A. Stark, N. Tomek, J. Scheuer, F. Frank, K. D. Jahnke, C. Müller, S. Schmitt, M. H. Metsch, T. Uden, T. Gehring, A. Huck, U. L. Andersen, L. J. Rogers, F. Jelezko, “Qudi: A Modular Python Suite for Experiment Control and Data Processing,” *SoftwareX* **2017**, *6*, 85.
- [80] L. Papula, “Mathematische Formelsammlung,” Vieweg+Teubner Verlag, **2003**.
- [81] H. Schäfer, B. Milow, L. Ratke, “Synthesis of Inorganic Aerogels via Rapid Gelation Using Chloride Precursors,” *RSC Adv.* **2013**, *3*, 15263.

- [82] Y. Xia, X.-M. Zhao, E. Kim, G. M. Whitesides, "A Selective Etching Solution for Use with Patterned Self-Assembled Monolayers of Alkanethiolates on Gold," *Chem. Mater.* **1995**, *7*, 2332.
- [83] T. Meinhardt, D. Lang, H. Dill, A. Krueger, "Pushing the Functionality of Diamond Nanoparticles to New Horizons: Orthogonally Functionalized Nanodiamond Using Click Chemistry," *Adv. Funct. Mater.* **2011**, *21*, 494.
- [84] R. D. Akiel, X. Zhang, C. Abeywardana, V. Stepanov, P. Z. Qin, S. Takahashi, "Investigating Functional DNA Grafted on Nanodiamond Surface Using Site-Directed Spin Labeling and Electron Paramagnetic Resonance Spectroscopy," *J. Phys. Chem. B* **2016**, *120*, 4003.
- [85] E. E. Romanova, R. Akiel, F. H. Cho, S. Takahashi, "Grafting Nitroxide Radicals on Nanodiamond Surface Using Click Chemistry," *J. Phys. Chem. A* **2013**, *117*, 11933.
- [86] A. Krüger, Y. Liang, G. Jarre, J. Stegk, "Surface Functionalisation of Detonation Diamond Suitable for Biological Applications," *J. Mater. Chem.* **2006**, *16*, 2322.
- [87] Z. Wang, X. Yao, Y. Wang, "Swelling-Induced Mesoporous Block Copolymer Membranes with Intrinsically Active Surfaces for Size-Selective Separation," *J. Mater. Chem.* **2012**, *22*, 20542.
- [88] C. Spudat, C. Meyer, K. Goss, C. M. Schneider, "Peapod Synthesis Depending on the Number of Nanotube Sidewalls," *Phys. Status Solidi Basic Res.* **2009**, *246*, 2498.
- [89] M. Thommes, K. Kaneko, A. V. Neimark, J. P. Olivier, F. Rodriguez-Reinoso, J. Rouquerol, K. S. W. Sing, "Physisorption of Gases, with Special Reference to the Evaluation of Surface Area and Pore Size Distribution (IUPAC Technical Report)," *Pure Appl. Chem.* **2015**, *87*, 1051.
- [90] J. Konishi, K. Fujita, K. Nakanishi, K. Hirao, "Phase-Separation-Induced Titania Monoliths with Well-Defined Macropores and Mesosstructured Framework from Colloid-Derived Sol-Gel Systems," *Chem. Mater.* **2006**, *18*, 864.
- [91] J. Konishi, K. Fujita, K. Nakanishi, K. Hirao, "Monolithic TiO<sub>2</sub> with Controlled Multiscale Porosity via a Template-Free Sol-Gel Process Accompanied by Phase Separation," *Chem. Mater.* **2006**, *18*, 6069.
- [92] D. C. M. Dutoit, M. Schneider, A. Baiker, "Titania-Silica Mixed Oxides 1. Influence of Sol-Gel and Drying Conditions on Structural Properties," *J. Catal.* **1995**, *153*, 165.
- [93] K. Y. Jung, S. Bin Park, "Enhanced Photoactivity of Silica-Embedded Titania Particles Prepared by Sol-gel Process for the Decomposition of Trichloroethylene," *Appl. Catal.*

- B Environ.* **2000**, *25*, 249.
- [94] F. Kleitz, F. Bérubé, R. Guillet-Nicolas, C. M. Yang, M. Thommes, "Probing Adsorption, Pore Condensation, and Hysteresis Behavior of Pure Fluids in Three-Dimensional Cubic Mesoporous KIT-6 Silica," *J. Phys. Chem. C* **2010**, *114*, 9344.
- [95] M. Thommes, K. A. Cychosz, "Physical Adsorption Characterization of Nanoporous Materials: Progress and Challenges," *Adsorption* **2014**, *20*, 233.
- [96] S. Yun, H. Luo, Y. Gao, "Superhydrophobic Silica Aerogel Microspheres from Methyltrimethoxysilane: Rapid Synthesis via Ambient Pressure Drying and Excellent Absorption Properties," *RSC Adv.* **2014**, *4*, 4535.
- [97] A. A. Popov, S. Yang, L. Dunsch, "Endohedral Fullerenes," *Chem. Rev.* **2013**, *113*, 5989.
- [98] A. Mishra, P. Bäuerle, "Small Molecule Organic Semiconductors on the Move: Promises for Future Solar Energy Technology," *Angew. Chemie - Int. Ed.* **2012**, *51*, 2020.
- [99] S. D. Collins, N. A. Ran, M. C. Heiber, T. Q. Nguyen, "Small Is Powerful: Recent Progress in Solution-Processed Small Molecule Solar Cells," *Adv. Energy Mater.* **2017**, *7*, 1602242.
- [100] S. S. Babu, H. Möhwald, T. Nakanishi, "Recent Progress in Morphology Control of Supramolecular Fullerene Assemblies and Its Applications," *Chem. Soc. Rev.* **2010**, *39*, 4021.
- [101] A. C. Stelson, S. J. Penterman, C. M. L. Watson, "Hierarchical Fullerene Assembly: Seeded Coprecipitation and Electric Field Directed Assembly," *Small* **2017**, *13*, 1.
- [102] A. Swinnen, I. Haeldermans, M. Vande Ven, J. D'Haen, G. Vanhoyland, S. Aresu, M. D'Olieslaeger, J. Manca, "Tuning the Dimensions of C60-Based Needlelike Crystals in Blended Thin Films," *Adv. Funct. Mater.* **2006**, *16*, 760.
- [103] C. D. Bain, E. B. Troughton, Y. T. Tao, J. Evall, G. M. Whitesides, R. G. Nuzzo, "Formation of Monolayer Films by the Spontaneous Assembly of Organic Thiols from Solution onto Gold," *J. Am. Chem. Soc.* **1989**, *111*, 321.
- [104] E. Pensa, E. Cortes, G. Corthey, P. Carro, C. Vericat, M. H. Fonticelli, G. Benítez, A. A. Rubert, R. C. Salvarezza, "The Chemistry of the Sulfur-Gold Interface: In Search of a Unified Model," *Acc. Chem. Res.* **2012**, *45*, 1183.
- [105] H.-J. Butt, K. Graf, M. Kappl, "Physics and Chemistry of Interfaces," Wiley-VCH, Weinheim, **2003**.
- [106] E. Ueda, P. A. Levkin, "Emerging Applications of Superhydrophilic-Superhydrophobic

- Micropatterns,” *Adv. Mater.* **2013**, *25*, 1234.
- [107] L. Xue, Y. Han, “Pattern Formation by Dewetting of Polymer Thin Film,” *Prog. Polym. Sci.* **2011**, *36*, 269.
- [108] D. Gentili, G. Foschi, F. Valle, M. Cavallini, F. Biscarini, “Applications of Dewetting in Micro and Nanotechnology,” *Chem. Soc. Rev.* **2012**, *41*, 4430.
- [109] E. Meyer, H. G. Braun, “Controlled Dewetting Processes on Microstructured Surfaces - A New Procedure for Thin Film Microstructuring,” *Macromol. Mater. Eng.* **2000**, 276–277, 44.
- [110] Z. Zhang, Z. Wang, R. Xing, Y. Han, “How to Form Regular Polymer Microstructures by Surface-Pattern-Directed Dewetting,” *Surf. Sci.* **2003**, *539*, 129.
- [111] Y. Xing, L. Dai, “Nanodiamonds for Nanomedicine,” *Nanomedicine* **2009**, *4*, 207.
- [112] A. S. Barnard, “Diamond Standard in Diagnostics: Nanodiamond Biolabels Make Their Mark,” *Analyst* **2009**, *134*, 1751.
- [113] C. Fu, H. Lee, K. Chen, T. Lim, H. Wu, P. Lin, P. Wei, P. Tsao, H. Chang, W. Fann, “Characterization and Application of Single Fluorescent Nanodiamonds as Cellular Biomarkers,” *PNAS* **2007**, *104*, 727.
- [114] R. Schirhagl, K. Chang, M. Loretz, C. L. Degen, “Nitrogen-Vacancy Centers in Diamond: Nanoscale Sensors for Physics and Biology,” *Annu. Rev. Phys. Chem.* **2014**, *65*, 83.
- [115] A. Gruber, A. Dräbenschmidt, C. Tietz, L. Fleury, J. Wrachtrup, C. Von Borczyskowski, “Scanning Confocal Optical Microscopy and Scanning Confocal Optical Microscopy and Magnetic Resonance on Single Defect Centers,” *Science* **1997**, *276*, 2012.
- [116] R. D. Akiel, V. Stepanov, S. Takahashi, “High-Frequency Electron Paramagnetic Resonance Spectroscopy of Nitroxide-Functionalized Nanodiamonds in Aqueous Solution,” *Cell Biochem. Biophys.* **2017**, *75*, 151.
- [117] B. V. Yavkin, V. A. Soltamov, R. A. Babunts, A. N. Anisimov, P. G. Baranov, F. M. Shakhov, S. V. Kidalov, A. Y. Vul’, G. V. Mamin, S. B. Orlinskii, “Defects in Nanodiamonds: Application of High-Frequency Cw and Pulse EPR, ODMR,” *Appl. Magn. Reson.* **2014**, *45*, 1035.
- [118] Y. Matsuzaki, H. Morishita, T. Shimooka, T. Tashima, K. Kakuyanagi, K. Semba, W. J. Munro, H. Yamaguchi, N. Mizuochi, S. Saito, “Optically Detected Magnetic Resonance of High-Density Ensemble of NV Centers in Diamond,” **2015**, *1*.
- [119] A. H. Heffernan, A. D. Greentree, B. C. Gibson, “Nanodiamond Arrays on Glass for Quantification and Fluorescence Characterisation,” *Sci. Rep.* **2017**, *7*, 1.



- 
- [120] M. Jiang, J. A. Kurvits, Y. Lu, A. V. Nurmikko, R. Zia, "Reusable Inorganic Templates for Electrostatic Self-Assembly of Individual Quantum Dots, Nanodiamonds, and Lanthanide-Doped Nanoparticles," *Nano Lett.* **2015**, *15*, 5010.
- [121] S. K. Lee, J. H. Kim, M. G. Jeong, M. J. Song, D. S. Lim, "Direct Deposition of Patterned Nanocrystalline CVD Diamond Using an Electrostatic Self-Assembly Method with Nanodiamond Particles," *Nanotechnology* **2010**, *21*, DOI 10.1088/0957-4484/21/50/505302.
- [122] D. Suter, F. Jelezko, "Single-Spin Magnetic Resonance in the Nitrogen-Vacancy Center of Diamond," *Prog. Nucl. Magn. Reson. Spectrosc.* **2017**, *98–99*, 50.
- [123] M. W. Doherty, N. B. Manson, P. Delaney, F. Jelezko, J. Wrachtrup, L. C. L. Hollenberg, "The Nitrogen-Vacancy Colour Centre in Diamond," *Phys. Rep.* **2013**, *528*, 1.
- [124] A. Jarmola, V. M. Acosta, K. Jensen, S. Chemerisov, D. Budker, "Temperature- and Magnetic-Field-Dependent Longitudinal Spin Relaxation in Nitrogen-Vacancy Ensembles in Diamond," *Phys. Rev. Lett.* **2012**, *108*, 1.
- [125] A. Dréau, M. Lesik, L. Rondin, P. Spinicelli, O. Arcizet, J. F. Roch, V. Jacques, "Avoiding Power Broadening in Optically Detected Magnetic Resonance of Single NV Defects for Enhanced Dc Magnetic Field Sensitivity," *Phys. Rev. B - Condens. Matter Mater. Phys.* **2011**, *84*, 1.
- [126] J. P. Tetienne, T. Hingant, L. Rondin, A. Cavaillès, L. Mayer, G. Dantelle, T. Gacoin, J. Wrachtrup, J. F. Roch, V. Jacques, "Spin Relaxometry of Single Nitrogen-Vacancy Defects in Diamond Nanocrystals for Magnetic Noise Sensing," *Phys. Rev. B - Condens. Matter Mater. Phys.* **2013**, *87*, 1.
- [127] M. A. C. Campos, J. M. J. Paulusse, H. Zuilhof, "Functional Monolayers on Oxide-Free Silicon Surfaces via Thiol-ene Click Chemistry," *Chem. Commun.* **2010**, *46*, 5512.
- [128] T. Lummerstorfer, H. Hoffmann, "Click Chemistry on Surfaces: 1,3-Dipolar Cycloaddition Reactions of Azide-Terminated Monolayers on Silica," *J. Phys. Chem. B* **2004**, *108*, 3963.
- [129] G. K. Such, J. F. Quinn, A. Quinn, E. Tjipto, F. Caruso, "Assembly of Ultrathin Polymer Multilayer Films by Click Chemistry," *JACS* **2006**, *128*, 9318.
- [130] C. Wendeln, S. Rinnen, C. Schulz, H. F. Arlinghaus, B. J. Ravoo, "Photochemical Microcontact Printing by Thiol-Ene and Thiol-Yne Click Chemistry," *Langmuir* **2010**, *26*, 15966.
- [131] J. Mehlich, B. J. Ravoo, "Click Chemistry by Microcontact Printing on Self-Assembled
-

- Monolayers: A Structure–reactivity Study by Fluorescence Microscopy,” *Org. Biomol. Chem.* **2011**, *9*, 4108.
- [132] D. I. Rozkiewicz, D. Janczewski, W. Verboom, B. J. Ravoo, D. N. Reinhoudt, “Click Chemistry by Microcontact Printing,” *Angew. Chem. Int. Ed.* **2006**, *45*, 5292.
- [133] J. R. Trantum, Z. E. Eagleton, C. A. Patil, J. M. Tucker-Schwartz, M. L. Baglia, M. C. Skala, F. R. Haselton, “Cross-Sectional Tracking of Particle Motion in Evaporating Drops: Flow Fields and Interfacial Accumulation,” *Langmuir* **2013**, *29*, 6221.
- [134] H. Hu, R. G. Larson, “Marangoni Effect Reverses Coffee-Ring Depositions,” *J. Phys. Chem. B* **2006**, *110*, 7090.
- [135] “Zeonex,” can be found under <https://www.zeonex.com/optics.aspx.html>, **2018**.
- [136] H. Bach, N. Neuroth, “The Properties of Optical Glass,” Springer-Verlag Berlin Heidelberg, **1998**.
- [137] G. Woyessa, A. Fasano, C. Markos, A. Stefani, H. K. Rasmussen, O. Bang, “Zeonex Microstructured Polymer Optical Fiber: Fabrication Friendly Fibers for High Temperature and Humidity Insensitive Bragg Grating Sensing,” *Opt. Mater. Express* **2017**, *7*, 286.
- [138] R. Ye, T. Oyama, K. Ohta, M. Baba, “Flexible Pentacene Thin Film Transistors with Cyclo-Olefin Polymer as a Gate Dielectric,” *Phys. Procedia* **2011**, *14*, 172.
- [139] I. Botiz, S. B. Darling, “Optoelectronics Using Block Copolymers,” *Mater. Today* **2010**, *13*, 42.
- [140] R. Glass, M. Arnold, J. Blümmel, A. Küller, M. Moller, J. P. Spatz, “Micro-Nanostructured Interfaces Fabricated by the Use of Inorganic Block Copolymer Micellar Monolayers as Negative Resist for Electron-Beam Lithography,” *Adv. Funct. Mater.* **2003**, *13*, 569.
- [141] A. B. Ebrahim Attia, Z. Y. Ong, J. L. Hedrick, P. P. Lee, P. L. R. Ee, P. T. Hammond, Y. Y. Yang, “Mixed Micelles Self-Assembled from Block Copolymers for Drug Delivery,” *Curr. Opin. Colloid Interface Sci.* **2011**, *16*, 182.
- [142] K. Kataoka, A. Harada, Y. Nagasaki, “Block Copolymer Micelles for Drug Delivery: Design, Characterization and Biological Significance,” *Adv. Drug Deliv. Rev.* **2001**, *47*, 113.
- [143] S. B. Darling, “Block Copolymers for Photovoltaics,” *Energy Environ. Sci.* **2009**, *2*, 1266.
- [144] L. Qiang, Z. Ma, Z. Zheng, R. Yin, W. Huang, “Novel Photo-Crosslinkable Light-Emitting Rod/Coil Copolymers: Underlying Facile Material for Fabricating Pixelated Displays,” *Macromol. Rapid Commun.* **2006**, *27*, 1779.

- 
- [145] Q. Li, J. He, E. Glogowski, X. Li, J. Wang, T. Emrick, T. P. Russell, "Responsive Assemblies: Gold Nanoparticles with Mixed Ligands in Microphase Separated Block Copolymers," *Adv. Mater.* **2008**, *20*, 1462.
- [146] J. Q. Lu, S. S. Yi, "Uniformly Sized Gold Nanoparticles Derived from PS-b-P2VP Block Copolymer Templates for the Controllable Synthesis of Si Nanowires," *Langmuir* **2006**, *22*, 3951.
- [147] S. G. Jang, E. J. Kramer, C. J. Hawker, "Controlled Supramolecular Assembly of Micelle-like Gold Nanoparticles in PS-b-P2VP Diblock Copolymers via Hydrogen Bonding," *J. Am. Chem. Soc.* **2011**, *133*, 16986.
- [148] J. Chai, F. Huo, Z. Zheng, L. R. Giam, W. Shim, C. A. Mirkin, "Scanning Probe Block Copolymer Lithography," *PNAS* **2010**, *107*, 20202.
- [149] J. H. Lim, C. A. Mirkin, "Electrostatically Driven Dip-Pen Nanolithography of Conducting Polymers," *Adv. Mater.* **2002**, *14*, 1474.
- [150] M. S. Onses, C. Song, L. Williamson, E. Sutanto, P. M. Ferreira, A. G. Alleyne, P. F. Nealey, H. Ahn, J. A. Rogers, "Hierarchical Patterns of Three-Dimensional Block-Copolymer Films Formed by Electrohydrodynamic Jet Printing and Self-Assembly," *Nat. Nanotechnol.* **2013**, *8*, 667.
- [151] A. Urtizbera, M. Hirtz, "A Diffusive Ink Transport Model for Lipid Dip-Pen Nanolithography," *Nanoscale* **2015**, *7*, 15618.
- [152] S. Basu, M. M. Sharma, "Measurement of Critical Disjoining Pressure for Dewetting of Solid Surfaces," *J. Colloid Interface Sci.* **1996**, *181*, 443.
- [153] H. I. Kim, C. M. Mate, K. A. Hannibal, S. S. Perry, "How Disjoining Pressure Drives the Dewetting of a Polymer Film on a Silicon Surface," *Phys. Rev. Lett.* **1999**, *82*, 3496.
- [154] J. Zhao, S. Granick, "How Polymer Surface Diffusion Depends on Surface Coverage," *Macromolecules* **2007**, *40*, 1243.
- [155] P. W. Voorhees, "The Theory of Ostwald Ripening," *J. Stat. Phys.* **1985**, *38*, 231.
- [156] M. J. Skaug, J. N. Mabry, D. K. Schwartz, "Single-Molecule Tracking of Polymer Surface Diffusion," *JACS* **2014**, *136*, 1327.
- [157] D. Kim, J. M. Zuidema, J. Kang, Y. Pan, L. Wu, D. Warther, B. Arkles, M. J. Sailor, "Facile Surface Modification of Hydroxylated Silicon Nanostructures Using Heterocyclic Silanes," *JACS* **2016**, *138*, 15106.
- [158] Y. Pan, A. Maddox, T. Min, F. Gonzaga, J. Goff, B. Arkles, "Surface-Triggered Tandem Coupling Reactions of Cyclic Azasilanes," *Chem. Asian J.* **2017**, *12*, 1198.
-

- [159] Y. Wang, Y. Qin, A. Berger, E. Yau, C. He, L. Zhang, U. Gösele, M. Knez, M. Steinhart, "Nanoscopic Morphologies in Block Copolymer Nanorods as Templates for Atomic-Layer Deposition of Semiconductors," *Adv. Mater.* **2009**, *21*, 2763.
- [160] D. P. Puzzo, A. C. Arsenault, I. Manners, G. A. Ozin, "Electroactive Inverse Opal: A Single Material for All Colors," *Angew. Chemie - Int. Ed.* **2009**, *48*, 943.
- [161] Y. C. Wing, S. B. Clendenning, A. Berenbaum, A. J. Lough, S. Aouba, H. E. Ruda, I. Manners, "Highly Metallized Polymers: Synthesis, Characterization, and Lithographic Patterning of Polyferrocenylsilanes with Pendant Cobalt, Molybdenum, and Nickel Cluster Substituents," *J. Am. Chem. Soc.* **2005**, *127*, 1765.
- [162] J. A. Massey, K. N. Power, M. A. Winnik, I. Manners, "Organometallic Nanostructures: Self-Assembly of Poly(Ferrocene) Block Copolymers," *Adv. Mater.* **1998**, *10*, 1559.
- [163] Y. Gou, X. Tong, Q. Zhang, H. Wang, B. Wang, S. Xie, Y. Wang, "Synthesis of Hyperbranched Polyferrocenylsilanes as Preceramic Polymers for Fe/Si/C Ceramic Microspheres with Porous Structures," *J. Mater. Sci.* **2015**, *50*, 7975.
- [164] B. Tang, R. Petersen, D. A. Foucher, A. Lough, N. Coombs, R. Sodhib, I. Manners, "Novel Ceramic and Organometallic Depolymerization Products from Poly(Ferrocenylsilanes) via Pyrolysis," *J. Chem. Soc., Chem. Commun.* **1993**, 523.
- [165] S. Lastella, H. Yang, D. Rider, I. Manners, P. M. Ajayan, C. Y. Ryu, "Influences of Organometallic Polymer-Derived Catalyst Dispersion on SWNT Growth," *J. Polym. Sci. Part B Polym. Phys.* **2007**, *45*, 758.
- [166] J. Q. Lu, D. A. Rider, E. Onyegam, H. Wang, M. A. Winnik, I. Manners, Q. Cheng, Q. Fu, J. Liu, "Carbon Nanotubes with Small and Tunable Diameters from Poly(Ferrocenylsilane)-Block-Polysiloxane Diblock Copolymers," *Langmuir* **2006**, *22*, 5174.
- [167] S. Lastella, G. Mallick, R. Woo, S. P. Karna, D. A. Rider, I. Manners, Y. J. Jung, C. Y. Ryu, P. M. Ajayan, "Parallel Arrays of Individually Addressable Single-Walled Carbon Nanotube Field-Effect Transistors," *J. Appl. Phys.* **2006**, *99*, DOI 10.1063/1.2161820.
- [168] J. Q. Lu, T. E. Kopley, N. Moll, D. Roitman, D. Chamberlin, Q. Fu, J. Liu, T. P. Russell, D. A. Rider, I. Manners, M. A. Winnik, "High-Quality Single-Walled Carbon Nanotubes with Small Diameter, Controlled Density, and Ordered Locations Using a Polyferrocenylsilane Block Copolymer Catalyst Precursor," *Chem. Mater.* **2005**, *17*, 2227.
- [169] J. Gavillet, A. Loiseau, C. Journet, F. Willaime, F. Ducastelle, J. C. Charlier, "Root-Growth Mechanism for Single-Wall Carbon Nanotubes," *Phys. Rev. Lett.* **2001**, *87*,

- 275504.
- [170] D. J. Ellenberger, D. A. Miller, R. O. Williams, "Expanding the Application and Formulation Space of Amorphous Solid Dispersions with KinetiSol®: A Review," *AAPS PharmSciTech* **2018**, *19*, 1933.
- [171] K. Göke, T. Lorenz, A. Repanas, F. Schneider, D. Steiner, K. Baumann, H. Bunjes, A. Dietzel, J. H. Finke, B. Glasmacher, A. Kwade, "Novel Strategies for the Formulation and Processing of Poorly Water-Soluble Drugs," *Eur. J. Pharm. Biopharm.* **2018**, *126*, 40.
- [172] R. Al-Kassas, M. Bansal, J. Shaw, "Nanosizing Techniques for Improving Bioavailability of Drugs," *J. Control. Release* **2017**, *260*, 202.
- [173] H. D. Williams, N. L. Trevaskis, S. A. Charman, R. M. Shanker, W. N. Charman, C. W. Pouton, C. J. H. Porter, "Strategies to Address Low Drug Solubility in Discovery and Development," *Pharmacol. Rev.* **2013**, *65*, 315.
- [174] M. A. Repka, S. Bandari, V. R. Kallakunta, A. Q. Vo, H. McFall, M. B. Pimparade, A. M. Bhagurkar, "Melt Extrusion with Poorly Soluble Drugs – An Integrated Review," *Int. J. Pharm.* **2018**, *535*, 68.
- [175] J. Norman, R. D. Madurawe, C. M. V Moore, M. A. Khan, A. Khairuzzaman, "A New Chapter in Pharmaceutical Manufacturing: 3D-Printed Drug Products," *Adv. Drug Deliv. Rev.* **2017**, *108*, 39.
- [176] S. Pravin, A. Sudhir, "Integration of 3D Printing with Dosage Forms: A New Perspective for Modern Healthcare," *Biomed. Pharmacother.* **2018**, *107*, 146.
- [177] Y. Liu, J. Zhao, L. Wang, B. Yan, Y. Gu, P. Chang, Y. Wang, "Nanocrystals Technology for Transdermal Delivery of Water-Insoluble Drugs," *Curr. Drug Deliv.* **2018**, *15*, 1221.
- [178] C. E. Mora-Huertas, H. Fessi, A. Elaissari, "Polymer-Based Nanocapsules for Drug Delivery," *Int. J. Pharm.* **2010**, *385*, 113.
- [179] B. Kumar, K. Jalodia, P. Kumar, H. K. Gautam, "Recent Advances in Nanoparticle-Mediated Drug Delivery," *J. Drug Deliv. Sci. Technol.* **2017**, *41*, 260.
- [180] M.-L. Chen, M. John, S. L. Lee, K. M. Tyner, "Development Considerations for Nanocrystal Drug Products," *AAPS J.* **2017**, *19*, 642.
- [181] R. Jog, D. J. Burgess, "Pharmaceutical Amorphous Nanoparticles," *J. Pharm. Sci.* **2017**, *106*, 39.
- [182] V. Patel, O. P. Sharma, T. Mehta, "Nanocrystal: A Novel Approach to Overcome Skin Barriers for Improved Topical Drug Delivery," *Expert Opin. Drug Deliv.* **2018**, *15*, 351.

- [183] E. Merisko-Liversidge, G. G. Liversidge, "Nanosizing for Oral and Parenteral Drug Delivery: A Perspective on Formulating Poorly-Water Soluble Compounds Using Wet Media Milling Technology," *Adv. Drug Deliv. Rev.* **2011**, *63*, 427.
- [184] D. Arora, B. Khurana, G. Rath, S. Nanda, A. K. Goyal, "Recent Advances in Nanosuspension Technology for Drug Delivery," **2018**.
- [185] C. Guguta, I. Eeuwijk, J. M. M. Smits, R. De Gelder, "Structural Diversity of Ethinyl Estradiol Solvates," *Cryst. Growth Des.* **2008**, *8*, 823.
- [186] P. P. Constantinides, M. V. Chaubal, R. Shorr, "Advances in Lipid Nanodispersions for Parenteral Drug Delivery and Targeting," *Adv. Drug Deliv. Rev.* **2008**, *60*, 757.
- [187] A. A. Date, N. Vador, A. Jagtap, M. S. Nagarsenker, "Lipid Nanocarriers (GeluPearl) Containing Amphiphilic Lipid Gelucire 50/13 as a Novel Stabilizer: Fabrication, Characterization and Evaluation for Oral Drug Delivery," *Nanotechnology* **2011**, *22*, 275102.
- [188] B. S. Chu, S. Ichikawa, S. Kanafusa, M. Nakajima, "Preparation of Protein-Stabilized  $\beta$ -Carotene Nanodispersions by Emulsification-Evaporation Method," *JAOCS, J. Am. Oil Chem. Soc.* **2007**, *84*, 1053.
- [189] Z. L. Zhang, Y. Le, J. X. Wang, H. Zhao, J. F. Chen, "Development of Stabilized Itraconazole Nanodispersions by Using High-Gravity Technique," *Drug Dev. Ind. Pharm.* **2012**, *38*, 1512.